UNIVERSITÀ DELLA CALABRIA

UNIVERSITA' DELLA CALABRIA

Dipartimento di Ingegneria Meccanica, Energetica e Gestionale

Dottorato di Ricerca in
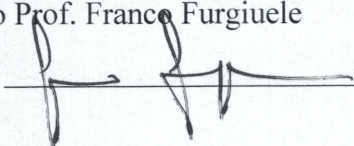
Ingegneria Civile e Industriale
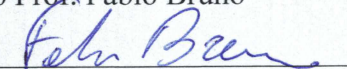
CICLO

XXXI

INNOVATIVE MANIPULATION TECHNIQUES FOR UNDERWATER ROBOTICS

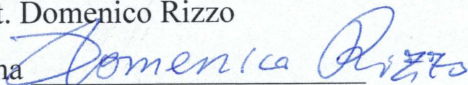**Settore Scientifico Disciplinare ING-IND/15**

Coordinatore: Ch.mo Prof. Franco Furgiuele

Firma _____

Supervisore/Tutor: Ch.mo Prof. Fabio Bruno

Firma _____

Dottorando: Dott. Domenico Rizzo

Firma _____

To Elena and my Family.

"E in mezzo a questo mare

Cercherò di scoprire quale stella sei

Perché mi perderei

Se dovessi capire che stanotte non ci sei."

La sera dei miracoli, Lucio Dalla, 1980

Abstract

This thesis is concerned with innovative manipulation techniques for underwater robotics and ocean engineering. In particular, it focuses on challenging problems of three different areas of the underwater manipulation, regarding the position feedback of the robotic arm, the visual feedback, and the manipulation of fragile objects.

First, the position feedback has been addressed studying the kinematic performance of a hydraulic manipulator, in term of its accuracy and repeatability, used for underwater artifact cleaning activity. The manipulator has been re-designed during the CoMAS (In-situ conservation planning of Underwater Archaeological Artefacts) project. The results of the study have been of fundamental importance in the development of the control strategies for the control of the ROV and its manipulator. In fact, on the basis of the maximum error positions found and the kinematic performance of the arm it has been defined a "safety range" that allows avoiding collisions among the end-effector's tool and the artifacts.

Second, the visual feedback has been addressed presenting an augmented reality visualization of scene depth for aiding ROV (Remotely Operated Vehicle) pilots in underwater manipulation. The architecture and the software of the system have been developed during the CoMAS project, while in this thesis has been provided the calibration of the whole system. In particular, combining the kinematics of the robotic arm and the standard photogrammetric model of the stereo camera, it has been possible to generate a depth map that shows to the pilots the distances of the surface of the scene objects from the end-effector's pose. Experimental trials have been carried out in the laboratory and in the water tank in order to evaluate and improve the performance of the system, approaching the target softly.

Despite the development of these feedbacks, currently, existing robotic manipulators are often too powerful and awkward to handle delicate or complex objects without damaging them. To figure this out, soft end effectors have been studied during my research internship at the faculty of Ocean Engineering of the University of Rhode Island (USA). The research activity has been carried out at the Robotics Laboratory for Complex

Underwater Environments (R-CUE). In particular, it focuses on continues the development, prototyping, and testing of compliant jamming grippers based on Soft Robotics technologies. Specifically, the subject is divided into two main projects, studying both a universal jamming gripper and a hybrid toroidal soft gripper. The main purpose the universal jamming gripper has been to complete the integration with the existing arm, design and perform experiments with the gripper in the water tank, and propose refinements to the design of the mechanical and hydraulic system. While, the hybrid toroidal soft gripper has been designed, prototyped, and integrated with the existing arm and hydraulic system, to the end of carrying out a qualitative performance of the gripper in the water tank. The first extended trials of the hybrid toroidal soft gripper have been carried out at the Department of Mechanics, Energy, and Management (DIMEG) at the University of Calabria.

Sommario

Il presente lavoro di tesi affronta in maniera organica diverse problematiche legate alle tecniche di manipolazione adoperate per la robotica subacquea e l'ingegneria marina. In particolare, si concentra sulle tecniche adottate per ridurre e migliorare il carico di lavoro a cui, spesso, piloti dei veicoli filoguidati, denominati ROVs (Remotely Operated Vehicles), biologi, oceanografi e ricercatori si trovano ad affrontare per raggiungere un obiettivo di manipolazione in ambiente subacqueo tramite bracci robotici.

A tal fine, il presente lavoro affronta le problematiche relative a tre linee di ricerca della manipolazione subacquea, riguardanti il feedback di posizionamento dell'end-effector del braccio robotico, l'arricchimento scena inquadrata con un feedback in realtà aumentata e infine di valutare la possibilità di manipolare oggetti fragili senza danneggiarli.

Le attività di ricerca riguardante i feedback di posizionamento e visivi si sono concretizzate studiando le tematiche emerse nell'ambito del progetto CoMAS (COnservazione programmata in situ di Manufatti Archeologici Sommersi). Nello specifico, durante il progetto è stato progettato un ROV, equipaggiato con un braccio robotico a 5 gradi di libertà, una stereo camera ottica e altri sensori acustici.

In primo luogo, la ricerca affronta il feedback di posizione studiando le prestazioni cinematiche di un manipolatore idraulico, utilizzato per l'attività di pulizia di manufatti archeologici subacquei. Nello specifico, sono state calcolate le performance del braccio robotico, in termini di accuratezza e ripetibilità, in maniera tale da definire un "safety range" che permette al pilota del ROV di approcciare l'end-effector al manufatto subacqueo in maniera delicata.

In secondo luogo, il feedback visivo è stato affrontato sviluppando una tecnica in realtà aumentata per la visualizzazione della mappa di profondità della scena inquadrata da una stereo camera in ambiente subacqueo in relazione alla posa dell'end-effector del braccio robotico. In particolare, combinando la cinematica diretta del braccio robotico e il modello geometrico fotogrammetrico della stereo camera, è stato possibile generare una mappa di profondità che mostra ai piloti ROV le distanze tra la superficie degli oggetti nella scena e la posizione dell'end-effector. Nella presente tesi si è affrontato il problema

della calibrazione del sistema complessivo, composto dallo skid del ROV in cui sono posizionati il braccio robotico (descritto precedentemente) e una camera stereoscopica. In particolare, sono state condotte le attività di determinazione sperimentale del centro ottico della stereo camera e della posa relativa tra quest'ultima e la base del braccio, utilizzando differenti metodi presenti in letteratura. Infine sono stati condotti dei test di caratterizzazione del sistema sia in laboratorio che in vasca, in maniera da valutare l'avvicinamento controllato ai target.

Infine, soft grippers da montare come end-effector di bracci robotici trasportati da veicoli filoguidati sono stati studiati durante il periodo di ricerca all'estero, presso la facoltà di Ocean Engineering dell'Università del Rhode Island (USA). L'attività ha riguardato lo studio, l'ottimizzazione, la prototipazione e i test di grippers innovativi basati sull'approccio della Soft Robotics. Nello specifico, tali soft grippers sono capaci di modulare la rigidezza di materiale granulare contenuto all'interno di una membrana, in maniera tale da limitare passivamente la forza applicata a oggetti fragili, semplificandone la manipolazione. L'argomento è composto da due progetti principali, riguardanti lo studio e test del gripper "universale", composto da una membrana, e il gripper "ibrido toroidale", composto da due mambrane. Parte della fase sperimentale di caratterizzazione del gripper "ibrido toroidale" è stata successivamente condotta presso il Dipartimento di Ingegneria Meccanica, Energetica e Gestionale (DIMEG) dell'Università della Calabria.

Acknowledgements

Table of Contents

List of Figures

Introduction

Underwater manipulation has been widely investigated during the last few years. In fact, it is a key technology for marine industries and exploration that can be efficiently adopted in other application fields, such as underwater archaeology, biological manipulation, scientific expedition, as well as offshore construction in the Oil and Gas industry.

All these operations require a high quality of the work and a precise positioning of the manipulator's end-effectors, that makes intervention capacity of the ROV/AUV very challenging while working with manipulators under water. To this end, the aim of the scientific community in the field of underwater robotics is to develop a force-position feedback manipulator able to protect sensitive equipment on the seabed, as well as the environment. Nevertheless, the physical properties of an underwater manipulator may differ from the corresponding ideal values due to geometric errors, such as manufacturing tolerances and assembly misalignments, and non-geometric errors, such as the elastic deflection of the links, thermal deformations, and vibrations. Then, in many cases, manipulators do not behave according to their design but they make mistakes in achieving a specific pose or following trajectories. An error compensation process, that allows to identify and compensate these errors in the mathematical model of the robotic arm, needs to be carried out in order to overcome these limitations and improve the accuracy of the end-effector.

Additionally, underwater manipulation is performed remotely by expert pilots thanks to the visual feedback provided by one or more cameras but without any information about the distance between the end-effector and the target. To this end, different solutions have been presented in the literature improving the visual feedback in the operated underwater manipulation, by reducing the burden on the human operator.

Despite the development of these feedbacks, currently, existing robotic manipulators are often too powerful and awkward to handle delicate or complex objects without damaging them. Soft and compliant grippers have been shown to dramatically simplify the problem of grasping complex objects with robotic manipulators. They can be designed to passively

limit the force that is applied to fragile or sensitive objects, even when the exact shape of the object is unknown prior to grasping. For these reasons, (ease of grasping, force limiting without sensors, and inherent robustness) soft robotic grippers are an excellent match for the challenging problems that confront marine archaeologists and marine biologists sampling in the deep ocean.

To this end, this thesis addresses the challenging problem of three different area of underwater manipulation:

- position feedback;
- visual feedback;
- manipulation of fragile objects.

In particular, the position feedback has been addressed studying the kinematic performance of a hydraulic manipulator, used for underwater artifact cleaning activity. The manipulator has been re-designed during the CoMAS project. Firstly, the forward kinematic model of the robotic arm has been defined according to D-H notation. Subsequently, a data acquisition phase is carried out by collecting the joint angle values that are known by reading the absolute encoders mounted on the robotic arm. The forward kinematic model and the joint angle values collected are integrated in order to obtain a set of predicted end-effector poses. An external metrology system has been adopted in order to measure the actual end-effector pose in some different configurations. Next, the measurements of the predicted and the actual poses are compared in order to have an estimation of the positioning errors that are necessary for the definition of the kinematic performance of the robotic arm. And finally, the kinematic performance of the robotic arm, consisting in the repeatability and accuracy, are calculated according to the ISO standard 9283:1998.

The visual feedback has been addressed presenting an augmented reality visualization of scene depth for aiding ROV pilots in underwater manipulation. The architecture and the software of the system have been developed during the CoMAS project, while in this thesis has been provided the calibration of the whole system.

In particular, combining the kinematics of the robotic arm and the standard photogrammetric model of the stereo camera, it has been possible to generate a depth

map that shows to the pilots the distances of the surface of the scene objects from the end-effector's pose. Experimental trials have been carried out in the laboratory and in the water tank in order to evaluate and improve the performance of the system.

Finally, soft end effectors have been studied during my research internship at the faculty of Ocean Engineering of the University of Rhode Island (USA). The research took place at the Robotics Laboratory for Complex Underwater Environments (R-CUE) under the supervision of Prof. Stephen Licht. In particular, the research focuses on continues the development, prototyping, and testing of the compliant jamming grippers developed at the R-CUE. Specifically, the subject is divided into two main projects, studying both a universal jamming gripper and a hybrid toroidal soft gripper. The main purpose the universal jamming gripper has been to complete the integration with the existing arm, design and perform experiments with the gripper in the water tank, and propose refinements to the design of the mechanical and hydraulic system. While, the hybrid toroidal soft gripper has been designed, prototyped, and integrated with the existing arm and hydraulic system, to the end of carrying out a qualitative performance of the gripper in the water tank. The first extended trials of the hybrid toroidal soft gripper have been carried out at the Department of Mechanics, Energy, and Management (DIMEG) at the University of Calabria.

Thesis started with an overview of thesis main topics and objectives, presented in this Introduction Chapter. The work encompasses different topics (underwater robotics, underwater manipulation, soft robotics, and underwater soft robotics and grippers). Chapter 1 tries to give an extensive background of all problems tackled in the thesis, of chosen approaches and relevant possible alternatives.

Then, Chapter 2 treats a study conducted for evaluating the kinematic performance of a hydraulic underwater manipulator for artifacts cleaning.

Chapter 3 discusses a novel system based on a sensorized robotic arm, stereoscopic 3D perception and augmented reality visualization to support ROV's pilots in underwater manipulation tasks.

In Chapter 4, focused on the development, prototyping, and testing of compliant jamming grippers, for the challenging problems that confront marine archaeologists and marine

biologists sampling in the deep ocean, developed during my internship at the University of Rhode Island (USA).

Finally, a Conclusion Chapter summarizes topics and results and considers possible further developments and research lines.

1. State of the art

In this section, a review of commonly employed underwater robotics is presented, in line with the purpose of the thesis. First, a brief introduction showing the constantly expanding role of marine robotics in ocean engineering is given, considering some historical backgrounds given by projects that have succeeded over the years. Next, the effort will be focused on research aspects of underwater robotics, regarding manipulators, vehicles and control systems, that together are defined as Underwater Vehicle Manipulator System (UVMS). In particular, have been analyzed different solutions implemented in literature with the end of improving the visual and positioning feedback, as well as guidance and control algorithms of the UVMS.

Next, we will focus on relievable scientific aspects of underwater manipulations, related to the use of robotic arms mounted on underwater vehicles to accomplish specific biological/scientific tasks.

Finally, the proliferation of soft robotics research worldwide has brought substantial achievements in terms of principles, models, technologies, techniques and prototype of soft robots. After a review, we will focus on relievable technologies and applications that can be actually adopted to ensure a soft touch in the underwater field.

1.1. Underwater robotics

Water covers more than 70% of our planet and, owning to hostile condition of deep seas, only a little percentage of seafloor is known and explored. The remaining part represents a potential huge source of information for biologists, geologists, archaeologists and many other researchers. The first scientific explorations were conducted primarily through the use of diving and human-occupied submersibles. Nowadays, technology progress provides tools and methodologies to investigate this unknown world. Underwater vehicles can represent a powerful tool for every kind of underwater activities. In many

circumstances, their employment is indispensable because of hostile time and condition operation. Scuba diver operations are, indeed limited up to fifty meters. Moreover, the operation time is inversely proportional to the depth. Even if they can noticeably differ from each other in size, costs, and capabilities, a general classification divides underwater vehicles in manned and unmanned (UUVs); the latter can be differentiated in Remotely Operated Vehicles (ROVs) and Autonomous Underwater Vehicles (AUVs). Manned submersible can dive up to known depths, directly driven by an operator, and sometime, hosting more than one human per mission. They can recover artifacts, manipulate the environment having scientist in-situ. Big disadvantages are the extremely high costs, both of vehicle and of deployment operation, and the limited underwater time.

Underwater Unmanned Vehicles (UUVs) can perform surveys in areas inaccessible to humans, and deploy a wide range of sensors useful for acquiring relevant data. At the present day, ROVs are probably the most used platforms, able to operate with guidance from outside while doing a survey. There is a link between the surface and the underwater vehicle made up by a so-called umbilical cable, which is used for the vehicle control, energy supply and data exchange. They are characterized by having their own means of propulsion. Generally, ROVs can perform different operations uninterruptedly and are able to recover artefacts. Apart from operator fatigue, their main constraints are due to the umbilical that limits depths, range and mobility; moreover, for large depths the umbilical winch increases and consequently the size of the ship that can support it. AUVs have a high degree of autonomy in the sense that they can navigate and locate itself using only their on-board sensors, and without permanent communication. AUVs have unmanned and untethered design, which makes them well suited to extended exploratory surveys requiring minimal user intervention and support. Meanwhile, their autonomous free-swimming capability has added a new paradigm of ocean sampling to the scientific user community as demonstrated. They complement the capabilities of tethered remotely operated vehicles (ROVs). They have relatively low operational costs, also because of fast surveying capabilities. Main drawbacks are the limited battery autonomy and the self-position estimation inside surveyed scene that can drift in large areas. Moreover, capability of recovering and interventions are nowadays limited and object of studies. Furthermore, researcher and scientists are increasingly interested in the use of

unmanned surface vehicles (USVs) for a variety of missions and applications. The term USV refers to any vehicle that operates on the surface of the water without a crew.

Several research projects have succeeded over the years, showing interest in underwater robotics. In the TRIDENT project, different mechatronic systems were integrated into the Girona-500 AUV to operate autonomously in specific underwater manipulation tasks (Ribas, et al., 2015). One of the most interesting projects has been carried out by the University of Hawaii, which has produced an AUV capable of carrying out manipulation tasks autonomously (Marani & Yuh, 2009). The project, which gives the vehicle's name, is called SAUVIM (Semi-Autonomous Underwater Vehicle for Intervention Mission). The vehicle is equipped with a manipulator with 7 DOF that, thanks to a force and torsion sensors positioned upstream of the wrist, and a camera tracking system is able to follow the position of the end-effector with a feedback, to carry out various autonomous operations.

Also worthy of note is the study carried out within the project AMADEUS (Advanced MAnupilator for DEep Underwater Sampling). AMADEUS is a dexterous subsea robot hand incorporating force and slip contact sensing, using fluid-filled tentacles for fingers (Lane, et al., 1998). In addition to the mechanical design, development of the hand has also considered closed loop finger position and force control, coordinated finger motion for grasping, force and slip sensor development/signal processing, and reactive world modeling/planning for supervisory 'blind grasping'. Furthermore, the project focused on the realization of a set-up composed of two 7-DOF ANSALDO manipulators to be used in cooperative mode (Casalino, et al., 2001).

ALIVE is a 4 DOF intervention AUV with a 7 DOF manipulator which is capable of autonomous navigation towards a position nearby an underwater intervention panel, detection of the panel and, finally, approaching and docking to the panel with two hydraulic grabs. Other projects are reported in Table 1.1. Each project involves different instrumentations and obviously a vehicle equipped with one or two manipulators (Table 1.1).

Project	Vehicle	Manipulator
ALIVE	ALIVE	7-DOF manipulator
VENUS	KAIKO	JAMSTEC 7 DOF manipulator
TRIDENT	GIRONA-500	CSIP Light-weight ARM 5E
SAUVIM	SAUVIM	ANSALDO MARIS 7080 7-DOF
AMADEUS	Heriot - Watt ANGUS 002	ANSALDO MARIS 7080 7-DOF
NEPTUNE	ROPOS	2 x Shilling Robotics TITAN 4

Table 1.1. Underwater projects succeeded over the years.

The effort developed in these projects make marine a challenging engineering problem with strong connections to several engineering domains. In fact, a major challenge concerning underwater robotics is the interaction with the environment by means of one or more manipulators. Autonomous UVMSs are still the object of research; the current trend is in developing the first semiautonomous robotic devices, which might be acoustically operated; moreover, if physically possible, the capability to dock to the structure where the intervention is needed might significatively simplify the control. The final aim might be to develop a completely autonomous UVMS, able to localize the intervention site, recognize the task to be performed, and act on it without docking to the station and without human intervention. This might make it possible to perform missions that are currently impossible such as autonomous archaeological intervention at deep sites.

1.1.1. Visual and positioning feedback solutions adopted to UVMSs

Here the attention will focus on different solutions implemented in literature, to the end of improving the visual and positioning feedback, as well as guidance and control algorithms of the UVMS.

In the research work performed by (Sagara & Ambar, 2015) are addressed the control problems of an underwater robot equipped with two electrical 3-DOF (degree of freedom) manipulators. The innovation introduced into the state of the art is the development and prototype of a simple and intuitive master-controller, capable of moving the vehicle and the two arms simultaneously (Figure 1. 1).
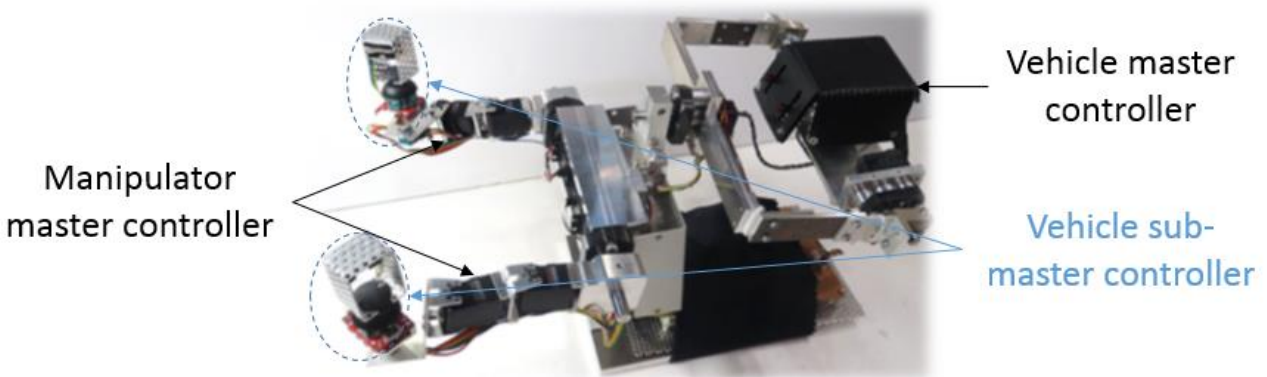
Figure 1. 1. Master controller prototype of the manipulators and the vehicle. Image taken from (Sagara & Ambar, 2015).

The robot base main master controller enables the user to control the motion of a slave robot in 3-dimensional space (3-DOF position and 3-DOF attitude) using only one hand. First, the translational motion of a robot (x, y, and z-axes) can be controlled using three slide-type potentiometers installed in a box-shaped controller. The translational speed of the robot is proportional to the changes of electrical potential (voltage) from the

potentiometers. Thus, the translational speed of the robot base can be controlled by adjusting the slide potentiometer levers (Figure 1. 2).
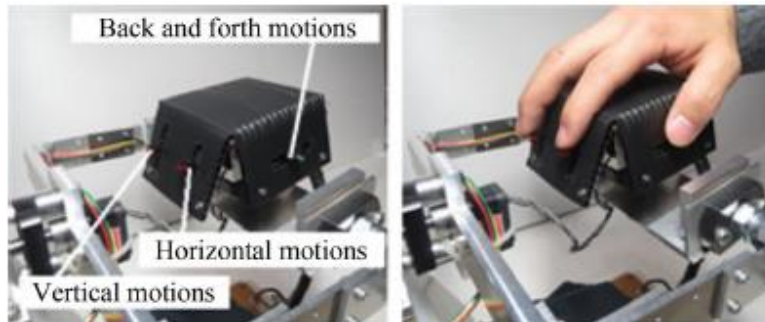
Figure 1. 2. Potentiometers. Images taken from (Sagara & Ambar, 2015).

The robot base controller consists of three servo actuators, with which is possible to control the Euler angles (Roll, Pitch, and Yaw) of the slave vehicle (Figure 1. 3).
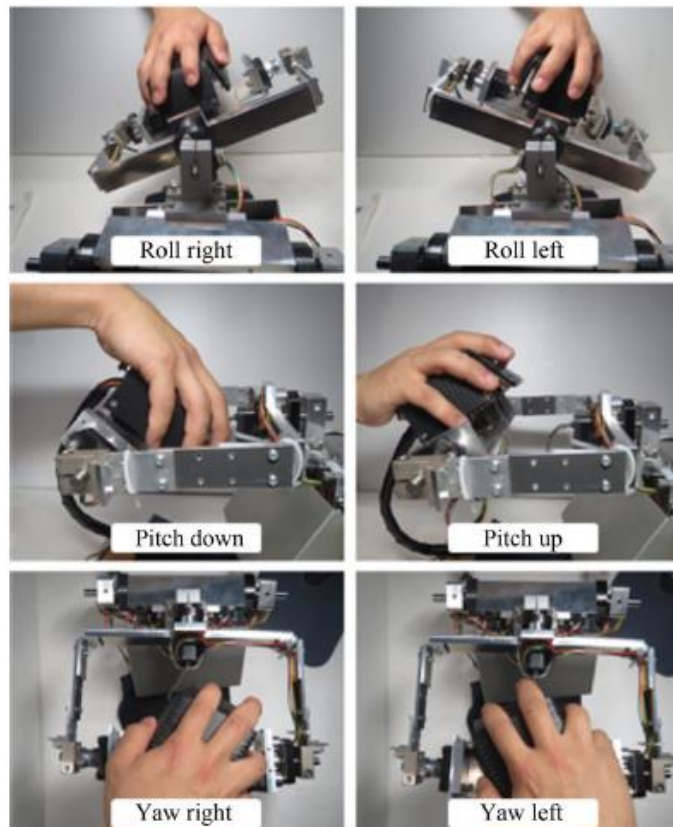
Figure 1. 3. Servo actuators. Images taken from (Sagara & Ambar, 2015).

Each joint is actuated by an RS302CD servo actuator (Futaba Corporation) using an RS-485 communication protocol. These servo actuators are used to provide the desired joint angles for the manipulators of the slave robot including keeping any desired postures of the slave robot manipulators. Each end-tip of the manipulator master controller is attached with a vehicle sub-master controller that consists of a joystick and tactile switches (SparkFun Electronics). The experiment was carried out in a water tank. The position and attitude of the robot can be calculated by monitoring the movement of three LEDs' light sources via CCD cameras. The data from CCD cameras were converted to position data using an X–Y video tracker (Figure 1. 4).
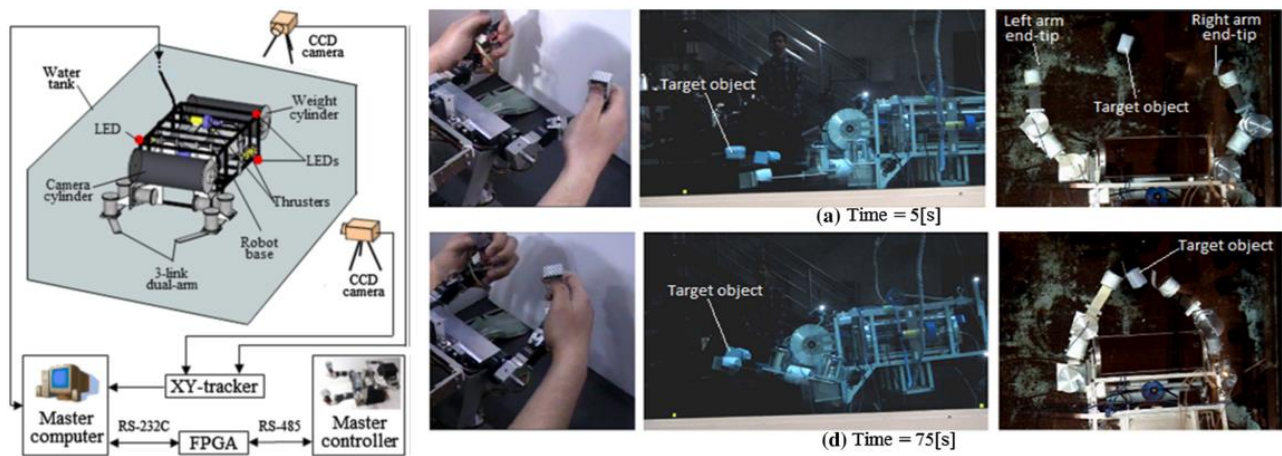
Figure 1. 4. UVMS trials on the water tank. Images taken from (Sagara & Ambar, 2015).

The research also highlights the feedback control of UVMS through Resolved Acceleration Control (RAC) Method (Sagara, et al., 2014). The desired and actual manipulator joint angles' is shown in Figure 1. 5.
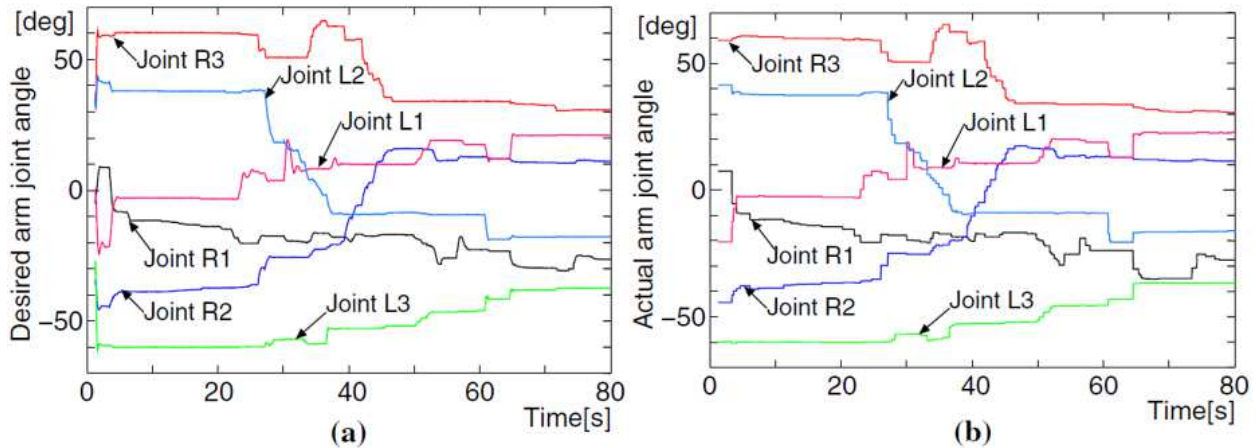
Figure 1. 5. Desired (a) and actual (b) manipulator joint angles'. Images taken from (Sagara & Ambar, 2015).

The authors demonstrate that the actual robot position and attitude correspond to the desired position and attitude imposed by the master controller.

Similar research work highlights the control of a human-sized ROV equipped with a pair of electrical manipulators adaptable to different underwater tasks (Sakagami, et al., 2010). In particular, the research is focused on the development of an ROV able to vary the attitude system through a mobile floating block, moving the arms toward the seabed or upwards. A master controller that replicates exactly UVMS movements has been presented (Figure 1. 6).
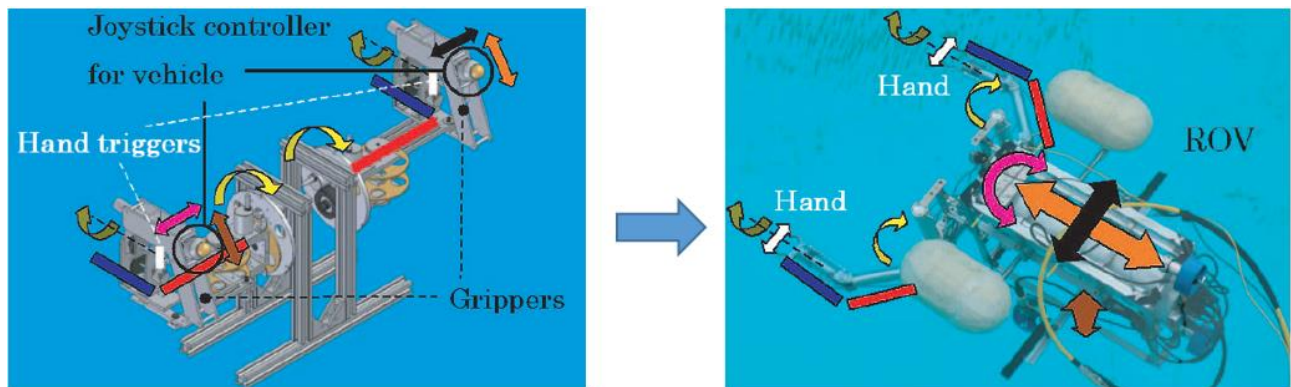
Figure 1. 6. Master-slave controller. ROV. Images taken from (Sakagami, Shibata, & Inoue, 2010).

The controller has 10 DOF that is equal to the total number of DOF of the vehicle-manipulators system. Moreover, two small joysticks are mounted on the controller to control the vehicle motion. A field trial in Lake Biwa (Japan) was conducted in order to carry out the qualitative capabilities of the developed UVMS (Figure 1. 7).

Figure 1. 7. Field trials. Images taken from (Sakagami, Shibata, & Inoue, 2010).

According to the growing interest in this field of research, my research team presented an interesting solution that can be applied to the UVMS. In particular, in (Barbieri, et al., 2018) has been proposed a modular architecture for a lightweight arm, which can be mounted on a small-sized ROVs. The arm has been equipped with an adaptive gripper that, taking advantage of the additive manufacturing techniques, is able to easily grip differently shaped objects (Figure 1. 8).

Figure 1. 8. Physical prototype of the arm. Image taken from (Barbieri et al., 2017).

The arm is controlled through a Master-Slave approach. Experimental tests have been carried out to measure and evaluate the gripping and manipulation capability of the robotic arm (Figure 1. 9) and the performance of the proposed control system (Figure 1. 10).
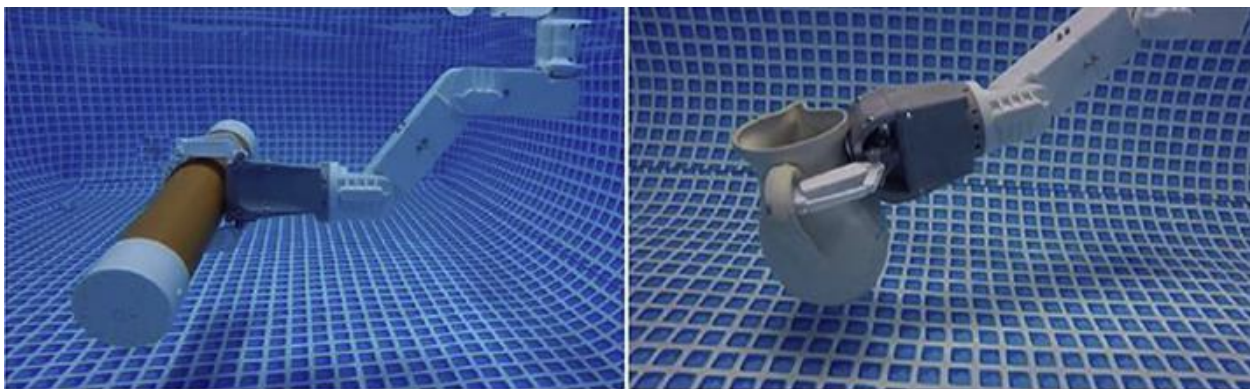
Figure 1. 9. Qualitative trials in the water tank. Image taken from (Barbieri et al., 2017).
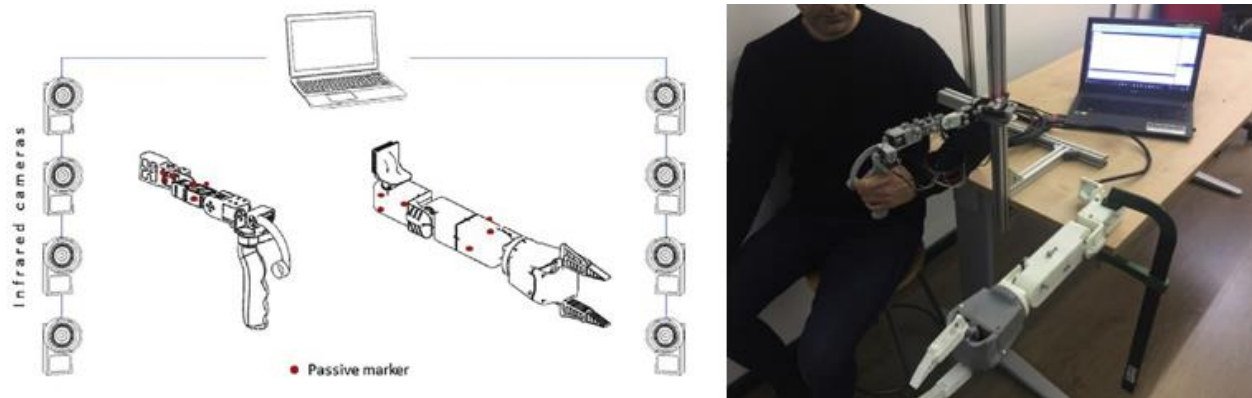
Figure 1. 10. Characterization of the performance of the Master-Slave system. Image taken from (Barbieri et al., 2017).

Other research in the field has shown a greater interest in the use of a hydraulic arm mounted on the underwater vehicle, especially for deep-sea exploration tasks. In (Wang, et al., 2009) is denoting a more difficult joints control compared to electrical one. In particular, the approach lies in the use of sensorized robotic arms to whom is required a feedback between the actually reached position and the desired one, compensating the deviations with the hydraulic system. Position feedback from each slave arm joint is compared with position data from each master arm joint, and any differential initiates the application of hydraulic power to appropriate slave arm joints until position correspondence is achieved. When the joint feedback data corresponds with the position data commanded by the master controller the servo control is closed and slave arm stops moving. Extended trials are carried out in the field. A number of complex issues due to the unstructured, hazardous undersea environment make it difficult to travel in the ocean. For an underwater manipulator, control errors denote the system is unable to accurately control one or more joints. Continuity errors denote a joint position sensor reported an unexpectedly large position change in a short time. This error may indicate the sensor has failed, or an external force, like a collision or extreme or immovable load, has pushed the joint out of position.

This issue has been examined and partly solved by (Shim, et al., 2010), compensating the non-linearity errors between the angle of joints and the linear actuator excursion (Figure 1. 11).
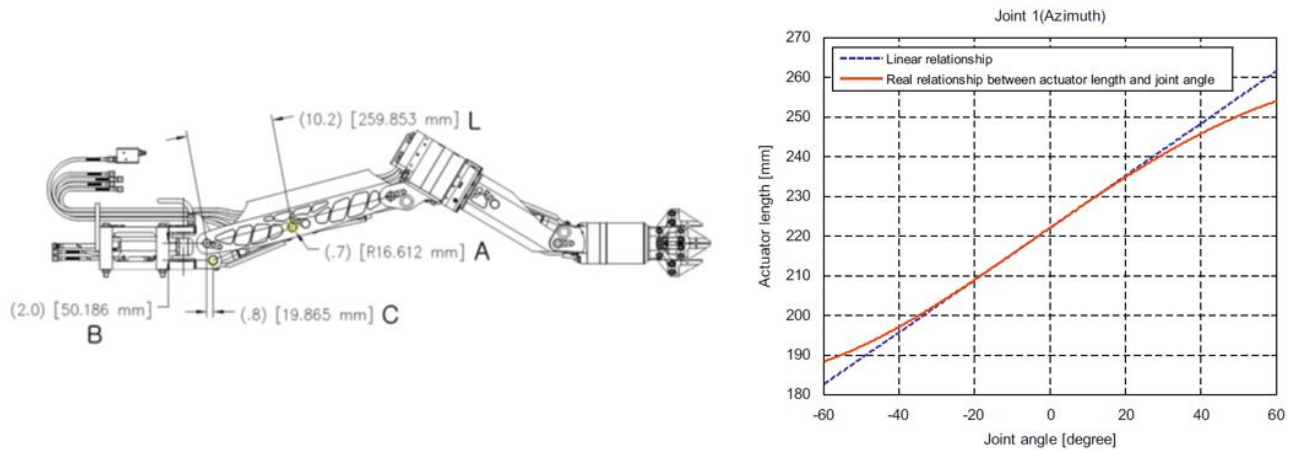
Figure 1. 11. ORION manipulator. A nonlinear relationship between the piston excursion and the joint angle. Images taken from (Shim et al., 2010).

The dynamic compensation of the hydraulic system remains unsolved since it is out of user's ability because the hydraulic valve is controlled by the slave controller with factory setting gain. The working tasks were carried out in the open water, sampling deep water and soil core (Figure 1. 12).

Figure 1. 12. Trial tasks. Images taken from (Shim et al., 2010).

Additionally, to these researches, few studies have been conducted on controlling the end effector of the underwater manipulator through visual-based methods (Marchand, et al., 2001). In particular, the authors proposed a closed-loop system based on eye-to-hand

visual servoing approach with which is not required a precise control of the end-effector motion. The important aspect is to maintain the end-effector in the field of view of the camera. In fact, has been used a 4 DOF, not instrumented, and open-loop controlled with joystick arm, called Sherpa. This arm is mounted on the Ifremer Victor 6000 underwater ROV. The paper presents an image-based control motion of the manipulator, the image processing algorithm able to track the motion, and finally some laboratory trials in dry ambient using a fully instrumented 6 DOF arm. In this way, the desired pose of the end-effector is calculated, while the actual pose is calculated using the proposed visual method (Figure 1. 13).
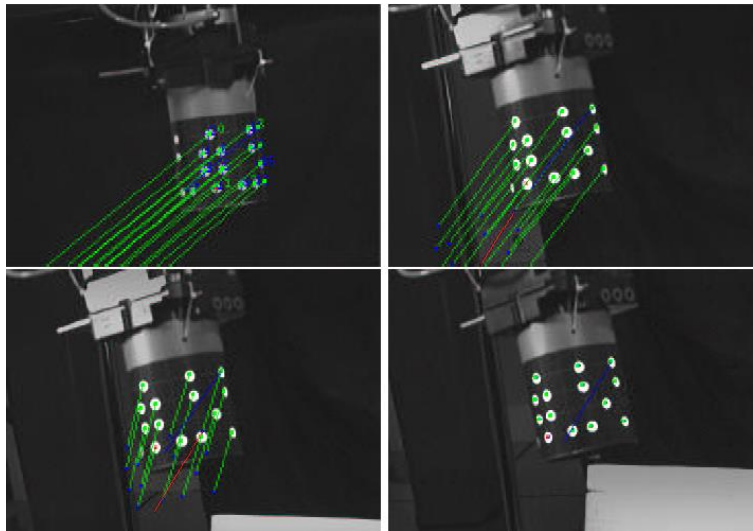
Figure 1. 13. Some instant of the experimentation. Green lines represent virtual links between the current and desired position of the markers in the image. Image taken from (Marchand et al., 2001).

Although the substantial contribution to scientific innovation from these studies, experiments in the field are increasingly dependent on operator capacity to pilot the UVMS, the high costs to support trials using a fiber optic umbilical, and support vessels. For these reasons, recently attention of the scientific community in the field of underwater mechatronics is focusing on the use of manipulators capable of performing the tasks in an autonomous or semi-autonomous mode using an Autonomous Underwater Vehicle (AUV).

In this context it clearly appears the need of using advanced sensors such as sonars (good properties of sound propagation in the water in a long distances), laser rangefinders (light absorption problem, and floating particles), visual-based approach (that represent the cheapest alternative, but not useful on turbid waters, untextured floors, or in the darkness) such as camera motion tracker systems, or structured light techniques (Prats, et al., 2012). Structured light is also a cheap alternative, can work on untextured grounds on short distances, can emit in the wavelengths that are less absorbed by the water, and offer a good accuracy even in the darkness, although they need to be combined with a camera for doing triangulation (Figure 1. 14).
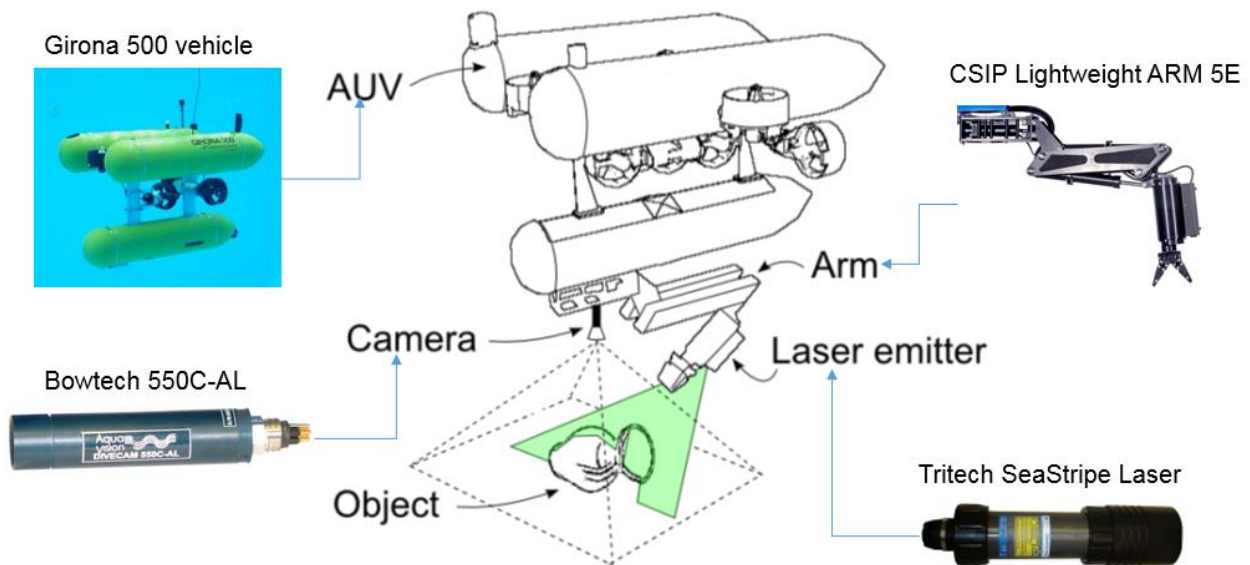
Figure 1. 14. An approach for Semi-Autonomous Recovery of Unknown Objects in Underwater Environments. (Prats et al., 2012).

Since the quality of these feedbacks is strongly affected by many factors, underwater manipulation becomes a very complex and tricky operation that requires considerable experience of the pilot.

Finally, an area of research has focused on the development of a small ROV agent as the end effector of an AUV, connected by a smart flexible cable (Kim, et al., 2013).

1.2. Underwater manipulations

Here, the discussion is focused on relievable scientific aspects related to the use of robotic arms mounted on underwater vehicles to accomplish a specific task.

Underwater manipulation conducted in shallow and deep water is an essential operation for performing underwater works in several application fields like offshore construction and ocean engineering, such as inspections, welding, drilling, connector matching tasks etc. These operations are usually performed by means Remotely Operated Vehicles (ROVs) that are remotely controlled thanks to the visual feedback provided by one or more cameras that allow pilots to estimate the morphology of the submerged environment. Furthermore, a manipulator (robot arm) is considered to be the most suitable tool for executing subsea intervention operations.

To this end, a brief review of the existing commercial underwater manipulators able to operate in deep waters is reported. Today all the existing commercially available underwater manipulators and most of the experimental/prototype underwater manipulators developed for research purposes run on either oil hydraulic or electric power, both of which have their advantages and disadvantages.

In general, hydraulic actuators are capable of producing an output force/torque much larger than the force applied on the input without the use of mechanical components such as gears and levers (direct drive), which is a necessity for the implementation with electric actuators. Thus, hydraulic systems have a higher power to weight ratio, referred to payload capability. Additionally, hydraulic systems are inherently pressurized, i.e. the internal pressure is higher than the ambient pressure so they are not as susceptible to the sea water ingress as are their electric counterparts. Electric underwater manipulators are less frequent in commercial use but are often custom made as prototypes for research purposes. Actuators which are commonly used are brushless DC (BLDC) electric motors with harmonic drive gears featuring low backlash and large reduction ratio. In Table 1.2 are reported specifications of existing commercial underwater manipulators (Sivčeva, et al., 2018).

Manufacturer	Model	Actuation	DOF	Weight in air [kg]	Weight in water [kg]	Lift capacity max nom. (full ext.) [kg]	Wrist torque [Nm]	Grip force [kgf]	Depth rating [m]	Max. reach [m]	Power Source	Material	Actuators	Sensors	Control	Price [$]
Ansaldo	MARIS 7080	Electric	7	65	45	8 (/)	/	20.4	6000	1.4	72VDC	Al	BLDC	Resolvers, F/T	Semi Automatic	/
Cybernetix	Maestro	Hydraulic	6	85	65	100 (96)	190	150	6000	2.4	50 Hz 220VAC 210bar 18lpm	Ti	Rot. vane & gerotor	Resolvers	Pos. & force fb.	~1m
Eca Hytec	Arm 7E	Electric	6	69	49.2	40 (40)	25	80	6000	1.79	24-36VDC	Al 6082 T6	BLDC in oil	/	Prop. & torque	~110k
Eca Hytec	Arm 7E Mini	Electric	6	51	30	25 (25)	25	50	3000	1.44	24-36VDC	Al 6082 T6	BLDC in oil	/	Prop. & torque	~110k
Eca Hytec	Arm 5E	Electric	4	27	18.5	25 (25)	25	60	6000	1	24-30VDC	Al 6082 T6	BLDC in oil	/	Prop.	~40k
Eca Hytec	Arm 5E Mini	Electric	4	23	15	25 (25)	25	50	6000	0.85	24-40VDC	Al 6082 T6	BLDC in oil	/	Prop.	~40k
Eca Hytec	Arm 5E Micro	Electric	4	10	2.7	10 (10)	10	50	6000	0.64	24-30VDC/240VAC	Al 6082 T6	BLDC in oil	/	Prop.	~25k
Forum Perry	TA40	Hydraulic	6	98	65	125 (210)	150	509	11000	2	No electrical 210bar 9lpm	Al, SS	Cylinders, rot. vane & gerotor	No	Pos./Rate/ Hybrid fb.	/
Forum Perry	TA60	Hydraulic	4	82	60	380 (300)	250	509	11000	1.44	No electrical 210bar 9lpm	Al, SS	Cylinders, rot. vane & gerotor	No	Rate/Hybrid fb.	/
Forum Perry	TA60J	Hydraulic	4	76	51	380 (300)	250	509	11000	1.38	No electrical 210bar 9lpm	Al, SS	Cylinders, rot. vane & gerotor	No	Rate/Hybrid fb.	/
Forum Perry	TA16	Hydraulic	4	50	40	147 (102)	108	226	11000	1.06	No electrical 210bar 9lpm	Al, SS	Cylinders, rot. vane & gerotor	No	Rate/Hybrid fb.	/
Graal Tech	UMA	Electric	6 (7)	28	14	10 (/)	/	/	100	1	24VDC	Al	BLDC	Yes	Position	~75k
Hydro-Lek	40400	Hydraulic	4	45	30	150 (210)	75	/	11000	1.42	210 bar	SS 316, Al HE30, PE	Cylinders & gerotor	No	Rate	~16k
Hydro-Lek	40500(R)	Hydraulic	6	59	40	150 (210)	75	/	11000	1.5	210 bar	SS 316, Al HE30, PE	Cylinders & gerotor	No	Rate	~30k
Hydro-Lek	43000	Hydraulic	4	6	4	10 (20)	8	/	11000	0.53	160 bar	SS 316, PE	Cylinders & gerotor	No	Rate	~4k
Hydro-Lek	CRA6	Hydraulic	5	28	14.5	32 (32)	38	/	11000	1.5	140 bar	SS 316, Al HE30, PE	Cylinders & gerotor	No	Rate	~12k
Hydro-Lek	EH5	Hydraulic	4	12	9.5	25 (25)	14	/	11000	0.8	140 bar	Al E30, SS 316	Cylinders & gerotor	No	Rate	~7k
Hydro-Lek	HD5	Hydraulic	4	21.5	16.5	40 (40)	38	/	11000	0.819	140 bar	SS 316, Al HE 30, PE	Cylinders & gerotor	No	Rate	~9k
Hydro-Lek	HD6W HD6R	Hydraulic	5	29	21	40 (40)	38	/	11000	1.12	140 bar	SS 316, Al HE30, PE	Cylinders & gerotor	No	Rate	~12k
Hydro-Lek	MB4	Hydraulic	3	13.3	11	40 (40)	40	/	11000	0.63	140 bar	SS 316, Al HE30, PE	Cylinders & gerotor	No	Rate	~5k
Hydro-Lek	RHD5(W)	Hydraulic	4	30	20	80 (80)	38	/	11000	0.95	210 bar	SS 316, Al HE30, PE	Cylinders & gerotor	No	Rate	~11k
ISE Ltd.	Magnum 7	Hydraulic	6	63.5	30	454 (295)	108	205	11000	1.5	70bar 19lpm	Al, SS	Cylinders	Potentio-meters	Pos./Rate	~59k
ISE Ltd.	Magnum 5	Hydraulic	4	50	27	454 (295)	108	160	5000	1.16	70bar 19lpm	Al, SS	Cylinders	Yes	Pos./Rate	~52k
ISE Ltd.	Magnum 6 Mini	Hydraulic	5	57	30.6	454 (317)	108	160	5000	0.96	70bar 19lpm	Al, SS	Cylinders	No	Rate	~56k
ISE Ltd.	Magnum 5	Hydraulic	4	34	24	68 (23)	14	35	5000	0.71	35bar 19lpm	Al, SS	Cylinders	No	Rate	~46k

Manufacturer	Model	Actuation	DOF	Weight in air [kg]	Weight in water [kg]	Lift capacity max nom. (full ext.) [kg]	Wrist torque [Nm]	Grip force [kgf]	Depth rating [m]	Max. reach [m]	Power Source	Material	Actuators	Sensors	Control	Price [$]
KNR Systems Inc.	HYDRA UW3	Hydraulic	6	130	/	300 (121)	350	300	500	2.035	210bar 19lpm	Al, SS, Ti	Cylinders & rotary vane	Encoders	Position	~175k
Kraft	Predator	Hydraulic	6	80	51	227 (91)	135	135	6500	1.64	50 Hz 220VAC 210bar 19lpm	Al, SS	Cylinders, rot. vane & gerotor	Yes	Pos. & force fb.	~200k
Kraft	Raptor	Hydraulic	6	75	44	227 (91)	135	135	6500	1.52	50 Hz 220VAC 210bar 19lpm	Al, SS	Cylinders, rot. vane & gerotor	Yes	Pos. & force fb.	~200k
Kraft	Grips	Hydraulic	6	59	41	82 (45)	20	90	3000	1.556	50 Hz 220VAC 210bar 11lpm	Al, SS	Cylinders, rot. vane & gerotor	Yes	Pos. & force fb.	~200k
Ocean Innovation System	BE5-500	Electric	4	15	8	/(16)	1.6	100	500	0.7	24 VDC	Al 5083, PE	BLDC	Hall	Rate	~30k
Oceaneering	Atlas Hybrid	Hydraulic	6	73	50	454 (250)	205	454	6500	1.66	90-260VAC 206bar 19lpm	Al 6061 T6, SS	Cylinders, rot. vane & gerotor	Solid State Pos.	Hybrid Pos./ Rate	/
Profound Technology	M1P	Hydraulic	6	115	77	275 (250)	175	652	4000	2.1	/	Al, SS	Cylinders & rotary	Yes	Pos./Rate	/
Schilling	Titan 2	Hydraulic	6	80	61	/(109)	68	136	6500	1.92	90-260VAC 210bar 19lpm	Ti	Cylinders, rot. vane & gerotor	Resolvers	Pos. & force fb.	/
Schilling	Titan 3	Hydraulic	6	/	/	/(/)	/	/	6500	1.92	90-260VAC 210bar 19lpm	Ti	Cylinders, rot. vane & gerotor	Resolvers	Pos. & force fb.	/
Schilling	Titan 4	Hydraulic	6	100	78	454 (122)	170	417	7000	1.92	90-260VAC 210bar 19lpm	Ti	Cylinders, rot. vane & gerotor	Resolvers	Pos. & force fb.	/
Schilling	Conan 7P	Hydraulic	6	107	73	273 (159)	205	454	3000	1.8	90-260VAC 210bar 19lpm	Al 6061, SS	Cylinders, rot. vane & gerotor	Potentio-meters	Pos.	/
Schilling	Orion 7P/ 7R	Hydraulic	6	54	38	250 (68)	205	454	6500	1.85	90-260VAC 210bar 19lpm	Al, SS	Cylinders, rot. vane & gerotor	Potentio-meters	Pos./Rate	/
Schilling	Atlas 7R	Hydraulic	6	73	50	500 (250)	205	454	6500	1.66	90-260VAC 210bar 19lpm	Al 6061 T6, SS	Cylinders, rot. vane & gerotor	No	Rate	/
Schilling	RigMaster	Hydraulic	4	64	48	270 (181)	205	454	6500	1.37	No electrical 210bar 19lpm	Ti, Al, SS 630	Cylinders, rot. vane & gerotor	No	Rate	/
Schilling	Orion 4R	Hydraulic	3	30	21	136 (/)	205	454	6500	0.68	No electrical 210bar 19lpm	Al, SS	Cylinders rot. vane & gerotor	No	Rate	/
Seamor	7F-H-ARM	Hydraulic	6	32	/	/(5)	/	/	300	1.07	300V 35bar 4.5lpm	SS 316, Al 6061 T6	/	/	/	/
TitanRob	M700	Hydraulic	6	30	20	50 (40)	45	80	3000	1.05	140bar min 1.5lpm	Ti, SS 316	Cylinders, rot. vane & gerotor	No	Rate	~45k
TitanRob	G500	Hydraulic	4	20	15	100 (80)	80	250	3000	0.8	140bar min 1.5lpm	Ti, SS 316	Cylinders & rotary	No	Rate	~40k
TitanRob	M501	Hydraulic	4	14	11	50 (40)	45	80	3000	0.95	140bar min 1.5lpm	Ti, SS 316	Cylinders & rotary	No	Rate	~35k

Manufacturer	Model	Actuation	DOF	Weight in air [kg]	Weight in water [kg]	Lift capacity max nom. (full ext.) [kg]	Wrist torque [Nm]	Grip force [kgf]	Depth rating [m]	Max. reach [m]	Power Source	Material	Actuators	Sensors	Control	Price [$]
Western Space & Marine	The ARM	Hydraulic	6	145	97	45.4 (29.5)	/	150	11000	1.7	24VDC 204bar 7.6lpm	/	/	/	Force fb.	/
Western Space & Marine	MK37	Hydraulic	6	43	16	23 (/)	/	114	11000	0.94	24(±15)VDC 204bar 4.5lpm	/	/	/	Force fb.	/

Note./- Information not available; Pos. - Position; Prop. - Proportional; Fb. - Feedback.

Table 1.2. Specifications of existing commercial underwater manipulators. Table taken from (Sivcev et al., 2018).

In order to be able to operate in deep waters and cope with the harsh conditions of subsea environment, specialized materials are used in the construction of underwater manipulators. Additionally, depending on the task for which they are designed, underwater manipulators have to meet relevant requirements regarding the size of the workspace in which they are to operate, lifting capacity, wrist torque, etc., as reported in the above reported Table. The most common materials used in construction of underwater manipulators are metal alloys such as titanium Ti 6–4, anodized aluminium alloys, steel alloys as well as some plastics (Polyethylene). The properties of these materials are relatively high strength and corrosion resistance and good machinability. To reduce the weight in the water and minimize the actuator burden, some experiments have been done on using buoyant materials on underwater manipulators (Ishimi et al., 1991). Typically, commercially available underwater manipulators are rated between 3000 and 6500m of sea water (msw); however, some manipulators can operate in depths up to 7000 msw, e.g. Schilling Robotics Titan 4 and a prototype manipulator developed by Zhang et al. (2014). Additionally, there are some systems designed for full ocean depth (11000 msw). Woods Hole Oceanographic Institute in collaboration with Kraft Robotics designed one such manipulator for the purpose of Mariana Trench exploration mission (Bowen et al., 2008). Maximum wrist torque which underwater manipulators are capable of producing ranges from 8Nm to 250Nm. The weight (in air) is between 6 kg and 150 kg; however, their weight in water is more important, as it determines the buoyancy needed on the base vehicle in order to compensate for the manipulator. Finally, manipulators are equipped on the underwater vehicle to accomplish a task. In Table 1.3 is reported a list of remotely operated vehicles (ROVs) equipped with one or more manipulators for scientific use.

Vehicle	Depth (m)	Institution	Manipulator
Kaiko	11000	JAMSTEC	7-DOF manipulator

Jason	6500	WHOI	Schilling Titan 4, and Kraft Predator II
ISIS	6500	NOC	Kraft Predator, and Schilling Titan 4
Victor	6000	IFREMER	6-DOF Maestro, and 4-DOF Sherpa
Hercules	4000	IFE	Kraft Predator and ISE Magnum 7-function

Table 1.3. ROV and manipulator for scientific use.

The Marine Technology and Engineering Center (MARITEC) of the Japan Agency for Marine-Earth Science and Technology (JAMSTEC) developed KAIKO vehicle (Figure 1. 15), which has reached the deepest part of the ocean 10911.4m in the Mariana Trench on 24 March 1995. The KAIKO was a two-vehicle system: the launcher, which connected to the support vessel via electro-optical umbilical, and a free-swimming vehicle that could operate around the launcher within a 200 m radius.

Figure 1. 15. KAIKO vehicle. Courtesy of JAMSTEC, http://www.jamstec.go.jp/e/

The vehicle is equipped with two "home-made" 7 DOF manipulators, with which it was possible to collect different biological sediment in the Mariana Trench during the second expedition on February 1996 (Figure 1. 16).
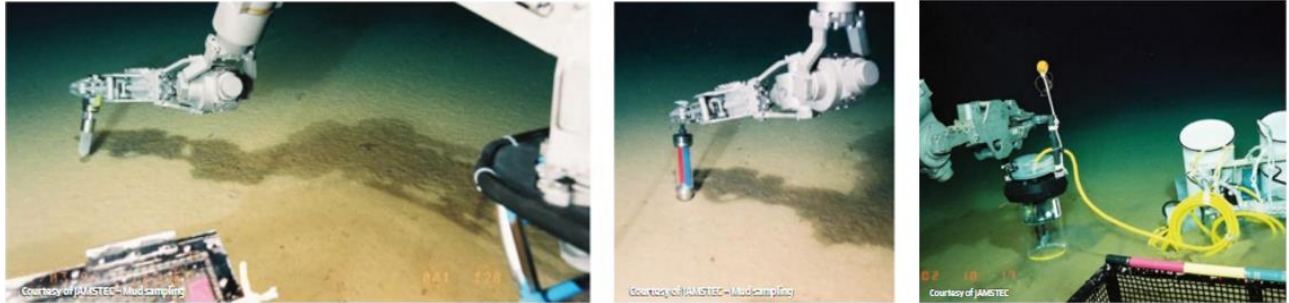
Figure 1. 16. Biological sediment collecting with KAIKO vehicle in the Mariana Trench. Courtesy of JAMSTEC. Images taken from ROV Planet journal, n° 2, pp 17-18.

The Kaiko vehicle is famous to the scientific community because it was lost at the sea off Shikoku Island during Typhoon Chan-Hom on 29 May 2003.

Another well-known ROV work class is Jason (Figure 1. 17), designed to operate to a maximum depth of 6500 meters by the Woods Hole Oceanographic Institution (WHOI) for scientific investigation of the deep ocean and seafloor and for underwater archaeology. Jason is equipped with two 7-function 6 DOF hydraulic arms, the Schilling Titan 4 and Kraft Predator II.

Figure 1. 17. The ROV Jason. Image courtesy of Woods Hole Oceanographic Institution,
http://www.whoi.edu/

Jason allowed scientists to view the deepest volcanic eruption known to man, at West Mata volcano 1200 meters below the ocean surface in the northeast Lau Basin (Figure 1. 18, Figure 1. 19), and the Expedition to the Deep Slope in the Gulf of Mexico.
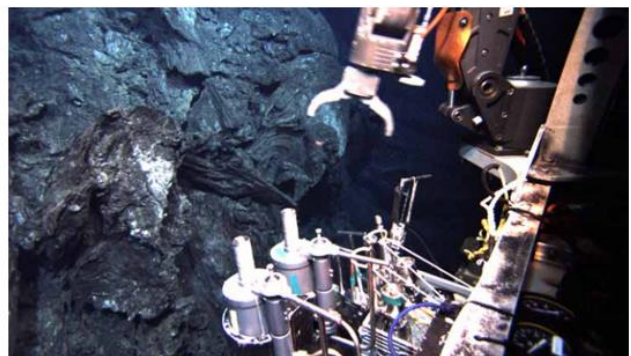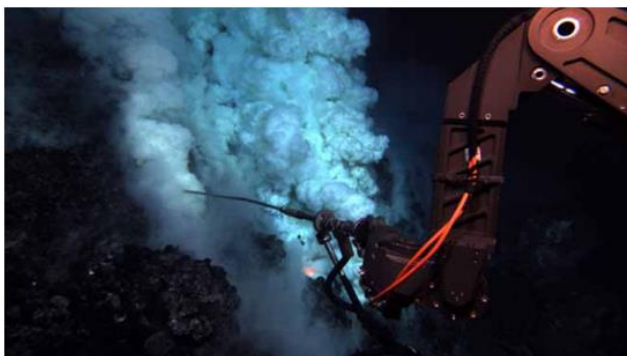
Figure 1. 18. Fluid and rocks lava sampling. Images courtesy of NOAA,
https://oceanexplorer.noaa.gov/welcome.html

Figure 1. 19. The top and the tip of the chimney sampling. Images courtesy of NOAA.

The ROV ISIS is a 6500 m deep vehicle of the National Oceanography Centre (NOC) developed in collaboration with WHOI. ISIS is equipped with two mechanical arms, the Kraft Predator and the Schilling Titan 4, able to perform different biological manipulation (Figure 1. 20).

Figure 1. 20. The ROV ISIS during the ERC CODEMAP2015 expedition. Courtesy of NOC, http://www.noc.ac.uk/

The ROV Victor 6000 of the Institut Français d'Exploitation de la Mer, Ifremer, dedicated to scientific ocean research in a deep-water. Victor is equipped with two manipulators, the 6-DOF Maestro and 4-DOF Sherpa (Figure 1. 21).

Figure 1. 21. The ROV Victor 6000. Courtesy of Ifremer, http://flotte.ifremer.fr/fleet. Images taken from (Marchand et al., 2001).

The ROV Victor 6000 was successfully used for scientific operations on the Mid-Atlantic Ridge south of the Azores during two geological cruises IRIS (2001) and Seahma-1 (2002), depicted in Figure 1. 22.
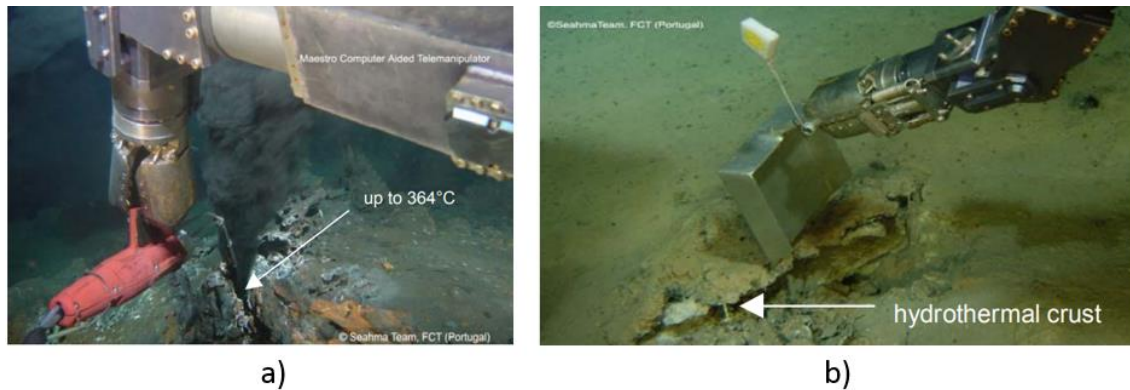
Figure 1. 22. Manipulation tasks with the ROV Victor 6000 and the Maestro manipulator during Seahma-1 cruise. a) Precise temperature measurements in a black smoker. b) Delicately shoveling of a hydrothermal crust deposited within the sediment. Images taken from (Jean-Louis et al., 2003).

The ROV Hercules (Figure 1. 23) is a neutrally buoyant vehicle specifically designed by the Institute for Exploration (IFE) to be used as a scientific tool while descending to depths of 4000 meters. Currently is used to support archaeology discovery and excavation mission (Figure 1. 24) on board of the E/V Nautilus of Professor Robert Ballard, best known for his 1985 discovery of the RMS Titanic. Hercules is equipped with two manipulators, the Kraft Predator, and ISE Magnum 7-function.
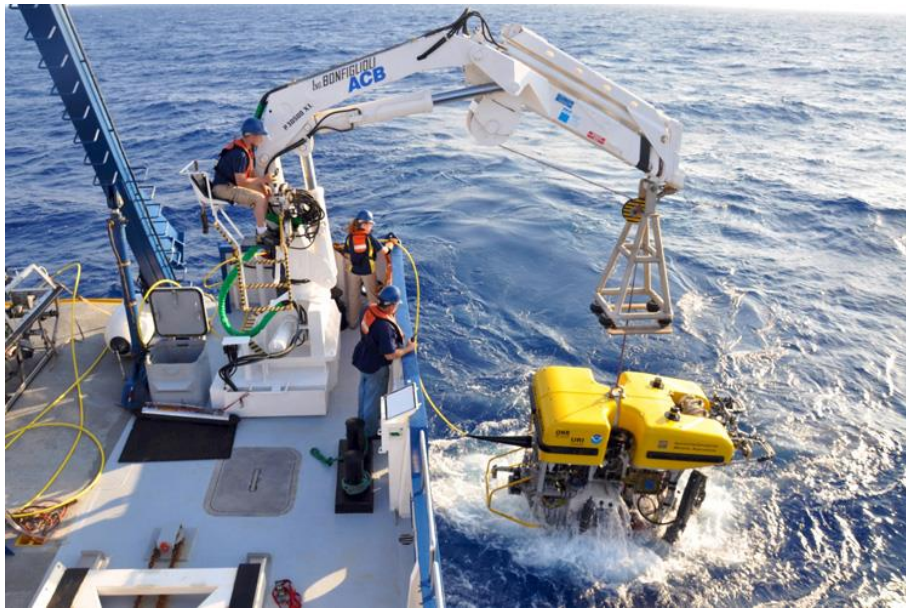
Figure 1. 23. The ROV Hercules during recovery operations on board of the E/V Nautilus. Image courtesy of The Ocean Exploration Trust, http://www.oceanexplorationtrust.org/
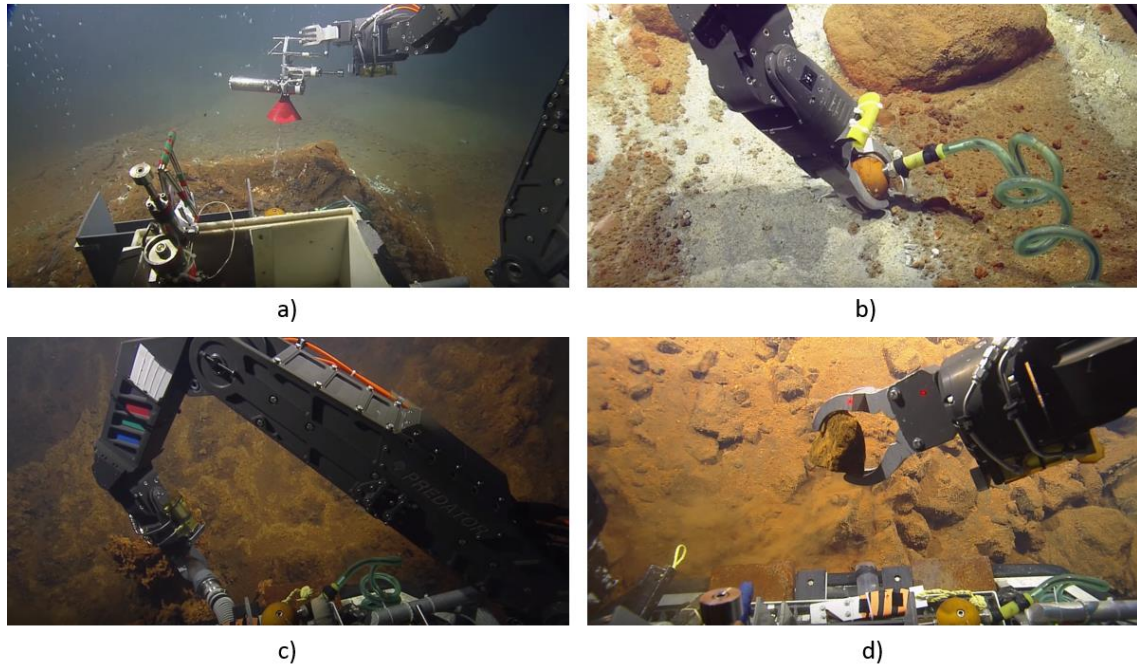
Figure 1. 24. Underwater manipulation tasks of the ROV Hercules. a) Gas sampling. b,c,d) Sediment sampling. Pictures courtesy of Nautilus Live, http://www.nautiluslive.org/

1.3. Soft robotics

The growing need for robots in service tasks, in unstructured environments, in contact with humans, is leading to release the basic assumption of rigid parts in robotics.

The role of soft body parts to increase adaptability and robustness appears clear in natural organisms. To this end, it should be clarified that, as reported in Springer Handbook of Robotics:

> "*Bio-inspired robotics tends to adapt to traditional engineering approaches some principles that are abstracted from observation of some living creature, whereas biomimetic robotics tends to replace classical engineering solution by as detailed mechanisms or processes that is possible to reproduce from observation of this creature*".

Compliance, or softness, are also needed for implementing the principles of embodied intelligence, or morphological computation, a modern view of intelligence, attributing a stronger role to the physical body and its interaction with the environment.

Soft robotics is an interdisciplinary field in robotics that deals with robots built out of soft and deformable materials capable to actively and safely interact with humans and with complex natural environments. However, softness can be intended in various way: soft texture, soft and deformable materials, soft movement, elastic materials, and variable compliance actuators.

Nowadays, soft technologies used in robotics involve essentially actuation, stiffness modulation, and soft materials. Despite the importance and considerable demands, the field of Soft Robotics faces a number of fundamental scientific challenges. In fact, one of the biggest challenges in soft robotics is designing a flexible actuation system capable of high forces. Currently, there are three popular actuation techniques. The first one is to use dielectric elastomeric actuators (DEAs) made of soft materials that actuate through elastomeric forces. In (Shintake, et al., 2016) are reported an important development in the, depicted in Figure 1. 25.

The gripper consists of a pre-stretched elastomer membrane with patterned compliant electrodes laminated between two passive silicone layers Figure 1. 25 (a). Despite its relatively high performance, this technique has limitations regarding the complex design and fabrication process.
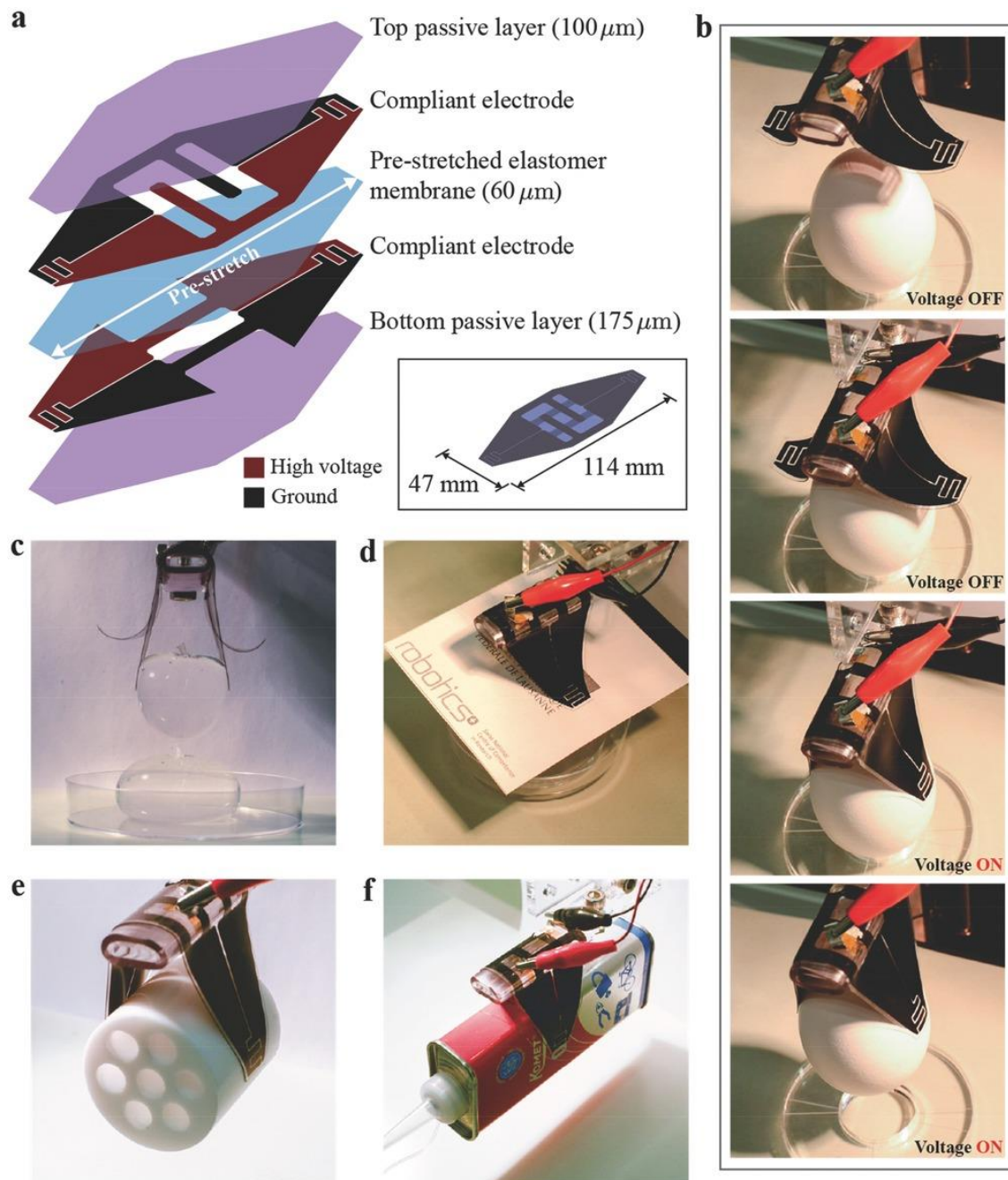
Figure 1. 25. Structure of the electro-adhesion enabled soft gripper integrated with DEAs (a), and demonstration of gripping different objects (b, c, d, e, f). Image taken from (Shintake et al., 2016).

The second technique is to use shape-memory alloys (SMAs) actuators. Typically, these actuators are composed of SMA materials (most common nickel-titanium alloys) integrated into a soft structure, and force generation depends on temperature change. Pioneer in this area is the octopus-inspired robot developed by Biorobotics Institute at the Sant'Anna School of advanced studies in Pisa, reported in (Laschi, et al., 2012), and depicted in Figure 1. 26. A plastic fiber braid constitutes the highly deformable mechanical structure of this robot arm, whereas soft actuators comprised of SMA springs are arranged transversely and longitudinally to produce local deformations.
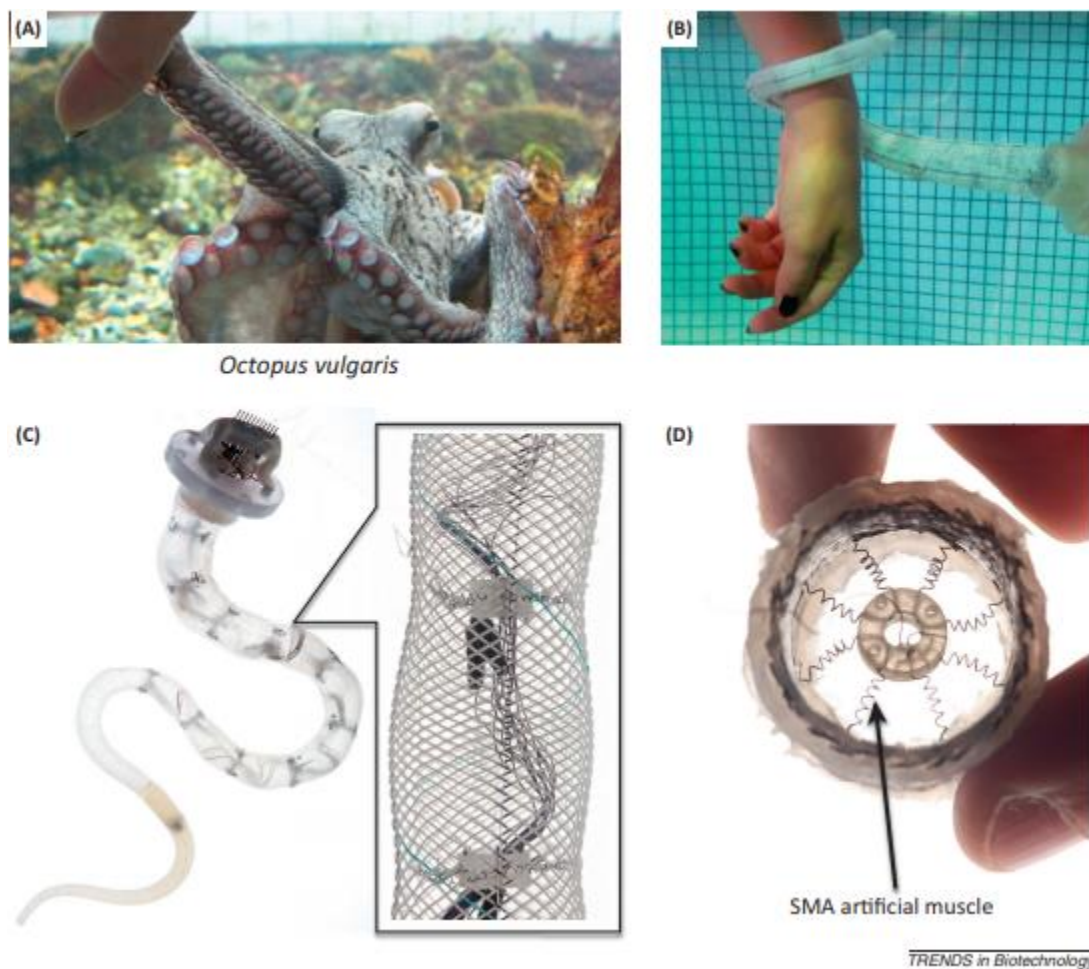
Figure 1. 26. Octopus-inspired robot. (A) Octopus vulgaris grasping a human finger. (B) An octopus-like robot arm wrapping around a human wrist in the water. (C) Detail of the design. (D) Detail of the SMA spring. Image taken from (Kim et al., 2013).

The third technique of actuation is to use compressed air (Shepherd, et al., 2011) and pressurized fluids, as depicted in Figure 1. 27.

Figure 1. 27. A multigait soft walker powered by compressed air. Image taken from (Shepherd et al., 2011).

The studies of unconventional soft materials and stiffness modulation are still in their exploration phase: tools and methods for fabrication and assembly are not fully established; kinematics and dynamics modeling cannot be directly used because the structure is a continuum and deformation id highly nonlinear owing to large strain; it is not fully understood how to achieve sensing, actuation, and control in soft-bodied robots; and researcher are still exploring what are the good ways to test, evaluate, and communicate the soft robotics technologies.

Furthermore, the term "soft robotics" is improperly used in the literature. In fact, as reported in (Laschi, et al., 2016):

"The term "soft robotics" was formerly used to indicate robots with rigid links and mechanically (or passively) compliant joints with variable stiffness, or compliance or impedance control".

Then, the following definition about soft robotics was given:

"Soft robotics manipulators are continuum robots made of soft materials that undergo continuous elastic deformation and produce motion through the generation of a smooth backbone curve".

1.3.1.   Soft robotic grippers

Considering the above mentioned definitions, it should be cleared that the resting part of this section is focused on Soft Robotic Grippers, that can be mounted on robotic arms with rigid links.

In order to have an exhaustive overview, here we focus on categorizing soft robotic grippers based on technologies with which grasping is enabled. It should be noted that grasping is the ability to pick up objects against external disturbances. In particular, according to (Shintake, et al., 2018), the soft gripper can be categorized into three gripping technologies: a) by actuation, b) by controlled stiffness, and c) by controlled adhesion. Moreover, many devices make use of combinations of two technologies.

Gripping by actuation consists of bending gripper fingers or elements around the object, and can be achieved using passive structure with external motors (Figure 1. 28 a, b), fluid elastomer actuators (Figure 1. 28 c), electroactive polymers (Figure 1. 28 d, e), and shape memory materials (Figure 1. 28 f, g).
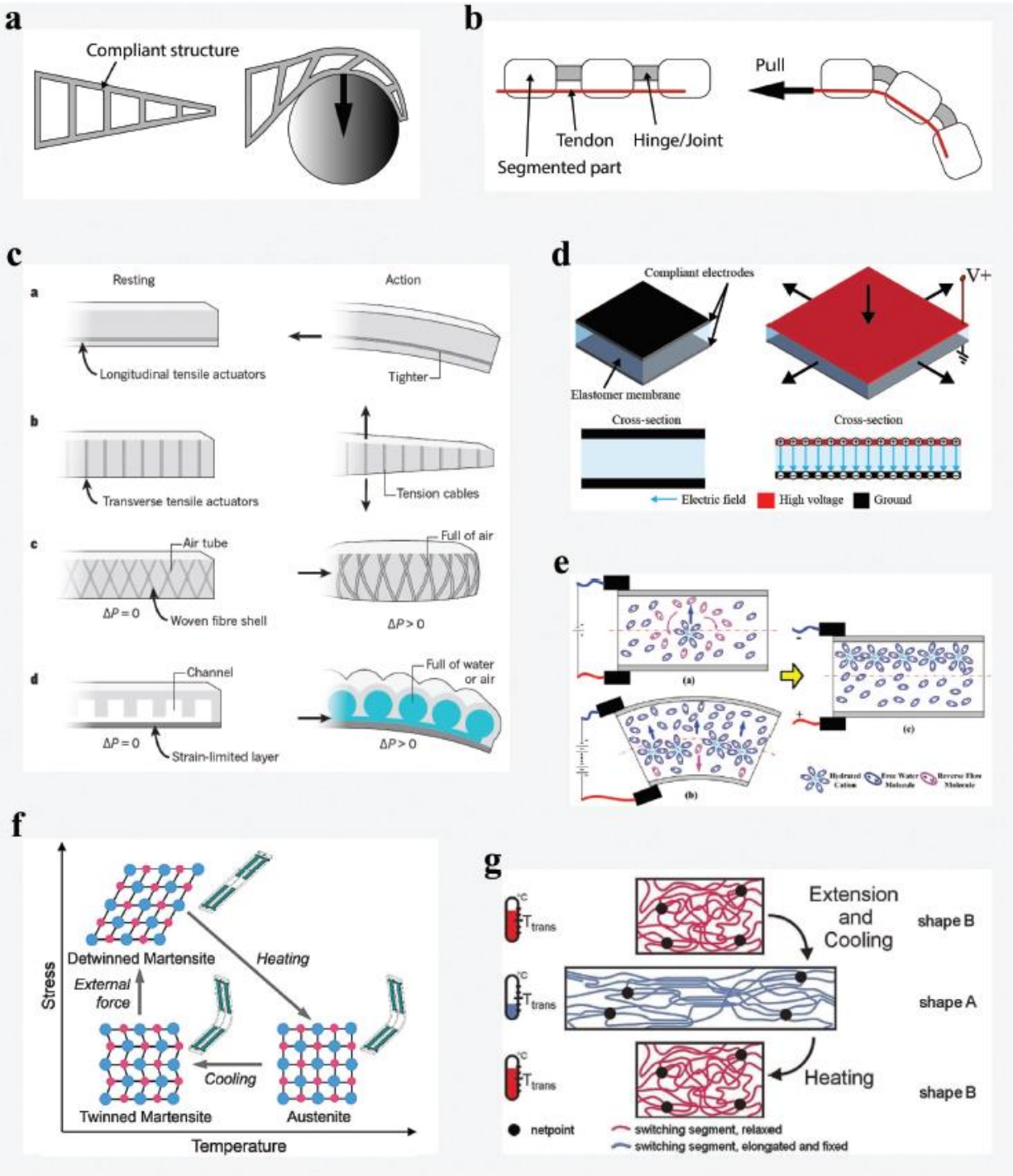
Figure 1. 28. Gripping by actuation. a) Contact-driven deformation. b) Tendon-driven. c) Fluidic elastomer actuators (FEAs). Courtesy of (Rus and Tolley, 2015). d) Dielectric elastomer actuators (DEAs). e) Ionic polymer-metal composites (IPMCs). Courtesy of (Sun et al., 2013). f) Shape memory alloys (SMAs). Courtesy of (Wang et al., 2016). g) Shape memory polymers (SMPs). Courtesy of (Behl et al., 2007). Image taken from (Shintake et al., 2018).

Regarding the passive structure with external motors, several Fin Ray, compliant mechanisms, and tendon-driven soft gripper have been developed, as depicted in Figure 1. 29.
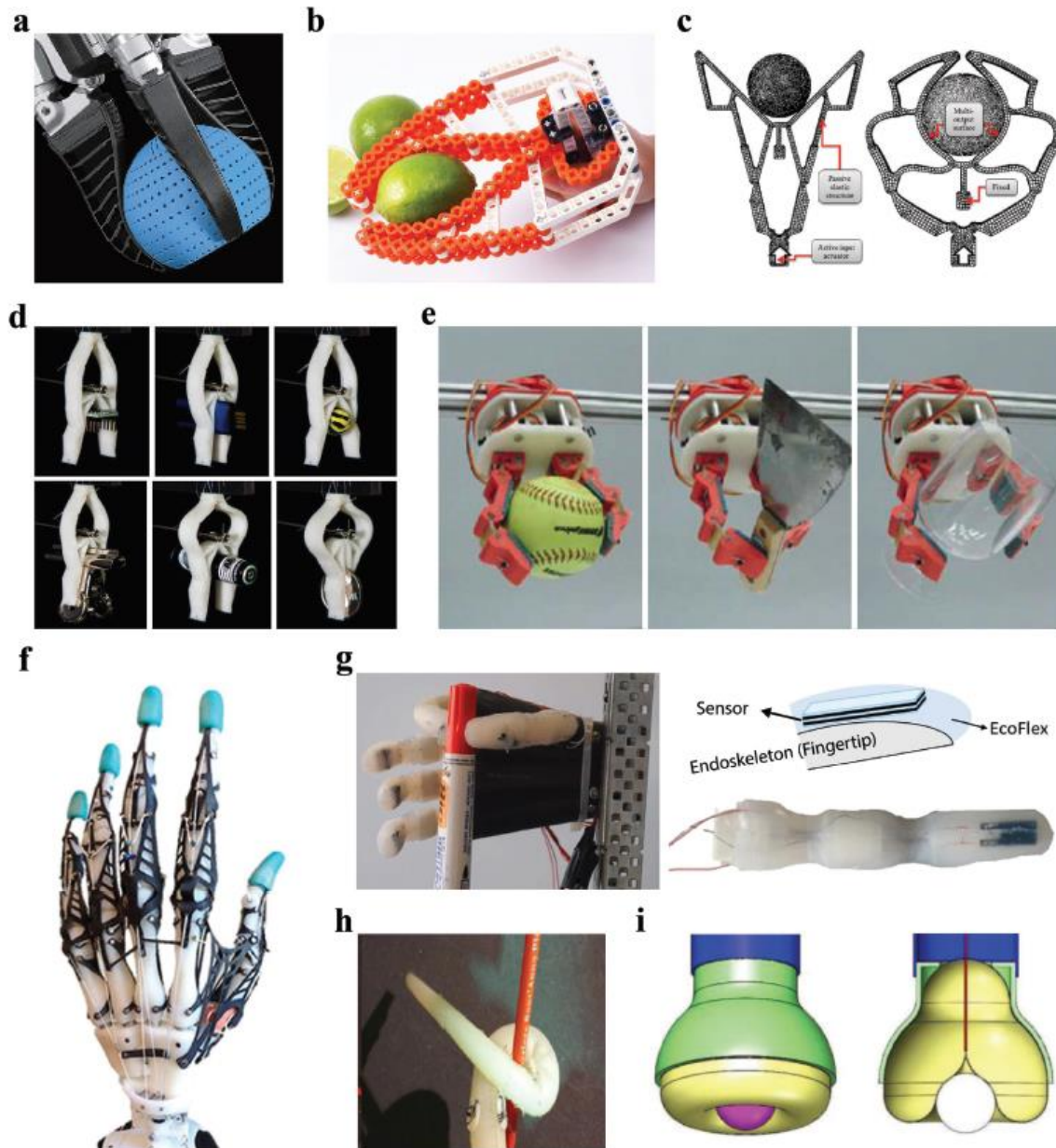
Figure 1. 29. Soft grippers using passive structure with external motors. a) Fin Ray robotic gripper. Courtesy of Festo Co. Ltd. b) Fin Ray (toy). Courtesy of BionicToys HmbH. c) Working principle of compliant mechanism (Petkovic et al., 2013). d) Compliant mechanism (Liu et al., 2017). e) Tendon-driven with elastic hinges (Ma et al., 2017). f) Anthropomorphic tendon-driven (Xu and Todorov, 2016). g) Tendon-driven with sensor embedded soft skin (Tavakoli et al., 2017). h) Tendon-driven elastomeric manipulator (Calisti et al., 2011). i) Tendon-driven with a compliant elastomeric bag (Zhu et al., 2016). Images taken from (Shintake et al., 2018).

Fluidic elastomer actuators (FEAs) are among the oldest but still the widespread actuation technologies for soft robotic grippers due to a number of advantages, including easy fabrication, robustness, and low-cost elastomer materials. Actuation is obtained through the pressure exerted by a fluid (liquid or gas) on a chamber made by highly deformable materials. (Suzumori, et al., 1991, 1992) conducted some the earliest work on FEA gripping, in which he created continuum-style soft actuators that consisted of three parallel, fiber-reinforced elastomeric chambers spaced evenly around a central axis, shown in Figure 1. 30 a. Following the early developments, new grippers were realized (Figure 1. 30).
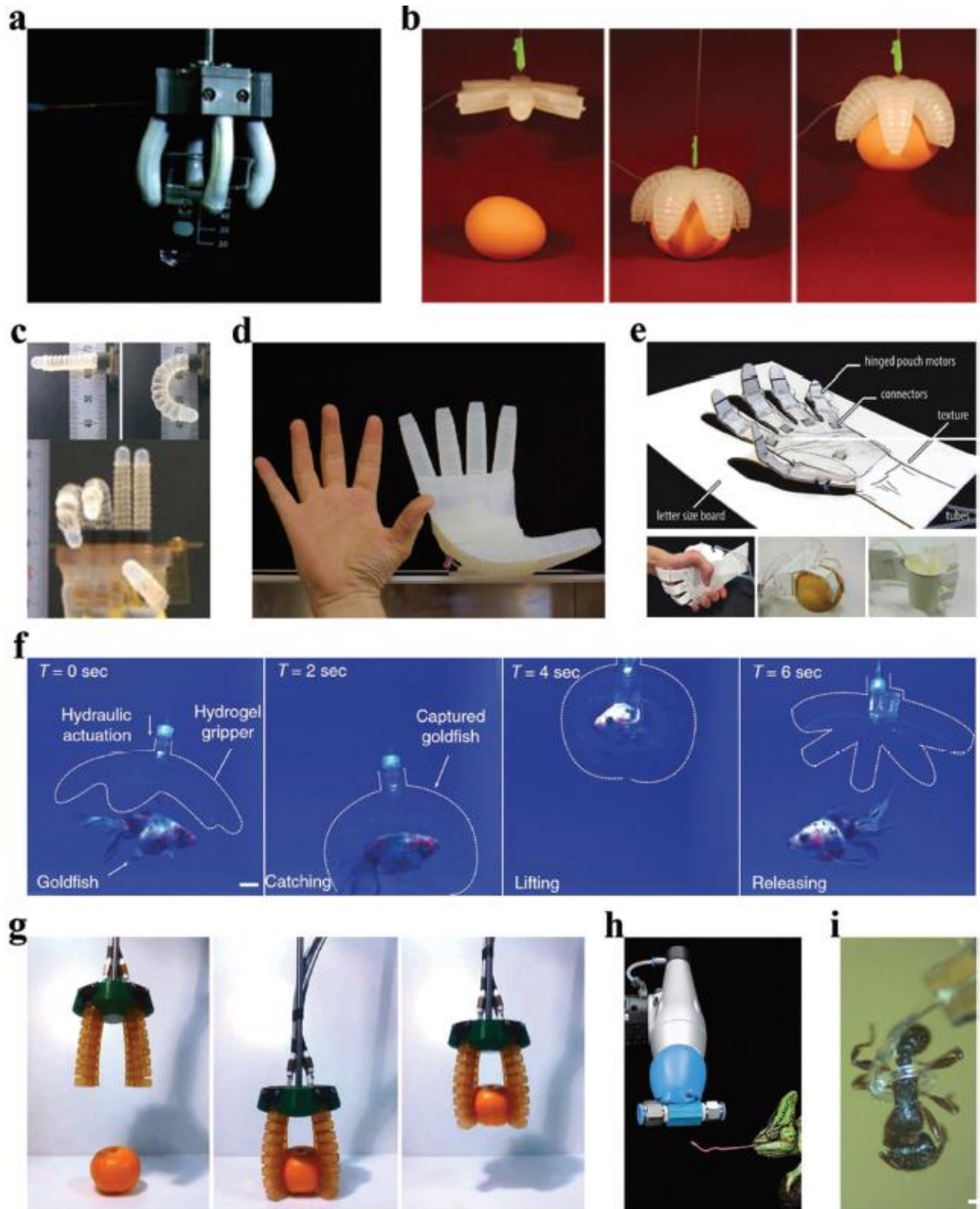
Figure 1. 30. Soft grippers using fluidic elastomer actuators (FEAs). a) Suzumori's multichambered fingers. b) PneuNets (Ilievski et al., 2011). c) Fingers actuated by electrohydrodynamics (Yamaguchi et al., 2011). d) Bio-inspired hand (Deimel and Brock, 2016). e) Pouch motors. f) Hydraulically actuated hydrogels (Yuk et al., 2018). g) Self-healing polymers (Terryn et al., 2018). h) Chameleon's tongue

Dielectric elastomer actuators (DEAs) are composed of a thin elastomer membrane sandwiched between two compliant electrodes. Electromechanical actuation is obtained by applying a high voltage across the electrodes, which generates an electrostatic attraction (known as Maxwell stress) between them, squeezing the elastomer membrane, resulting in elastomer thickness reduction and area expansion. Developments on DEA-based soft grippers are shown in Figure 1. 31.

Figure 1. 31. Soft grippers using dielectric elastomer actuators (DEAs) and ionic-polymer-metal composites (IPMCs). a) Dielectric elastomer minimum energy structure (DEMES) (Kofod et al., 2007). b) Segmented DEMES (Lau et al., 2017). c) DEA with stiff fibers (Shian et al., 2015). d) IPMC fingers (Bar-Cohen et al., 1998). e) Micro-IPMC fingers (Deole et al., 2008). Images taken from (Shintake et al., 2018).

Materials that change their properties in response to stimuli can greatly expand the functionalities of soft grippers, such as shape memory alloys (SMAs) and shape memory polymers (SMPs). SMAs exhibit a shape memory effect due to crystallographic change of the alloy between the martensite phase and austenite phase induced by temperature. At low temperature, the alloy is in martensitic form with lower modulus and can be plastically deformed by an external stress. Heating above the transition temperature transforms the alloy into austenitic form with a higher modulus, leading to the recovery of the shape to its original undeformed state. SMPs consist of a polymer network composed of elastic domains and transition domains. Heating above the transition temperature causes the transition domain to soften, allowing the deformation of the elastic domain in response to an external force. After cooling, the transition domain stiffens and blocks the deformation of the elastic domain. Heating the material again releases the elastic domain and the device recovers its original, undeformed, state. Examples of these typologies of soft grippers are reported in Figure 1. 32.
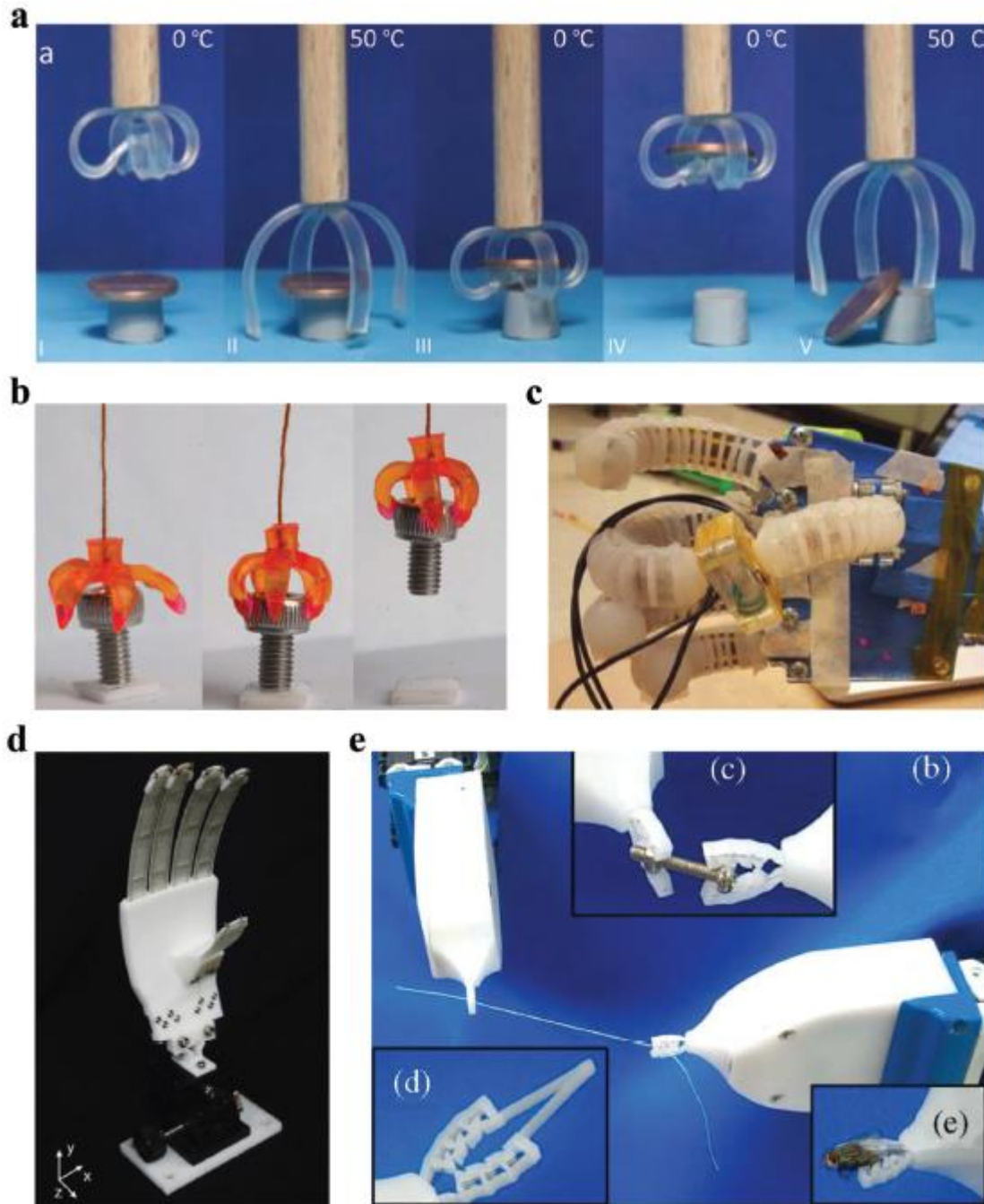
Figure 1. 32. Soft grippers using actuation of shape memory materials. a) Bidirectional shape memory polymers (SMPs) (Behl et al., 2013). b) 3D printed SMP structure (Ge et al., 2016). c) Shape memory alloys (SMAs) with elastomeric fingers structure (She et al., 2016). d) Articulated elastomeric structure with SMA wires (Kim et al., 2016). e) SMA microfingers (Lan et al., 2011). Images taken from (Shintake et al., 2018).

Gripping using controlled stiffness exploits the large change in rigidity of some materials or material combinations to hold an object. An actuator is needed to envelop the object

with part of the gripper, but as the gripper is in the soft state, the actuation force can be very low, allowing very delicate objects to be caged. Key examples on controlled stiffness grippers are represented by granular jamming grippers. Particle jamming is accomplished by creating a pressure differential between the inside of a particle-filled flexible membrane and the fluid surrounding the membrane. When the flexible membrane is filled with fluid, the membrane does not obstruct the motion of the particle inside (soft state). The particles can move around each other freely, and the membrane is free to take the shape of the object that it is pressed against. To make membrane harden in its current shape, fluid is removed from the inside of the membrane. The particles can no longer flow around each other and the whole mass becomes rigid (hard state). One representative example is the universal jamming gripper developed by (Brown, et al., 2010), shown in Figure 1. 33 a. The high compliance of the ground coffee-filled bag adapts to the object, and evacuation of air provides sufficient rigidity to hold and lift it up. This gripper successfully handled objects with highly diverse shapes, such as small flashlight bulbs, small plastic bags, LEDs, bottle caps, plastic tubing, foam earplugs, and a variety of hardware items and office supplies in addition to the objects shown in Figure 1. 33 b.
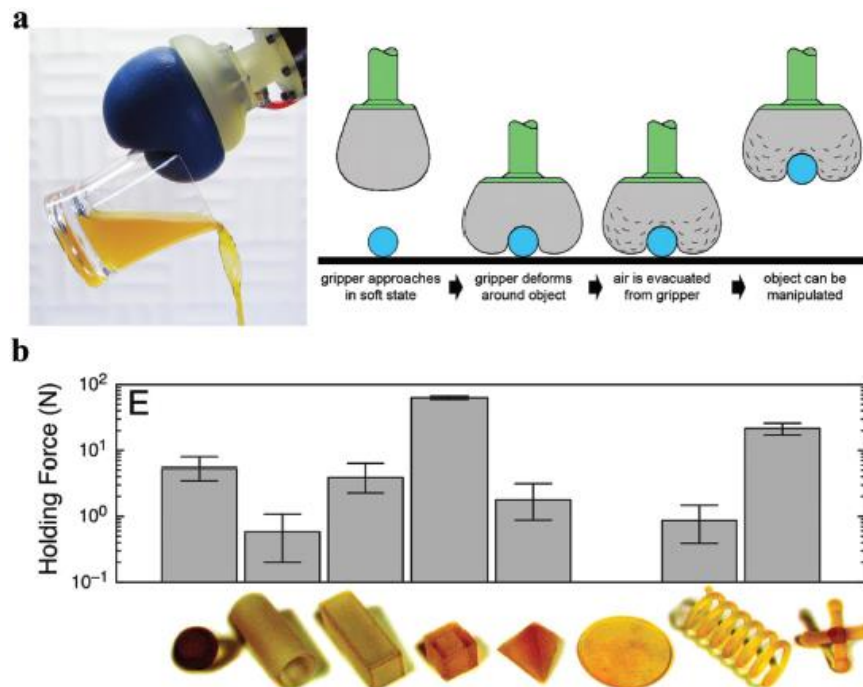
Figure 1. 33. Soft gripper using particle jamming. a) Representative configuration, its working mechanism. b) Holding force for different types of object geometry. Image taken from (Brown et al., 2010).

Figure 1. 34 a presents a two-fingered robotic hand developed by (Amend & Lipson, 2017), where each finger is equipped with a particle jamming membrane. As a variable stiffness element, granular jamming can also be combined with other actuation technologies into soft grippers. (Yang, et al., 2018) (Wei, et al., 2016) integrated a jamming component into a fluidic elastomer actuator (Figure 1. 34 b). The bending deformation of the actuator elongates and squeezes the jamming part. This confines granules inside, realizing passive stiffening without the need for vacuum.

Figure 1. 34. Soft grippers using particle jamming. a) Two-fingered configuration (Amend and Lipson, 2017). b) Combination with fluidic elastomer actuator (Yang et al., 2018). Images taken from (Shintake et al., 2018).

Gripping using controlled adhesion can generate high holding forces thanks to the large shear friction force. At the same time, the closing force normal to the surface of the object is much smaller than when gripping by actuation, allowing the manipulation of very fragile objects. There are two major adhesion technologies used in soft grippers: electro-adhesion (Figure 1. 35) and gecko-adhesion (Figure 1. 36).
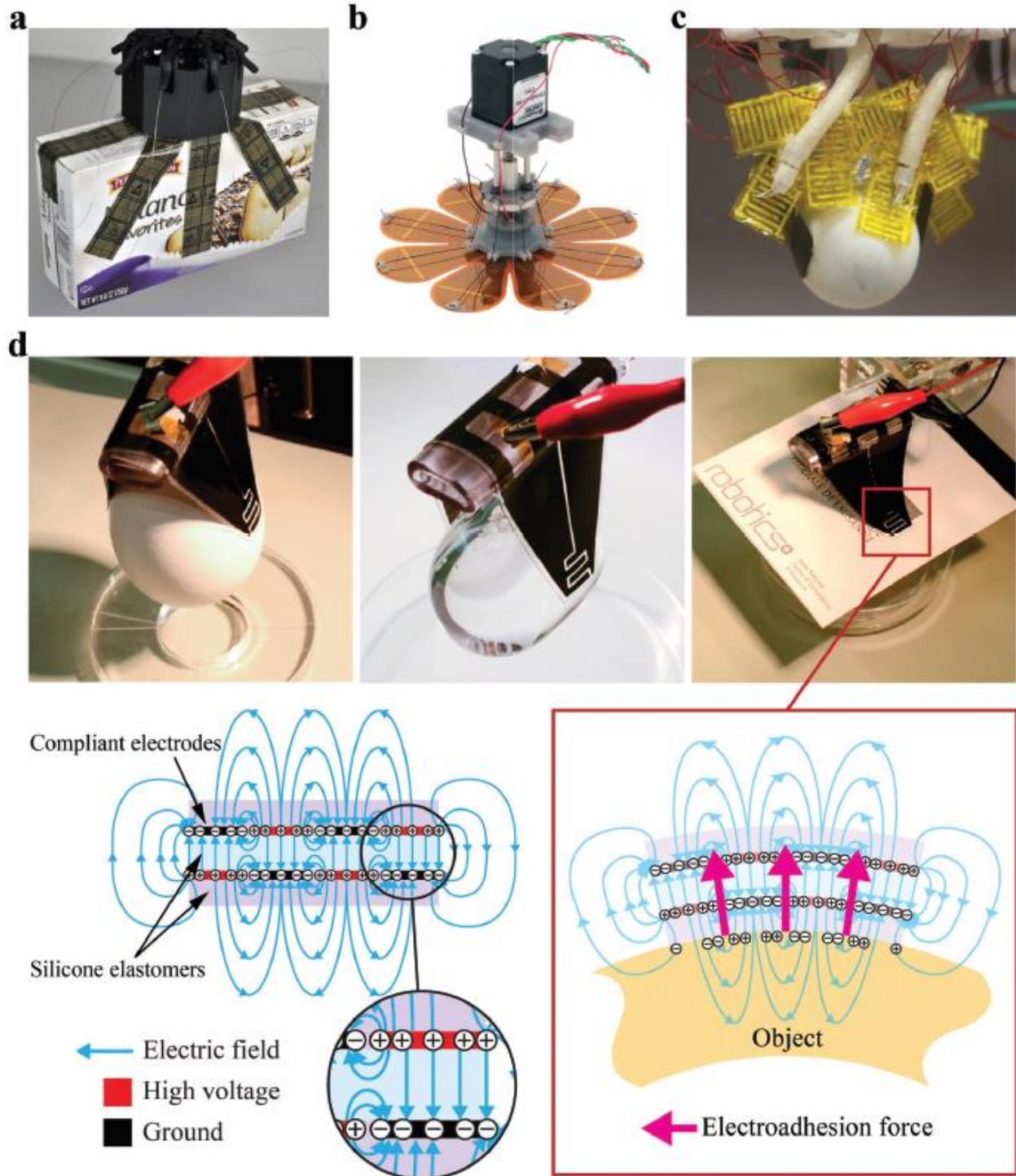
Figure 1. 35. Soft grippers using electro-adhesion. a) Flexible-PCB with external magnetic motors. Courtesy of Grabit Inc. b) Flexible-PCB with external magnetic motors (Schaler et al., 2017). c) Combination with fluidic elastomer actuators (FEAs) (Liang et al., 2017). d) Integration with dielectric elastomer actuators (DEAs). Images taken from (Shintake et al., 2017, 2018).
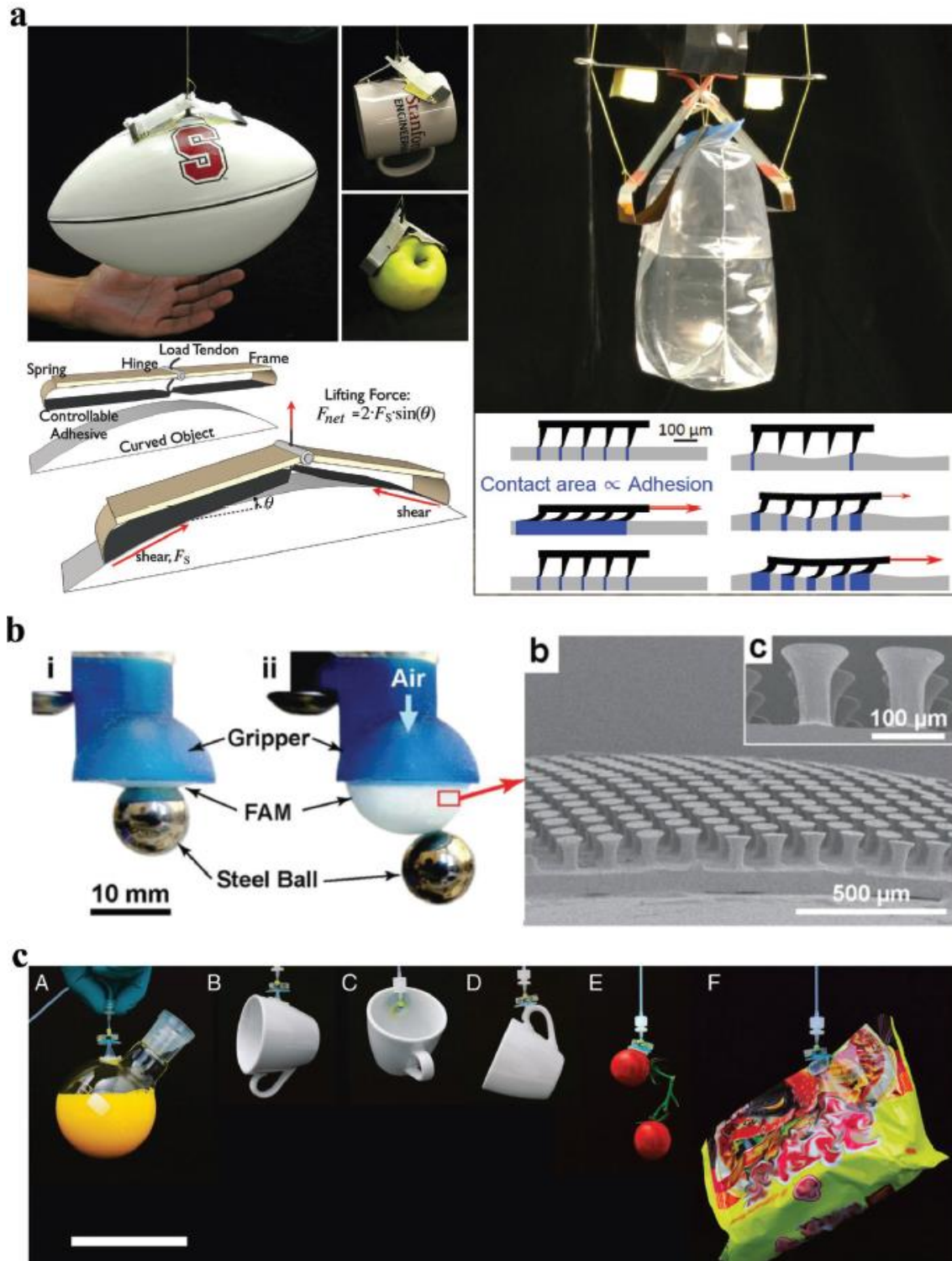
Figure 1. 36. Soft grippers using gecko-adhesion. a) Combination with a passive mechanism that pre-loads microfibers arranged on a flexible film substrate (Hawkes et al., 2015; Suresh et al., 2015). b) Combination with fluidic elastomer actuators (FEAs) (an inflatable membrane) (Song and Sitti, 2014). c) Holding of different items by an elastomer membrane with mushroom-shaped microfibers (Song et al., 2017). Images taken from (Shintake et al., 2017, 2018).

1.3.2.   Underwater soft robotics

Soft and compliant grippers have been shown to dramatically simplify the problem of grasping complex objects with robotic manipulators and are increasingly being used in terrestrial applications. They can be designed to passively limit the force that is applied to fragile or sensitive objects, even when the exact shape of the object is unknown prior to grasping. Furthermore, the softness, the compliance, has the added benefit of increasing the robustness of the grippers themselves – bend rather than break, just like a tree. For these reasons, (ease of grasping, force limiting without sensors, and inherent robustness) it is reasonable to believe that soft robotic grippers can give an excellent match for the challenging problems that confront marine archaeologists and marine biologists sampling in the deep ocean (Figure 1. 37).
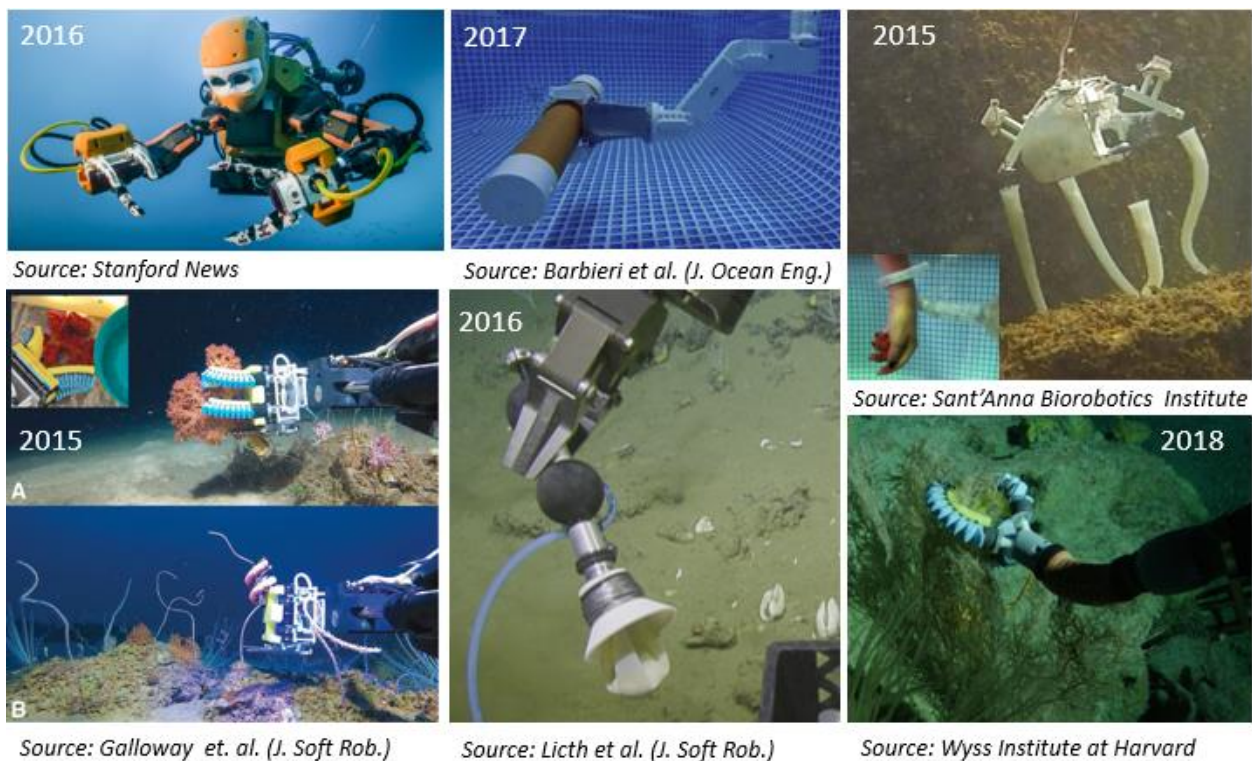
Figure 1. 37. Underwater soft grippers developed during the years.

Pioneering underwater soft grippers were developed by (Lane, et al., 1998), designing a soft robotic subsea hand with a version of continuum actuator fingers.

Recent research from Stanford University explored the development of a compliant, underactuated tendon-driven gripper to augment human capabilities and reduce strain-related injuries for professional divers working at a depth up to 100m, mounted on a humanoid robotic diver called OceanOne. Their gripper mimics the grasp needed to manipulate welding equipment and power tools that would otherwise be used by human hands (Figure 1. 38).
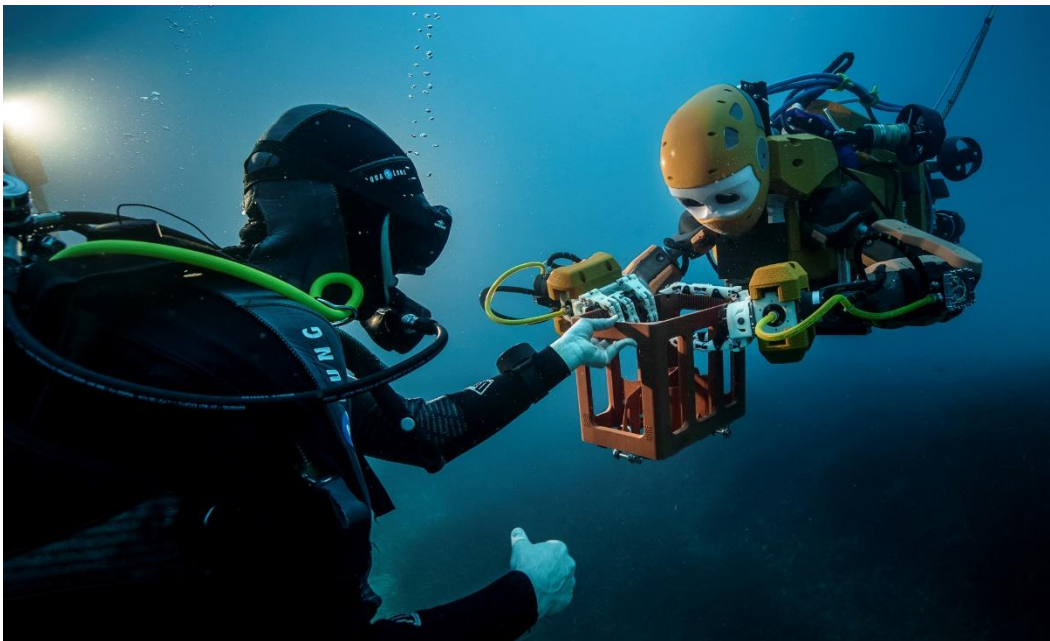
Figure 1. 38. OceanOne while helping diver operations. Credit: Stanford University.

(Galloway, et al., 2016) presents the development of two type of fluidic elastomer actuators (FEAs) underwater grippers to delicately manipulate and sample fragile species on the deep reef. In particular, they presented a bellows-type soft actuator (Figure 1. 39), and boa-type fiber reinforced actuator (Figure 1. 40). Trials in situ at a depth of 100m demonstrate a vast potential to the marine biological community of using these soft grippers, as depicted in Figure 1. 37.
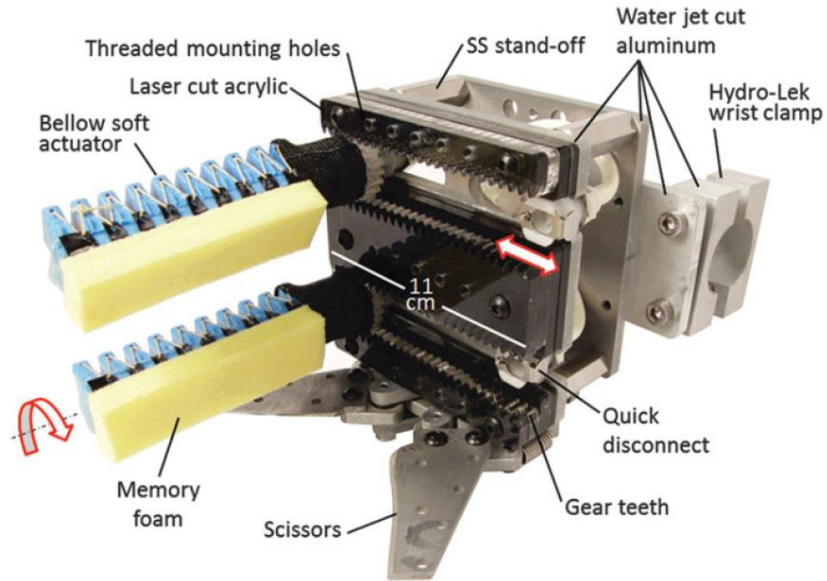
Figure 1. 39. Bellows-type soft gripper. Image taken from (Galloway et al., 2016).
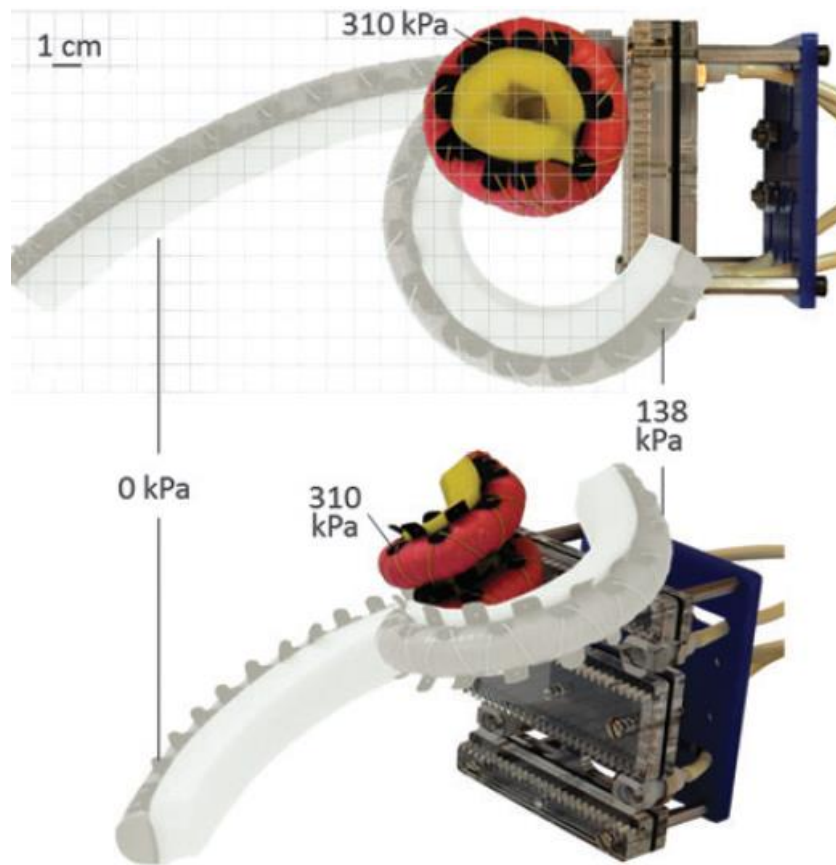
Figure 1. 40. Boa-type soft gripper. Image taken from (Galloway et al., 2016).

Furthermore, a new fabrication technique for a rapid production of bellows-type actuators soft gripper has been investigated by Wyss Institute at Harvard University. This leads to a modified version of the gripper with only two fingers that can perform both a "power grasp" for holding large objects and a "pinch grasp" for holding small objects, much like a human hand (Figure 1. 41).
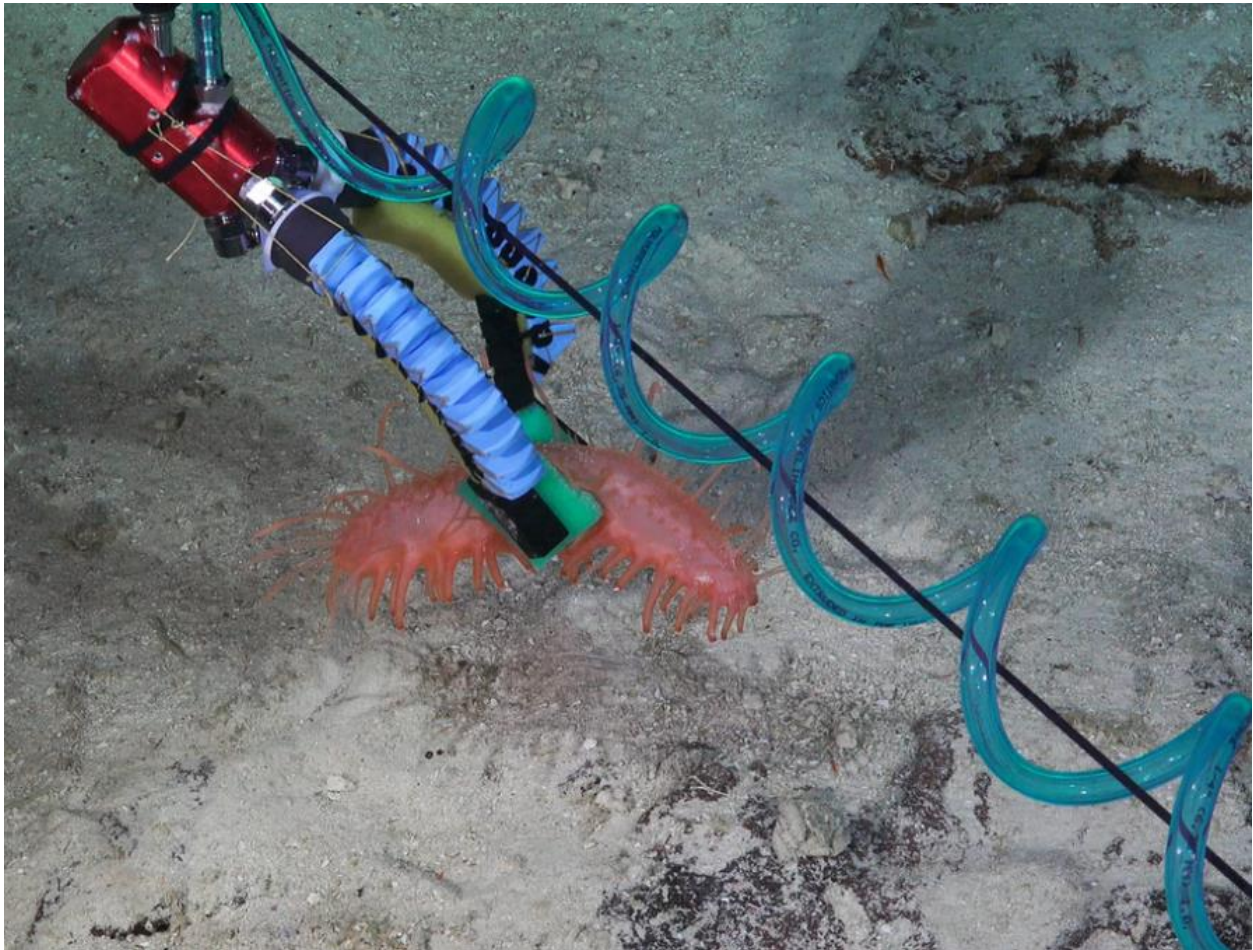
Figure 1. 41. Two finger gripper with bellows-type actuators grasping a delicate sea cucumber. Credit: Wyss Institute at Harvard University.

Another version of the gripper with three fingers is depicted in Figure 1. 42.

Figure 1. 42. Tree finger gripper with bellows-type actuators grasping a sea anemone. Credit: Wyss Institute at Harvard University.

Taking advantage of the additive manufacturing techniques a fully 3D-printed version of the gripper (Figure 1. 43) has been fabricated using a photopolymer 3D printer (Stratasys Objet Connex500) and tested in the deep water (Figure 1. 44).

Figure 1. 43. Fully 3D-printed version of the gripper. Credit: Wyss Institute at Harvard University.

Figure 1. 44. Trials in the deep water. Image taken from ROV Planet Journal, n.14 pp. 32.

Currently, a new system built by scientists at the Wyss Institute, Baruch College, and the University of Rhode Island (URI) uses a glove equipped with wireless soft sensors to control simultaneously a modular, soft robotic arm, and the bellow-type soft gripper (Figure 1. 45). The research is reported in (Phillips, et al., 2018).
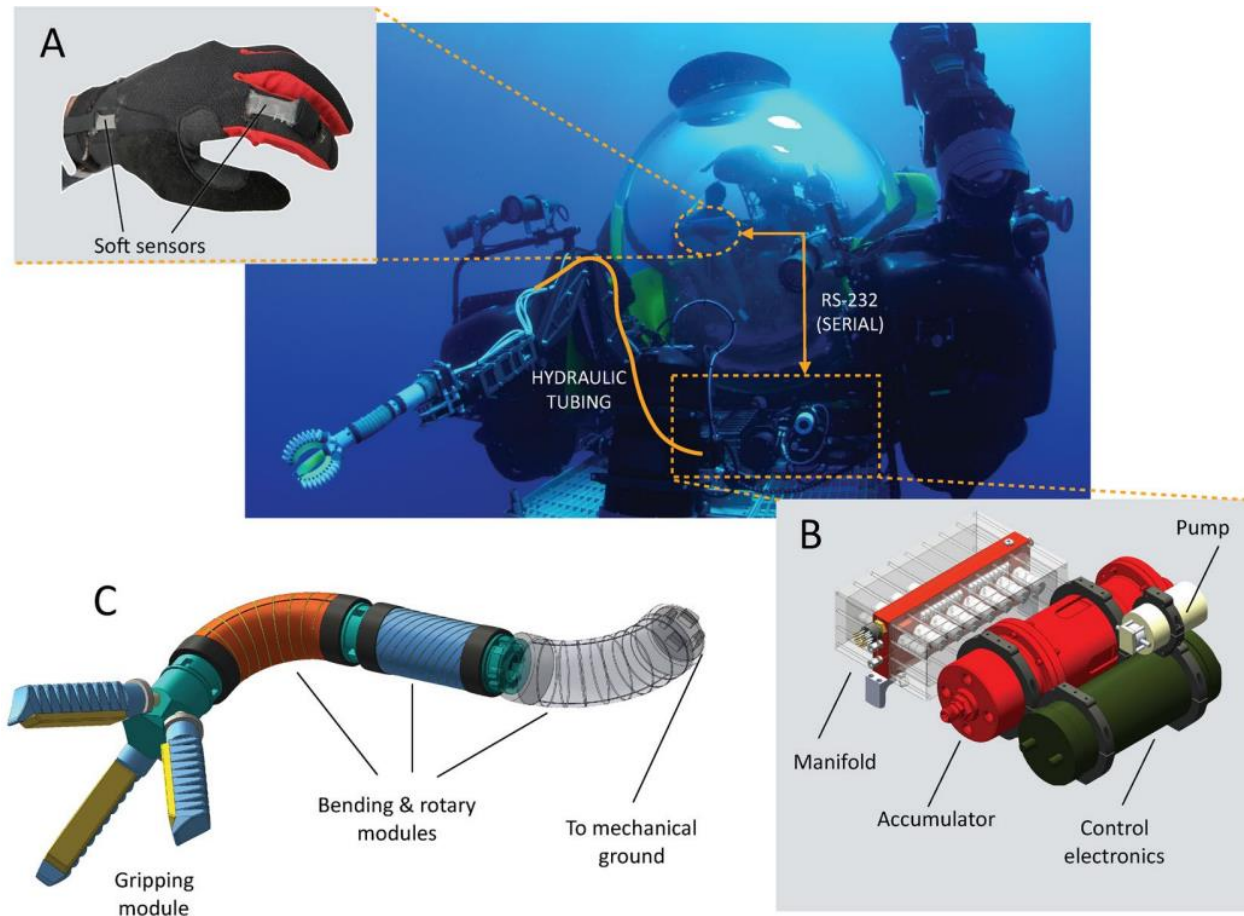
Figure 1. 45. Overview of the deep-sea soft robotic arm system. (A) Control of actuators is achieved using a sensorized wireless glove, which coordinates the control of independent proportional valves that distribute pressure to the arm and end-effector actuators. (B) A custom open-circuit seawater engine regulates hydraulic pressure to independent ports, and can operate at depths of at least 2500m. (C) The soft arm, consisting of bending, rotary, and gripping modules, can be mounted independently or as part of an existing manipulator system. Image taken from (Phillips et al., 2018).

The manipulator system has been successfully operated in depths exceeding 2300m and has been field-tested onboard a manned submersible vehicle (Figure 1. 46).
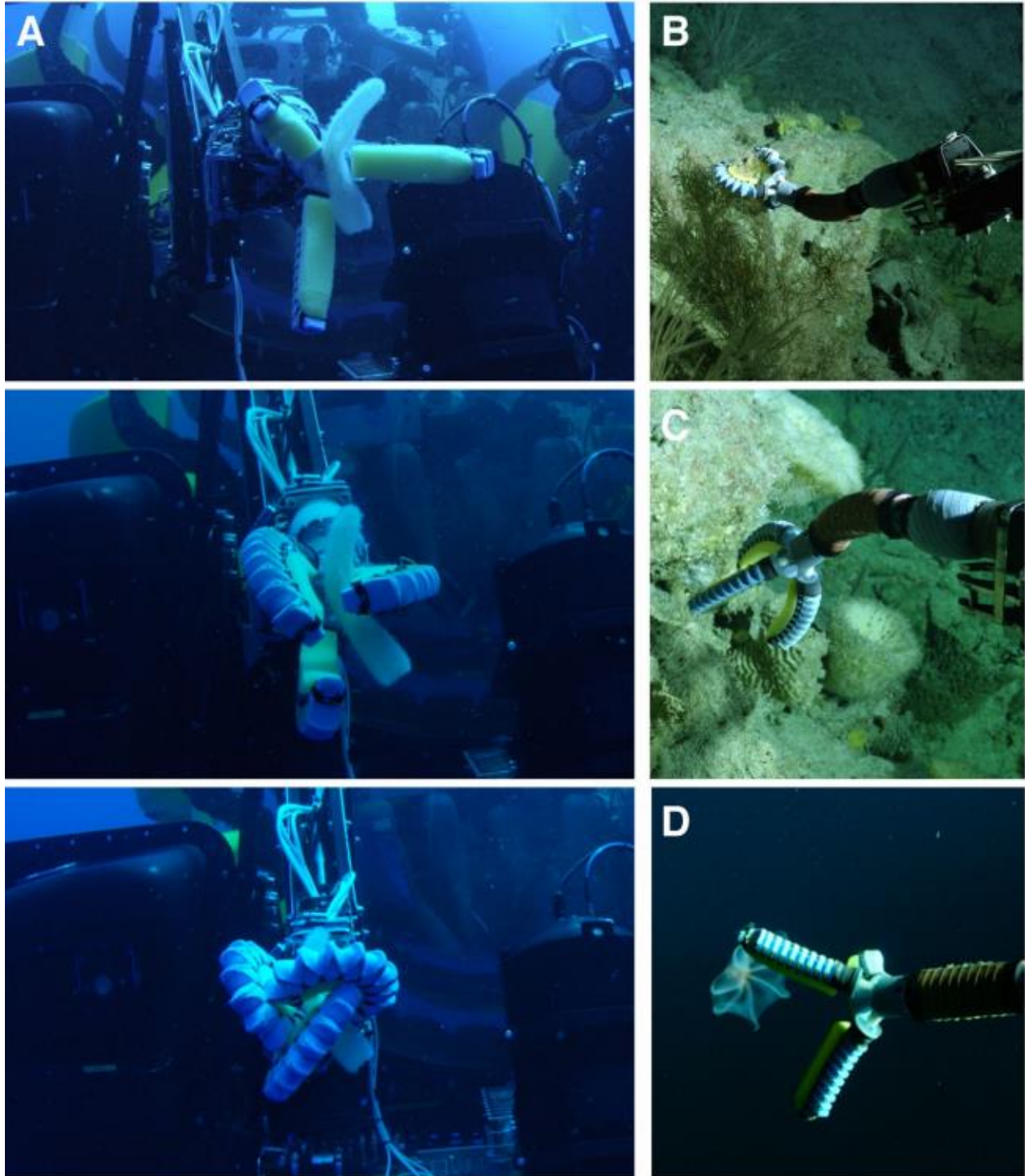
Figure 1. 46. Field testing using a Triton 3K3 manned submersible vehicle. (A) Image sequence of the soft manipulator grasping a midwater pyrosome (Pyrosoma atlanticum) in the water column, as observed from a diver. (B) The soft manipulator articulating upwards to grasp a coral at approximately 300m depth and (C) downwards to grasp a sponge. (D) Manipulator straightened out to approach the deep-sea octopus. Image taken from (Phillips et al., 2018).

Moreover, a new device developed by a University of Rhode Island engineer, Brennan Phillips, and researchers at Harvard University, Zhi Ern Teoh, safely traps delicate sea creatures inside a folding polyhedral enclosure and lets them go without harm using a novel, origami-inspired design (Figure 1. 47).
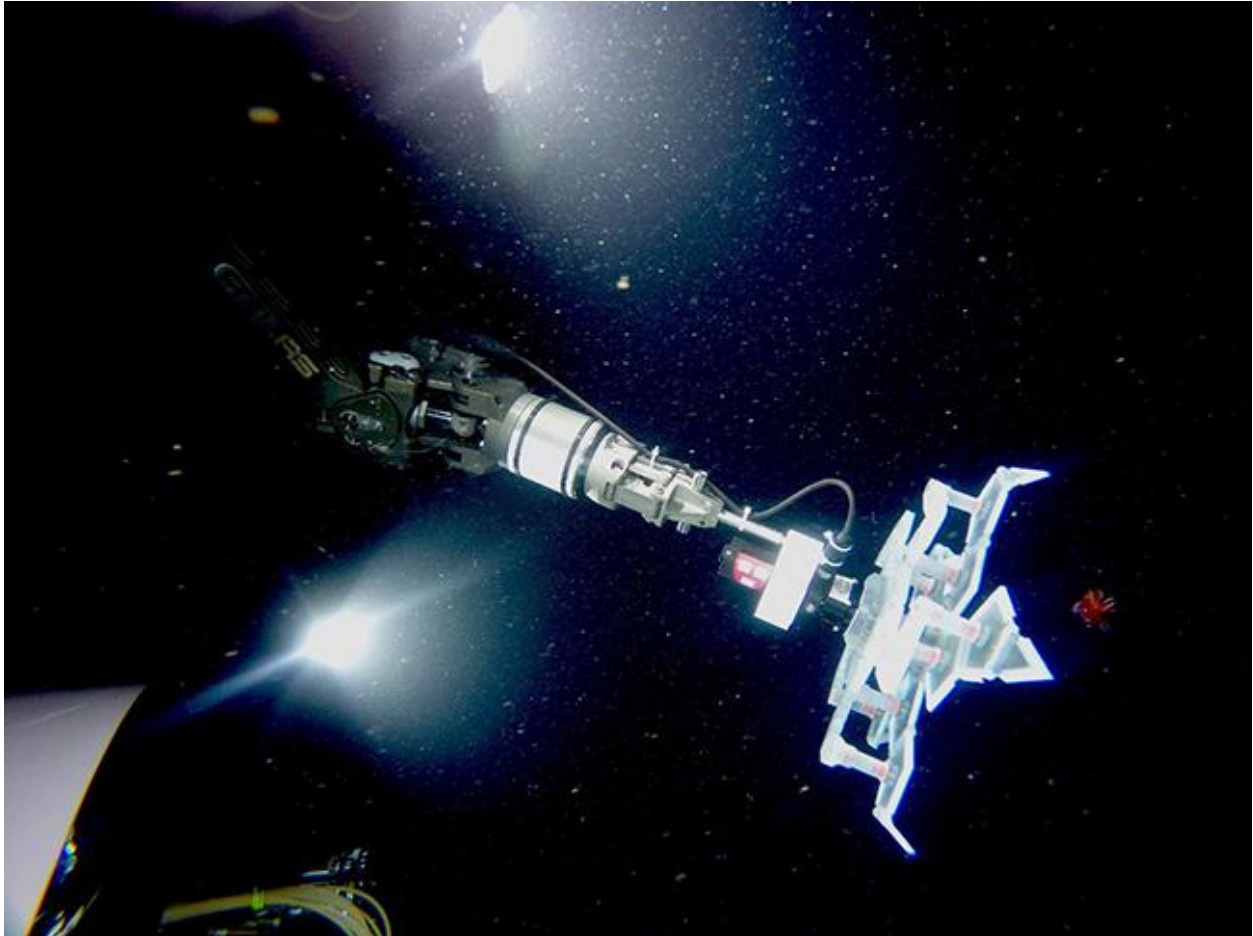
Figure 1. 47. The rotary actuated dodecahedron sampler, invented by researchers at URI and Harvard, has five origami-inspired "petals" arranged around a central point that fold up to safely capture marine organisms. Credit: Wyss Institute at Harvard University.

The device that Phillips and Teoh built consists of five identical 3D-printed polymers "petals" attached to a series of rotating joints that are linked together to form a scaffold. When a single motor applies a torque to the point where the petals meet, it causes the entire structure to rotate about its joints and fold up into a hollow dodecahedron (like a twelve-sided, almost-round box), earning it the name of Rotary Actuated Dodecahedron

(RAD). The idea is to make a device that can help describe new species directly in the deep sea without actually bringing them back up.

Finally, (Licht, et al., 2017) employed jamming gripper as an end effector of a remotely operated vehicle for deep sea sampling, and showed that the gripper was able to generate over 35 N of pulling force on a sample (stainless steel rod) at a depth of 1200 m (Figure 1. 48). This prototype has been developed at the Robotics Laboratory for Complex Underwater Environments of the University of Rhode Island, directed from Prof. Stephen Licht, and represent the starting point with which my research internship has begun at that university (Chapter 4).
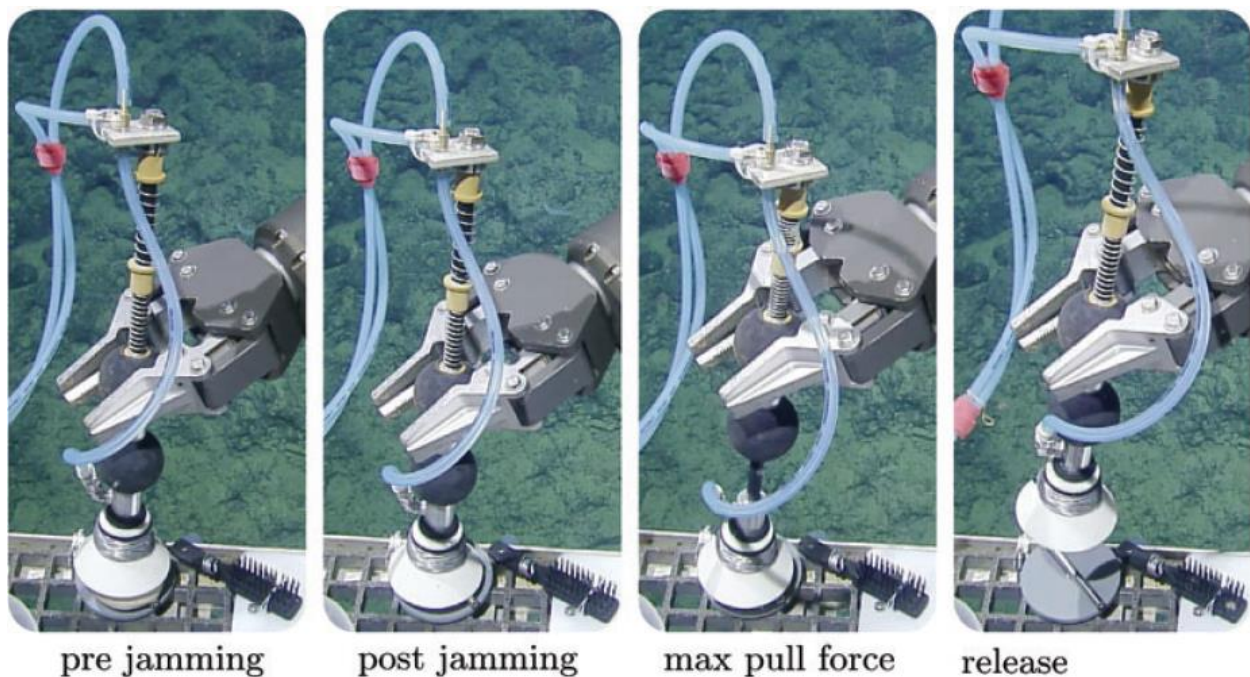
Figure 1. 48. Underwater soft jamming gripper holding force test in deep sea. Image taken from (Licht et al., 2017).

2. An underwater hydraulic arm for artifacts cleaning

As previously mentioned, underwater manipulation is widely employed in various operations for performing a diverse range of applications in the submerged environment, such as inspections, mapping, collecting biological sediment and fragile creature. All these operations require high quality of the work and a precise positioning of the end-effectors, that makes intervention capacity of the ROV/AUV very challenging while working with manipulators under water. To this end a force-position feedback manipulator is required in order to protect sensitive equipment on the seabed, and the environment as well. Nevertheless, the physical properties of an underwater manipulator may differ from the corresponding ideal values due to geometric errors, such as manufacturing tolerances and assembly misalignments, and non-geometric errors, such as the elastic deflection of the links, thermal deformations, and vibrations. Then, in many cases, manipulators do not behave according to their design but they make mistakes in achieving a specific pose or following trajectories. An error compensation process, that allows to identify and compensate these errors in the mathematical model of the robotic arm, needs to be carried out in order to overcome these limitations and improve the accuracy of the end-effector.

Most of the underwater manipulation tasks, such as maintenance of ships, underwater pipeline or weld inspection, surveying, oil and gas searching, cable burial and mating of underwater connector, exploration and salvage, require the manipulator mounted on the vehicle to be in contact with the underwater object or environment (Dunnigan and Russell, 1998; Heshmati-Alamdari et al., 2016). As a consequence, the development of autonomous underwater vehicles equipped with one or more manipulators (UVMS - Underwater Vehicle-Manipulator System) has gained in the last two decades a large attention (Fossen, 1994; Antonelli, 2006; Marani et al., 2009). Then manipulators have been largely adopted on ROV (Kyo et al., 1995; Shim et al., 2010; Sagara and Ambar,

2015; Lee et al., 2007), mainly in remotely controlled or in a master-slave configuration, and on fully-autonomous and semiautonomous underwater vehicles too (Yuh et al., 1998; De Novi et al., 2009; Lane et al., 1997; Fujii and Ura, 1996; Simetti et al., 2014). The need for a single or multiple robotic underwater manipulators has been expressed also by diverse submerged science projects such as Venus (Kawaguchi et al., 1998), Neptune (Delaney et al., 2003) and CoMAS (Bruno et al., 2016). In the terrestrial environment, the kinematic performances of manipulators and their calculation methods are known to scientific community since the dawn of robotic (Wu, 1983). In particular, well-established techniques to improve end-effector accuracy have been widely applied in the robotic and automation fields. (Stone, 1987), (Mooring et al,1991) and (Hollerbach, 1989) treated its fundamental and main aspects, extensively dealing with the whole methodology, giving a related comprehensive bibliography and historical background as well. Typically, robot position accuracy is improved using compensation procedures (Hollerback, 1989; Roth et al., 1986; Hollerback and Wampler, 1996; Zhuang et al., 1996), based on error models (Waldron and Kumar, 1979; Wu, 1984; Vaichav and Magrab, 1987; Miman and Gupta, 1993), that identify a more accurate functional relationship between the joint transducer readings and the actual workspace position of the end-effector based on experimental calibration measurements. These methods require both accurate measurement instruments and elaborate experimental setup, such as the laser interferometry tracking (Alici and Shirinzadeh, 2005; Shirinzadeh et al., 2010), stereo vision feedback (hager and al., 1995), mechanical dime (Gatti and Danieli, 2008), theodolites and stereo triangulation (Zhuang et al., 1995). The complexity of the unstructured underwater environment introduces other issues that affect the effective accomplishment of specific tasks by means of the manipulator units. These problems are mainly due to the external disturbances (hydrodynamic effects), kinematic redundancy, dynamic coupling forces between the underwater vehicle and manipulators and gravity forces which can affect the trajectory performances of the manipulator's end-tips. In fact, until the 1990s there were very few research studies related to underwater vehicles equipped with manipulators due to various issues related to the submerged environment (Yuh, 2000). But, in the last years, due to the increase in demand for more dexterous and precise underwater manipulation, many researches involving for the kinematic and dynamic analysis of the

underwater manipulator have been performed (Shim et al., 2010). These studies include the dynamic model and efficient dynamic simulation of an underwater vehicle with a robotic manipulator (Tam et al., 1996; McMillan et al., 1995), the reduction of the dynamic coupling between manipulator and underwater vehicle (Dunnigan and Russell, 1998), and the manipulability analysis of underwater robotic arms on ROV (Jun et al., 2004). Also, there have been many studies on manipulator control for enhancing efficiency of underwater manipulation, such as the force feedback control of manipulators mounted on ROVs (Ryu et al., 2001), motion planning, and control of UVMS (Sarkar and Podder, 2001), computer-based control, and real-time motion compensation of UVMS (Hildebrandt et al., 2009).

This section presents a study conducted for evaluating the kinematic performances of a hydraulic underwater manipulator, developed in the CoMAS (In situ conservation planning of Underwater Archaeological Artifacts - http://www.comasproject.eu) project, equipped on an ROV to support maintenance operations in underwater archaeological parks.

2.1. Previous work

The arm has been re-designed starting from a commercial Hydro-Lek HLK-43000 5-functions hydraulic arm, which incorporates a continuous jaw rotate mechanism with an integrated rope cutter tool (Bruno, et al., 2015b). Firstly, this arm has been modified in order to ensure a greater working volume The length of the modified arm is 1050 mm, 497 mm more than the original one. Furthermore, in the modified arm has been integrated three Acuro AR-63 waterproof CAN-bus magnetic encoder in order to measure the angular position of the first three joints and a pair of RE22 SSI magnetic encoder to measure the movement of the Pan & Tilt assembly. The original rope cutter tool has been removed, modifying the continuous jaw rotate mechanism in a pan-tilt system which handles an electric brush in order to satisfy the purpose of the CoMAS project (Bruno, et al., 2016) (Figure 2. 1).
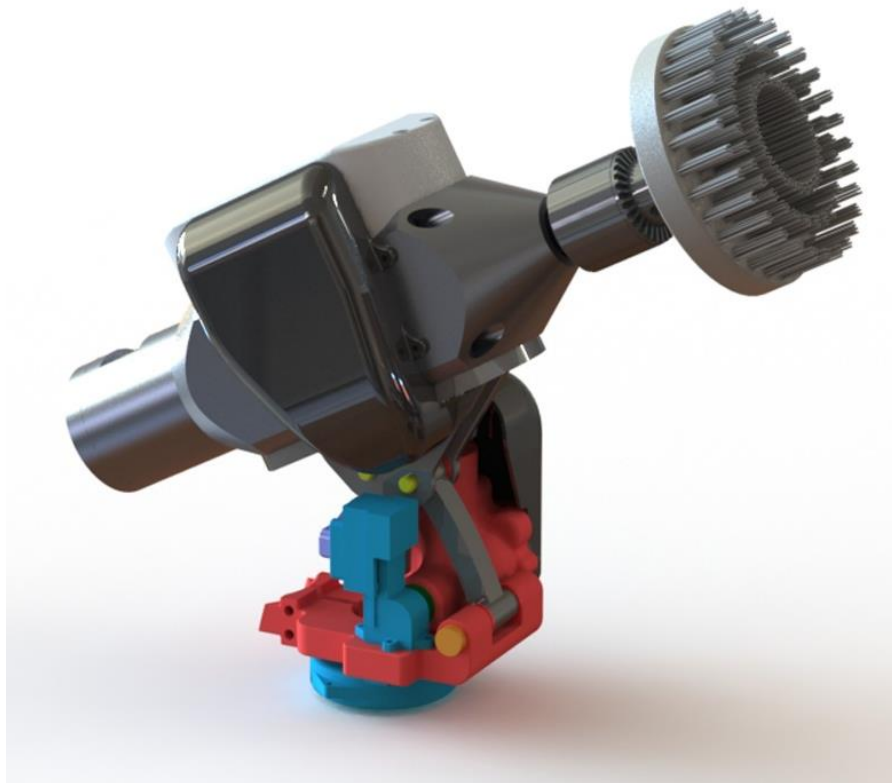
Figure 2. 1. The rendering of the electromechanical brush mounted on the redesigned Pan & Tilt assembly.

The electromechanical brush has been equipped with three sensors S2Tech BC302-20 kg for measuring the axial force. Moreover, it uses a 1200 W brushed motor with a maximum torque of 15 Nm at 1250 rpm, and can handle different types of brushes to perform all the planned maintenance operations.

The components of the modified arm have been realized using conventional CNC machines and rapid prototyping techniques. In particular, the complex geometries of the pan-tilt assembly have been printed in polyamide using the EOS Formiga P110 SLS machine available at the Department of Mechanical, Energy, and Management Engineering of the University of Calabria. The arm with the hydraulic and electrical system mounted on the ROV's skid is depicted in Figure 2. 2.

Figure 2. 2. Modified arm and electric brush mounted on the ROV's skid.

The electronics, connected to the ROV's pod through CAN-bus protocol, measures parameters such as rotational speed, motor temperature, torque, axial force, and the encoder values.

2.2. Kinematic performance evaluation

The procedure for evaluating the kinematic performances of the underwater manipulator consists of six main steps, as shown in Figure 2. 3.
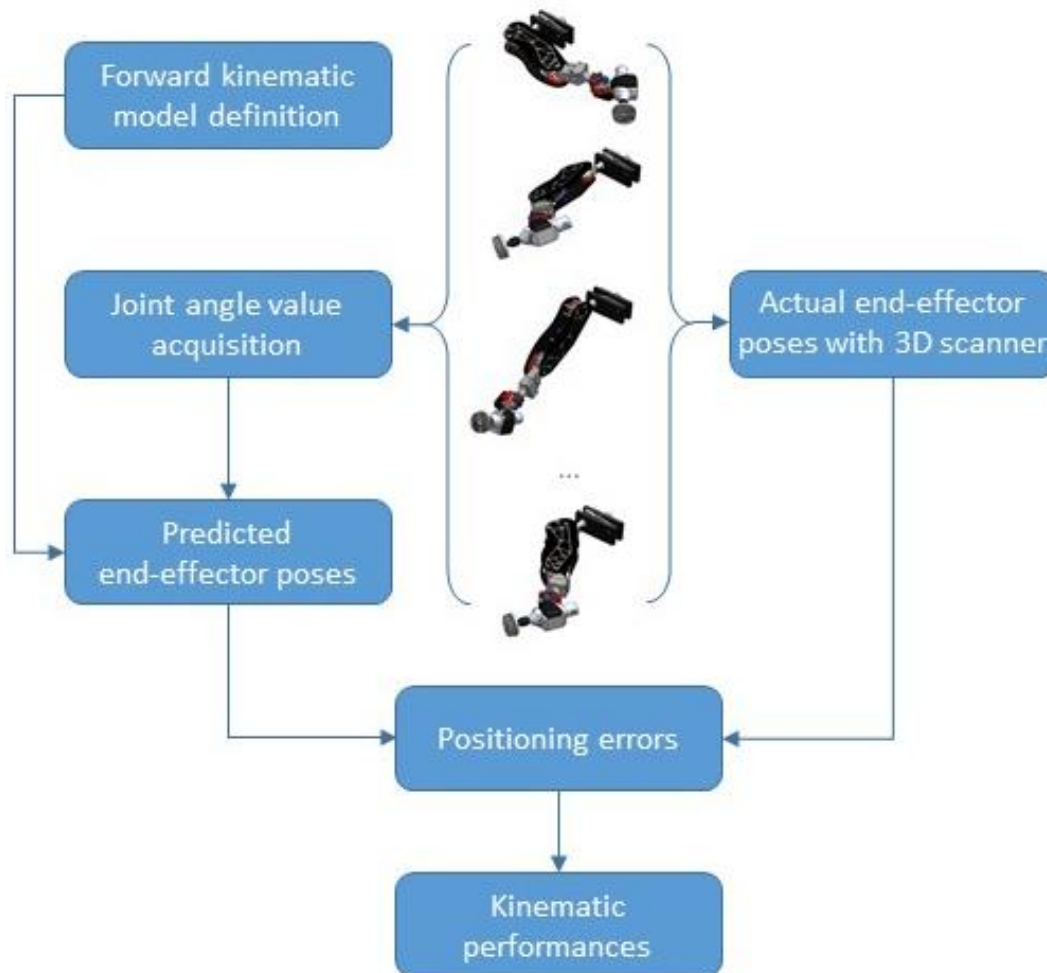
Figure 2. 3. Method for evaluating the kinematic performances of the robotic arm.

In the first step, the forward kinematic model of the robotic arm is defined according to D-H notation (Denavit & Hartenberg, 1955). This forward kinematic model allows the estimation of the end-effector pose with respect to the joint angles of the robotic arm. In particular, a zero-reference configuration of the robotic arm is established in order to infer

the equation of homogeneous matrix transformations that is calculated on the basis of the D-H notation.

In order to estimate the end-effector pose of the robotic arm, the kinematic model needs to be expressed with respect to the joint angles. For this reason, in the second step, a data acquisition phase is carried out by collecting the joint angle values that are known by reading the absolute encoders mounted on the robotic arm. The data reading and data logging tasks are performed via software on different poses of the manipulator. Therefore, the robotic arm is commanded to move its end-effector to different poses in the workspace, and for each pose, the joint angle values are measured with respect to the zero-reference position by means of data provided by the absolute encoders.

In the third step, the forward kinematic model defined in the first step and the joint angle values collected in the second step are integrated in order to obtain a set of predicted end-effector poses.

These predicted poses could differ from the real ones because they are estimated on the basis of the forward kinematic model of the robotic arm without taking into account the errors that affect the overall mechanism. In fact, the physical properties of manipulators (e.g., the joint axis orientation and the concentricity with their housing, true dimensions of the links) are affected by geometric errors, such as manufacturing tolerances, assembly errors and misalignment of the joints, and non-geometric errors, like as the elastic deflection of the links, thermal deformations and vibrations. For these reasons, in the fourth step, an external metrology system has to be adopted in order to measure the actual end-effector pose in some different configurations. In particular, the arm's configurations that have been adopted in the second step are acquired by a 3D laser scanner that allows a fast and accurate scanning of the poses. Subsequently, the measurements of the predicted and the actual poses are compared in the fifth step in order to have an estimation of the positioning errors that are necessary for the definition of the kinematic performance of the robotic arm.

And finally, in the last step, the kinematic performances of the robotic arm, consisting in the repeatability and accuracy, are calculated according to the ISO standard 9283:1998. These two characteristics are defined as follows: the repeatability is the ability of the

system's end-effector to measure a previously achieved pose; the accuracy is the ability of the system's end-effector to measure a specified pose.

2.2.1. Experimentation

The experimentation activities have been carried out on the underwater manipulator, developed in the CoMAS project, on basis of the first steps detailed in the previous section about the measurement of the predicted and actual end-effector's poses.

Kinematic modelling

The mathematical description of the kinematic chain of the 5-DOF underwater manipulator has been obtained according to the DH-parameter notation. The DH notation allows to identify the DOFs and number the links starting from the basement, denoted as the link [0], of the robotic arm. As depicted in Figure 2. 4, the robotic arm has five joints and five links, four of which are revolute joints, with rotation along the z-axes, and the last one, represented within the orange box, is the tilt mechanism.
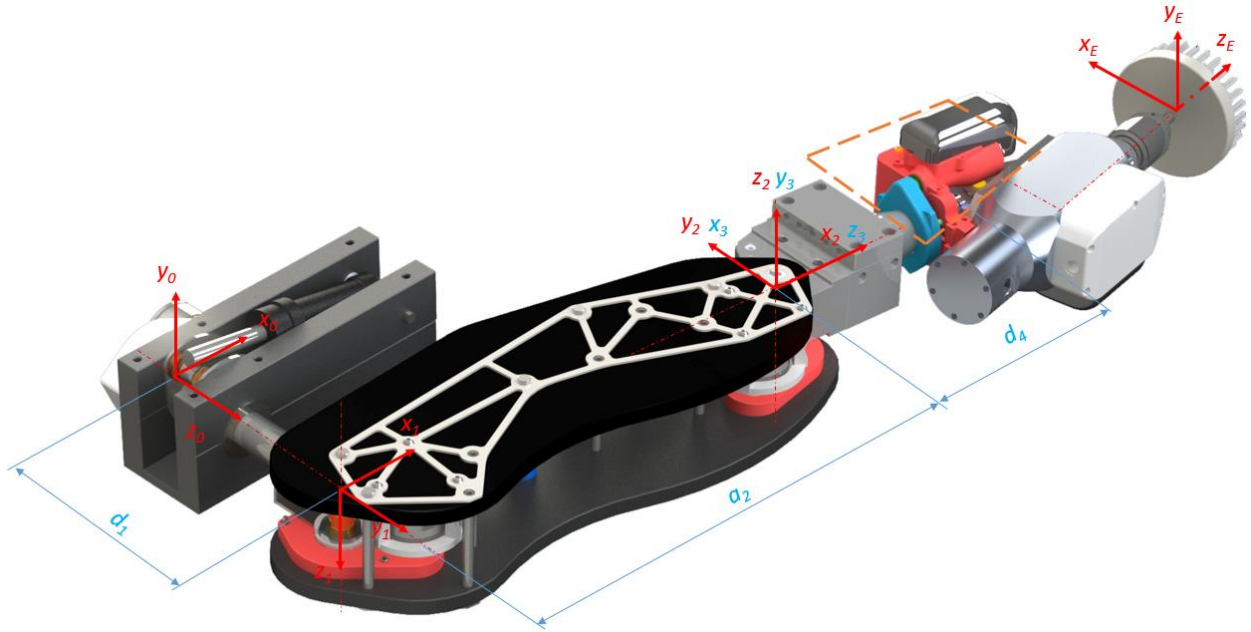
Figure 2. 4. Zero-reference configuration of the robotic arm and DH notation.

The schematic representation of the arm is depicted in Figure 2. 5, where the reference frame {B} is coincident with {0}, and the frame {E} is referred to the end-effector's tool. Here the articulated quadrilateral is represented within the green box area.
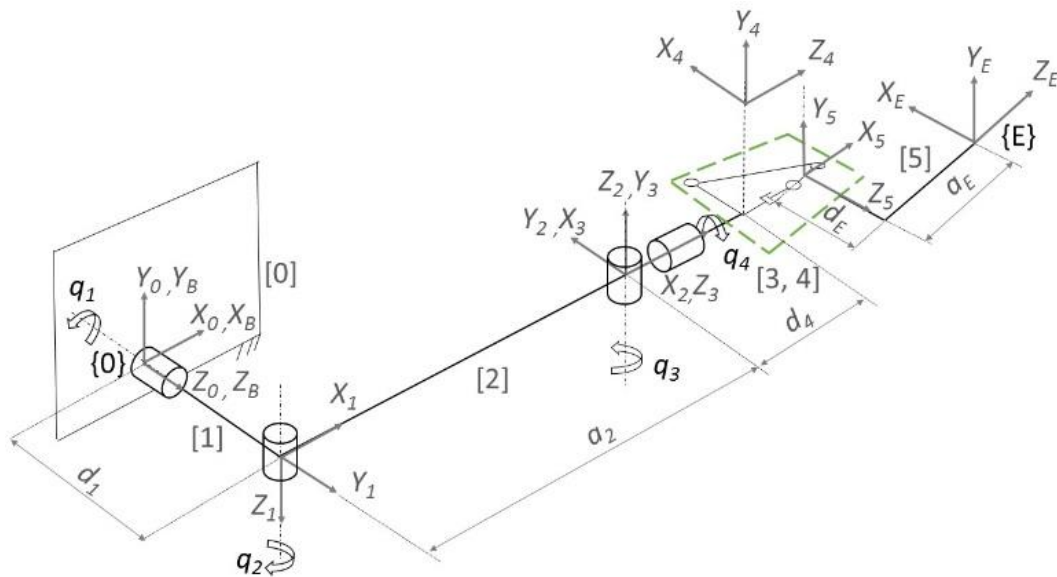
Figure 2. 5. Schematic representation of the underwater manipulator with D-H convention and parameters.

A standard D-H convention has been adopted for the definition of the forward kinematics of the first four joints of the manipulator. Its geometric parameters have been established on the basis of the zero-reference configuration, and the resultant D-H parameters are shown in Table 2.1, where: T_i^{i-1} are the homogeneous transformation matrices which describe the pose of each joint frame with respect to the preceding frame; θ_i are the z-axis rotations, d_i are the frame's offsets along the z-axis, a_i are the link lengths along the x-axis, and α_i are the x-axis rotations.

$^{i-1}T_i$	θ_i [deg]	d_i [mm]	a_i [mm]	α_i [deg]	Limit q_i [deg]
$^0T_1$	q_1	229	0	90	20 to -90
$^1T_2$	q_2	0	450	180	-10 to 80
$^2T_3$	$q_3 + 90$	0	0	-90	0 to 45
$^3T_4$	q_4	225	0	0	0 to 180

Table 2.1. D-H parameters.

In particular:

$^0T_1$= Rz(q1) Dz(d1) Rx(90°);

$^1T_2$= Rz(q2) Dx(a2) Rx(180°);

$^2T_3$= Rz(q3) Rz(90°) Rx(-90°);

$^3T_4$= Rz(q4) Dz(d4).

Regarding the resolution of the direct kinematics of the tilt mechanism (Figure 2. 6), it is a quadrilateral mechanism that can been expressed as follows:

$^4T_5$ = Dz(b)·Ry(δ)·Dz(c/2)·Ry(-δ)·Ry(-φ)·Ry(q5)

where b, δ, c and φ are the parameters of the four-bar linkage, and the q_5 angle rotation can vary between 0 to 90 degrees.
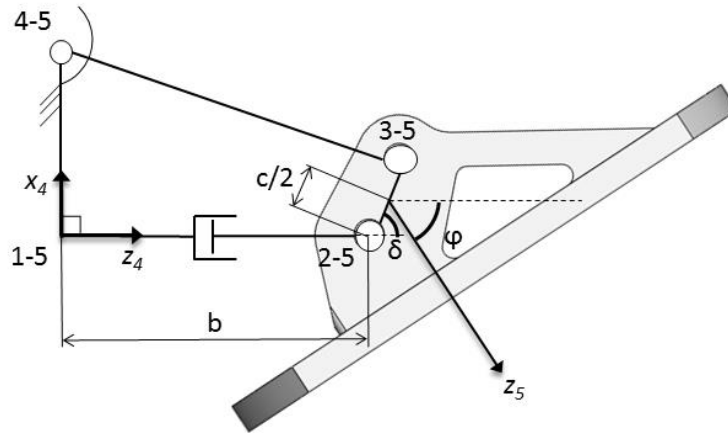
Figure 2. 6. Schematic representation of the quadrilateral mechanism and characteristic parameters.

Similarly, the last transformation matrix referred to the end-effector of the robotic arm (Figure 2. 7) has been formulated as follows:

$$^5T_E = \mathrm{Dz}(\mathrm{d_E}) \cdot \mathrm{Dx}(\mathrm{a_E}) \cdot \mathrm{Ry}(90°)$$

where $\mathrm{d_E}$ is the frame's offset along the z-axis and $\mathrm{a_E}$ is the link length along the x-axis.
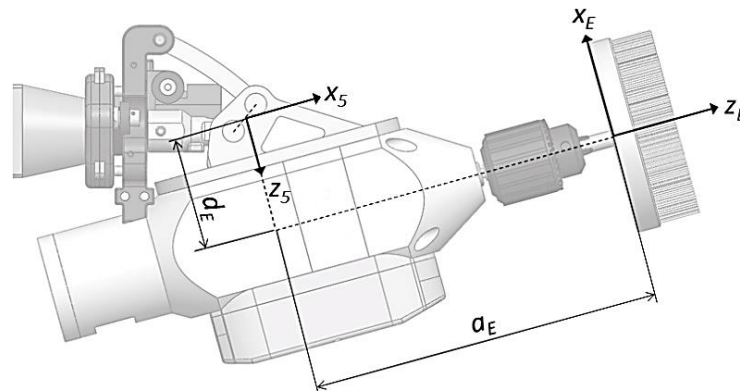
Figure 2. 7. Local reference frame and geometric parameters of the end-effector tool.

On the basis of the above-mentioned considerations, the kinematic model of the underwater manipulator, that specifies the relative pose of the end-effector and the base coordinate system, is expressed by means of the homogeneous transformation matrix:

$$^0T_E = \begin{bmatrix} ^0R_E & S \\ 0_{1x3} & 1 \end{bmatrix} = {^0T_1} \cdot {^1T_2} \cdot {^2T_3} \cdot {^3T_4} \cdot {^4T_5} \cdot {^5T_E}$$

where the submatrix ^0R_E and the array S = [x y z]^T are respectively rotational matrix and the end-effector's position vector.

Joint angle value acquisition

The second step starts with the "homing" procedure in which the absolute encoders have been set in their home position with regard to the zero-reference configuration of the robotic arm. The results of the homing procedure are reported in Figure 2. 8, where is pointed out the encoder value respect to the joint angle.
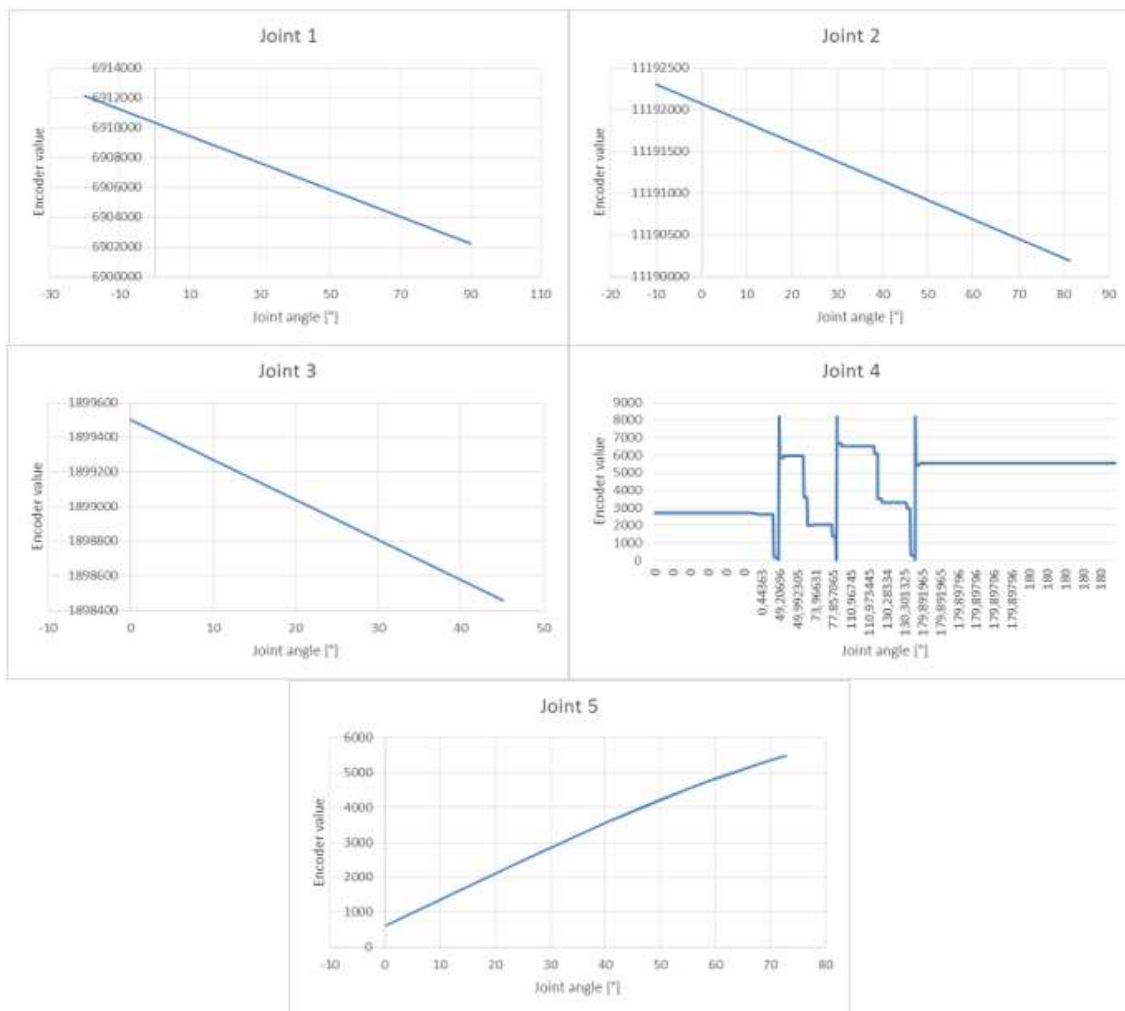
Figure 2. 8. Homing procedure: encoder value to joint angle. The encoder of the 4th joint is configured in multi turn mode.

The encoder data acquisition starts in the zero-reference configuration and continues while commanding the robotic arm in order to reach ten different poses in the workspace. In particular, for each pose, the value of the encoders are transmitted by means a can-bus communication to a personal computer on which a software, developed ad hoc, records the data and operates a conversion of the hexadecimal raw values into their equivalent decimal representation (Figure 2. 9).
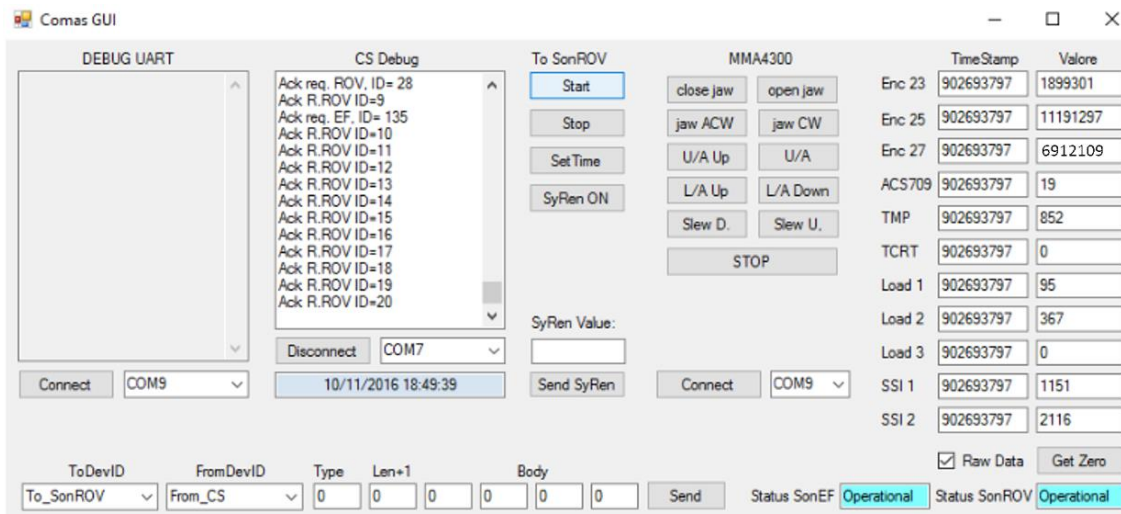
Figure 2. 9. Data acquisition software of the arm's sensors. The absolute encoders are pointed out with the name Enc 23, 25, 27, SSI 1 and 2.

The proposed software is able to save a log of data with the value of the encoders (Table 2.2).

POSE	N° JOINT	VALUE ENCODER [step]	JOINT ANGLE [°]	PISTON EXCURSION [mm]
1	1	6912109	20,00	92,50
	2	11190130	93,22	91,78
	3	1899500	0,00	105,00
	4	6750	90,00	
	5	604	0,05	0,00
2	1	6907600	-30,10	63,35
	2	11190830	59,57	70,19
	3	1898300	51,92	35,77
	4	5547	180,00	
	5	5475	71,16	27,18

	1	6912110	20,01	92,51
	2	11190210	89,38	89,31
3	3	1899500	0,00	105,00
	4	2711	0,00	
	5	5380	71,16	27,18
	1	6912110	20,01	92,51
	2	11190210	89,38	89,31
4	3	1899499	0,04	104,94
	4	3570	120,00	
	5	604	0,05	0,00
	1	6910767	-5,09	83,82
	2	11190700	65,82	74,20
5	3	1898700	34,62	58,85
	4	5547	180,00	
	5	2479	25,07	10,59
	1	6910759	5,00	83,77
	2	11191122	45,53	61,18
6	3	1898458	45,09	44,88
	4	5547	180,00	
	5	5587	69,50	13,40
	1	6908059	-25,00	66,32
	2	11191085	47,31	62,32
7	3	1898460	45,00	45,00
	4	2711	0,00	
	5	5575	70,70	27,06
	1	6912097	19,87	92,42
	2	11190203	89,71	89,52
8	3	1898518	42,49	48,35
	4	5547	180,00	
	5	5541	73,98	27,89
	1	6902203	-90,07	28,46
	2	11190768	62,55	72,10
9	3	1898536	41,71	49,38
	4	5547	180,00	
	5	5575	73,91	27,87
	1	6902203	-90,07	28,46
	2	11190768	62,55	72,10
10	3	1899500	0,00	105,00
	4	5547	180,00	
	5	2976	31,84	13,40

Table 2.2. Encoders Log.

Then, these values are taken as input to an algorithm, implemented in Matlab, that takes into account the absolute encoders' resolution and transmission ratio in order to provide the joint angles as output. In particular, three encoders are configured for 12-bit resolution (≈0.088°/step), while the encoders of the pan-tilt system of the robotic arm achieve 13-bit resolution (≈0.043°/step). The high-precision absolute encoders are connected to the respective joints by meshing with gear wheels, with a transmission ratio of τ = 0.5 for the encoders of the first three joints, τ = 0.19 and τ = 1, respectively for pan and tilt movements, of the last two joints.

Integrated kinematic model

Then the forward kinematic model, defined in the first step, and the joint angle values, collected in the previous step, have been integrated into Matlab® in order to obtain a set of predicted end-effector poses $p^{(i)} = [x_E, y_E, z_E]^T$. In particular, each pose has been reached twice in order to calculate the mean value $\bar{p}^{(i)}$ that is adopted in the last step for evaluating the kinematic performances of the robotic arm [34,46]. The predicted poses are reported in Table 2.3, where with "M" has been pointed out the length of the 3D vector.

POSE		$\bar{p}^{(i)}$	POSE		$\bar{p}^{(i)}$
1	X	-256,55	6	X	492,89
	Y	-94,31		Y	11,95
	Z	1106,92		Z	688,55
	M	1140,17		M	846,87
2	X	305,63	7	X	430,26
	Y	-350,12		Y	-350,96
	Z	800,37		Z	250,74
	M	925,52		M	609,23
3	X	15,85	8	X	16,3
	Y	-46,59		Y	-134,6
	Z	996,06		Z	1006,27
	M	997,27		M	1015,36
4	X	-183,51	9	X	-215
	Y	-64,1		Y	-547,05
	Z	1108,25		Z	890
	M	1125,17		M	1066,58
5	X	373,26	10	X	-215
	Y	-101,46		Y	-400,9
	Z	883,9		Z	1039,75
	M	964,83		M	1134,91

Table 2.3 Predicted poses.

3D laser scanning of the actual poses

The metrology instrument used to measure the actual end-effector poses is a Stonex X300 laser scanner. This 3D scanner allows creating a 3D point cloud of the acquired scene with an accuracy of 6 mm at 50 meters from the acquired object and a scan rate about 40000 points/sec. The scanning setup, as depicted in Figure 2. 10, consists of a compact 3D scanning station placed to a fixed distance from the robotic arm.

Figure 2. 10. Scanning setup for acquiring actual end-effector poses.

Since the frame {0}, of the zero-reference configuration (Figure 2. 5), is located in the housing of the encoder and it cannot be acquired by the laser scanner, then an additional coordinate system of the base frame has been added. As showed in Figure 2. 11, the coordinate system {B} has been placed on a visible corner of the basement of the robotic arm.
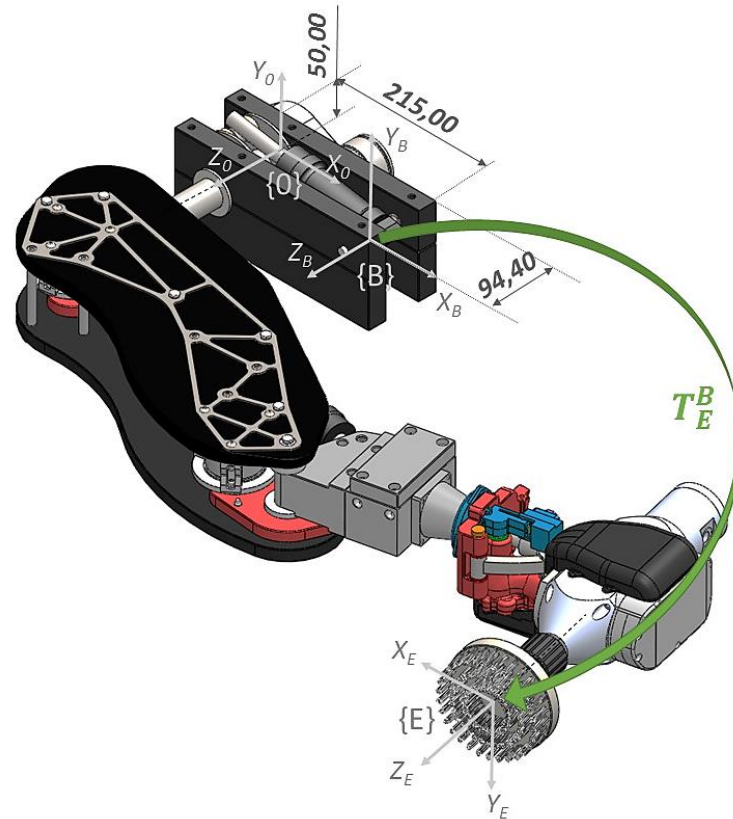
Figure 2. 11. Coordinate system {B} adopted in the scanning activities.

After the acquisition phase, the 3D point clouds are processed by means of a software, provided by Stonex, that allows to analyze and elaborate the data in order to define the homogeneous transformation matrix T_E^B of the end-effector {E} with reference to the coordinate systems {B}. Figure 2. 12 shows the calculation of the end-effector pose with reference to the base of the arm. In particular, $\vec{V}_1$ is the vector distance from the optical center {Opt} of the laser scanner instrument with regard to the base of the arm {B}; $\vec{V}_2$ is the vector distance from the optical center {Opt} of the laser scanner instrument with respect to the end-effector of the arm {E}; and $\vec{V}_3$ represents the difference vector ($\vec{V}_2 - \vec{V}_1$) in regard to the reference system {Opt}.
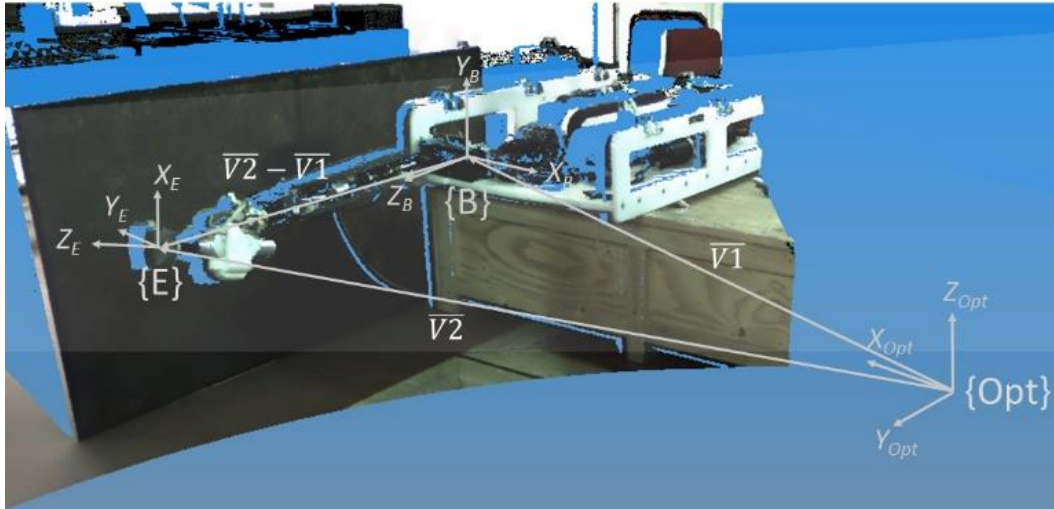
Figure 2. 12. 3D point cloud and reference system {Opt} of the laser scanner optical center.

Therefore, from the transformation matrix T_E^B a measured end-effector position vector $p_m^{(i)} = [x_E, y_E, z_E]^T$ is derived for each pose i. The results are reported in Table 2.4.

POSE		$\overrightarrow{V_1}$	$\overrightarrow{V_2}$	$\overrightarrow{V_3} = \overrightarrow{V_2} - \overrightarrow{V_1}$	$p_m^{(i)}$
1	X	631,40	-448,75	-1080,15	-253,50
	Y	3327,40	2994,50	-332,90	-109,92
	Z	-643,50	-755,49	-111,99	1101,70
	M	3447,37	3120,76	1135,82	1135,82
2	X	934,07	209,39	-724,68	306,10
	Y	3474,45	3001,15	-473,30	-326,10
	Z	-612,39	-900,86	-288,47	795,20
	M	3649,56	3140,43	912,35	912,35
3	X	925,10	-58,09	-983,19	13,30
	Y	3495,20	3308,33	-186,87	-100,50
	Z	-630,70	-731,20	-100,50	1000,70
	M	3670,15	3388,67	1005,82	1005,82
4	X	932,20	-187,08	-1119,28	-184,00
	Y	3495,20	3484,68	-10,52	-140,50
	Z	-615,20	-755,70	-140,50	1104,10
	M	3669,32	3570,58	1128,11	1128,11
5	X	929,30	130,49	-798,81	369,60
	Y	3472,50	2956,35	-516,15	-51,10
	Z	-625,00	-676,10	-51,10	876,30
	M	3648,63	3035,48	952,43	952,43
6	X	931,10	354,40	-576,70	487,80
	Y	3483,70	2886,69	-597,01	-83,20
	Z	-613,30	-696,50	-83,20	671,60
	M	3657,77	2990,60	834,22	834,22
7	X	929,60	752,78	-176,82	437,00
	Y	3463,00	2988,08	-474,92	-302,50
	Z	-639,40	-941,90	-302,50	256,60
	M	3642,16	3222,18	590,19	590,19
8	X	945,30	-37,50	-982,80	20,00
	Y	3478,30	3284,69	-193,61	-190,00
	Z	-627,20	-817,20	-190,00	1001,50
	M	3658,63	3385,03	1019,55	1019,56
9	X	923,10	19,72	-903,38	-205,40
	Y	3495,30	3544,58	49,28	-493,59
	Z	-634,10	-1127,70	-493,60	881,10
	M	3670,33	3719,70	1030,61	1030,61
10	X	945,30	-112,37	-1057,67	-210,90
	Y	3478,30	3505,96	27,66	-375,00
	Z	-627,20	-1002,20	-375,00	1036,80
	M	3658,63	3648,12	1122,52	1122,52

Table 2.4. Measured poses.

2.2.2. Results

Once the experimentation activities are completed, the kinematic performances of the underwater robotic arm are evaluated.

Positioning errors

In this step, the positioning errors are calculated through comparison between the predicted and the actual poses. Since the predicted poses are calculated in regard of the coordinate reference system {0} (fig.3) while the actual poses are referred to {B}, then a preliminary operation has to be performed before to proceed with the comparison of the end-effector positions. In particular, a rigid translation of the coordinate frame {B} has made as follows $T_E^0 = T_E^B (T_0^B)^{-1} = T_E^B \, T_B^0$ in order to recalculate the actual end-effector positions with regard to the reference system {0}. This transformation has been carried out taking into account the distances (fig.5) between the two reference systems by means the matrix T_0^B=Dz(-94.40)·Dx(-215.00)·Dy(-50.00). Then, the positioning errors have been calculated through the following equation $\vec{e} = \left| \bar{p}^{(i)} - p_m^{(i)} \right|$, represented in Table 2.5.

POSE		$\bar{p}^{(i)}$	$p_m^{(i)}$	$\vec{e} = \left|\bar{p}^{(i)} - p_m^{(i)}\right|$
1	X	-256,98	-253,50	3,48
	Y	-94,68	-109,92	15,24
	Z	1107,00	1101,70	5,30
	M	1140,37	1135,82	16,51
2	X	305,37	306,10	0,73
	Y	-350,44	-326,10	24,34
	Z	800,40	795,20	5,20
	M	925,58	912,35	24,90
3	X	15,90	13,30	2,60
	Y	-46,78	-100,50	53,72
	Z	996,16	1000,70	4,54
	M	997,38	1005,82	53,97
4	X	-183,85	-184,00	0,15
	Y	-64,12	-140,50	76,38
	Z	1108,40	1104,10	4,30
	M	1125,37	1128,11	76,50
5	X	373,76	369,60	4,16
	Y	-101,51	-51,10	50,41
	Z	883,60	876,30	7,30
	M	964,75	952,43	51,11
6	X	492,41	487,80	4,61
	Y	11,89	-83,20	95,09
	Z	688,90	671,60	17,30
	M	846,87	834,22	96,76
7	X	430,10	437,00	6,90
	Y	-350,81	-302,50	48,31
	Z	250,85	256,60	5,75
	M	609,08	590,19	49,14
8	X	16,59	20,00	3,41
	Y	-134,29	-190,00	55,71
	Z	1006,00	1001,50	4,50
	M	1015,06	1019,56	55,99
9	X	-215,00	-205,40	9,60
	Y	-547,00	-493,59	53,41
	Z	890,00	881,10	8,90
	M	1066,55	1030,61	54,99
10	X	-215,00	-210,90	4,10
	Y	-400,88	-375,00	25,88
	Z	1039,80	1036,80	3,00
	M	1134,95	1122,52	26,37

Table 2.5. Positioning errors.

Kinematic performances

The procedure ends with the evaluation of the kinematic performances of the underwater manipulator (Gatti & Danieli, 2008) (Gatti & Danieli, 2006). Then the repeatability and the accuracy are determined according to ISO standard 9283:1998. In particular, the repeatability (RP) is calculated starting from the following error distribution:

$$E_{RP} = \begin{bmatrix} \left| \left| \bar{p}^{(1)} \right| - \left| p_I^{(1)} \right| \right| \\ \vdots \\ \left| \left| \bar{p}^{(10)} \right| - \left| p_I^{(10)} \right| \right| \end{bmatrix}$$

where, as above mentioned, $p^{(i)} = [x_E, y_E, z_E]^T$ is the predicted position of the ith end-effector pose. While $\bar{p}^{(i)} = (p_I^{(i)} + p_{II}^{(i)})/2$ is the arithmetic mean between the predicted positions of the same ith pose reached twice.

The accuracy (A) has been evaluated on the base of the following distribution of end-effector's position errors:

$$E_A = \begin{bmatrix} \left| \left| \bar{p}^{(1)} \right| - \left| p_m^{(1)} \right| \right| \\ \vdots \\ \left| \left| \bar{p}^{(10)} \right| - \left| p_m^{(10)} \right| \right| \end{bmatrix}$$

in which $p_m^{(i)}$ is the actual attained position, of the ith end-effector pose, measured through the external measuring system.

The mean (μ) and the standard deviation (σ) of the E_{RP} and E_A error distributions have been calculated in order to evaluate the repeatability and the accuracy of the robotic arm that are respectively: $RP = \mu_{E_{RP}} + 3\sigma_{E_{RP}} = 0.99mm$ and $A = \mu_{E_A} \pm 3\sigma_{E_A} = 50.62 \pm 24.21mm$. In particular, the accuracy along x and z-axes presents a value respectively of 3.97 ± 2.75 mm and 8.90 ± 7.13 mm, while for the y-axis it has been measured a value of 49.85 ± 24.13 mm whose growth is primarily due to the structural deflections of the robotic arm.

The results of the study have been of fundamental importance in the development of the control strategies for the control of the ROV and its manipulator. In fact, on the basis of

the maximum error positions found and the kinematic performances of the arm it has been defined a "safety range" that allows avoiding collisions among the end-effector's tool and the artifacts. In particular, when the end-effector's cleaning tool is within the safety range the operator controls the manipulator in order to approach the target very slowly until the contact feedback is provided by the load cell sensors.

3. Augmented Reality in underwater manipulation

Underwater manipulation is a key technology for marine industries and exploration that can be efficiently adopted in other application fields, such as underwater archaeology, biological manipulation, scientific expedition, as well as offshore construction in the Oil and Gas industry. It is performed remotely by expert pilots thanks to the visual feedback provided by one or more cameras but without any information about the distance between the end-effector and the target.

To this end, in this Chapter the effort is focused on an augmented reality (AR) visualization system which represents a new technological solution for the underwater cultural heritage (UCH) field to efficiently support and facilitate the manipulation of archaeological artefacts and, more specifically, the planned maintenance required to prevent the biological colonization of the submerged structures. Furthermore, the proposed system can be efficiently applied to marine science research activities, especially when collecting fragile biological samples. In particular, a novel system based on a sensorized robotic arm (see section 2), stereoscopic 3D perception and augmented reality visualization to support ROV's pilots in underwater manipulation tasks is presented.

The system provides a visual feedback of the submerged scene on which a depth map of the underwater workspace is augmented on thanks to the adoption of an optical-stereo camera. Combining the kinematics of the robotic arm and the standard photogrammetric model of the camera (Brown, 1971) it is possible to provide to the pilots the depth map with respect to the end-effector's pose.

This work has been carried out in the context of the CoMAS (In-situ conservation planning of Underwater Archaeological Artefacts) project (CoMAS project, 2013) that aimed to discover and develop new materials, techniques and methodologies for the conservation and restoration of marine sites in their natural environment (Bruno, et al., 2016, 2015a, 2015b).

3.1. Architecture

The system architecture consists of an ROV (Figure 3. 1) equipped with a custom-made sensorized underwater robotic arm and an optical-stereo camera for a stereoscopic 3D perception of the underwater scene.

The system has been designed for the CoMAS project to provide different degrees of automation for the various mechanical cleaning activities to be carried out in an archaeological site, and therefore to simplify the workflow by means of semi-automatized activities.

Figure 3. 1. The ROV equipped with the custom-made robotic arm and optical-stereo camera.

The ROV is a Perseo GTV by Ageotec company. It is a midsize multi-purpose vehicle optimized to perform both the visual and instrumental inspection and the manipulation of small- or medium-sized objects. The underwater vehicle is built around a supporting chassis in polypropylene with stainless steel brace for thrusters stiffening, lifting and

fixing. The underwater vehicle's propulsion derives from six thrusters driven by brushless electric motors, and it features auto-heading and auto-depth functions to move while keeping the proper path at a constant depth. The vehicle has been equipped with the following sensors: IMU Xsens MTI 300, an AA EasyTrack USBL, and a Link Quest 600 Micro DVL.

The underwater arm (Figure 3. 2), presented in the Chapter 2, has been re-engineered starting from a commercial 5-functions hydraulic arm, the Hydro-Lek HLK-43000, which incorporates a continuous jaw rotate mechanism with an integrated cutter tool. The manipulator has been modified to ensure a greater working volume to easily perform mechanical cleaning activity in the underwater archeological context. The original gripper tool has been removed and the continuous jaw rotating mechanism has been modified in a pan-tilt system to handle an electromechanical brush tool (Barbieri, et al., 2017).
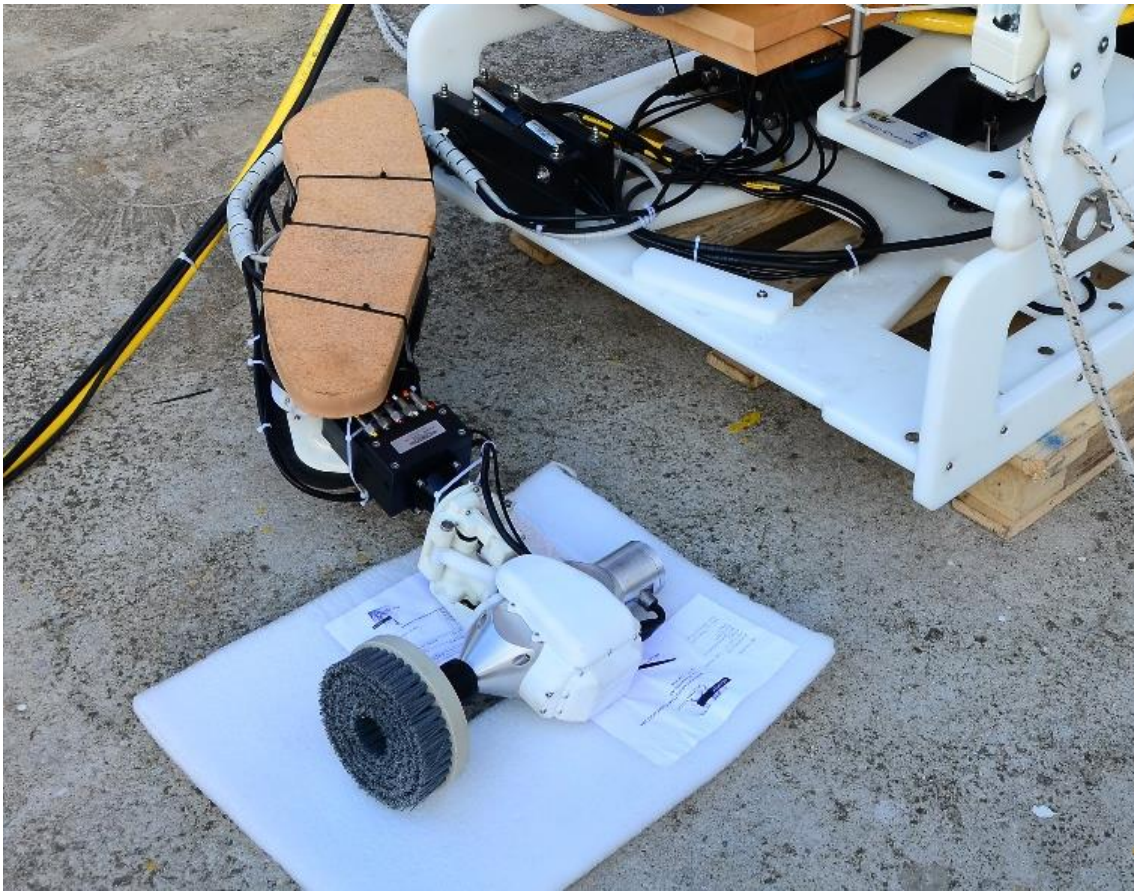
Figure 3. 2. The re-engineered underwater arm mounted on the skid of the ROV.

The arm has been sensorized with three Acuro AR-63 waterproof CAN-bus magnetic encoders, for measuring the angular position of each link, and a couple of RE22 SSI magnetic encoders, for the measuring of the pan-tilt head movements. While the electromechanical brush has been equipped with three sensors S2Tech BC302-20 kg for measuring the axial forces. The end-effector uses a 1200W brushed motor, with a maximum torque of 15Nm at 1250rpm, and can handle different types of brushes to perform all the planned maintenance operations.

The optical-stereo camera (Figure 3. 3) is the result of a research activity conducted in the field of the underwater stereo photogrammetry, both for passive and active applications (F. Bruno, et al., 2011) (F. Bruno, et al., 2011)(Skarlatos et al., 2010).
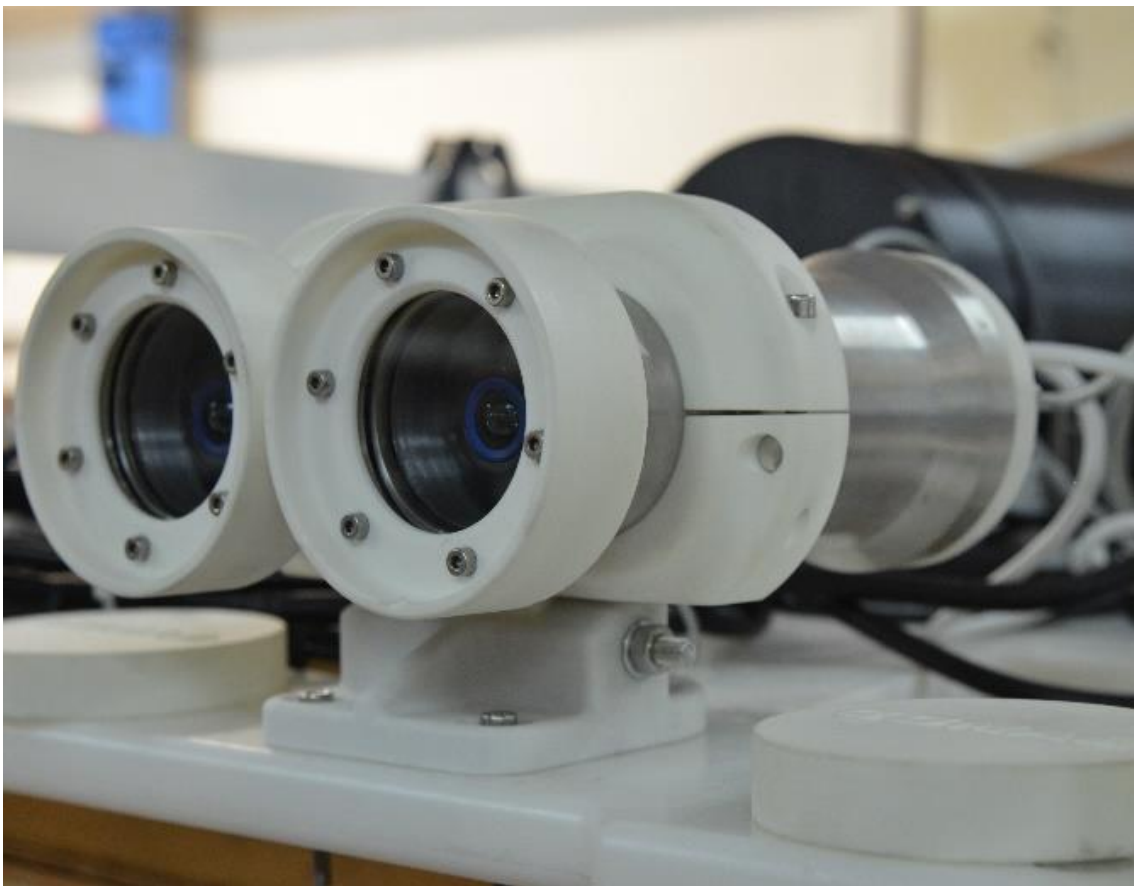
Figure 3. 3. Optical-stereo camera.

It consists of two cameras, in a stereo configuration, housed in custom-made waterproof cases. The digital cameras are two ultra-compact Imaging Source DFK 23G445 GigE color industrial camera with a 1/3-inch Sony CCD sensor format, a resolution of 1280 x 960 pixels, and a frame rate of 30 fps. They are equipped with a pair of Theia Technologies SL183A lenses that provide an ultra-wide field of view, with a distortion less than 1%, thanks to a focal length ranged from 1.8 to 3.0 mm and aperture F1.8. The custom-made waterproof cases are made of aluminum to ensure an efficient heat dissipation, while the flat port of the camera housings are made of polycarbonate. This solution leads to a reduction of the FOV caused by the refraction of the air-water interface, but its construction is easier.

3.2. Software

The underwater scene captured by the optical-stereo camera is furnished to the ROV operators by means of a software developed ad-hoc in the context of the CoMAS project. The software processes the raw images acquired by the stereoscopic camera to create layers of 3D information that are overlaid, by means of augmented reality techniques, to the main 2D video feedback. In particular, Libelas and OpenCV (OpenCV 2014) libraries have been adopted to perform an online augmented reality visualization of the 3D underwater scene. OpenCV library has been used for the rectification of the stereo pair, while Libelas library has been implemented in the software both for the stereo matching operation and the generation of the disparity map. The adoption of Libelas library allows generating 3D point clouds, of about 200,000 points, at a frame rate of 7 fps. Furthermore, its Efficient Large-scale Stereo (ELAS) algorithm (Geiger et al., 2011) allows for obtaining a more robust and accurate 3D point cloud in the underwater environment.

The software devoted to the AR visualization of the scene depth perception has been developed to feature a high customizability of user interfaces and a high flexibility of parameters to allow users to set the main parameters of the optical-stereo camera dependently by the conditions of the underwater environment. The following picture (Figure 3. 4) depicts the depth map, of the distance of the end-effector from a submerged

archaeological remain, augmented on the images of the underwater scenario acquired by the optical-stereo camera. In particular, the 3D point cloud of the underwater scene is shown on the right side of the screen, whereas, a stereo image pair of the acquired frame and the 3D depth map of the scene are broadcasted respectively on the upper and bottom left side of the screen.
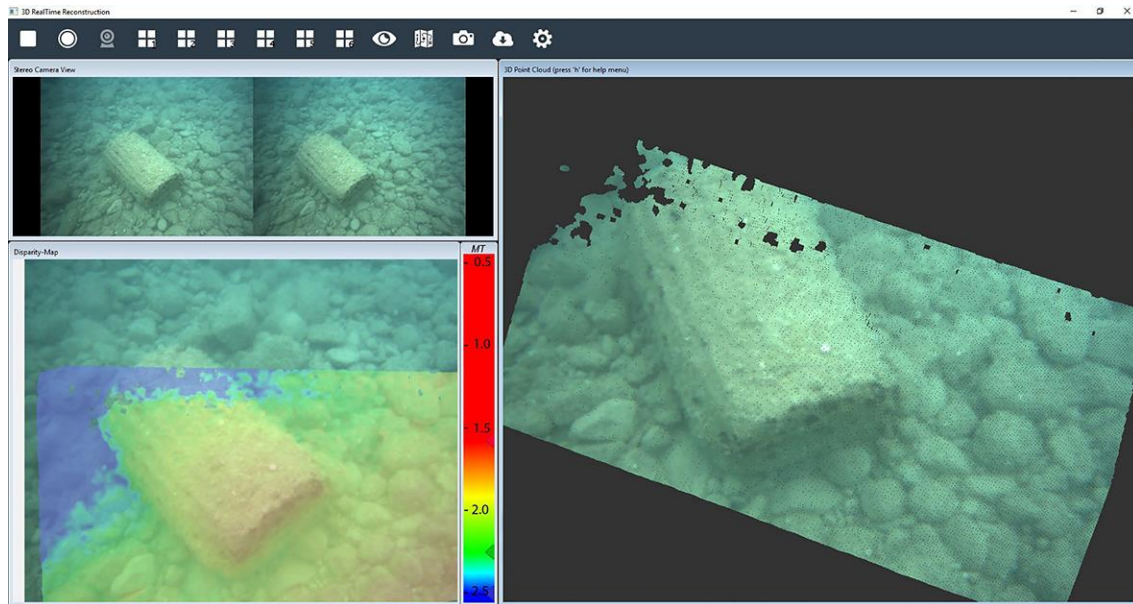
Figure 3. 4. Control software for the AR scene depth visualization.

Two methods have been embedded in the software for the calibration of the optical-stereo camera. The first one is the well-known calibration method proposed by Zhang (Zhang, 1999), the second one is the calibration method developed in (Rahman & Krouglicof, 2012) that offers robust performances regardless of the degree of lens distortion and therefore has better performance in underwater applications.

3.3 Calibration of the system

The following figure (Figure 3. 5) depicts the mathematical model adopted to generate a depth map in which the distance of a generic point P, acquired by the optical-stereo camera, is calculated with respect to the end-effector's position. The mathematical formulation considers both the direct kinematics of the robotic arm and the geometric model of the optical-stereo camera where {E}, {C} and {0} are the local reference frames respectively of: the end-effector's tool, the optical-stereo camera, and the robotic arm.
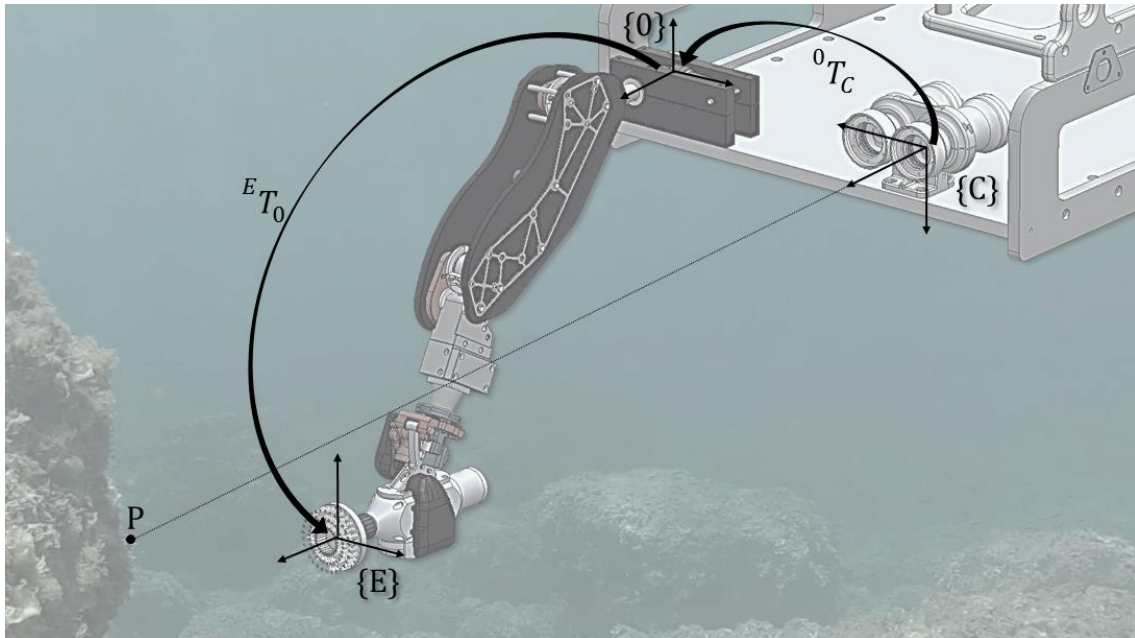
Figure 3. 5. Mathematical model representation of the proposed system.

Based on the above-mentioned mathematical model, the position of a generic point P can be calculated with respect to the end-effector's reference frame {E} by means of the following formulation:

$$^{E}P = {}^{E}T_0 \, {}^{0}T_C \, {}^{C}P \tag{3.1}$$

where $^{E}T_0$ is calculated by means of the forward kinematic model of the robotic arm and it represents the end-effector pose with respect to the frame {0}; $^{0}T_C$ is the homogeneous

transformation matrix of the frame {0} with respect to the frame {C}; and ^{C}P is the position vector of the generic point P referred to the coordinate system {C}.

3.3.1. Kinematic model of the arm

The mathematical description of the kinematic chains of the 5-DOF underwater manipulator has been defined according to the DH-parameter notation (Denavit and Hartenberg, 1955).

As shown in section 2, the kinematic model of the underwater manipulator, that specifies the relative pose of the end-effector and the base coordinate system, is expressed by means of the homogeneous transformation matrix:

$$^{0}T_{E} = \begin{bmatrix} ^{0}R_{E} & S \\ 0_{1x3} & 1 \end{bmatrix} = {}^{0}T_{1} \cdot {}^{1}T_{2} \cdot {}^{2}T_{3} \cdot {}^{3}T_{4} \cdot {}^{4}T_{5} \cdot {}^{5}T_{E} \tag{3.2}$$

where the submatrix $^{0}R_{E}$ and the array S = [x y z]^{T} are respectively the rotational matrix and the position vector of the end-effector.

3.3.2. Geometric model of the optical-stereo camera

The mathematical model used to describe the geometry of the optical stereo camera is the well-known pinhole camera model. It consists in the perspective projection of the 3D points of the scene framed in the image plane "I" with coordinate [x_u, y_u]^{T}. For each point of the scene framed

$$\begin{cases} x_u = \dfrac{f}{Z_P} X_P \\ y_u = \dfrac{f}{Z_P} Y_P \end{cases} \rightarrow \begin{bmatrix} x_u \\ y_u \end{bmatrix} = \dfrac{f}{Z_P} \begin{bmatrix} X_P \\ Y_P \end{bmatrix}$$

Where f is the focal length of the camera, [X_P Y_P Z_P]^{T} are the coordinate of the generic point of scene framed by the stereo camera respect to the world coordinate system.

Finally, it must be considered that a digital camera involves measures in terms of pixels, through an affine transformation which takes into account the translation of the principal point and a scaling along u and v axis in the image plane

$$
\begin{cases}
u = \lambda \dfrac{x_u}{d_x} + u_0 \\
v = \lambda \dfrac{y_u}{d_y} + v_0
\end{cases}
$$

Where (u_0, v_0) are the principal point location in pixel coordinates, given by the intersection of the optical axis with the image plane, (d_x, d_y) are the pixel size in u and v direction, respectively, and λ is the scale factor d_x/d_y.

In this model, a scene view is formed by projecting 3D points into the image plane using a perspective transformation. Under perspective projection, a 3D point "**x**" in space is projected to an image point "**m**" via a 3×4 rank 3 projection matrix "**P**" as

λ m = P x = K [R,t] x

where R and t are the rotation matrix and translation vector from the world system to the camera system, K is the camera calibration matrix in the form of

$$
K = \begin{bmatrix} f_u & s & u_0 \\ 0 & f_v & v_0 \\ 0 & 0 & 1 \end{bmatrix} = \begin{bmatrix} f_u & f_u ctg\theta & u_0 \\ 0 & rf_u & v_0 \\ 0 & 0 & 1 \end{bmatrix}
$$

where (f_u, f_v) represent the camera's focal length corresponding to the u and v axes of camera coordinates; (u_0, v_0) is the coordinates of the camera's principal point; $s=f_u$ ctg θ refers to the skew factor, with θ the included angle of u and v axes; $r=f_v/f_u$ is termed as the aspect ratio. For most CCD cameras, we can assume rectangle pixels, i.e. $\theta=90°$ or $s=0$. Then, the camera becomes a simplified one with only four intrinsic parameters. For some high quality-cameras, we may even assume square pixels, i.e. $s=0$ and $r=1$ ($f_u=f_v$), and the camera model is simplified to three parameters accordingly.

Therefore, under these conditions it has

$$
\lambda \begin{bmatrix} u \\ v \\ 1 \end{bmatrix} = \begin{bmatrix} f_u & 0 & u_0 \\ 0 & f_u & v_0 \\ 0 & 0 & 1 \end{bmatrix} [R, t] \begin{vmatrix} x \\ y \\ z \\ 1 \end{vmatrix}
$$

Given two images acquired from slightly different viewpoints, a stereo matching algorithm tries to identify the corresponding points of the epipolar line (solving the so-called correspondence problem) in both the images related to the same scene point (Figure 3.

6). Knowing these correspondences and the camera geometry, the 3D world coordinates can be reconstructed by triangulation. Specifically, the disparity, that encodes the depth of the scene, represents the distance between x-coordinates or a pair of correspondent points in left and right (rectified) images. Finding a pair of correspondent points is not so trivial. Since the scene is acquired from different points of view, it is possible to find false correspondences due to occlusion, radiometric distortion and perspective distortion.
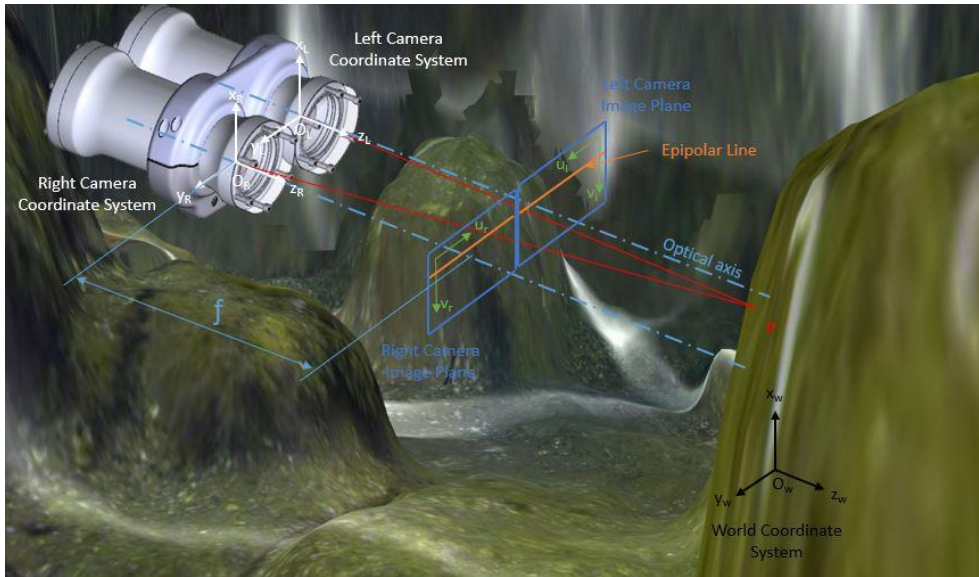
Figure 3. 6. Geometrical model of the stereo camera.

3.3.3. Camera to arm pose estimation

The estimation of the pose between the optical-stereo camera and the robotic arm, i.e., $^{0}T_{C}$ transformation matrix, has been experimentally determined by means of the geometric approach illustrated in the following figure (Figure 3. 7). Since the camera reference frame {C} is a theoretical point not known a priori, then a new reference frame {C'} has been added into an easily identifiable and accessible point located on the external waterproof case of the camera. As a consequence, the unknown rigid transformation matrix $^{c}T_{0}$ is obtained as follows:

$$^{0}T_{C} = {}^{0}T_{C'}{}^{C'}T_{C} \tag{3.3}$$
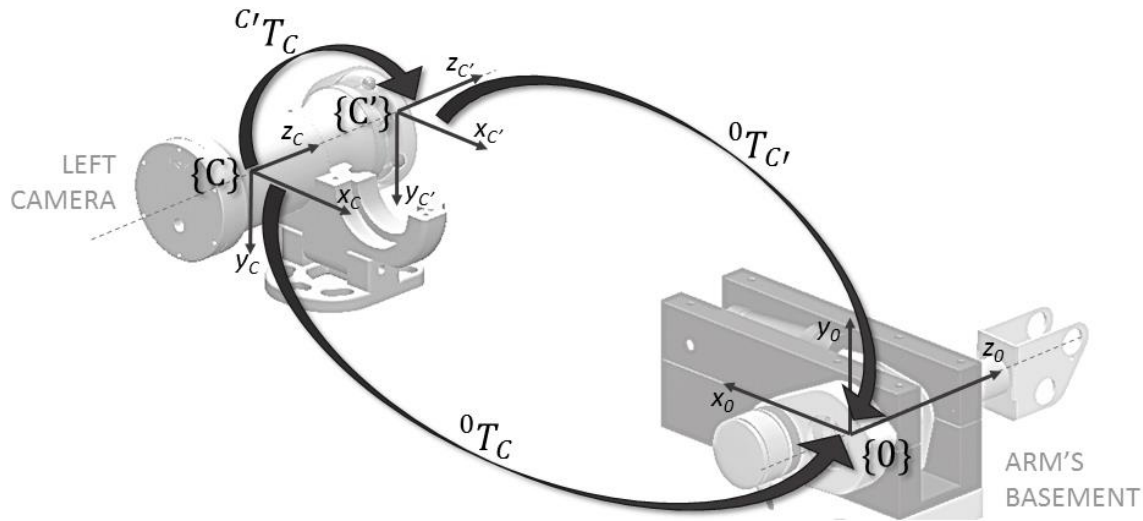
Figure 3. 7. Geometric approach to determine $^{0}T_{c}$ matrix.

In particular, the first rigid transformation $^{0}T_{C'}$ is calculated through geometric measurements taken from a 3D model generated with reverse engineering technique in order to minimize the uncertainty of 3D data. In fact, the adoption of a laser scanner allows reaching accuracy to a tenth of a millimeter. As an alternative to the laser scanner, when a high fidelity between the analytical and the physical prototype is assured, the geometric measurements can be taken directly from the CAD model.

About the second transformation matrix $^{C'}T_{C}$, as illustrated in Figure 3. 8, once the world reference frame {W} has been arbitrarily chosen, the rigid transformation from {C} to {C'} can be defined as follows:

$$^{C'}T_{C} = {}^{C'}T_{W}{}^{W}T_{C} = {}^{C'}T_{W}\left({}^{C}T_{W}\right)^{-1}$$

(3.4)

where $^{C}T_{W}$ matrix is the rigid transformation that brings the word reference frame {W} onto the optical-stereo camera reference frame {C}, and $^{C'}T_{W}$ is the transformation that binds {W} to {C'}.
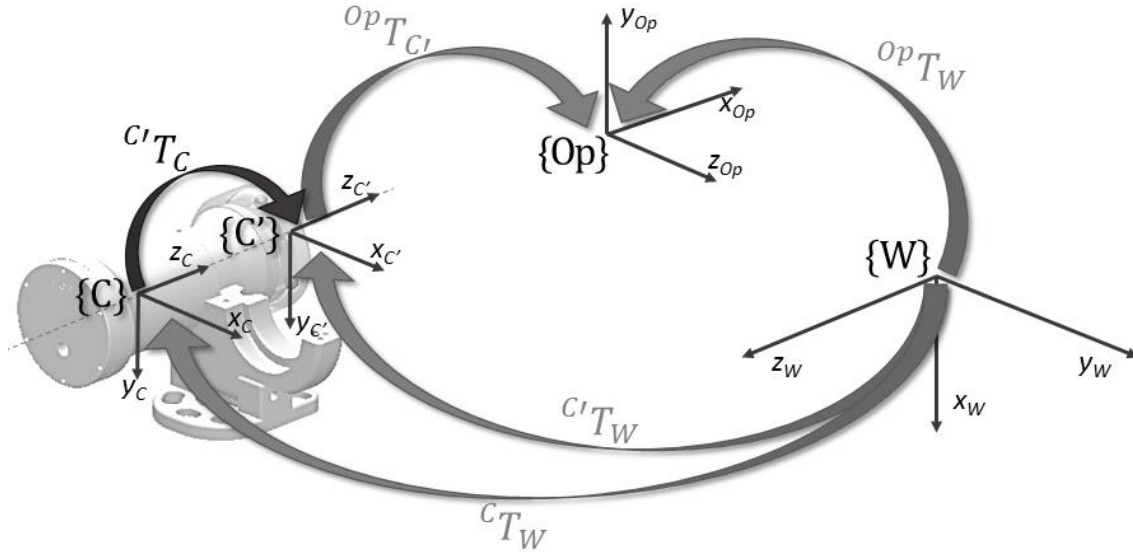
Figure 3. 8. Geometric approach to determine $^{c\prime}T_c$ matrix.

In particular, the ^cT_w transformation matrix is the exterior orientation of the stereo camera rig computed by means of a calibration procedure that takes into account the geometry of each camera defined according to the pinhole camera model (Brown, 1974). While $^{c\prime}T_w$ matrix is computed by means of an external measurement system consisting of an optical tracking system that allows reaching a sub-mm precision. Nevertheless, to the detriment of more precise and accurate measurements, the position of the optical center of the camera could be estimated without any specialized equipment, such as a millimeter grid plane (Peer, 2005). The introduction of the external measurement system entails the splitting of the $^{c\prime}T_w$ transformation matrix in two basic transformations, i.e., $^{op}T_w$ and $^{op}T_{c\prime}$, that are calculated with respect to the reference frame of the motion capture camera {OP}. As a consequence:

$$^{C\prime}T_W = \left(^{Op}T_{C\prime}\right)^{-1} {}^{Op}T_W = {}^{C\prime}T_{Op} {}^{Op}T_W \tag{3.5}$$

By considering equations (3.4) and (3.5), it follows:

$$^{C\prime}T_C = {}^{C\prime}T_W {}^{W}T_C = {}^{C\prime}T_{Op} {}^{Op}T_W {}^{W}T_C \tag{3.6}$$

Then finally, the unknown rigid transformation matrix $^cT_0$ is obtained as follows:

$$^{0}T_C = {}^{0}T_{C\prime} {}^{C\prime}T_C = {}^{0}T_{C\prime} {}^{C\prime}T_{Op} {}^{Op}T_W {}^{W}T_C \tag{3.7}$$

3.3.4. Determining the $^0T_{C'}$ transformation matrix

The following figure (Figure 3. 9) shows the resulting 3D point cloud (653˙331 points and a density of 4000 points/cm^2) of the camera-arm assembly acquired by means of a triangulation based laser scanner (NextEngine 3D Laser Scanner, 2017) placed at a distance of 450 mm from the ROV skid (Figure 3. 10).
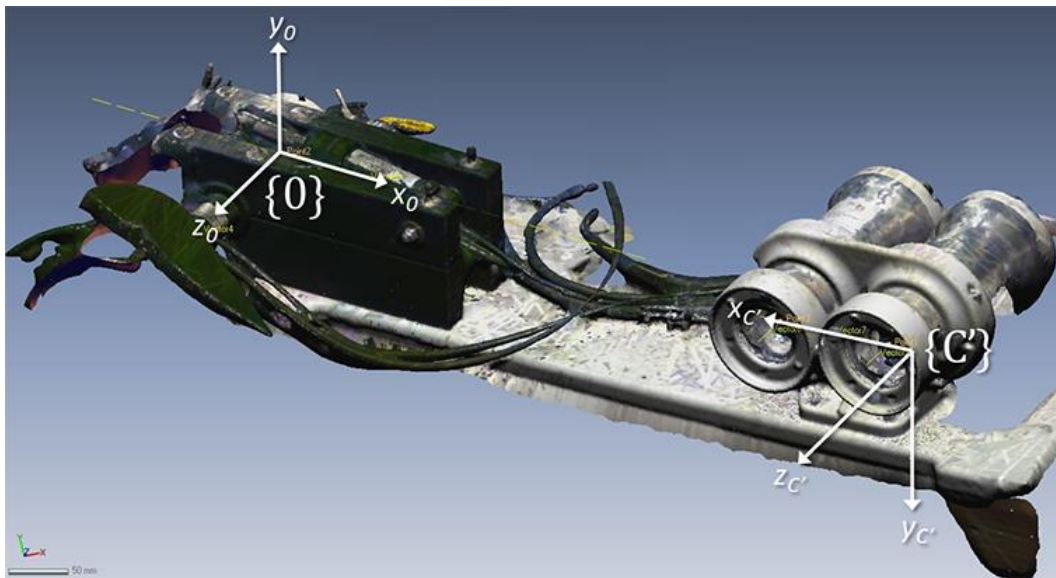
Figure 3. 9. 3D point cloud of the front side of the ROV skid obtained with laser scanner.
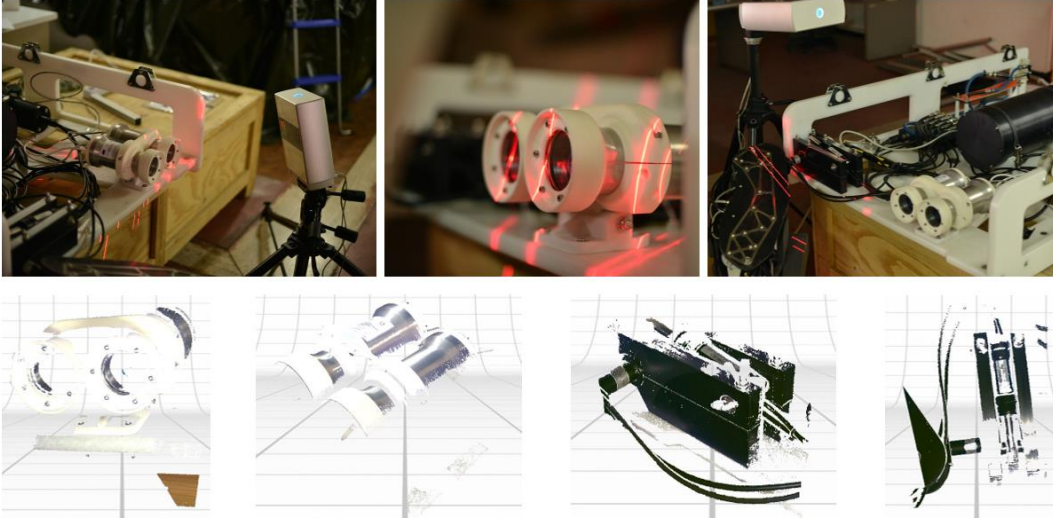
Figure 3. 10. Acquisition phase and single reconstruction result obtained with the NextEngine 3D laser scanner.

Best-fitting algorithms have been applied to the 3D point cloud to fix position and orientation of the local reference frames {C'} and {0}. Once the two reference frames have been defined, the following rigid transformation matrix $^0T_{C'}$ has been calculated:

$$^0T_{C'} = \begin{bmatrix} -0.2249 & -0.9744 & 0 & 679.4500 \\ -0.5359 & 0.1237 & 0.8352 & 38.4700 \\ -0.8138 & 0.1878 & -0.5500 & 125.8000 \\ 0 & 0 & 0 & 1 \end{bmatrix}$$

3.3.5. Determining the $^{C'}T_C$ transformation matrix

The set of the internal and external parameters of the optical-stereo camera has been computed by means the calibration method proposed by Zhang (Zhang, 1999), in its version implemented in Matlab by Bouguet (Bouguet, 2013). The interior and exterior orientation parameters of each camera have been obtained by correlating the coordinates of known points located on a calibration sample (i.e., a checkerboard) with the corresponding coordinates on the image plane. Subsequently, the exterior orientation of the optical system (stereo calibration) has been computed and the reference frame of the optical-stereo camera {C} (whose origin is the perspective center of the left camera) has

been related to the reference frame of the calibration sample {W} (whose position and orientation is shown in Figure 3. 11a). The results of the calibration process are shown in Figure 3. 11b.

Interior orientation parameters of the LEFT camera				
Focal length	[783,96808	779,40327] ± [1,08156	1,13528]	
Principal point	[686,52634	538,29116] ± [2,15627	1,47955]	
Skew	[0,00000] ± [0,00000] => angle of pixel axes = 90 degrees			
Distortion	[-0,01391 ± [0,00367	0,02260 0,00618	-0,00066 0,00061	-0,00349 0,00088	0,00000] 0,00000]

Interior orientation parameters of the RIGHT camera				
Focal length	[772,75669	769,98680] ± [1,09058	1,15890]	
Principal point	[615,08207	576,55641] ± [2,17247	1,47362]	
Skew	[0,00000] ± [0,00000] => angle of pixel axes = 90 degrees			
Distortion	[0,00546 ± [0,00353	0,01516 0,00484	0,00102 0,00065	-0,00194 0,00094	0,00000] 0,00000]

Relative orientation parameters		
Rotation vector	[-0,00132	-0,01011 -0,00336] ± [0,00201 0,00347 0,00039]
Translation vector	[-103,75 -1,43 -0,25] ± [0,10 0,10 0,47]	

a   b

Figure 3. 11. Results of the calibration process. (a) Pose estimation of the calibration sample with respect to the reference frame of the optical-stereo camera {C}. (b) Interior and exterior orientation parameters of the stereo rig.

To experimentally determine the position of the perspective center (Peer and Solina., 2006) of the camera, and therefore the rigid transformation matrix $^{C'}T_C$, three coordinate systems (Figure 3. 12) have to be taken into account: the camera system {C}, the underwater imaging system (composed of the camera body, the optical lens, and the waterproof case) {C'} and the calibration sample {W}.
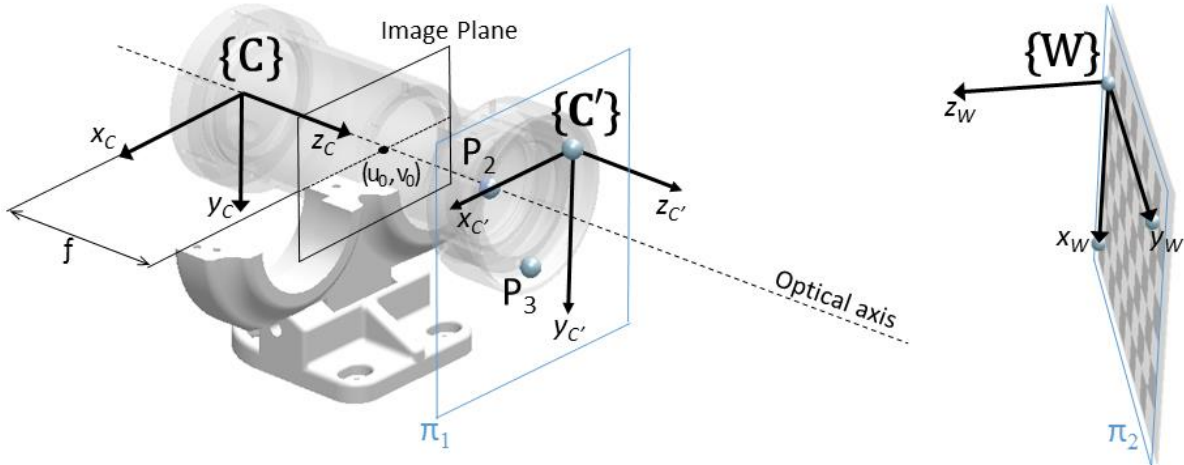
Figure 3. 12. Schematic layout of the set-up used to calculate the rigid transformation matrix $^{C'}T_C$.

The calibration method provides the relation between the first and the third system (the exterior orientation matrix $^{c}T_w$). In our case, we need the rigid transformation between the first and the second system, i.e. the rigid transformation matrix $^{C'}T_C$. We found this relation by establishing the transformation between the second and the third system $^{C'}T_w$ and then all the gathered information (the transformation between the first and the third coordinate system and those between the second and the third coordinate system) have been used to obtain the transformation between the first and second coordinate system (see equation 3.4).

An optical tracking system OptiTrack Flex 13 (NaturalPoint Inc., 2017) has been used to retrieve the rigid transformation matrix $^{C'}T_w$ (see equation 3.5). It is a motion capture system made up of eight infrared cameras with a resolution of 1.3 Megapixels (1280 × 1024) and a sample rate of 120 fps. The system performs 3D measurements with a sub-mm accuracy level using reflective markers of 7/16 inch (11.112 mm) in diameter.

The reference frame of the camera system {C'} has been defined with three reflective markers attached to the flange of the flat port of the left camera (Figure 3. 12). The origin of the coordinate measurement system has been fixed in the point P_1, with the π_1 plane coincident with the camera flange plane, and the Z-axis along the optical axis. Another set of three reflective markers has been attached to the calibration sample, that consists in a rectangular checkerboard, to define the position and the orientation of the reference

frame {W}. Both the optical-stereo camera (Figure 3. 13a) and the calibration sample have been mounted on a stable tripod and all infrared (IR) emitting devices and reflective surfaces within the capture volume have been removed or covered prior to performing the measurements (Figure 3. 13b).

a   b
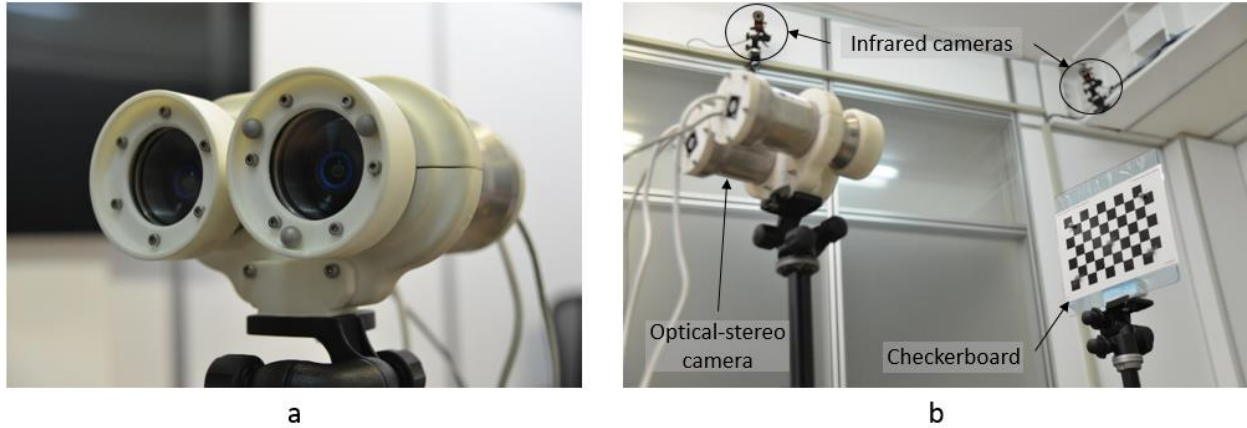
Figure 3. 13. (a) Optical-stereo camera mounted on tripod with reflective markers, (b) and experimental set-up.

A data record of 0.5 seconds, that corresponds to 60 3D position values for each marker, has been captured. Then, the 3D coordinates have been fitted through the least squares procedure to find the reference planes of the flange of the camera housing π_1 and of the calibration sample π_2 (Figure 3. 12).

From the measurements described in the previous steps, the relative pose of the key geometric elements of the camera system is known and the rigid transformation matrix $^{C'}T_C$ can be calculated.

Therefore, by adopting equation (3.6):

$$^{C'}T_C = \begin{bmatrix} -0.1923 & 0.9800 & 0.010556 & 30.3759 \\ 0.9836 & 0.1895 & -0.2543 & 31.4380 \\ 0.0033 & -0.0526 & 1.0320 & -16.1251 \\ 0 & 0 & 0 & 1 \end{bmatrix}$$

Once the two transformation matrixes, $^{0}T_C$, and $^{C'}T_C$, have been calculated the unknown rigid transformation matrix $^{C}T_0$ can be derived according to the equation (3.7):

$$^{C}T_{0}=\begin{bmatrix} -0.9152 & -0.4050 & 0.2355 & 641.9861 \\ 0.2275 & -0.5457 & 0.8011 & 13.2361 \\ 0.3394 & -0.7329 & -0.6600 & 116.8020 \\ 0 & 0 & 0 & 1 \end{bmatrix}$$

Alternative method of calculating $^{C}T_{0}$

According to (Bouguet, 2013), the optical center of the stereo camera lies on the optical axis of the left camera. The problem is that the exact spatial location of the optical center is not known a priori. Furthermore, it can be determined experimentally as explained in (Weng, et al., 2002). Essentially, the methodological steps to determine the optical center consist to compare the distance of some points of an object acquired by the stereo camera (internal measurement) and the same distance of these points using an external measuring instrument. The external measuring instrument used in this phase is the above mentioned optical tracking OptiTrack Flex 13.

To this end, the measurement performed by the external instrument is calculated with respect to a physical point of the camera and specifically respect to the vertical plane of the support of the left lens.

The acquired object is represented by a chessboard panel, usually used for the calibration routine of cameras. Firstly, the stereo camera and the chessboard are secured on micrometric tripods, they are leveled respect to the floor and spaced in order to perform iteratively a precise positioning using the OptiTrack. The experimental setup is the same as the previous one, depicted in Figure 3. 13. Subsequently, the pose of some motion capture markers, fixed on the plane of the support of the lens and on the chessboard, is acquired for a few instances by the OptiTrack. In particular, to mathematically define the pose of a generic plan in a space is necessary to define the coordinates of three markers at least. In 0.5 seconds, 60 poses are sampled for each marker, and the average value is calculated. Afterward, the equation of the plane passing through three points of the objects is calculated. Finally, the condition of parallelism is checked by calculating the rank of the coefficient matrix of the equation of the planes.

The plane π1 of the support of the lens, depicted in Figure 3. 14, is defined through the following points:

P1 = [X Y Z] = [1001.1070   1064.0609   477.0598] mm

P2 = [X Y Z] = [1001.1070   1010.8646   478.7017] mm

P3 = [X Y Z] = [1001.1070   1034.0473   509.7725] mm

The following vector product defines the normal vector of the plane π1 with origin in P1:

$\bar{n}_1$ = (P1 − P2) x (P1 − P3) = [-1690.9153   0   0]

The components of the normal vector represent the plane coefficients $\bar{n}_1$ = (A, B, C). While:

D = p1(1)* $\bar{n}_1$(1) + p1(2)* $\bar{n}_1$(2) + p1(3)* $\bar{n}_1$(3) = 1.6928e+06

Therefore, the plane π1 is defined as A*x + B*y + C*z + D = 0, that means -1690.9153 * x + 1.6928e+06 = 0

The following points define the plane π2 of the chessboard, depicted in Figure 3. 14:

P1' = [X Y Z] = [1800.6170   1163.3534   596.2915] mm

P2' = [X Y Z] = [1800.6170   1040.7238   596.1113] mm

P3' = [X Y Z] = [1800.6170   1089.8255   498.9972] mm

The following vector product defines the normal vector of the plane π2 with origin in P1':

$\bar{n}_2$ = (P1' − P2') x (P1' − P3') = [11917.9114   0   0]

Therefore, the plane π2 is defined as 11917.9114 * x - 2.1460e+07 = 0

The π1 and π2 planes are parallel if and only if the rank is equal to one, as shown in the following equation:

$$rank \begin{bmatrix} A & B & C \\ A' & B' & C' \end{bmatrix} = 1 \rightarrow rank \begin{bmatrix} -1690.9153 & 0 & 0 \\ 11917.9114 & 0 & 0 \end{bmatrix} = 1$$

The next step is to determine the distance between the two parallel planes. The procedure focused on the following fourth steps. In the first step, a point on the plane π1 (e.g. P1) is selected. In the next step, the equation of the straight line through P1 and perpendicular to the plane π1 is calculated as follows:

$$\frac{x - x_P}{A} = \frac{y - y_P}{B} = \frac{z - z_P}{C} \rightarrow \begin{cases} y = 1064.0609 \\ y - z = 587.0011 \end{cases}$$

The third step consists to calculate the intersection point "B" of the straight line with the plane π2 using the Cramer method:

B = [1796.1200   1064.0609   477.0598].

Lastly, through the difference between the coordinates of B and P1 it is possible to determine the distance between the planes π1 and π2 (Figure 3. 14):

B - P1 = [795.0130   0   0] mm.
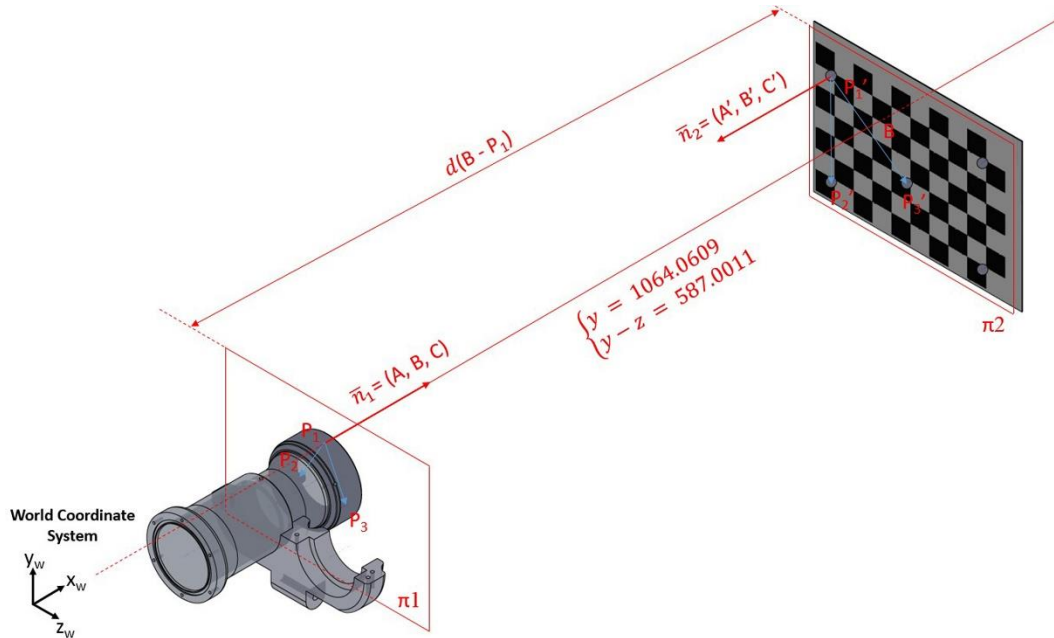
Figure 3. 14. Distance between the planes π1 and π2. For ease of understanding is visible only the left camera.

The position of the marker is calculated with respect to the centers of the spheres; therefore, the planes π1 and π2 are shifted by Sφ/2 with respect to the true surface. The diameter of the sphere of the markers is 7/16 in (11.1125 mm). Thus, the real distance between the support of the lens and the chessboard is d (B-P1) = 795.0130 + 11.1125 = 806.1255 mm.

The same experimental set-up is acquired by the optical stereo camera (internal measurement). Using the Camera Calibration Toolbox for Matlab (Buoguet) is possible to calculate the extrinsic parameters assigned to the image (once calibrated the single camera and the stereo system). The corners of the chessboard for the re-projection are 6 x 7 (Figure 3. 15a). For each point of the chessboard is carried out the vector of translation and rotation of the 2D coordinates with respect to the image plane of the camera. Having the extrinsic parameters of the same image for both cameras, it is

possible to determine the distance via triangulation (reprojection of epipolar points in the image plane). The triangulation process returns in output the 3D coordinates of each corner of the chessboard with respect to the optical center (Figure 3. 15b).

CORNER		Column 1	Column 2	Column 3	Column 4	Column 5	Column 6	Column 7
	X	98,9885	74,8544	50,5326	26,5702	2,2443	-21,7479	-45,8804
Row 1	Y	-143,8321	-143,7191	-144,3560	-144,4947	-145,1240	-144,8287	-145,0803
	Z	828,6266	827,3364	826,1307	828,8978	830,6681	828,2266	828,7225
	X	98,6261	74,5834	50,3144	26,1779	2,1800	-22,0741	-46,2200
Row2	Y	-119,5234	-119,8652	-120,0768	-120,4103	-120,2935	-120,7710	-121,0465
	Z	827,4406	828,8999	828,9925	829,7938	828,0492	829,0454	830,0788
	X	98,2912	74,2949	50,0694	25,8046	1,8743	-22,2263	-46,5391
Row 3	Y	-95,1554	-95,7243	-96,0126	-96,2685	-96,3146	-96,6420	-96,9419
	Z	826,7461	830,0982	830,5822	831,3907	829,4769	829,5673	831,1884
	X	98,2127	74,0751	49,8381	25,6997	1,6818	-22,3559	-46,9593
Row 4	Y	-71,2871	-71,4767	-72,0724	-71,9437	-72,2119	-72,2889	-72,9824
	Z	828,9098	829,2493	832,3151	829,1539	829,6343	828,0960	832,7012
	X	97,8215	73,8488	49,5278	25,4029	1,2483	-22,9886	-47,0290
Row 5	Y	-47,1353	-47,4110	-47,5787	-47,9580	-48,2337	-48,3935	-48,6367
	Z	830,6650	830,6026	829,6251	828,9168	830,9825	831,7735	831,0889
	X	97,5608	73,5707	49,2474	25,0366	1,1288	-23,3117	-47,3692
Row 6	Y	-22,9102	-23,1389	-23,3230	-23,8022	-24,0082	-24,3936	-24,5655
	Z	830,0049	831,2704	830,4121	830,9210	830,4208	832,9246	832,1167

Figure 3. 15. a) Re-projection of the corners of the chessboard on the plane image of the left camera. They were considered 6 x 7 corners of the chessboard. b) Coordinates of the corners of the chessboard with respect to the optical center of the stereo camera.

Finally, having both the external and internal measures, it is possible to determine the position of the optical center of the stereo camera, as reported below:

$$\begin{cases} Doptical\_center\ (1) = dZ\_Buoguet(1,1) - d(B - P1) = 828{,}6266 - 806{,}1255 = 22{,}5011\ mm \\ Doptical\_center\ (2) = dZ\_Buoguet(2,1) - d(B - P1) = 827{,}4406 - 806{,}1255 = 21{,}3155\ mm \\ \vdots \\ Doptical\_center\ (42) = dZ\_Buoguet(6,7) - d(B - P1) = 832{,}1167 - 806{,}1255 = 25{,}9912\ mm \end{cases}$$

In the final analysis, it is possible to determine the mean value and standard deviation:

Mean Value = 23,6779 mm; Standard Deviation= 1,5554 mm.

Once known the optical center of the stereo camera, is possible to calculate the transformation matrix $^{C}T_0$. In particular, the $^{C}T_0$ matrix is calculated with the aid of a CAD software (Figure 3. 16): $^{C}T_0$ = Dx(655) Dy(34) Dz(89.7) Rz(180°).
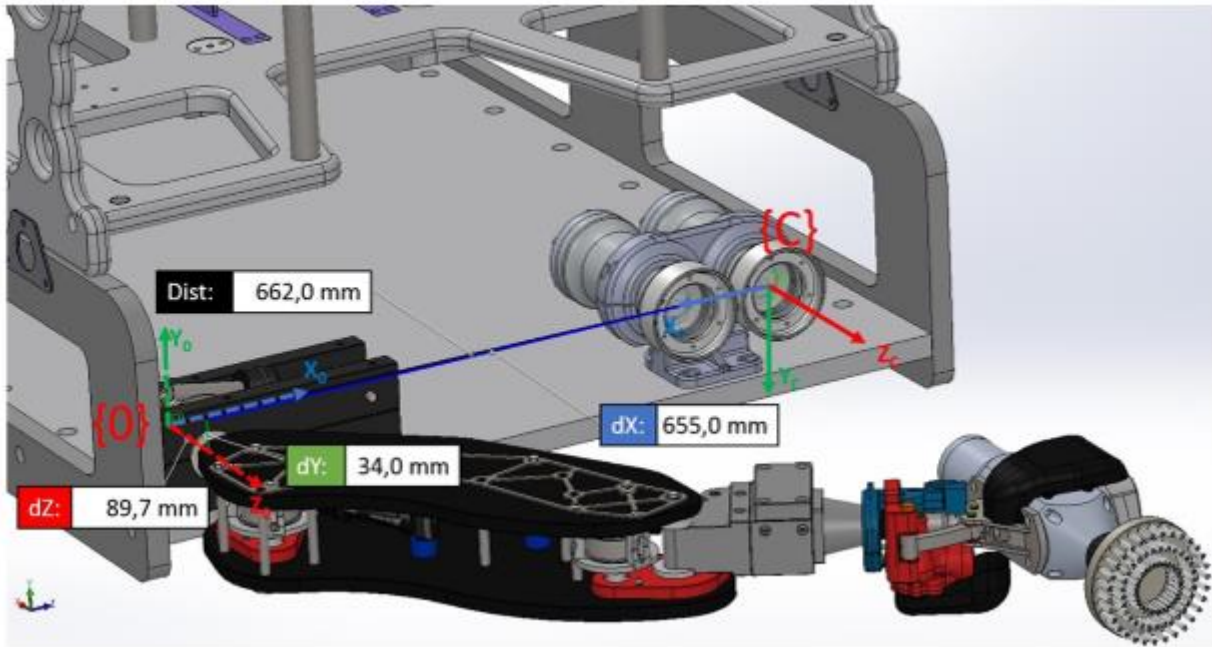
Figure 3. 16. The CAD representation of the roto-translation matrix between the reference systems {C} to {0}.

In other words:

$$^{C}T_0 = \begin{bmatrix} -0.5985 & 0.8012 & 0 & 655.0 \\ -0.8012 & -0.5985 & 0 & 34.0 \\ 0 & 0 & 1 & 89.7 \\ 0 & 0 & 0 & 1 \end{bmatrix}$$

Obviously, this alternative method is more approximate and poorly representative of the real condition respect to the first one described above. It was quoted here only for a comparison respect to the above-mentioned method.

3.4. Tests

This section presents the experimental results. First, the accuracy of the overall AR visualization system has been estimated through laboratory tests, as described in Section3.4.1. Then, the operational capability of the ROV to get closer to a target and to complete a precise cleaning operation by means of an electric brush tool has been assessed in Section 3.4.2.

3.4.1. Laboratory tests

The laboratory tests have been carried out at the Department of Mechanical, Energy, and Management Engineering (DIMEG) of the University of Calabria. The purpose of the test has been twofold: verify the capability of the proposed system to generate a depth map with respect to the end-effector position, and to evaluate the qualitative accuracy of the overall system.

The experimental set-up adopted in the laboratory tests is depicted in Figure 3. 17. It consists in the ROV's skid, on which the optical-stereo camera and the robotic arm are mounted, a 3D scanning station, that is a Stonex X300 laser scanner (Stonex, 2017), and various objects of different size, shape, and texture, placed at a distance varying from 0.5 to 3 meters from the skid.

Figure 3. 17. Experimental set-up.

The performance of the overall AR visualization system has been evaluated in three stages. First, the accuracy of the optical-stereo camera in measuring the distance of the objects present within its workspace and in reconstructing their shapes has been assessed. Then, the kinematic performances of the arm have been evaluated. Finally, we have assessed the accuracy obtained on combining the kinematics of the robotic arm and the standard photogrammetric model of the stereo camera to generate a depth map showing the distances of the surface of the scene objects from the end-effector's pose.

Optical-stereo camera accuracy evaluation

The setup of the underwater imaging system with cameras and lens behind a flat port, although easier to manufacturing, can lead to a degradation in accuracy if compared with its performances in the air, caused mainly by the refraction of the air-water interface. In particular, as reported in (Menna et al., 2018a, 2018b), with increasing the distance between the entrance pupils of the camera lens and the flat ports of the waterproof cases, the standard photogrammetric model used both in Libelas and OpenCV libraries to

perform the on-line AR visualization of the 3D underwater scene represents only a simplification of the underwater image formation process. On the basis of these studies, in order to use the standard photogrammetric model without introducing systematic errors, the cameras have been fixed within the cases through an appropriate support specifically designed to precisely set the distance between the entrance pupil of the camera and the internal surface of the flat port. In particular, a distance of 5 mm, behind a 20 mm thick viewport, has been used for this experimentation.

Previous works have experimentally verified in (Bianco et al., 2015; Lagudi et al., 2016) that the underwater performances of the optical-stereo camera in the present configuration are comparable with the ones obtained in air (an accuracy degradation ranging from 0.02% to 0.5% has been estimated depending upon the quality of the acquired images) allowing us to assess with a good approximation the operational accuracy of the optical-stereo camera based on the results obtained in the laboratory tests.

Various objects have been acquired at different distances from the optical-stereo camera to assess its measurement accuracy. Since the two calibration methods embedded in the control software (see section 3.2) achieve equivalent performances in the air, the camera has been calibrated using the method proposed by Zhang (see section 3.3.4). In particular, 30 point clouds for each pose of the objects have been acquired at a distance between 0.5 m and 3 m from the optical-stereo camera. Then, the distance of the objects has been measured for all the different poses by manually selecting points on the gathered point clouds.

For each measurement in the point cloud, the error has been evaluated as the absolute value of the difference between the distance of the object measured by means of the point cloud and those acquired by the laser scanner. The results are depicted in Figure 3. 18. The Root Mean Square Error (RMSE) grows from values below the centimeter (9.41 mm) when acquiring at short range, to larger values such as 96 mm obtained at longer distances. As expected, due to the short baseline used in the present setup (about 100 mm), the optical-stereo camera gives good results in close range acquisition, but deteriorate quickly at longer ranges.

Distance [mm]	RMSE [mm]	Standard Deviation	Maximum Error [mm]
713	9.2	0.632	10
1235.40	15	1.506	17.4
1806.50	30	2.506	34.5
2256.90	52.5	2.459	54.9
3000	96	9.848	106.1

a   b
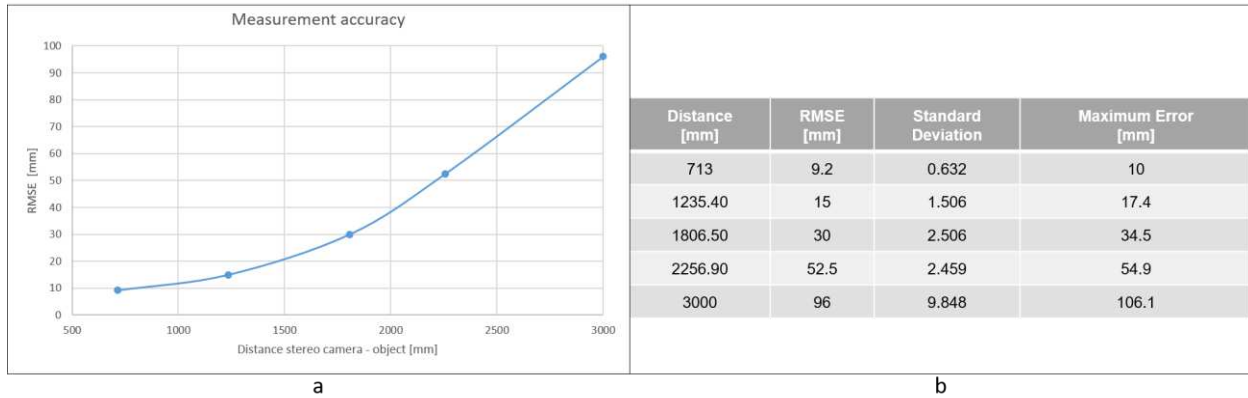
Figure 3. 18. Results of the optical-stereo camera measurement accuracy. (a) Trend of RMSE values for different distances between the optical-stereo camera and the objects in the workspace. (b) Statistics for accuracy estimation of the optical-stereo camera (mm).

To better assess the performance of the optical-stereo camera, an amphora has been acquired at an approximate distance of 1 m.

After manually selecting the points in the cloud that belong to the object, they are registered using Iterative Closest Point (ICP) against the reference 3D model obtained using the NextEngine 3D Laser Scanner. The results are presented in Figure 3. 19. It shows two elements. First, the reference 3D model in red overlaid with the gathered point cloud in white (Figure 3. 19a). Second, the acquired optical cloud where each point is colored according to its distance with respect to the reference 3D model (Figure 3. 19b). The histogram of these distances is shown in Figure 3. 20. It can be seen that the mean error is around one millimeter (RMSE of 1.57 mm and a standard deviation of 2.18 mm) with a maximum error of 21.20 mm. The resulting error is equivalent to a length accuracy of about 0.5%, that is consistent with the ones reported in the literature (Shortis, 2015).
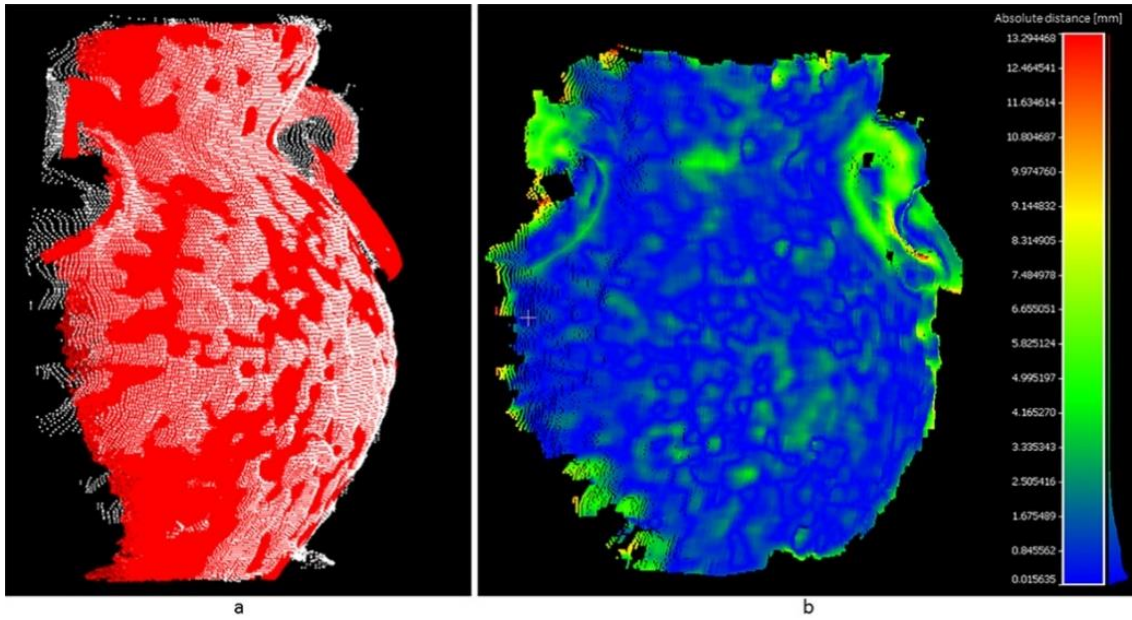
Figure 3. 19. (a) Reference 3D model overlaid on the gathered point cloud. (b) Gathered point cloud colored according to the distance between each point and the reference 3D model.
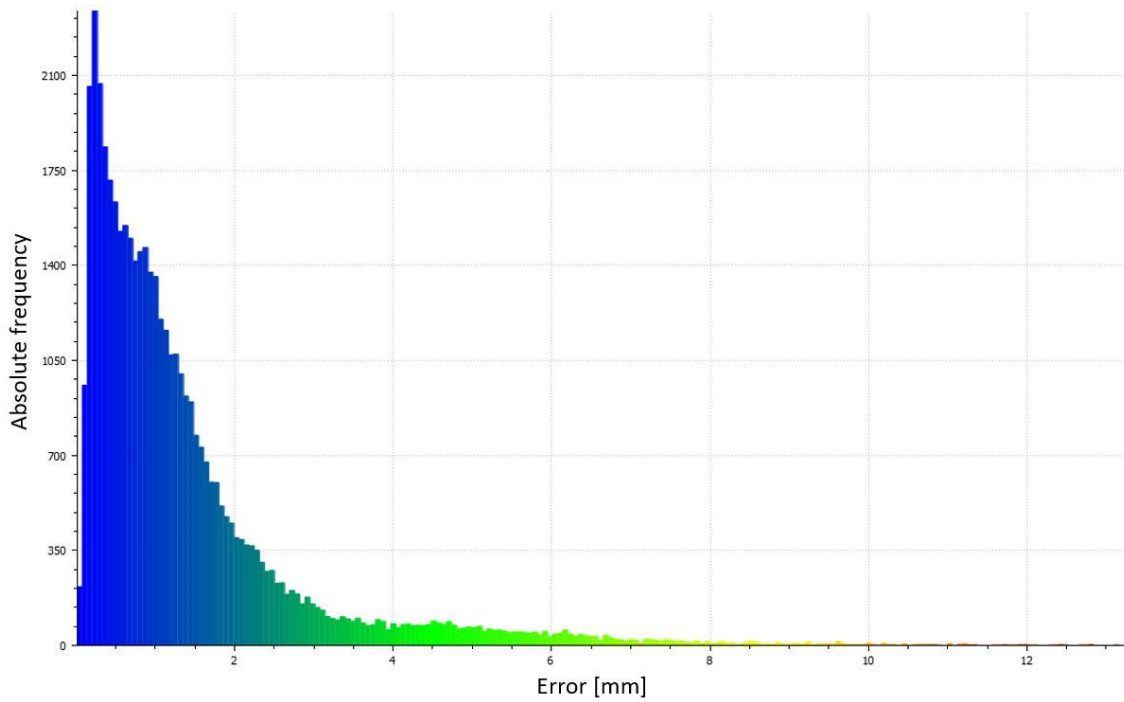
Figure 3. 20. Error histogram of the Euclidian distance (mm) between the point cloud and the reference 3D model representing the acquired amphora.

Kinematic performances of the arm

The forward kinematic model of the robotic arm is affected by errors that could compromise the estimation of the depth map, as explained in Chapter 2. In particular, the physical properties of the manipulator may differ from the corresponding ideal values due both to geometric and non-geometric errors, such as manufacturing tolerances, assembly errors and misalignment of the joints, elastic deflections of the links, thermal deformations, as well as measurement errors of the encoders itself. These errors can be taken into account by analyzing the kinematic performances of the robotic arm that are expressed in terms of its accuracy (A).

On the basis of the ISO standard 9283:1998 (ISO 9283, 1998), the accuracy (A) can be defined as the ability of the system's end-effector to measure a specified pose. It is measured experimentally by means the distribution of the positioning errors calculated by comparing predicted and actual poses of the end-effector arm. As shown in section 2, in a previous study (Rizzo et al., 2017), we have calculated the error distribution E_A by measuring the end-effector pose in some different configurations, with the resulting estimation of the accuracy of the robotic arm that is $A = \mu_{E_A} \pm \sigma_{E_A} = 50.62 \pm 24.21 \text{ mm}$

Accuracy of the AR visualization system

The accuracy of the overall system has been evaluated as the RMSE value between the different distances of the objects in the workspace, measured by means of the depth map (as predicted by the mathematical model of the system) and those acquired by the laser scanner (actual distances of the objects with regard to the end-effector' pose). In particular, three series of measurements have been performed, each corresponding to a different pose of the robotic arm (Figure 3. 21). The trials have been carried out in two step:

- Analyzing the accuracy of the AR visualization system variating the distance of a single object (amphora) acquired at a distance between 1.5 m and 3 m from the optical-stereo camera;

- Qualitative test using the experimental setup depicted in Figure 3. 17.
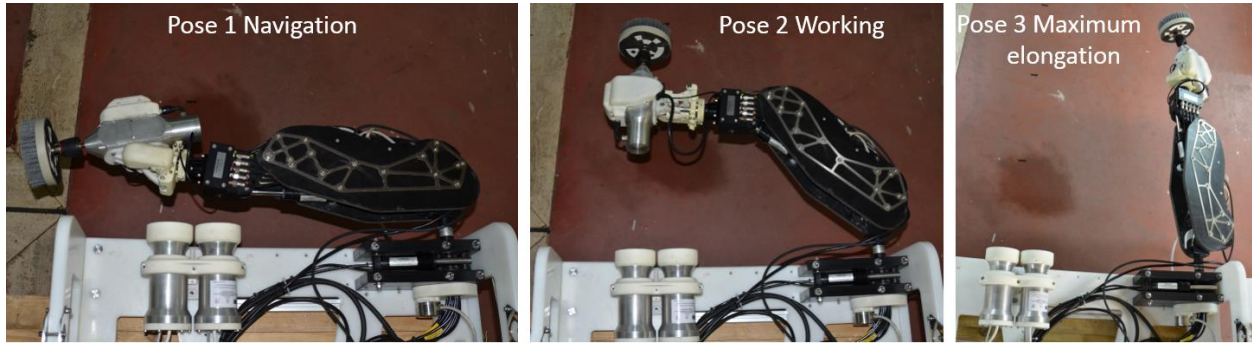
Figure 3. 21. Three different poses of the robotic arm within its working volume to perform the accuracy estimation.

Regarding the first step, after the survey, the acquired 3D point clouds have been processed by means of the software 3D Reconstructor, provided by Stonex, which allows to analyze and elaborate the data in order to calculate the actual distances of the objects from the end-effector pose. First, the system has been evaluated through the acquisition of a single object (amphora) at different distances in the three considered poses of the arm, corresponding to a navigation (pose 1), working (pose 2), and maximum elongation (pose 3). For each pose the matrix ^0T_E is calculated through the kinematic model of the arm developed in Matlab. Furthermore, $^CT_0$ has been calculated in the section 3.3.5. Consequently, the matrix $^ET_C = {}^ET_0\,{}^0T_C$ can be calculated. This information has been reported into the software of reconstruction developed in the CoMAS project (see section 3.2), to the end of setting manually the origin of the camera reference frame in the position of the end-effector reference frame. Based on the above-mentioned mathematical model, the position of a generic point P of the object can be calculated with respect to the end-effector's reference frame {E} by means of the following formulation $^EP = {}^ET_0\,{}^0T_C\,{}^CP$. Then, the distance of the objects respect to the end-effector has been measured for the three poses of the arm by manually selecting points on the gathered point clouds directly using the developed software. The point clouds generated by the laser scanner related to the pose 1 for a distance of the amphora of 1.5 m is depicted in Figure 3. 22, while the ones generated by the optical-stereo camera is depicted in Figure 3. 23.
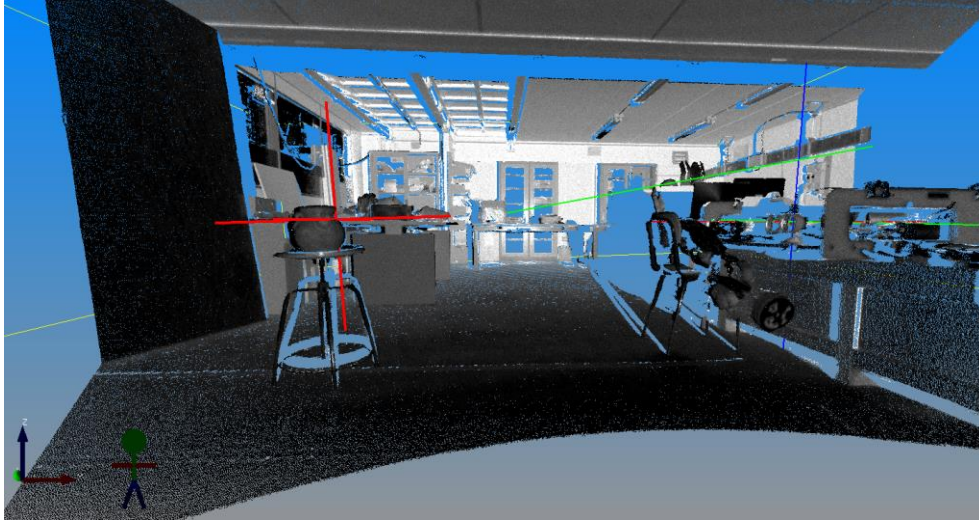
Figure 3. 22. The point clouds generated by the laser scanner visualized in JRC Reconstructor. Pose 1. Distance object 1.5 m.
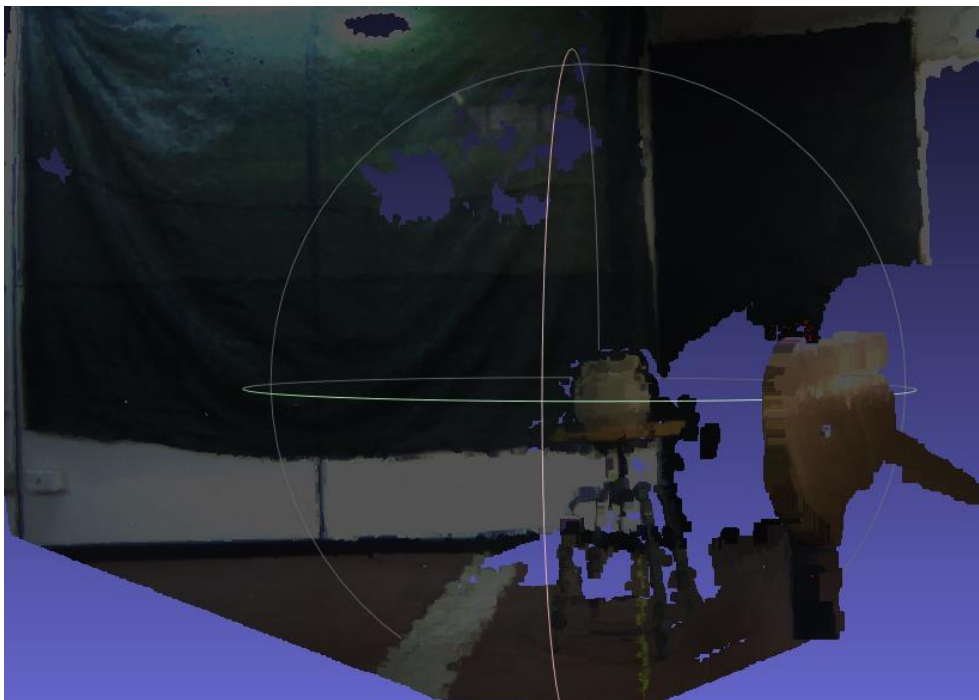
Figure 3. 23. The point clouds generated by the optical-stereo camera visualized in MeshLab. Pose 1. Distance object 1.5 m.

The point clouds generated by the laser scanner and by the optical stereo-camera related to the pose 2 for a distance of the amphora of 1.5 m is depicted in Figure 3. 24. Each measure has been repeated ten times for all configurations.
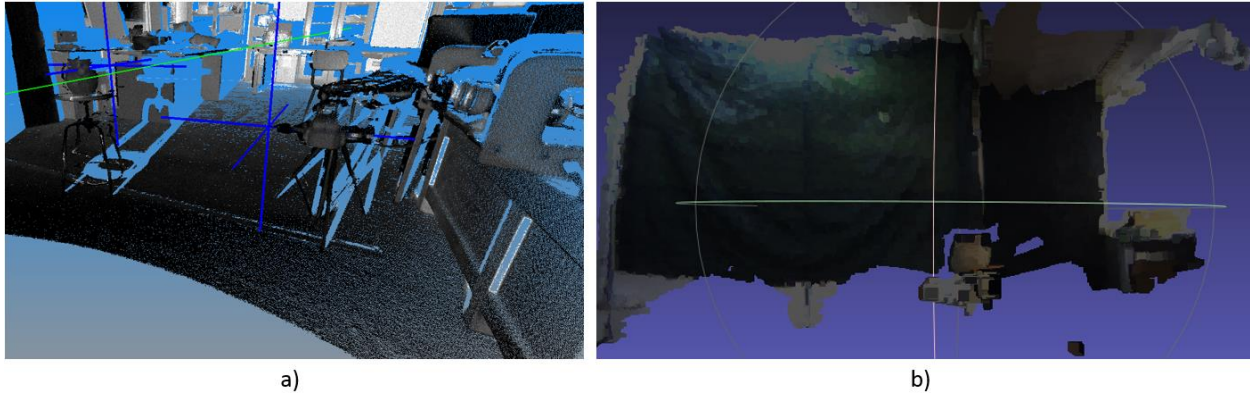
Figure 3. 24. The point clouds generated by the laser scanner and by the optical stereo-camera. Pose 2. Distance object 1.5 m.

The results for all configurations are depicted in Figure 3. 25.

Distance [mm]	Pose 0			Pose 1			Pose 2		
	RMSE	Standard deviation	Maximum error	RMSE	Standard deviation	Maximum error	RMSE	Standard deviation	Maximum error
1535,4	41	4,695	49,4	51,2	5,934	58,3	31,1	5,696	42,1
2021,4	62,55	7,516	75,95	73,4	5,507	81,3	53,25	5,322	62,35
2463	89,7	12,019	108,7	100,5	8,895	113,8	80,45	12,538	93,35
2953,5	126,55	5,442	134,05	148,5	17,856	177,3	113,4	13,223	136,6
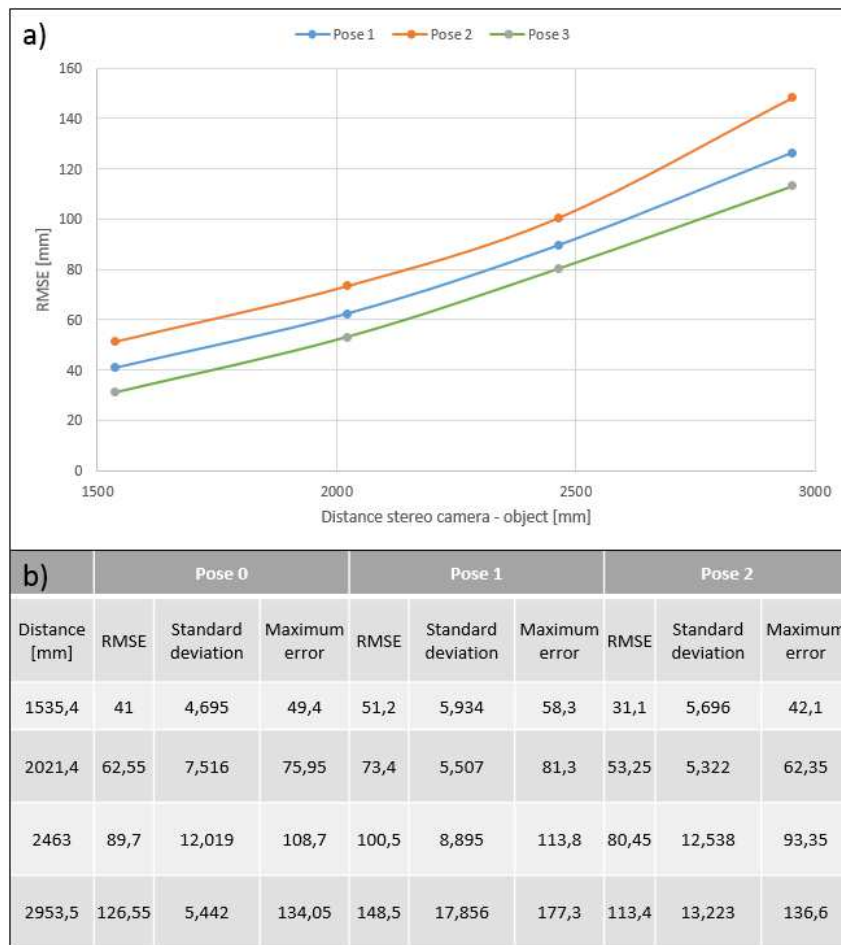
Figure 3. 25. (a) Comparison of the trend of RMSE values for three poses of the robotic arm when varying the distance between the optical-stereo camera and the objects in the workspace. (b) Statistics for accuracy estimation of the overall system (mm).

As expected, the RMSE values grow when the distance between the optical-stereo camera and the objects in the workspace increases. It is due to the loss of performance of the optical-stereo camera accuracy at longer distances (Figure 3. 18). The Pose 2 shows higher RMSE values in the workspace. It is due to the stationary deflection caused by gravity that is most severe for this pose of the robotic arm. Anyway, the performance should improve in the underwater environment because of the buoyancy that reduces the gravity effects and allows hydraulic joints to operate more accurately.

Finally, the system has been used in the experimental set-up depicted in Figure 3. 17 for qualitative evaluation for a generic static pose. The point clouds generated by the laser scanner is depicted in Figure 3. 26, while the ones generated by the optical-stereo camera is depicted in Figure 3. 27.
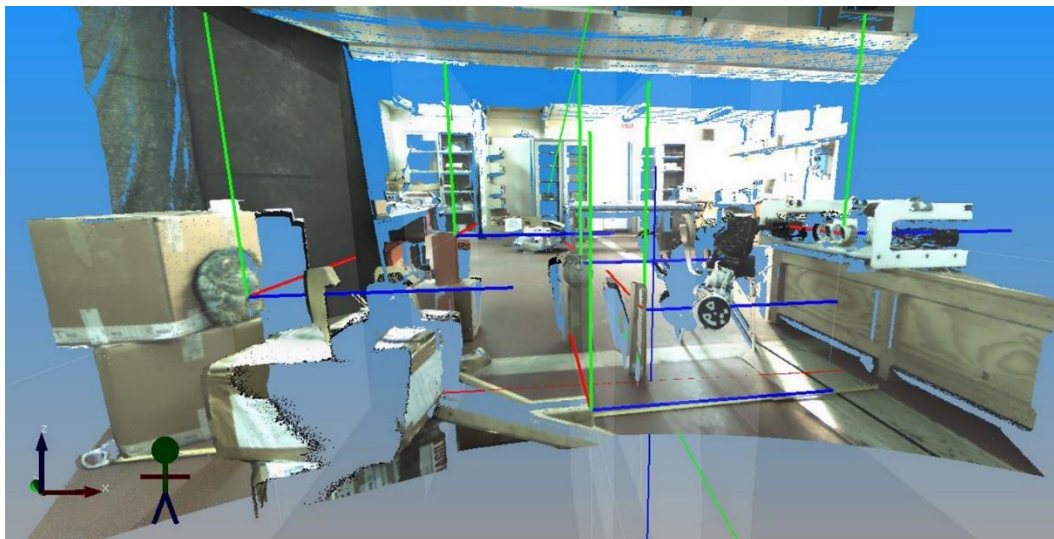
Figure 3. 26. The point clouds generated by the laser scanner visualized in JRC Reconstructor for a generic static pose.
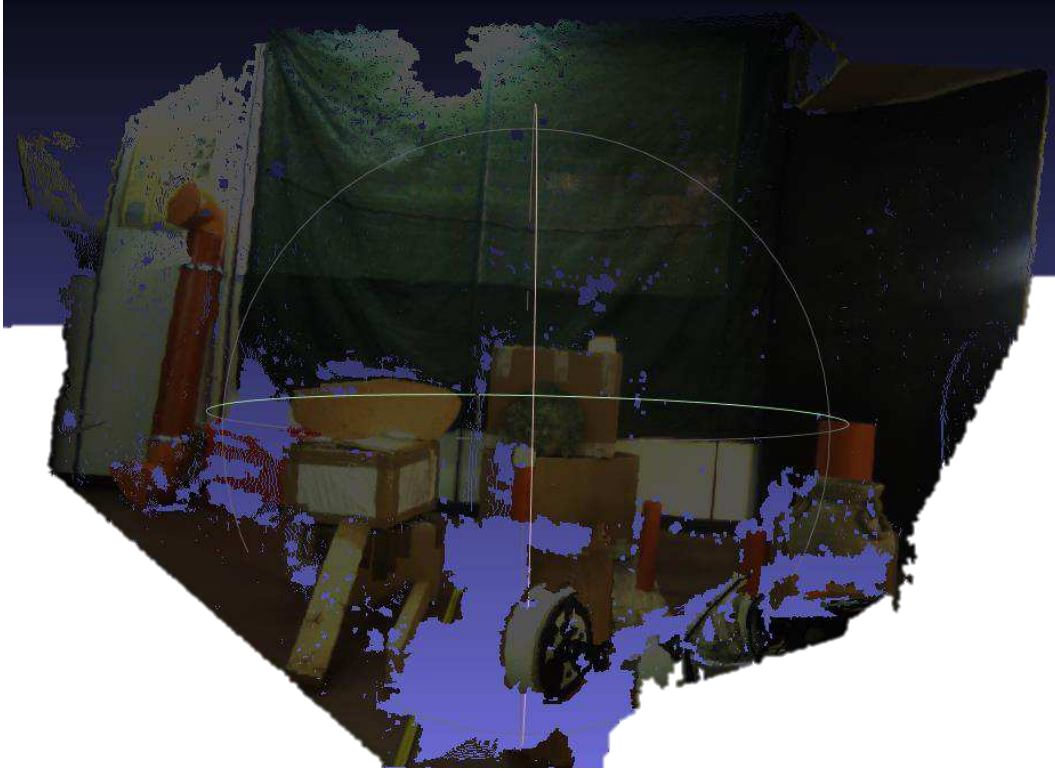
Figure 3. 27. The point clouds generated by the optical-stereo camera visualized in MeshLab.

The following image (Figure 3. 28) shows the depth map generated for a specific pose of the end-effector of the robotic arm.
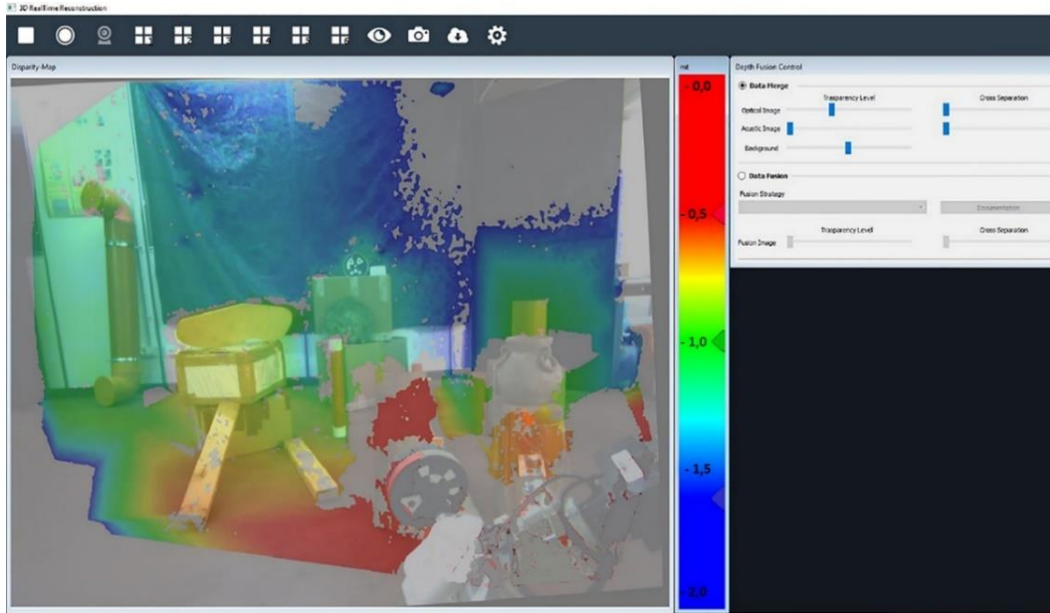
Figure 3. 28. Depth map augmented on the visual feedback.

To compute the depth map easier to read and interpret, it is visualized as an RGB color gradient map and augmented on the optical flow information provided by the camera. The RGB color scale provides information to interpret the depth map, e.g., the red colors are close objects and blue objects are far away, and its color component range can be customized by specifying the minimum and the maximum distance. The user interface provides also a set of widgets that allow the operator to interact with the software, through direct manipulation of graphical buttons and menus, in order to edit the main parameters of the stereo camera, customize the transparency of the depth map and manage the layout and number of display windows.

3.4.2. Field tests

The field tests have been carried out at the headquarters of WASS (Whitehead Alenia Sistemi Subacquei) S.p.A. in Livorno (Italy), one of the partners of the CoMAS project (Figure 3. 29).

Figure 3. 29. Field tests preparation in a large pool at the WASS SpA. The umbilical of the ROV is connected to the TMS (Tether Management System).

The tests have been performed in a large pool to gain better control of the environment, where the capability of the ROV to get closer to the target and to complete a precise cleaning operation by means of an electric brush tool was assessed with the arm in the working pose (Figure 3. 30).
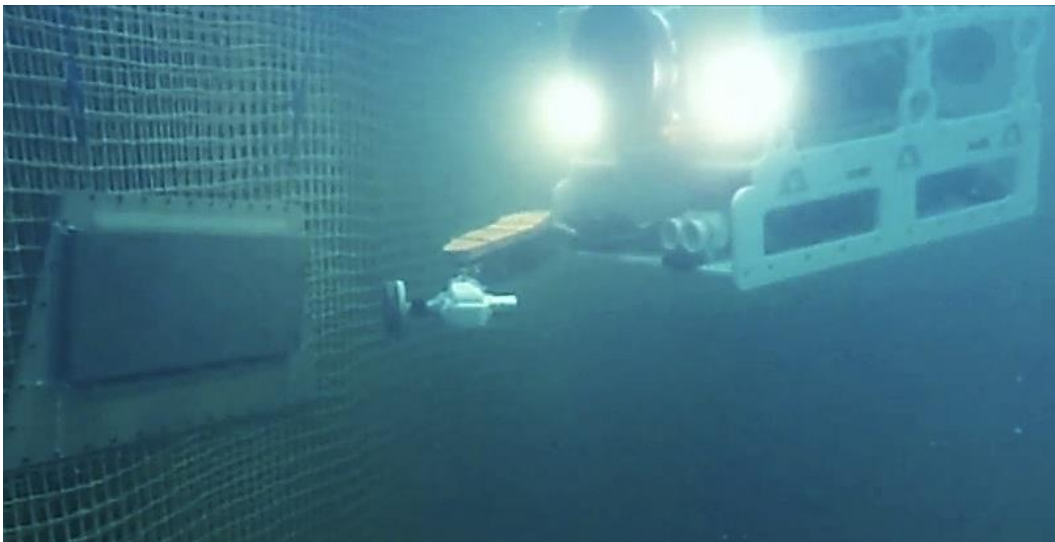
Figure 3. 30. The end-effector's brush approaches the target.

After assembling the Perseo ROV with the skid, on which the manipulator and the optical-stereo camera have been mounted, the vehicle has been immersed in the test pool by means of a gantry crane on rails. The ROV is operated according to a classic procedure in which an operator manages the vehicle and the robotic arm. Typically, the proposed ROV system is controlled by only one pilot. But two persons could possibly be involved for controlling the system, one lead pilot manages vehicle position and a co-pilot operates the underwater manipulator. The depth map provides only visual feedbacks that allows the co-pilot to obtain a reliable estimate of the distance between the end-effector and the target, and then to have an instrument that supports him/her for making decisions while maneuvering the manipulator.

The participants to the test were experienced ROV pilots, involved in the CoMAS project, which provided positive feedbacks and personal opinions about the enhanced situational awareness achieved thanks to the adoption of the proposed AR visualization system.

The following image (Figure 3. 31) shows the feedbacks provided by the stereo camera while the end-effector is approaching the target.
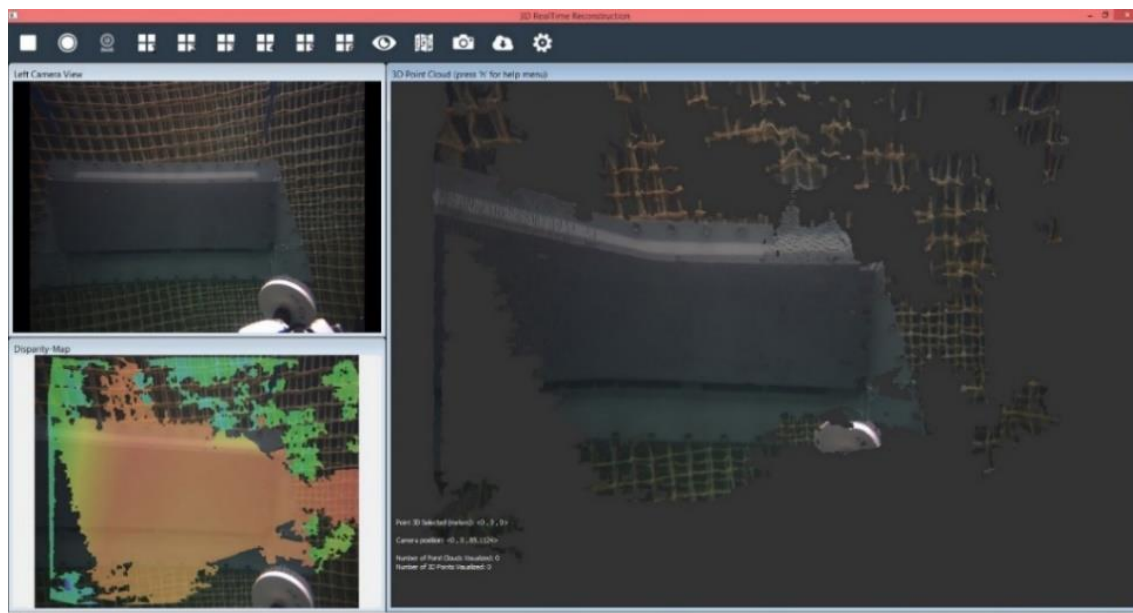
Figure 3. 31. User interface with different display windows.

The software features a high customizability of the user interfaces that allows switching between different visualization modes. In fact, the user has arranged the display windows in order to have 2D and 3D information feedbacks (Figure 3. 31). In particular, on the right, a display window shows the 3D point cloud of the acquired underwater scene, while, on the left, two windows provide to the user respectively the video broadcasted by the left camera and the depth map. Once the vehicle came close to the target, the layout has been rearranged by a user with a single display window (Figure 3. 32), in which the images broadcasted by the optical-stereo camera are enhanced through the depth map, in order to perform fine manipulation tasks. The distance between the end-effector and the target is approximately 1 meter.
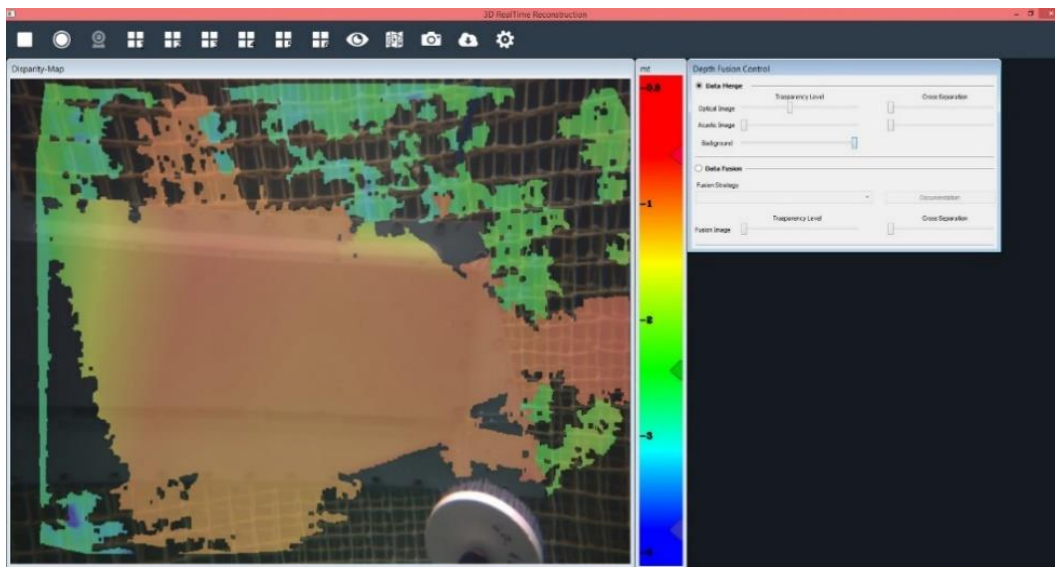
Figure 3. 32. RGB scalar field window of the camera control software.

The tests have demonstrated that the proposed AR visualization system increases the effectiveness of the control of the robotic underwater arm. In fact, the user can operate safely and accurately thanks to the distance information provided by the optical-stereo camera, instead of piloting the vehicle only by watching the visual feedbacks broadcasted by the camera. The users that have participated in the testing activity made positive remarks about the proposed system for its easily interpretable representation of the visual information and its high flexibility that allows adjustments of camera's parameters in order

to cope with the variable conditions of the underwater environment. In this phase of the research project, we were interested to verify the proper functioning and collect preliminary users' feedback of the proposed AR visualization system. Nevertheless, in future tests, objective metrics would be evaluated with end users in real tasks performed both in the freshwater testing pool and in open seawater condition.

As future works, the optical-stereo camera can be integrated with other sensors capable to calculate the depth map and perform an on-line 3D reconstruction of the underwater scene. In considering the limitations and disadvantages derived from the technologies now adopted in the underwater manipulation field, the proposed AR visualization system represents an added value especially in the Underwater Cultural Heritage field where soft touch is required for the manipulation of the archaeological artefacts.

4. Soft Robotic jamming grippers

Part of the research on "Innovative manipulation techniques for underwater robotics" has been conducted in collaboration with the Robotics Laboratory for Complex Underwater Environments (R-CUE) at the University of Rhode Island (USA).

Underwater manipulation for unmanned robots, and in particular, remotely operated vehicles (ROVs), is a fundamental part of deep-sea exploration. It is needed for variety Navy, archaeological and biological applications, like sensor anchoring on structures, a collection of submerged objects and corals, etc. However, currently, existing robotic arms are often too powerful and awkward to handle delicate or complex objects without damaging them.

Soft and compliant grippers have been shown to dramatically simplify the problem of grasping complex objects with robotic manipulators and are increasingly being used in terrestrial applications (see section 1.3). They can be designed to passively limit the force that is applied to fragile or sensitive objects, even when the exact shape of the object is unknown prior to grasping. Furthermore, the softness, the compliance, has the added benefit of increasing the robustness of the grippers themselves – bend rather than break. For these reasons, (ease of grasping, force limiting without sensors, and inherent robustness) soft robotic grippers are an excellent match for the challenging problems that confront marine archaeologists and marine biologists sampling in the deep ocean.

To try to solve this problem the Robotics Laboratory for Complex Underwater Environments (R-CUE) at the URI is researching compliant soft grippers that use the jamming of granular material in fluid enclosed by a thin membrane, as a method to grasp an object.

My research internship at the University of Rhode Island focuses on continues the development, prototyping, and testing of the compliant jamming grippers developed at the R-CUE. In particular, the subject is divided into two main projects, studying both a universal jamming gripper and a hybrid toroidal soft gripper.

4.1. The University of Rhode Island

Rhode Island (Figure 4. 1), officially the State of Rhode Island and Providence Plantations, is a state in the New England region of the northeastern United States. It is the smallest in the area, the eighth least populous, and the second most densely populated of the 50 U.S. states. Its official name is also the longest of any state in the Union. Rhode Island is bordered by Connecticut to the west, Massachusetts to the north and east, and the Atlantic Ocean to the south via Rhode Island Sound and Block Island Sound. It also shares a small maritime border with New York. The state capital and most populous city in Rhode Island is Providence.
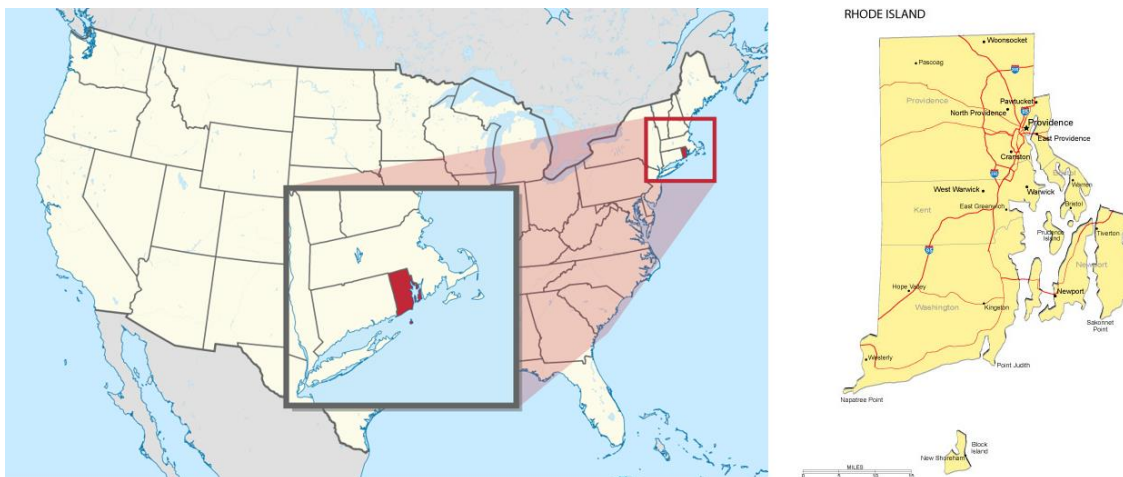
Figure 4. 1. Rhode Island.

The University of Rhode Island, commonly referred to as URI, is the principal public research as well as the land grant and sea grant university for the state of Rhode Island (Figure 4. 2).

Figure 4. 2. URI tagline.

Its main campus is located in the village of Kingston in southern Rhode Island (Figure 4. 3). Additionally, smaller campuses include the Feinstein Campus in Providence, the Rhode Island Nursing Education Center in Providence, the Narragansett Bay Campus in Narragansett, and the W. Alton Jones Campus in West Greenwich.

Figure 4. 3. URI Kingston Main Campus.

URI has a lead position on the development of Oceanic researches at Rhode Island, throughout their Graduate School of Oceanography and the Department Ocean Engineering. In fact, the Rhode Island's nickname is Ocean State. In particular, the Graduate School of Oceanography (GSO) has established a global reputation for excellence in marine research, teaching, outreach, and exploration of the world's oceans and coasts. With its home port at URI's Narragansett Bay Campus, the 185-foot research ship, R/V Endeavor represents the flagship of myriad research vessels and shore-based facilities operated by GSO (Figure 4. 4 and Figure 4. 5). The GSO houses also the Inner Space Center and Ocean Exploration Trust, which are international hubs for ocean exploration and education.

Figure 4. 4. URI Bay Narragansett Bay Campus.

Both the Graduate School of Oceanography (GSO) and Department of Ocean Engineering (OE) were created in 1966 and stated together at the Narragansett Bay Campus, to enable their tight relation and collaboration for future research studentship.

Figure 4. 5. GSO. R/V Endeavor.

At present, the OE department is divided in six main specialties in both teaching and research (Figure 4. 6): ocean instrumentation and robotics, underwater acoustics, marine hydrodynamics and tsunamis, coastal modeling, marine geomechanics, coastal and offshore structures, and offshore power generation.
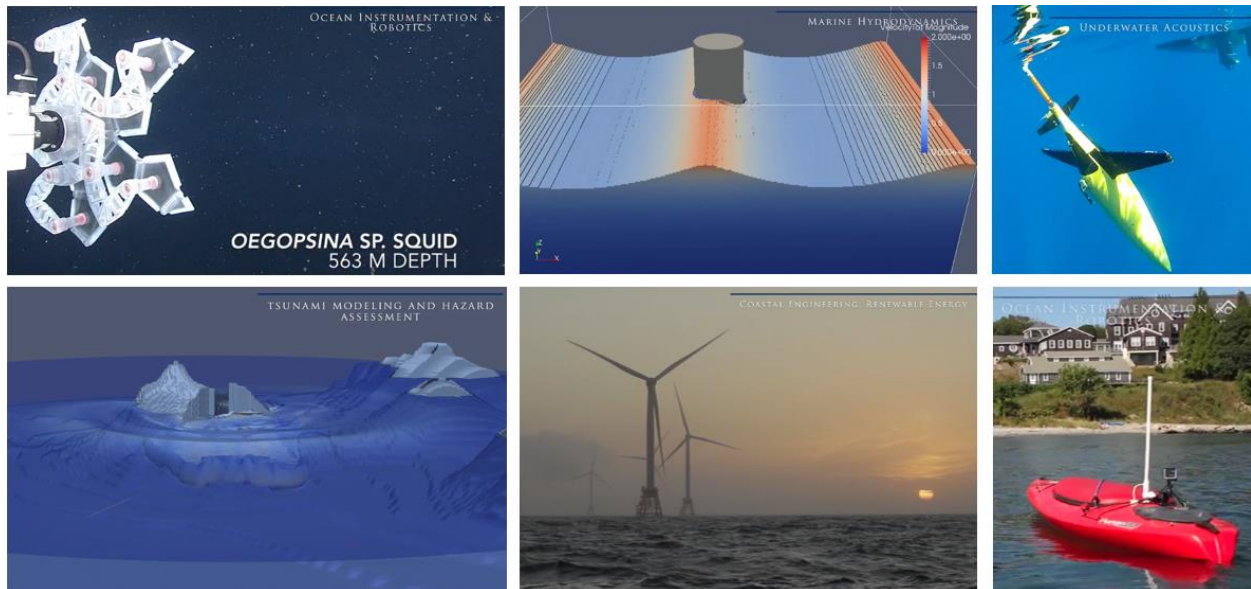
Figure 4. 6. Ocean Engineering research and teaching program.

The Robotics Laboratory for Complex Underwater Environment (R CUE) was created in 2012 with the arrival of Pr. Stephen Licht, my internship supervisor, to URI as part of the Ocean Engineering Department, with the goal of developing maritime robots with the ability to operate in dynamic and unpredictable environments. To this end, the members of the laboratory investigate biologically inspired propulsion as a means of providing high authority/high bandwidth thrust; a distributed pressure sensing for detection of flow structures and obstacles; model-based optimal control and trajectory generation strategies for maneuvering in dynamic conditions; and compliant underwater manipulation technologies.

4.2. Universal jamming soft gripper

4.2.1. Previous Work

Design evolution

Starting with the idea of the universal jamming gripper the R-CUE Lab has begun to explore the concept of particle jamming. A jamming gripper, as described by Brown et al. (2010) consists of a flexible membrane containing particles within a fluid medium (Figure 4. 7). Particle jamming is accomplished by creating a pressure differential between the inside of a particle-filled flexible membrane and the fluid surrounding the membrane. When the flexible membrane is filled with fluid at the same pressure of the surrounding fluid, the membrane does not obstruct the motion of the particles inside. The particles can move around each other freely, and the membrane is free to take the shape of any object that it is pressed against. To make the membrane harden in its current shape, fluid is removed from the inside of the membrane. The grains inside are jammed together by the membrane, which constricts under the external pressure. The grains can no longer flow around each other and the whole mass becomes rigid.

A universal jamming gripper uses a single elastic membrane filled with particles, where the membrane is suspended below a rigid disc or shallow cup. As shown in Figure 4. 7, the membrane is lowered onto the object to be grasped, fluid is pumped out to jam the particles together, and the object can then be picked up along with the gripper.
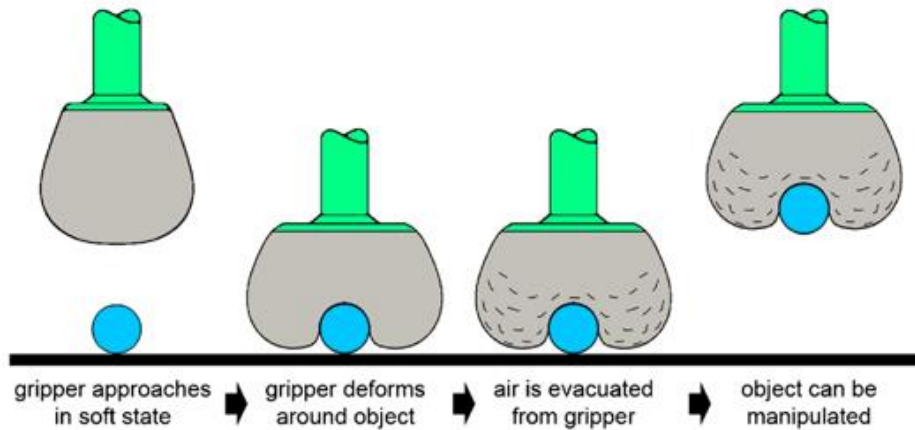
Figure 4. 7. Jamming gripper mechanism described in Brown et al (2010).

The performance of universal jamming grippers has been a topic of extensive quantitative characterization in air. It has been commercialized for factory automation Empire Robotics.

Soft robotics is particularly attractive in underwater applications because soft components can have densities close to that of the surrounding fluid. When operated underwater, soft robotics can use liquid, rather than gas, within the internal fluid circuits without making the robot too heavy to support itself. Indeed, an incompressible liquid is required to avoid the use of high-pressure gas reservoirs and attendant regulation apparatus, which would otherwise be needed to compensate for pressure at depth. A further benefit of using liquid s that it allows the use of a low volume closed-circuit fluid system to control particle jamming. Given that the jamming pressure is limited by the absolute ambient pressure, and that ambient pressure increases with water depth, a particle jamming-based gripper should increase in strength as it is carried deeper in the water column, making it an attractive choice as a deep water tool.

To this end, to implement the universal jamming gripper in the underwater field, a number of important modifications were required. Researchers using jamming grippers in air at approximately one atmosphere of external pressure, have used everything from coffee grounds and sawdust to breakfast cereals as the particles, with air as the internal fluid media. For operations at over 1000m depth (where the gripper experiences a 100-fold increase in ambient external pressure) it immediately becomes clear that the first

necessary modification is to replace the air inside the membrane with an incompressible fluid, and in all of our underwater applications we have used fresh water as the fluid media. The second necessary adaptation is the use of pressure tolerant particles in place of coffee grounds or the like. In our case, we have used glass beads as the jamming particles; in particular, sandblasting media with nominal 200-micron diameter.

A simple prototype was developed as proof of concept, depicted in Figure 4. 8.
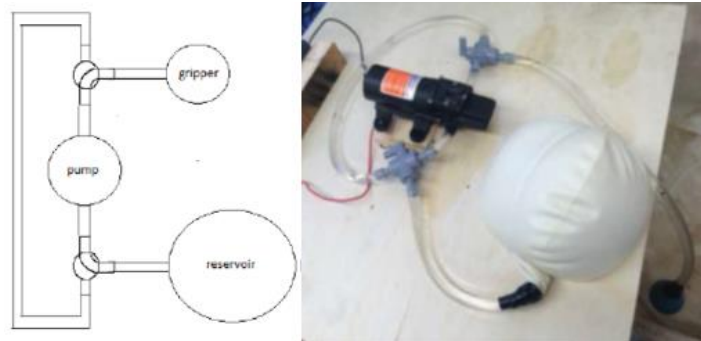
Figure 4. 8. First jamming gripper schematic and prototype. Source: Pr. Licht.

As a first proof of concept, the water and glass bead filled gripper was mounted to a VideoRay 3 observer class ROV. The internal pressure of the membrane was controlled using a shore-side bilge pump, running off of a 12V battery, which pumped water into and out of the membrane (a latex party balloon) through a 5m long flexible tube (Figure 4. 9).
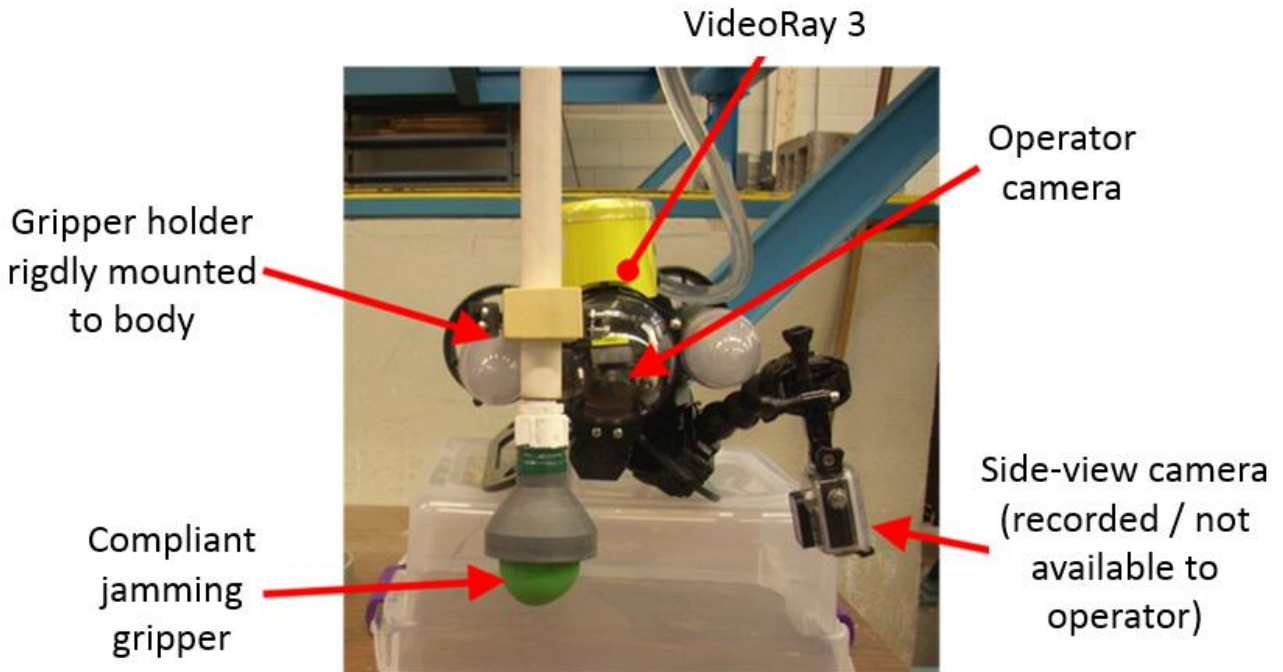
Figure 4. 9. Compliant jamming gripper mounted on the VideoRay 3. Source: Pr. Licht.

A GoPro camera in a waterproof housing was used to capture video during experiments, while the ROV pilot used the low resolution operator camera to pilot the vehicle and place the gripper on objects of interest.

The results from the first trial of the system were very promising. In a 5m deep concrete lined fresh water tank, it was possible to retrieve objects ranging from plastic zip ties, to aluminum rods, rings, as well as Allen wrenches, and most surprisingly from our point of view a steel washer lying flat on the tank bottom (Figure 4. 10). The vehicle lands, with the gripper pressed down over the object; the fluid is evacuated from the membrane to jam the particle, and the object is picked up when the vehicle lifts off the bottom.
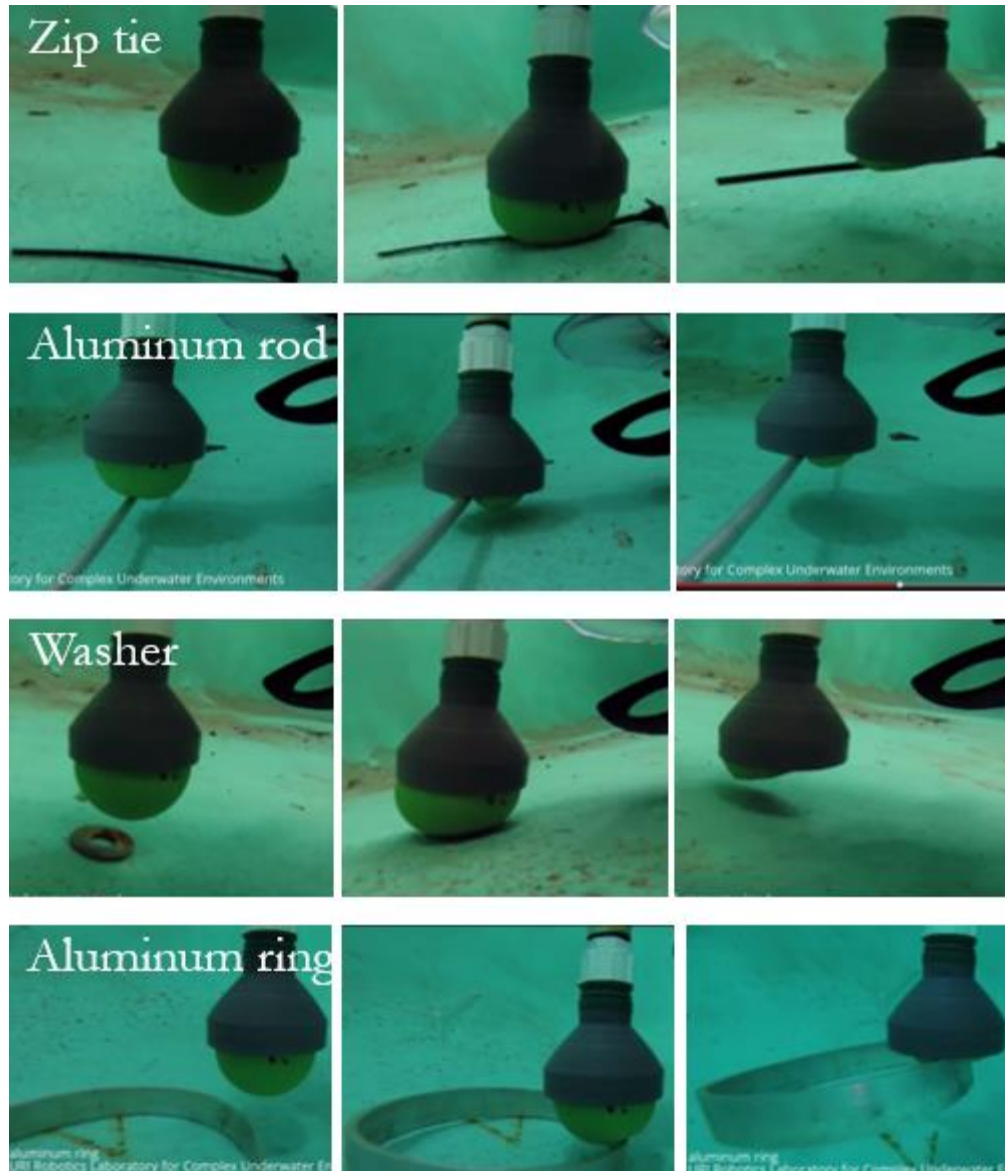
Figure 4. 10. Trials in the water tank. Collecting of objects resting on hard surface. Source: Pr. Licht.

All of the objects would have been impossible or nearly impossible to retrieve without lying it on a hard surface. The next step was to install a modified gripper on the 5-function HydroLek HLK-43000 arm of the Saab SeaEye Falcon ROV, with the purpose to carry out trials in 5 meters' fresh water tank (Figure 4. 11).
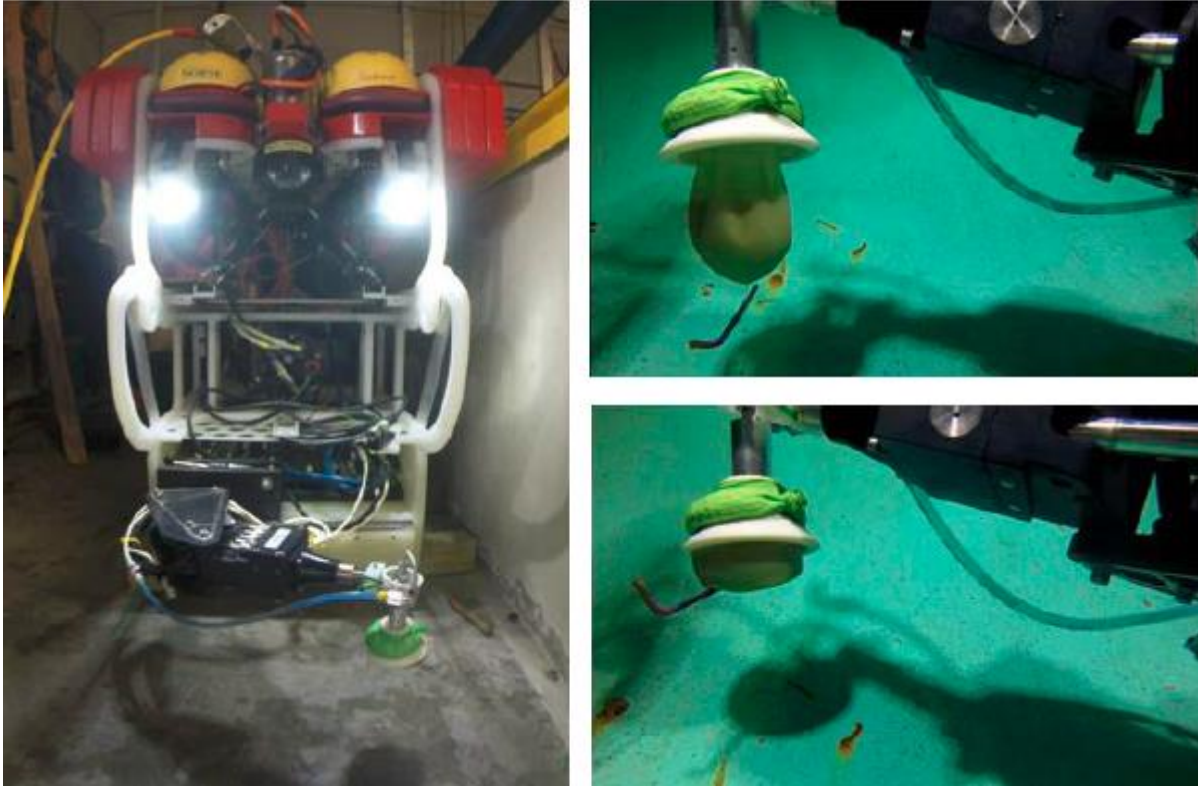
Figure 4. 11. An under-filled jamming gripper with floating cap mounted on the 5-DOF arm of SeaEye Falcon ROV, recovering a small object in a 5m water tank. Source: Pr. Licht.

These qualitative trials demonstrate the possibility to achieve the tasks in real manipulation conditions, without placing the objects with great accuracy, as well as using a no force and no control feedback arm. In fact, the arm control is accomplished joint by joint using serial on-off switches with an actuation delay from the switch to movement of as much as half second.

While the feedback from collecting a number of different objects was generally positive, the question that nearly all of them had (aside from "will it work at 100 atmospheres?") was whether it was possible to use this approach to pick up objects resting on soft substrates, since all objects successfully grasped, shown in Figure 4. 10 and Figure 4. 11, involved a fair amount of downward force applied to an object resting on concrete. The basic problem is that at most deep-sea archaeological sites, objects of interest are usually resting on sediment or saturated, degraded, and hence soft wooden beams and decking.

This problem has been partially solved by dramatically reducing the number of beads used, underfilling the membrane with as little as 25% of the volume of beads that could fit in the membrane. The result is that when the membrane comes into contact with the object to be sampled, it simply drapes over the object while the beads flow easily around. Essentially, if the beads do not fill the entire volume, you end up with a small hardened rigid mass around the object, but it is only supported by the latex neck of the balloon. This limitation was solved by introducing a number of bead chains attached only at the top to the rigid manifold through which fluid is pumped out of the balloon. The arrangement of the bead chains is shown in Figure 4. 12.

Figure 4. 12. The arrangement of the bead chains mounted on the prototype of the gripper. Source: Pr. Licht.

When the gripper is not jammed, the bead chains drape over the objects inside the membrane, and when the gripper is jammed they are surrounded by and embedded in the rigid matrix of the granular particles. In this way, the force required to lift the rigid

matrix, and the object that it holds, is transferred to the rigid manifold through the bead chains, rather than through the flexible membrane.

A schematic showing the design of the gripper membrane, manifold, cap, and handle is shown in Figure 4. 13.
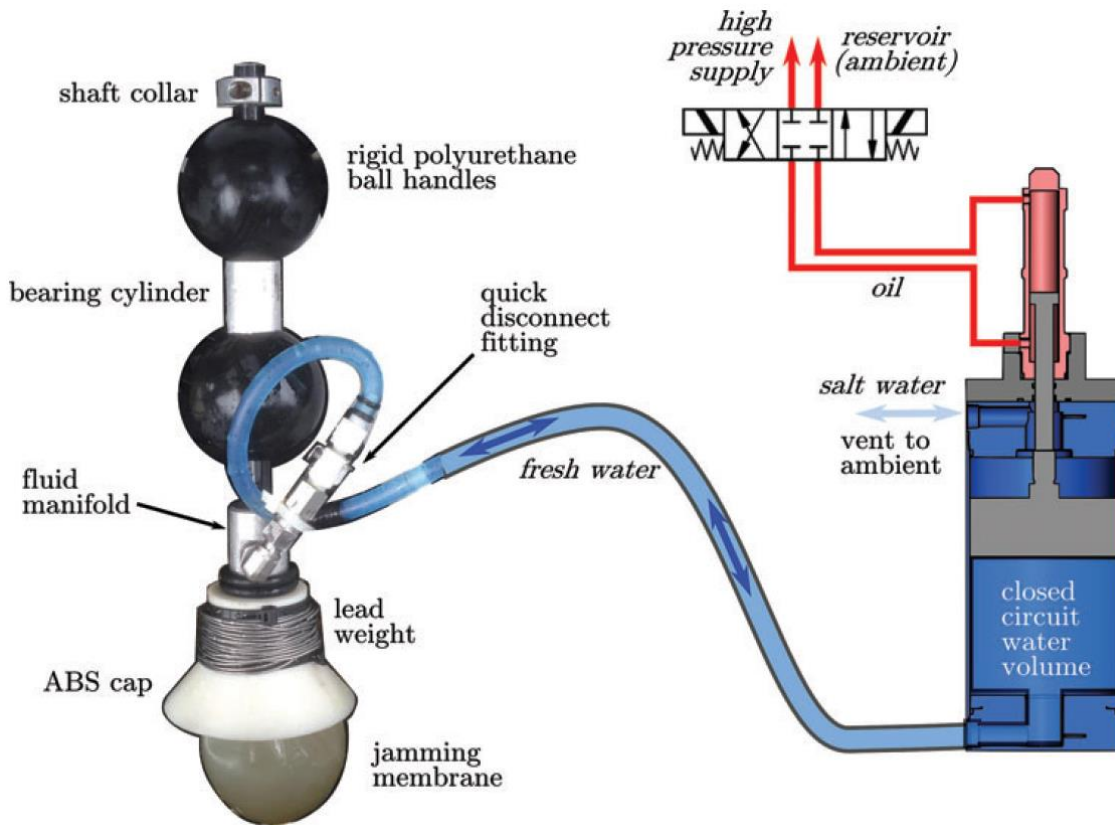
Figure 4. 13. Annotated schematic of gripper apparatus and fluid drive system. Ref: Licht et al. (2017).

The fluid manifold is machined from a 6061 aluminum rod and connects a single inlet-outlet port from the side to an internal cavity bored out from the bottom of the manifold. The bottom hole is covered with a filter (400 x 400 mesh stainless steel woven wire cloth) that allows water flow, but blocks the particles from entering the manifold. The manifold is inserted through the cap (3D printed in ABS using a Stratasys Dimension printer) and then into the neck of a latex balloon (Qualatex 18'' Diamond Clear Round) that is partially filled with 94 g of solid glass beads (Potters Ballotini® 212–300 µ impact beads). The average density of the bead material is 2.5 g/cc, the average density of the packed beads is 1.66 g/cc, and the uninflated volume of the membrane is about 225 cc. The beads are

thus 25% of maximum amount that can be contained without inflating the membrane. A blind threaded hole in the top of the cylinder is used to attach to the gripper handle shaft of nominal 0.5-inch diameter ceramic-coated aluminum.

A three-position four-way proportional valve, which is integrated with an existing 1500 psi oil hydraulic system onboard the ROV, is used to control the high-pressure cylinder. The maximum jamming pressure across the jamming membrane is 58 psi (3.95 atm), resulting from the hydraulic system pressure of 1500 psi and the 26:1 area ratio of the two cylinders. The pilot controls the valve from the surface through manual setting of the solenoid valve pulse width modulation (PWM) duty cycle; fine control of jamming pressure was not possible during the experiments described in this study due to the nearly 10-s latency in valve control and pressure response.

Furthermore, the gripper design includes a linear bearing, which limits the maximum vertical force applied to any sample to the in water weight of the gripper itself. A closed-circuit hydraulic system converts high-pressure, low-volume oil hydraulics to low-pressure, high-volume water hydraulics through an inline cylinder pair.

Laboratory tests

The gripper design was extensively tested using a triaxial load frame (GeoComp LoadTrac-II) with an integrated pressure chamber and flow control system (GeoComp FlowTrac-II) to measure the gripper lifting force. The experimental apparatus is pictured in Figure 4. 14.
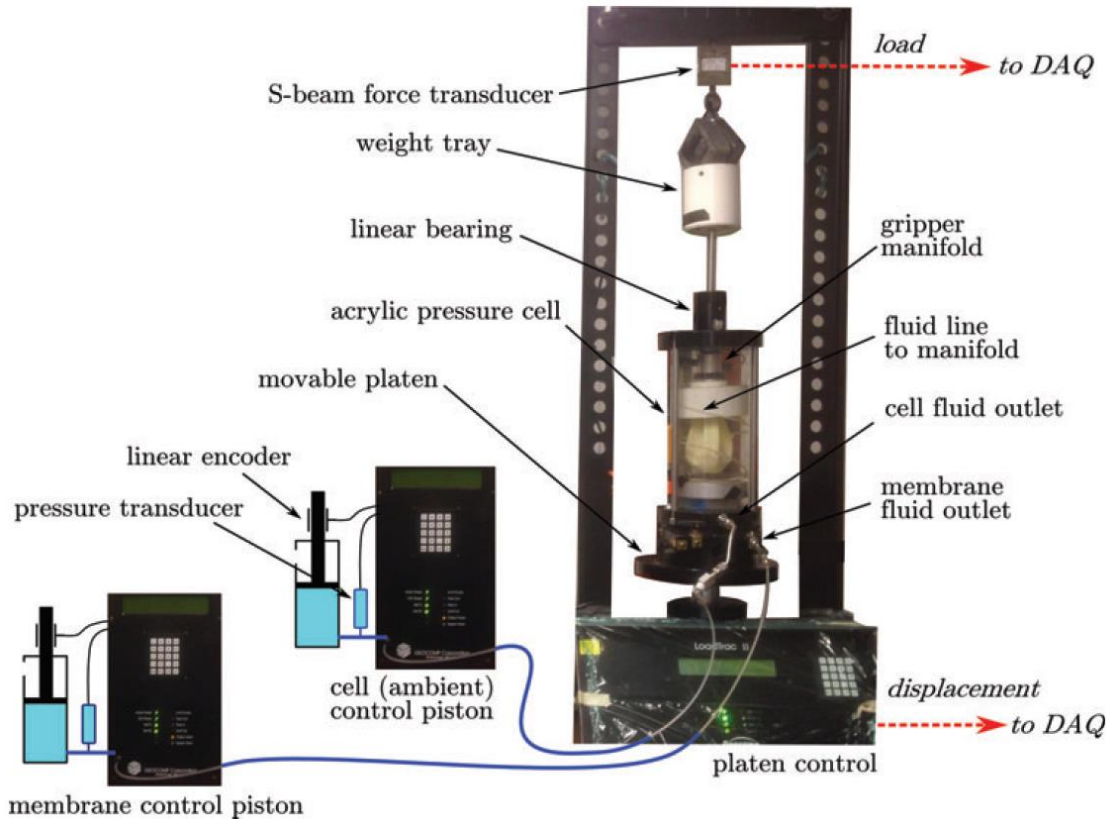
Figure 4. 14. Annotated schematic of bench top gripper experiments in a pressurized water chamber. Ref: Licht et al. (2017).

The pressure chamber is mounted rigidly to the movable platen of the load frame. The platen can follow preprogrammed velocity or force profiles, where force is measured using a single axis S-beam load cell mounted to the load frame above the pressure chamber, and velocity is measured using a spring-loaded linear probe in contact with the platen.

The top cap of the pressure chamber contains a shaft penetration consisting of a linear bearing with a dynamic O-ring seal. The gripper apparatus is contained inside the pressure chamber, supported from above by the gripper handle, which passes through the shaft penetration. Two fluid inputs to the chamber, accessed through fittings in the bottom cap, are connected externally to two independent FlowTrac-II systems, which consist of electrically driven water hydraulic cylinders instrumented for pressure and volume control. One flow control system is plumbed directly to the interior of the pressure chamber and controls ambient chamber pressure. The other flow control system is plumbed to a pass-through, which is connected inside the chamber to a length of flexible

tubing, which is in turn connected to the manifold. The flexible tubing is arranged in a spiral configuration to minimize vertical forcing on the gripper. The fluid circuits are isolated from one another and closed. All fluid used in these experiments is fresh water at room temperature.

A weight tray is mounted to the lower shaft, allowing the weight to be added to compensate for the vertical pressure force resulting from chamber pressures which are higher than the ambient pressure in the laboratory.

The sample object in all tests is a10-mm-long, 10-mm diameter stainless steel tube. The sample was mounted parallel to the surface of the aluminum base plate, with the lower surface held 6mm above the substrate with a 4-40 rod, which was threaded into a blind tapped hole in the center of the length. This sample geometry was chosen to simplify estimates of the downward force applied, eliminating the need for a submersible force sensor to distinguish between loads applied to the sample and the substrate.

For each experiment, as shown in Figure 4. 15, the gripper mechanism is allowed to come to rest on the sample before jamming, and to settle on the sample during jamming, under the weight of the gripper mechanism, shaft, and weight tray. Once the gripper is fully jammed, the shaft is connected to the load cell by a tension member, and the platen is lowered until the jammed gripper loses contact with the sample.

Figure 4. 15. Schematic illustrating motion of gripper and platen during benchtop experiments. Ref: Licht et al. (2017).

In this manner, it's possible to measure the total upward force applied by the gripper to the sample, while ensuring that the downward force applied does not exceed the total in water weight of the gripper and the handle, thus simulating operation at sea. Gripper holding force is calculated as the difference between the maximum load recorded by the load cell, and the load recorded immediately after all contact with the sample is lost, with the platen still in the downward motion.

The two flow control systems are used to independently control pressure and flow inside the membrane and surrounding the membrane. Throughout each experiment, the chamber pressure was regulated by injecting or removing fluid using proportional-integral-derivative (PID) feedback control, with external piston volume as the control input.

The membrane fluid flow is used to regulate either volume or pressure depending on the current stage of the grasping process. Before grasping, fluid is removed from the membrane in pressure regulation mode to achieve a small (10 kPa) difference between internal and external pressure, indicating the start of jamming. A controlled volume of fluid

is then injected in to the membrane to inflate it partially before application to the sample. This initial fluid volume is one of the parameters varied in the experiments described below. All tests are performed with the starting internal membrane pressure equal to the surrounding ambient pressure, as the balloon is never inflated to the point of elastic stretching. Once the gripper is applied to the sample, the gripper is "jammed" by removing fluid from the membrane, regulating pressure to achieve the desired jamming pressure. The result of this first lab test was the gripper lifting force F_L (Figure 4. 16). The gripper lifting force, F_L, was recorded while varying four experimental parameters: system weight in water, F_W, ambient pressure, P_A, jamming pressure, P_J, and initial membrane fluid volume, V_I. A series of 23 experiments were performed. In particular, F_L was recorded as a function of P_J = (30, 60, 85, 170, 255, 340) kPa with P_A = 4 atm, F_W = 5 N, and V_I = 120 mL.
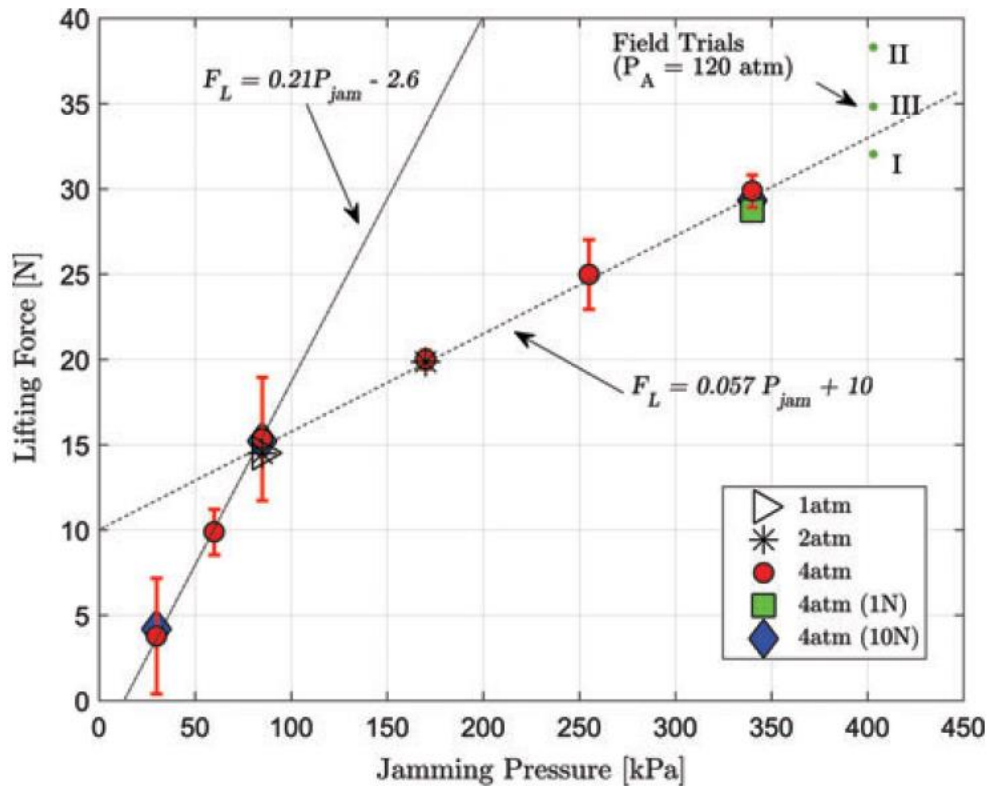
Figure 4. 16. Gripper lifting force, F_L, is shown at six jamming pressures, P_J, where ambient pressure P_A = 4 atm, gripper weight F_W = 5 N, and initial fluid volume V_I = 120 mL. Ref: Licht et al. (2017).

As seen in Figure 4. 16, F_L increases more than threefold, from 3.8 to 15.3 N, when P_J is increased from 30 to 85 kPa. F_L doubles again to 29.9N when P_J is increased to 340 kPa. F_L is clearly dependent on P_J, and exhibits a linear relationship for $P_J \geq 85$ kPa, with the linear regressions shown as the dashed lines. Three experiments were performed at reduced ambient pressures: $P_J = 85$ kPa at $P_A = 1$ atm, and $P_J = (85, 170)$ kPa at $P_A = 2$ atm; no dependence on P_A was found. Four experiments performed with varying water weight $F_W = (1, 10)$ N and three different values of P_J, no dependence on F_W was found. Furthermore, F_L was recorded as a function of $V_I = (40, 80, 100, 120, 140, 160)$ mL, while holding $P_A = 4$ atm and drawing $P_J = 340$ kPa. F_L increased monotonically with V_I as seen in Figure 4. 17.
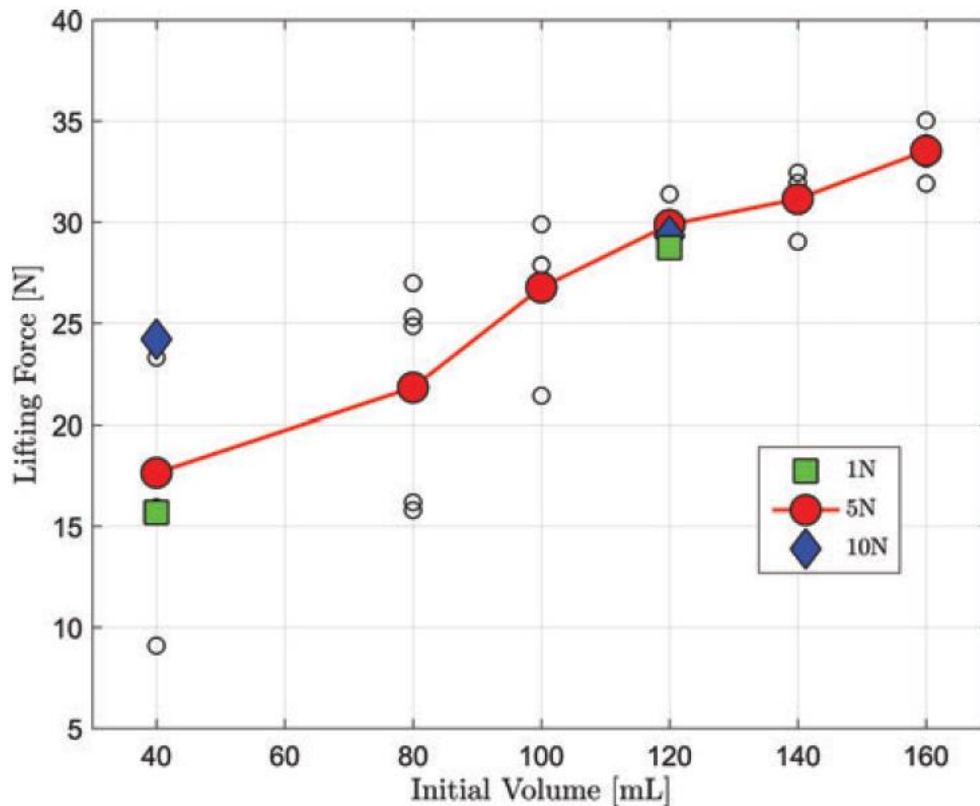
Figure 4. 17. Gripper lifting force, F_L, in function of initial fluid volumes V_I. Ref: Licht et al. (2017).

Images of the membrane at four different stages are shown in Figure 4. 18 for one trial each with $V_I = 40$ and $V_I = 120$mL, resulting in $F_L = 9$ and 30 N, respectively.
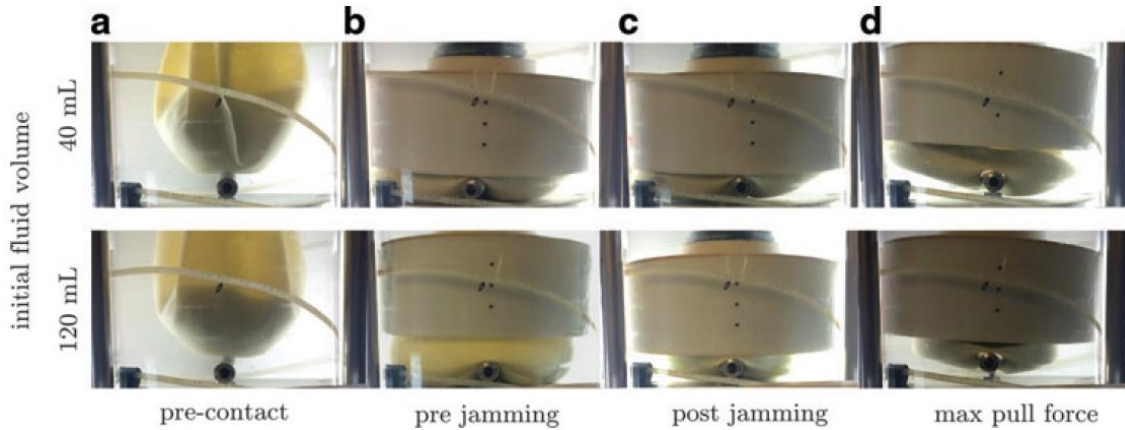
Figure 4. 18. Comparison of the membrane shape during grasp with V_I = 40 and V_I = 120 mL. (a) Just before contact. (b) Before jamming. (c) After jamming. (d) Max pull force. Ref: Licht et al. (2017).

Another extended laboratory trials were carried out to characterize the performance of the gripper, such as the downward forces applied to the object while grasping. To this end, the base plate of the triaxial load measurement was modified to rigidly mounted an A-beam load cell (Futek LSB210), as depicted in Figure 4. 19.
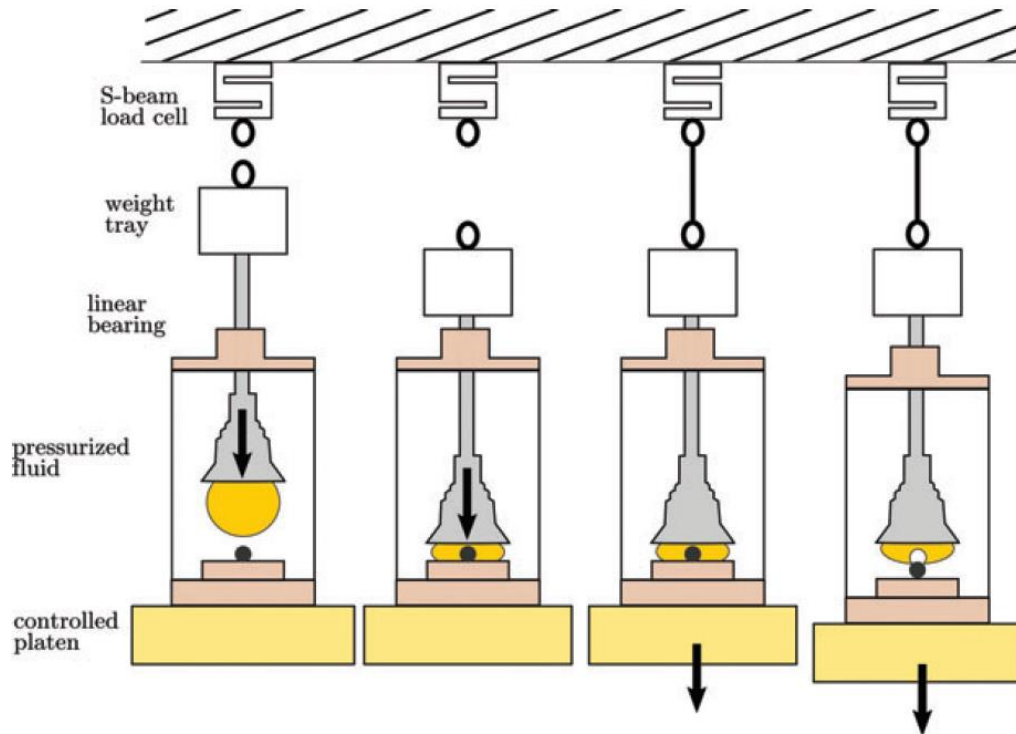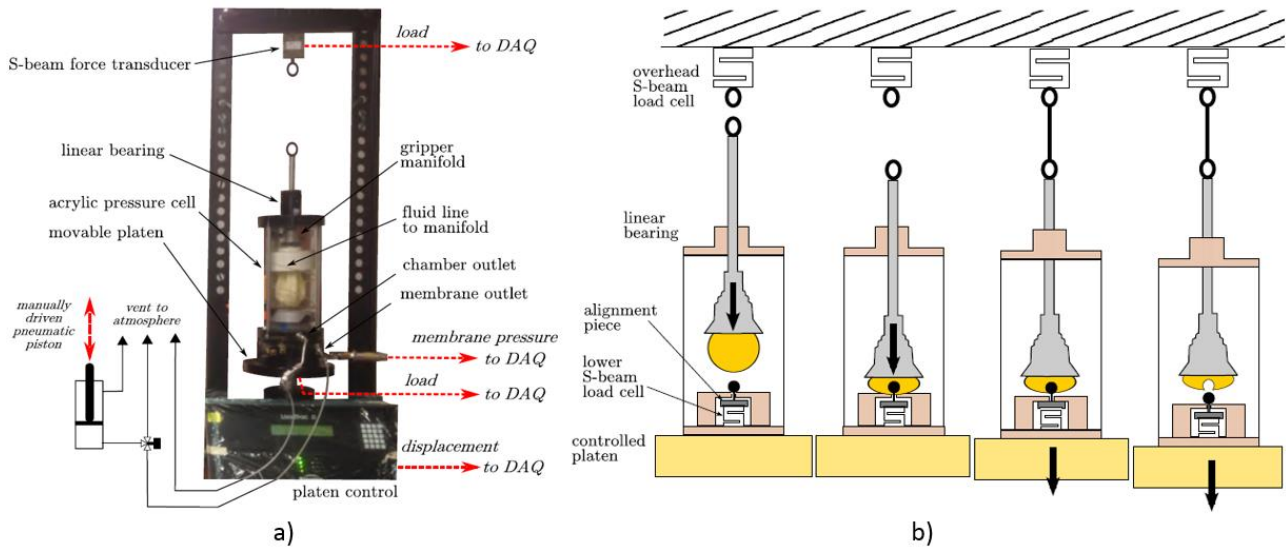

Figure 4. 19. a) Experimental apparatus. b) Schematic illustrating motion of gripper and platen during benchtop experiments. Ref: Licht et al. (2018).

When the target is loaded downward from above, it is mechanically isolated from the base plate, and the load cell measures only the force applied directly to the target. When the

target is lifted off of the lower load cell, the alignment piece immediately makes contact with the top of the cavity, and cannot be lifted any further.

Experiments were performed using three machined aluminum target objects, a 30mm long, Ø10mm cylinder held horizontally 6mm above the base plate, a 16mm long, Ø20mm cylinder held vertically with the bottom surface 1mm above the base plate, and a 1mm thick, Ø20mm disc held with the axis of rotation vertical and the bottom surface 6mm above the base plate.

The total uninflated volume of the membrane, defined as the maximum volume at which the membrane is not elastically deformed, is approximately 225mL. Experiments were performed with glass beads nominally filling 25%, 50%, and 100% of the uninflated volume by packed volume of glass beads. The density of the packed beads is 1.6g/cc. It has been defined the particle volume fraction, V_p, as the fraction of the membrane uninflated volume occupied by the packed particles, such that $V_p = 0.25$, 0.5, or 1.0. Furthermore, has been defined as initial volume fraction, V_i, such that V_i is the fraction of the membrane uninflated volume occupied by particles and fluid prior to jamming. V_i was varied between 0.25 to 1.45.

The gripper is shown for three cases in Figure 4. 20, with V_p = (0:25; 0:5; 1:0) and corresponding V_i = (0:47; 0:72; 1:22).
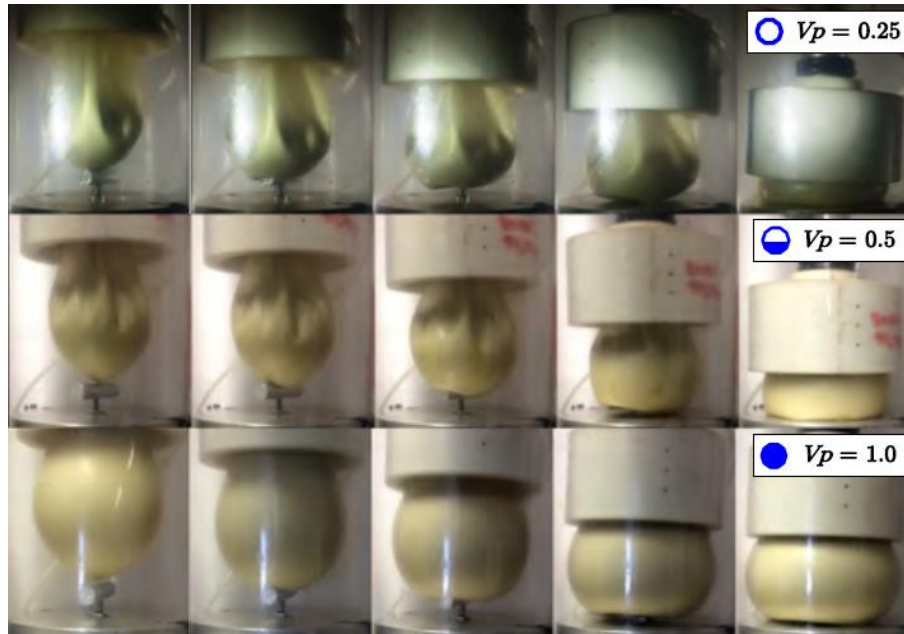
Figure 4. 20. Image sequences (left to right) from trials with the membrane 25% (top), 50% (middle), and 100% (bottom) full of jamming particles, and initial volume fractions (air + particles) Vi = 0.47, 0.72, and 1.22, respectively. Ref: Licht et al. (2018).

Prior to each experiment, the air was drawn out of the membrane until a non-zero vacuum pressure was observed across the membrane, after which 10mL of air was introduced to fully unjam the particles. Air was then introduced to the membrane from this zero datum point to set V_i prior to jamming.

The ratio of maximum lift to maximum support force as a function of V_i, and the maximum support force as a function of V_i, are shown for all three targets in both solid and vented configurations in Figure 4. 21.
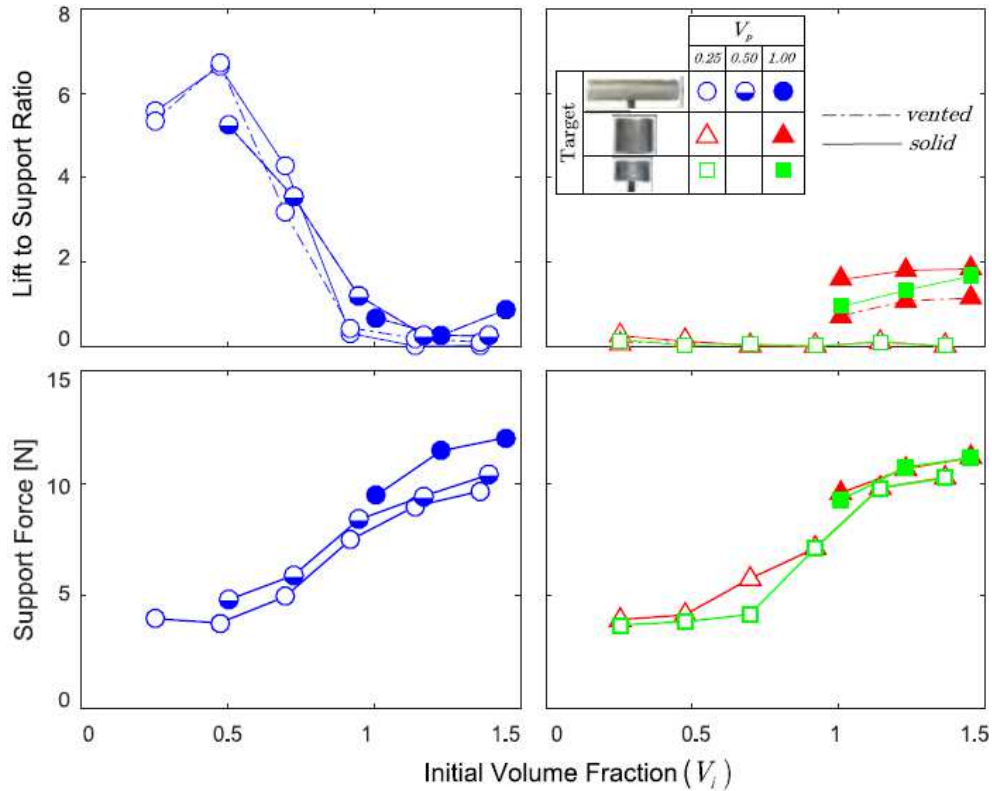
Figure 4. 21. Experimental results for all target configurations. For clarity, the rod results and the cylinder/disc results are shown separately; scaling is maintained to allow direct comparison. Ref: Licht et al. (2018).

The rod, cylinder, and disc targets are represented by the circle, triangle, and square symbols, respectively. Particle fractions V_p = 0.25, 0.5 and 1.0 are represented by empty, half filled, and solid color symbol. The gripper achieves an interlock grip on the horizontal rod for lower initial volume with the partially filled membrane. The gripper achieves a combination of friction and suction grip on the cylinder and disc for higher initial volumes with the fully filled membrane.

The maximum gripper lifting force and the corresponding force required to support the target from below are compared for all trials with the three solid targets in Figure 4. 22.
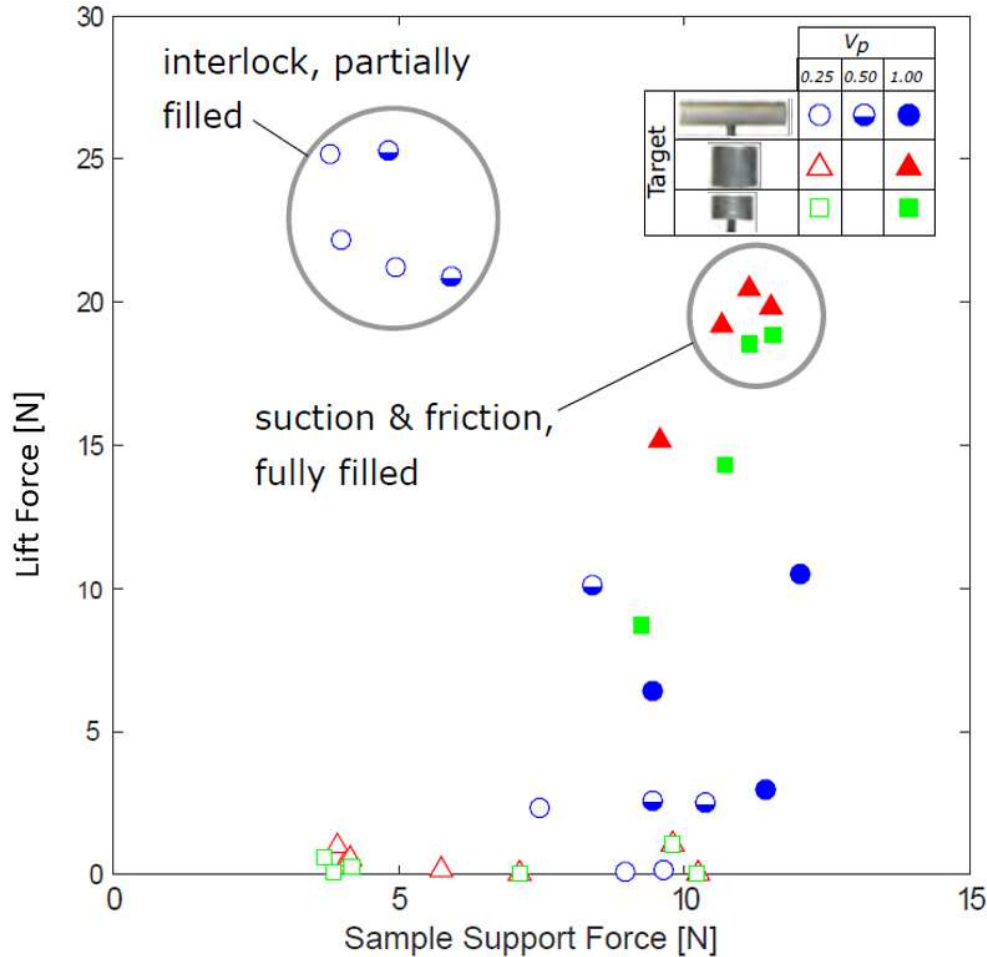
Figure 4. 22. Lift and support forces are compared for all trials with the three solid samples. Ref: Licht et al. (2018).

For the problem of sampling fragile objects resting on both hard and soft support surfaces, it is critical to minimize the support force required while the gripper is lowered on to the sample and to maximize the lifting force that can be achieved when the gripper attempts pickup. From Figure 4. 21, it is clear that the ratio of the lift force (grasp strength) to the required support force is strongly dependent on the total initial volume fraction, V_i, and the particle fill fraction, V_p. However, that relationship is qualitatively different for the different target shapes.

The clearest result is that interlock grasp on the high aspect ratio rod target is much stronger for lower initial membrane volumes. In fact, when the membrane is only 25% full of particles, it can achieve a lower initial volume while still providing enough structure to the jammed shape to achieve a strong grasp.

Furthermore, has been highlighted that the target aspect ratio affects whether interlock can be achieved. In fact, the disc and rod targets have identical thickness and height above the base plate and present comparable cross-sectional areas and perimeters from above. Despite these similarities, the partially filled membrane easily achieves an interlocking grip on the rod but fails to achieve an interlocking grip on the disc.

Finally, optimal particle volume depends on the target type. When an interlock grip is possible, very high lift forces are achieved with very low support forces using a partially filled membrane. Where suction and friction are the primary grip modes, the highest lift forces can be achieved with a fully filled membrane, but this comes at the cost of large support forces. The two scenarios are illustrated in Figure 4. 22.

Field tests

In July 2016, the R-CUE team were able to deploy the gripper prototype on the ROV Hercules (Figure 4. 23) during the E/V Nautilus (www.nautiluslive.org/tech) field campaign at the Southern California Margin, operated by the Ocean Exploration Trust. A Kraft Predator 7-DOF hydraulic arm with a rigid pincer end effector is used for all physical sampling tasks.
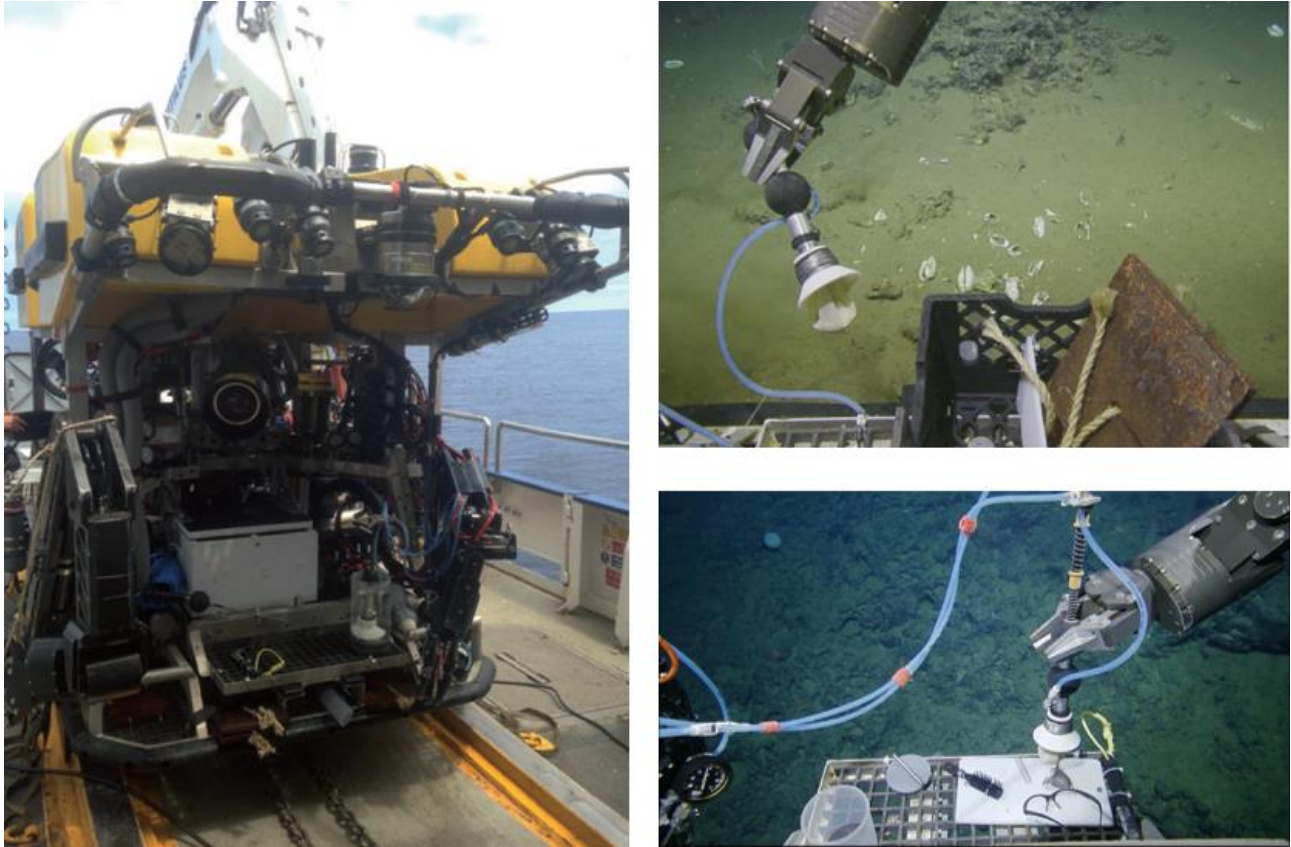
Figure 4. 23. (left) ROV Hercules stored on deck prior to dive. (upper-right) Image of the gripper held by the manipulator, captured from the main camera view used by the ROV pilot. (bottom-right) Image capture from operator video taken during testing of gripper on four objects resting on the 'front porch' of the ROV at a water depth of 1200m. Ref: Licht et al. (2017).

Two 2.5-inch-diameter rigid polyurethane balls are mounted on the cylinder bearing handle to give the manipulator pincer a secure grasp, depicted in Figure 4. 23 (upper-right). Four objects were brought with the ROV at the depth of 1200m as test samples (Figure 4. 23 bottom -right), a hairbrush, bell, pair of safety glasses, and a steel spring. Each of these objects was successfully grasped and lifted off of the plastic sheet (hard surface) with the partially filled gripper. Furthermore, has been possible to pick up targets of opportunity for biological research activity lying on a soft substrate, such as a clamshell depicted in Figure 4. 23 (upper-right).

For this study, the R-CUE team was able to perform a modification to the gripper to allow in situ measurement of the lifting force, using the target rod object from the laboratory experimental program described above. The stainless steel rod sample target was mounted on a flat polyvinyl chloride (PVC) disc on the front porch of the ROV Hercules.

Two stainless steel linear compression springs were installed on longer gripper handle shaft, between the shaft collar and the linear bearing as pictured in Figure 4. 24a.

The ROV manipulator was used to lower the gripper on to the sample from above, and then fluid was removed from the membrane to jam the gripper. The ROV manipulator was then used to raise the bearing cylinder. Each of the spring in series was compressed by the combined force of the gripper weight and the vertical force applied by the sample on the gripper. Gripper strength, F_L, was measured by using the maximum length change in the lower spring when compared with the length of the spring under the gripper weight alone. The linear spring constant, k, for the lower spring was found to be k = 0.60 N/mm during testing before deployment. The deformation of the upper spring cannot be used as it is clearly compressed beyond the linear compression range. The vertical length of the upper plain bearing was taken as a reference length of 25.4mm (1.0 inch), to account for changes in camera view angle. The experimentation is depicted in Figure 4. 24.
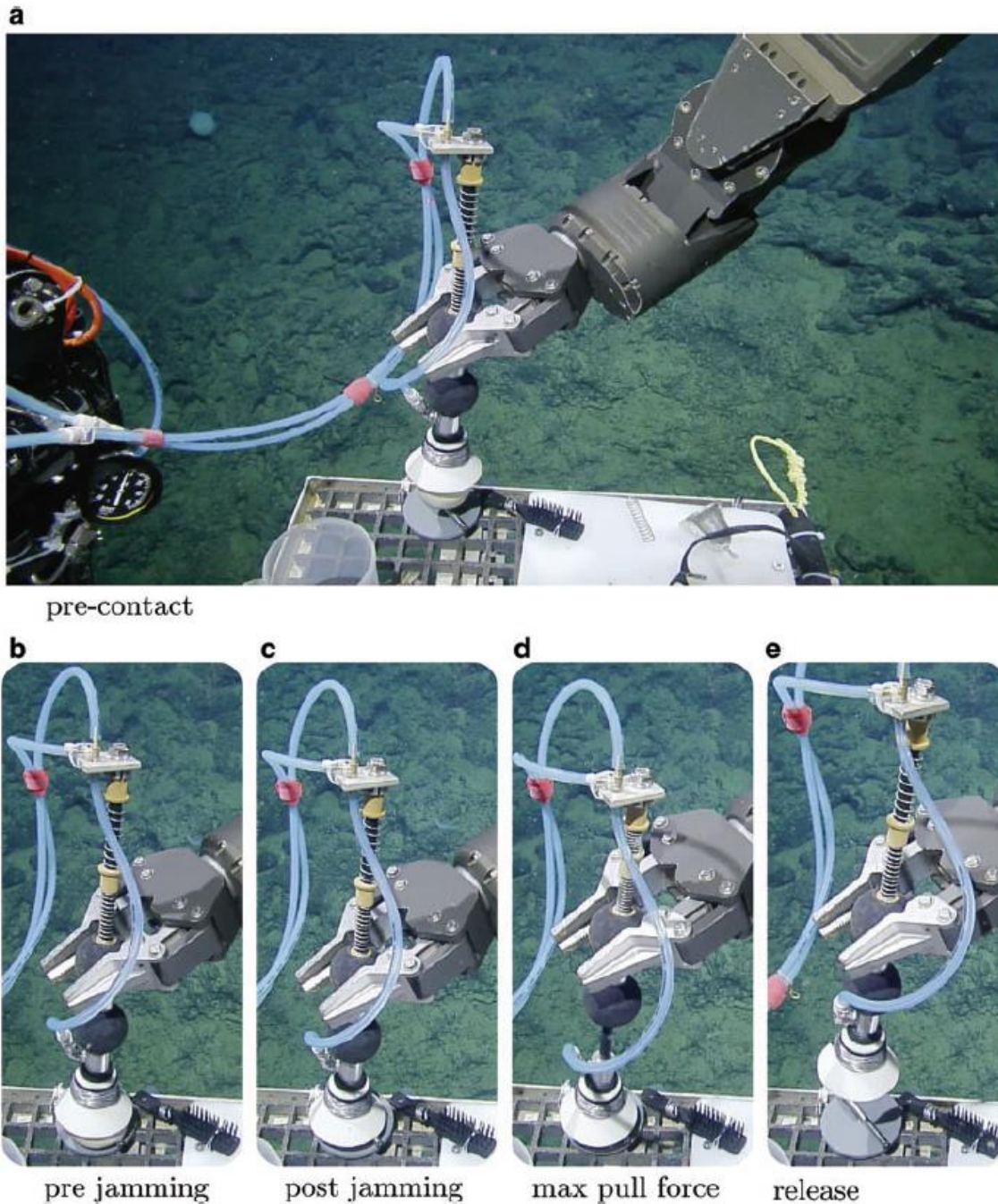
Figure 4. 24. Estimation of maximum lift forces were derived from video frames captures showing compression of the lower spring. Ref: Licht et al. (2017).

Three trials were performed on this target with the ROV at a depth of 1200 m, that is, with an ambient pressure >120 atm. Arm motion was manually controlled, resulting in motions that were not perfectly vertical. All operations were performed by the same ROV pilot in an attempt to maintain consistency in speed and accuracy. The estimated vertical forces

are 32, 38, and 35N for trials I, II, and III, respectively. An image showing the typical shape of the gripper immediately after grip failure is shown in Figure 4. 25.
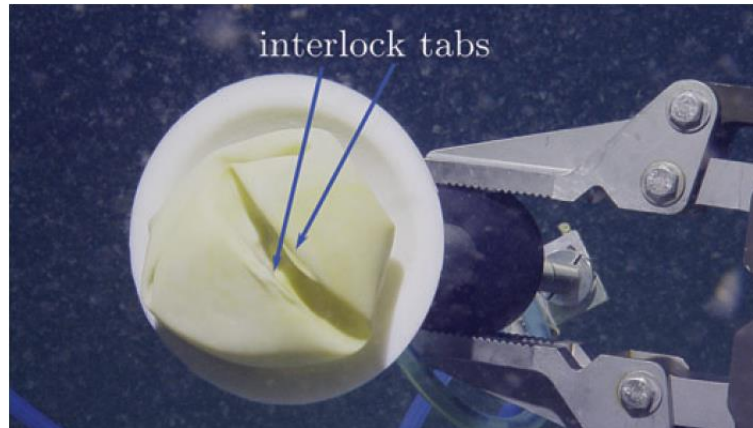
Figure 4. 25. Jammed gripper shapes immediately after pulling free from the sample rod during tests at depth on the ROV Hercules. The formation of the tabs indicates that interlock was achieved. Ref: Licht et al. (2017).

4.2.2. Integration of the gripper with Hydro-Lek arm

The main purpose of my internship research at URI was to complete the integration of the soft gripper with the existing arm, design and perform experiments with the gripper in the water tank, and propose refinements to the design of the mechanical and hydraulic system.

At the start of the design process, the designer is usually faced with a very poorly defined problem. In fact, before carrying out analyses and evaluations of the design proposal, the problem requires first to be understood and clarified.

The system consists of three main parts: the soft gripper, the arm, and the hydraulic system placed on the skid of the ROV. These parts must be connected and integrated between them to work together. The state of the art and the design evolution of the universal soft gripper has been investigated in section 4.2.1. In particular the last version of the gripper is depicted in Figure 4. 13. The existing arm is a commercial 5-function HLK-43000, manufactured by Hydro-Lek ltd. In particular, the wrist of the arm is the HLK-21020 Mini 180°, that integrate a rope cutter tool. Currently, the arm is mounted on the skid of the Saab SeaEye Falcon DR ROV owned by URI (Figure 4. 26). The manipulator skid is equipped with two manual valve to enable fine regulation of the inlet/outlet oil flow of one DOF of the arm, 3 pilot check block valves to ensure a positive hydraulic lock when the manipulator is not being operated, a bi-directional valve, and a 4-way valve pack.
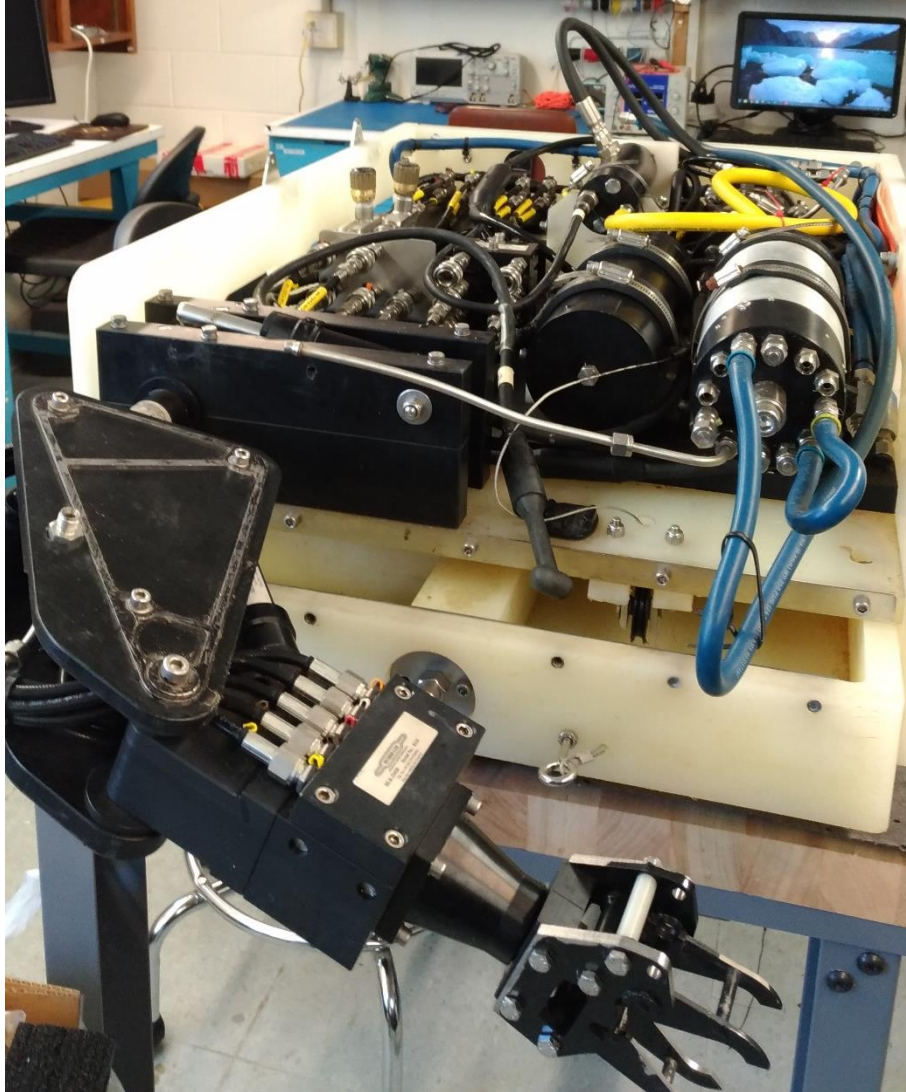
Figure 4. 26. Hydro-Lek HLK-43000 with the rope cutter tool mounted on the skid of the Saab SeaEye Falcon DR ROV.

Theoretically, the first solution should be to handle the soft gripper using a rope cutter of the arm, as shown in Figure 4. 24. The problem is that the movement of the arm is too jerky and inaccurate in order to manipulate and carry out a good performance of the gripper. Furthermore, the first attempt of this integration between the two system has been depicted in Figure 4. 11, denoting different problems regarding the possibility to control the direction and rotation of the gripper while picking up objects, and secondly due to low-detailed mechanical construction, with backlash and disassembling problem while the gripper is in use. For this reason, has been necessary to investigate other solutions

that would allow setting directions to the gripper and a more accurate mechanical design, representing the functional requirements of the design process. To this end, a proof exploration of the mechanical design of the wrist of the arm is required. In the cross-section of Figure 4. 27 is depicted the internal components of the wrist of the arm. In particular, the rack (in orange) meshes with the gear wheel of the cylinder (in green) generating the rotation, inside which the piston flows (in red) hydraulically actuated.
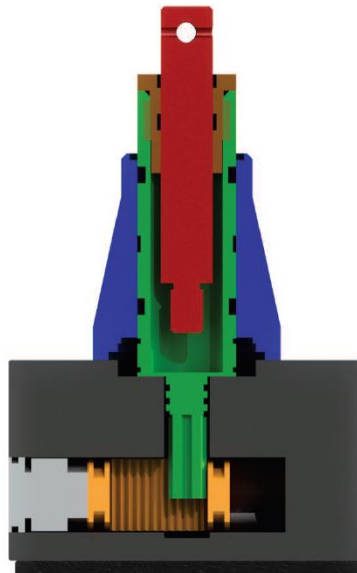
Figure 4. 27. Cross-section of the wrist of the arm.

The excursion of the piston is 28.8 mm, with maximum and minimum elongation of 40 mm and 11.20 mm respectively. The diameter of the piston is $\emptyset\ 16,00^{0}_{-0.12}$ mm. At the distance of 8.20 mm from the end of the piston, there is a drill hole of $\emptyset\ 6,00^{0}_{-0.05}$ mm, that is used with a pin to create the opening/closing mechanism of the rope cutter tool.

The original rope cutter tool of the arm can be removed, trying to modify the continuous jaw rotate mechanism and the excursion of the piston to create a pan-tilt system which handles the soft gripper. Different drawing solutions were generated, with the general idea to connect the two system with a four-bar linkage, as depicted in Figure 4. 28.
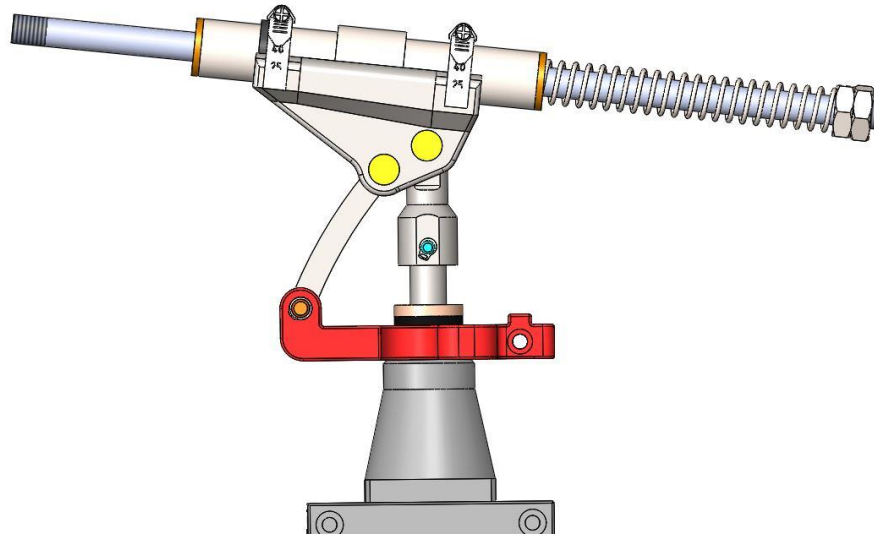
Figure 4. 28. First CAD model of the proposed solution.

The base of the model (component in red) is clamped around the cylinder of the wrist of the arm using an open carving section and a screw, to allow the gripper to rotate integrally with the rest of the structure. The gripper can be attached at end threaded side of the rod. The spring is used just to consider the future opportunity to measure the lifting force in the trials. The proposed solution has been optimized in order to get a tilt angle of about 45 degrees and simplified in function of the actual technology available in the laboratory. The final solution of the pan & tilt mechanism is depicted in Figure 4. 29.
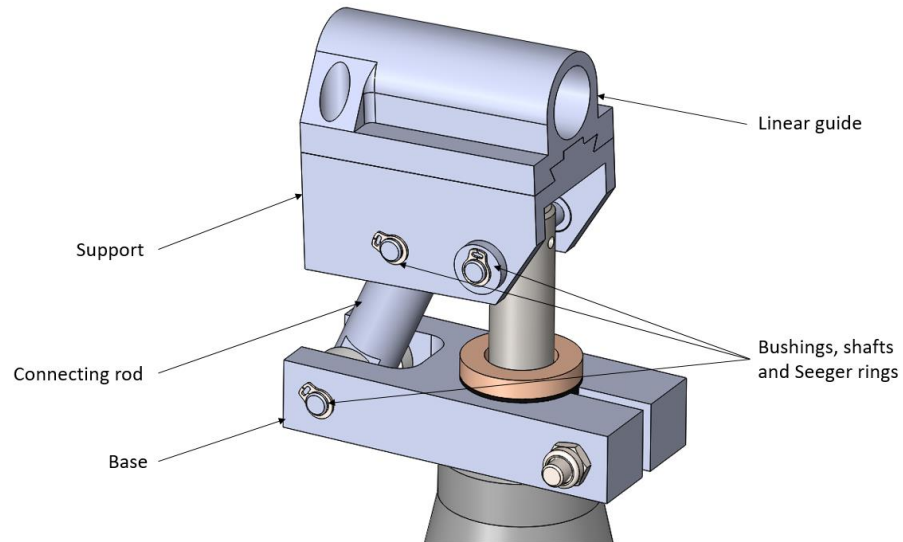
Figure 4. 29. The CAD model of the Pan & Tilt mechanism mounted on the wrist of the arm.

In particular, the pan & tilt mechanism is composed of:

- Base;
- Support;
- Linear guide;
- Connecting rod;
- Bushings, shafts and Seeger rings.

The connection between the Support and the Linear guide is performed thanks to the adoption of a linear guide, giving the opportunity to change quickly the end-effector for future development. To avoid the axial sliding between them there are designed a slope and two screws. The angle of work of the tilt movement is about 45°, as shown in Figure 4. 30.

Minimum piston excursion   Maximum piston excursion
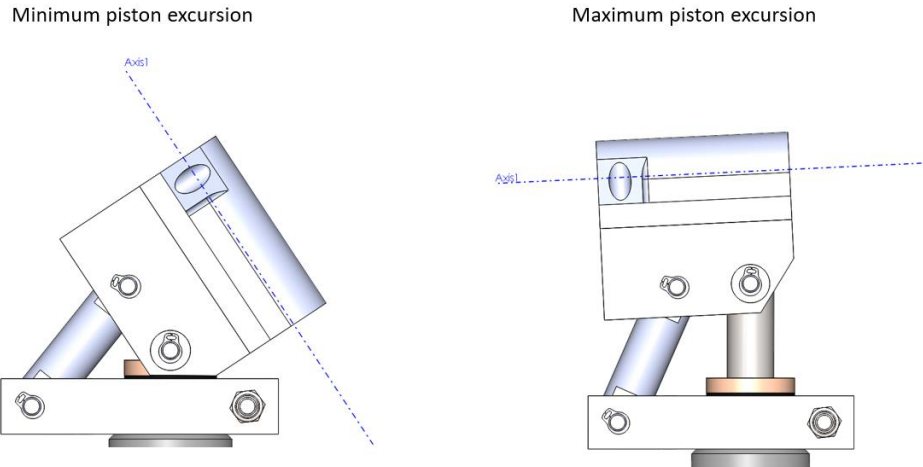
Figure 4. 30. Tilt movement due to the piston excursion.

Therefore, a wrist mechanism created for this effort enables a 45-degree wrist pronation along with full wrist rotation, as illustrated in Figure 4. 31.
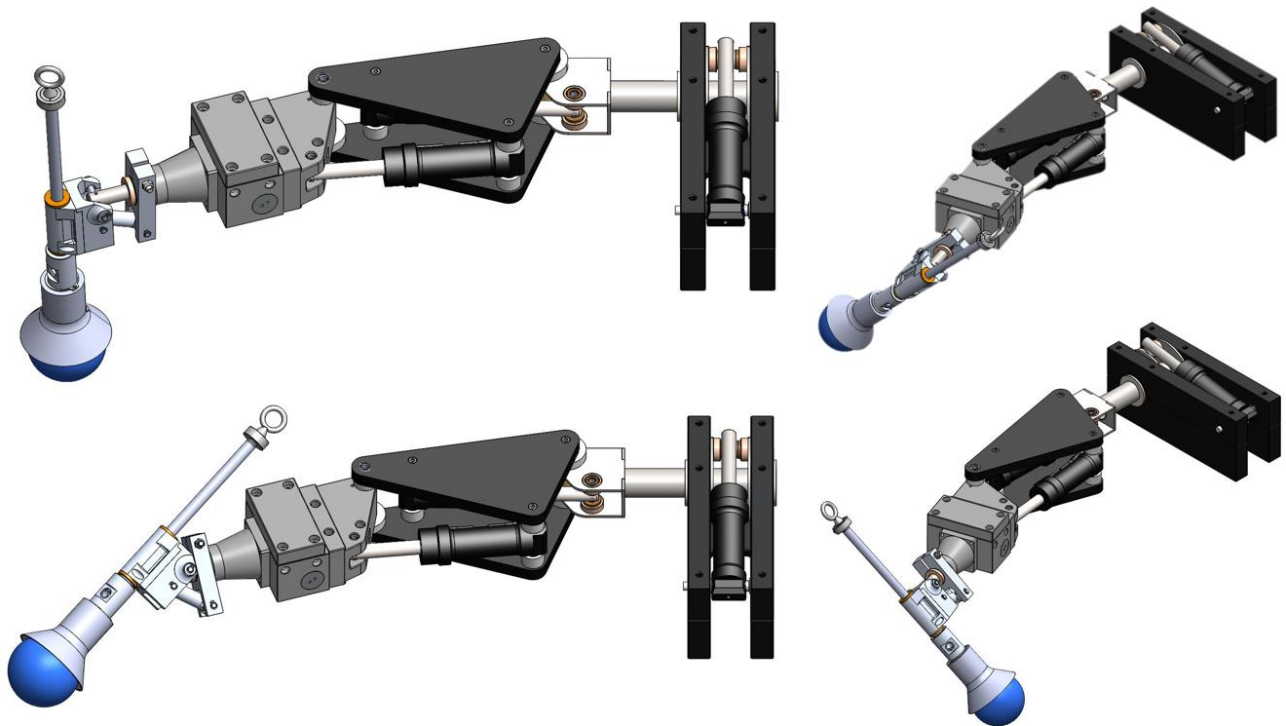
Figure 4. 31. The gripper was mounted on a Hydro-Lek 5-function arm, with the wrist degree of freedom actuated as shown.

Using a common FDM 3D printing with 1.75 mm ABS filament, the components of the pan & tilt mechanism have been prototyping. While, bushings, shafts, and Seeger retaining rings have been bought using McMaster-Carr platform. The result of this phase is depicted in Figure 4. 32.
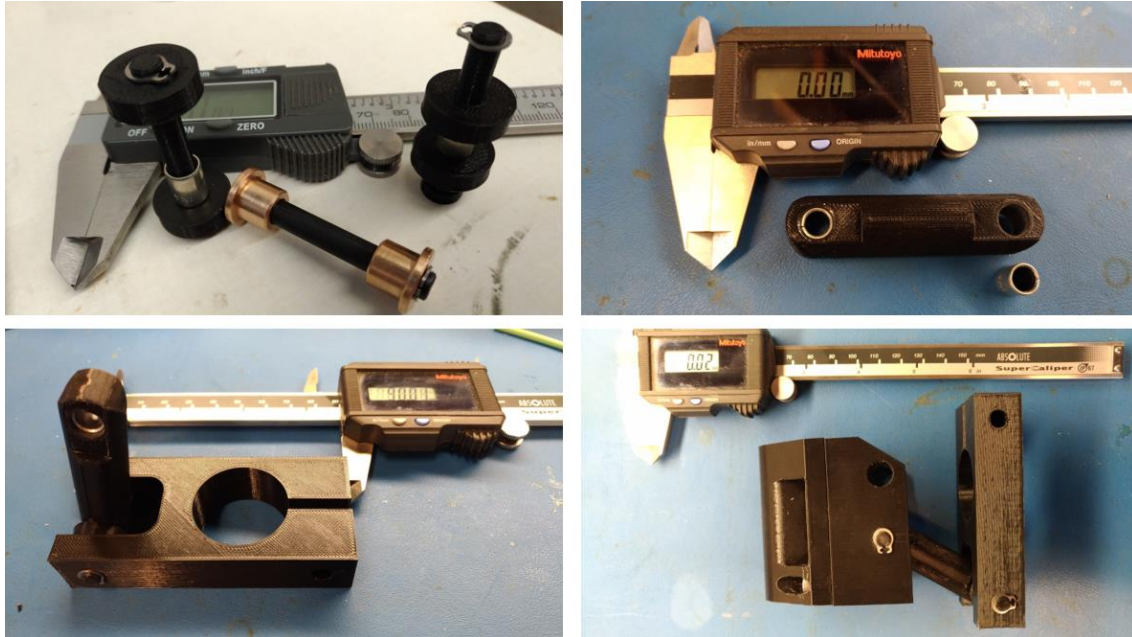
Figure 4. 32. The assembly phase of 3D printed and commercial components of the pan & tilt mechanism.

The soft gripper was connected to a commercial hydraulic stainless steel cylinder. The fluid drive system consists of a 127-mm bore stainless steel water-filled cylinder (TRD Manufacturing, RS Series) and a 25-mm bore oil-filled cylinder (Hydro-Lek 11060). The piston rods of the two cylinders are concentric and directly connected end to end.

The gripper connected with the hydraulic system has been assembled on the pan & tilt mechanism mounted on the arm, in turn, placed on the skid of the Saab SeaEye Falcon DR ROV (Figure 4. 33).
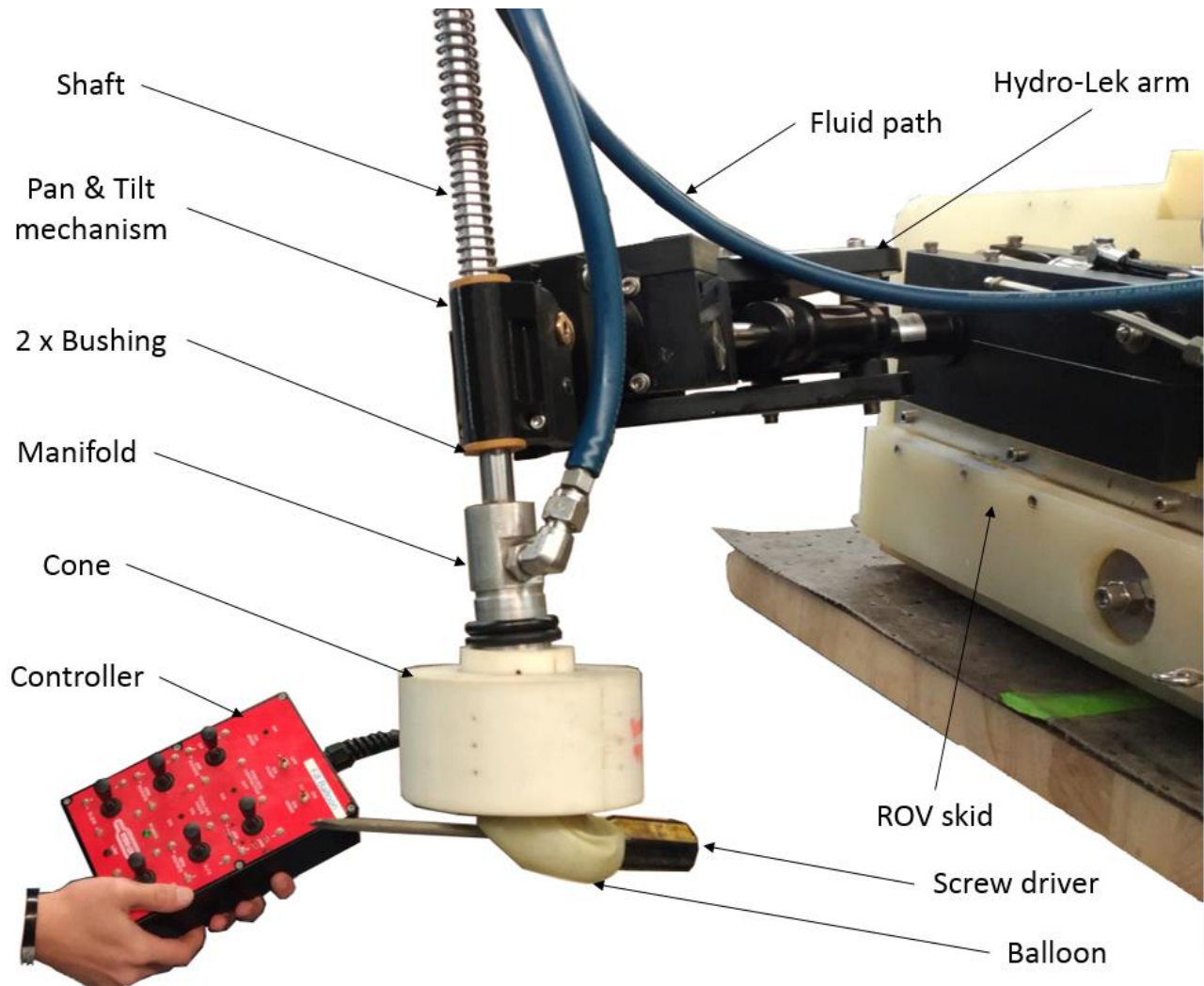
Figure 4. 33. Assembled soft gripper mounted on the Hydro-Lek arm, pictured while grasping objects (screw driver).

The system has been extensively tested on the air in order to get familiarity with the prototype of jamming gripper and grasping tasks as well. This phase was important also to understand both the procedure to approach the object to ensure a secure grasp, that the type of objects easily to being manipulated.

4.2.3. Underwater recovery of objects resting on the soft substrate

To test the findings in practice, the partially filled gripper was used underwater on a variety of objects resting on sediment and on foam. Given the results of the bench top experiments described in the Laboratory tests, has been selected a range of demonstration objects with relatively high aspect ratios and/or long edges, with a major dimension larger than 80% of the gripper diameter, as shown in Figure 4. 34.

Figure 4. 34. Objects used in demonstration. (a) weighted hair brush (b) lightbulb (c) metal spring (d) lightbulb (e) wine glass (f) wine glass (g) shell (h) weighted GoPro housing (i) shell (j) plastic safety glasses (k) clam shell.

Two types of tests were performed. Manual tests were performed in a large plastic bin filled with water, and robotic tests were performed fully submerged in a 1.5m deep water tank (Figure 4. 35).

Figure 4. 35. Preparation of the wave tank for the trials at the URI.

The manual test is a less stringent test of grasping, as the operator holding the handle bearing can precisely adjust the position of the gripper throughout the test. For the robotic tests, the gripper was mounted on a Hydro-Lek 5-Function hydraulic arm. Before start with trials is necessary check the functionality of the whole system (mechanical, hydraulic, electrical, and control). This arm has no force feedback, and only one degree of freedom can be actuated at a time. Based on past experience, failure to grasp in the manual test uniformly indicates failure on the more difficult robotic arm test. Success in the manual test is not always replicated in piloted arm tests.

Partially filled gripper

The partially filled gripper was demonstrated using the robotic test. The operators viewed the experiment through the forward video camera of a VideoRay Pro3 micro-ROV (Figure 4. 36). Furthermore, all tests were filmed using a GoPro3 camera in a waterproof housing.
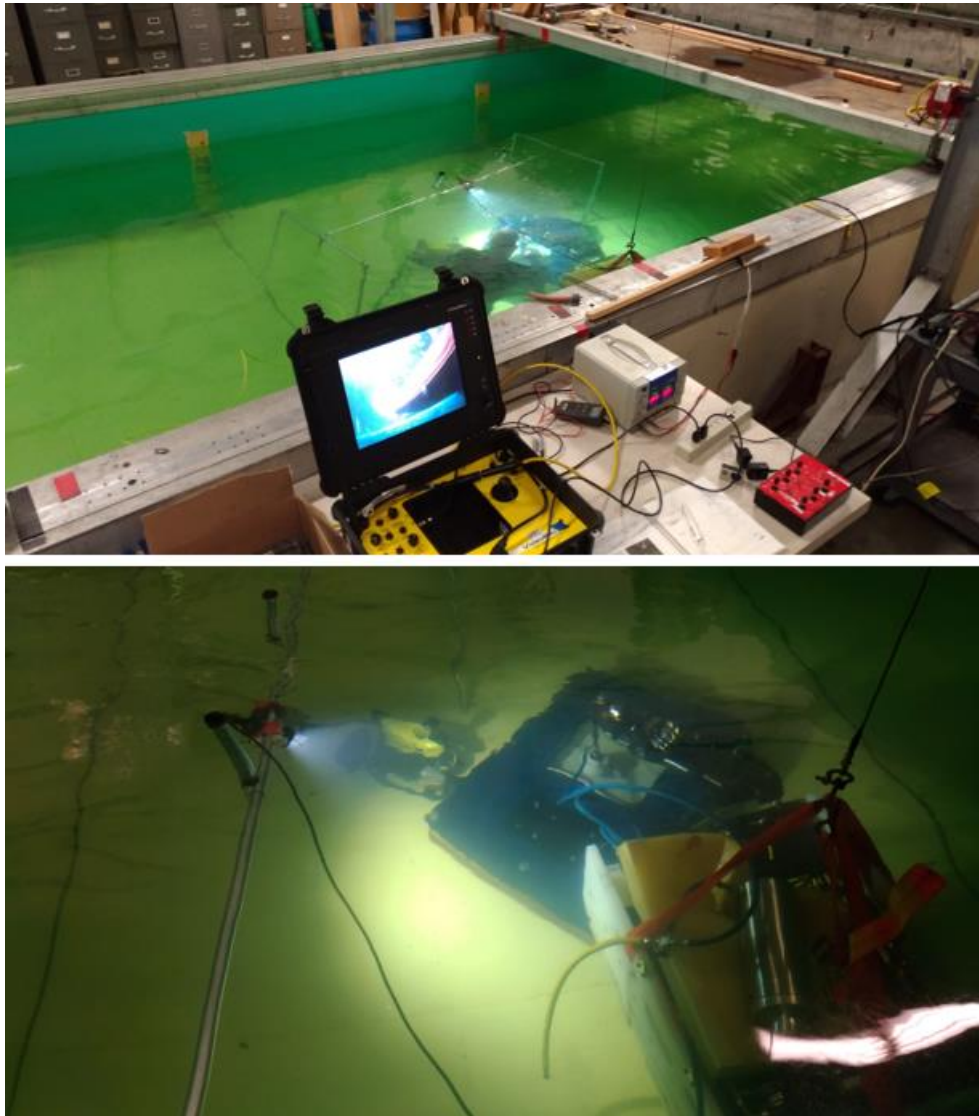
Figure 4. 36. Experimental set-up in the water tank.

The trials lasted about two weeks, with about 500 minutes of video to analyze.

In the first, a 10cm deep sandbox (filled with 200μ glass beads) and rigid plastic board are placed within the arm workspace, and in the second the sandbox and a 15cm thick piece of memory foam are used, as shown in Figure 4. 37.
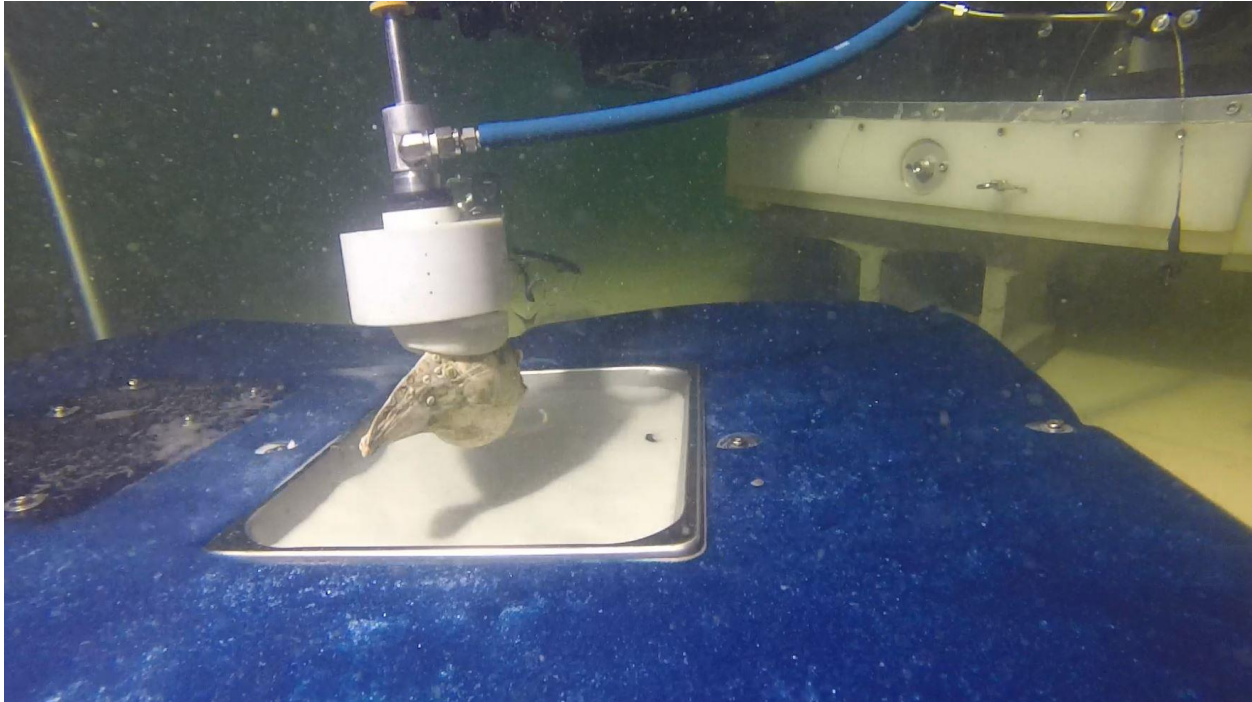
Figure 4. 37. VideoRay operator point of view. Homemade base with memory foam and the sandbox. Meanwhile, the gripper is picking up a big shell.

Furthermore, after two days of failed tests it was necessary to set a procedural protocol to carry out the trials, investigating a single movement of the arm, the gripper and the state of the particle inside the balloon. In particular, the sequence of operations is reported as follows:

– Place the object to pick up in the sandbox;

– Start experiment with the arm closed;

– Jam the particle inside the balloon (using the foam as support);

– Open the arm using just the joint 2 (the movement must to be parallel to the base);

– Orient the gripper using pan & tilt mechanism and other joints of the arm;

– Approach the object with the balloon in jammed state (Figure 4. 38a);

– Fill the balloon before contact (2-5 cm above the object - Figure 4. 38b);

- Wait a time necessary to cover the object under the weight of the gripper (Figure 4. 38c);

- Jam the particle inside the balloon (Figure 4. 38d);

- Lift the object (Figure 4. 38e);

- Close the arm above the foam;

- Lower the gripper;

- Release the object, filling the balloon (Figure 4. 38f);

- Repeat the experiment recollecting the object on the foam versus the sandbox.

Figure 4. 38 gives a clear demonstration of the above mentioned procedure to carry out the trials, while collecting a GoPro housing.
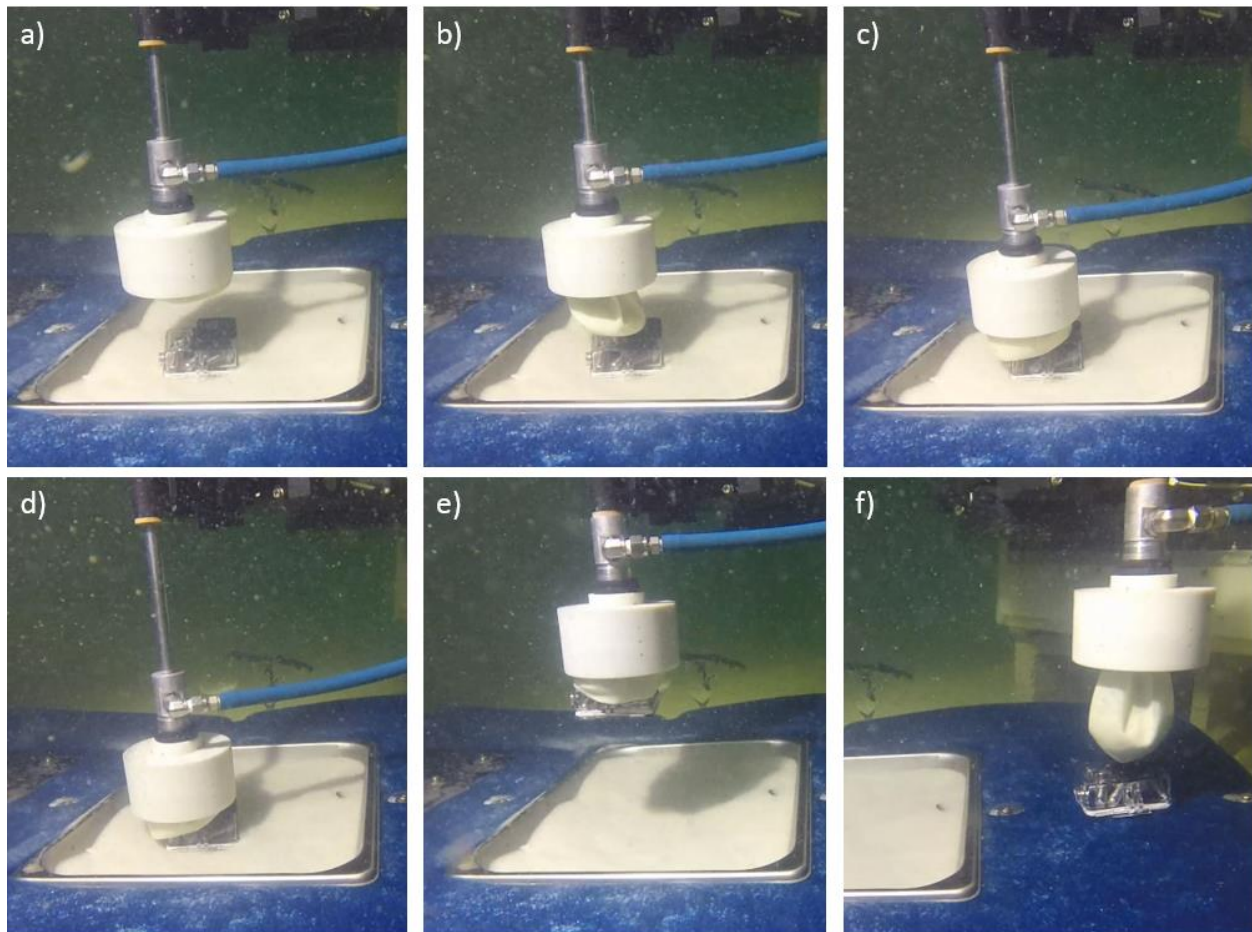
Figure 4. 38. Procedural protocol to carry out the trials. a) Approach the object with the balloon in jammed state; b) Fill the balloon before contact (2-5 cm above the object); c) Cover the object under the weight of the gripper; d) Jam the particle inside the balloon; e) Lift the object; f) Release the object on the foam.

Figure 4. 39 shows several views of the two configurations of the robotic experimental apparatus. In particular, thanks to the adoption of the Pan & Tilt mechanism, the arm was able to orient the gripper vertically above any object within the workspace of the arm, prior to releasing the gripper to fall vertically onto the target under its own weight.
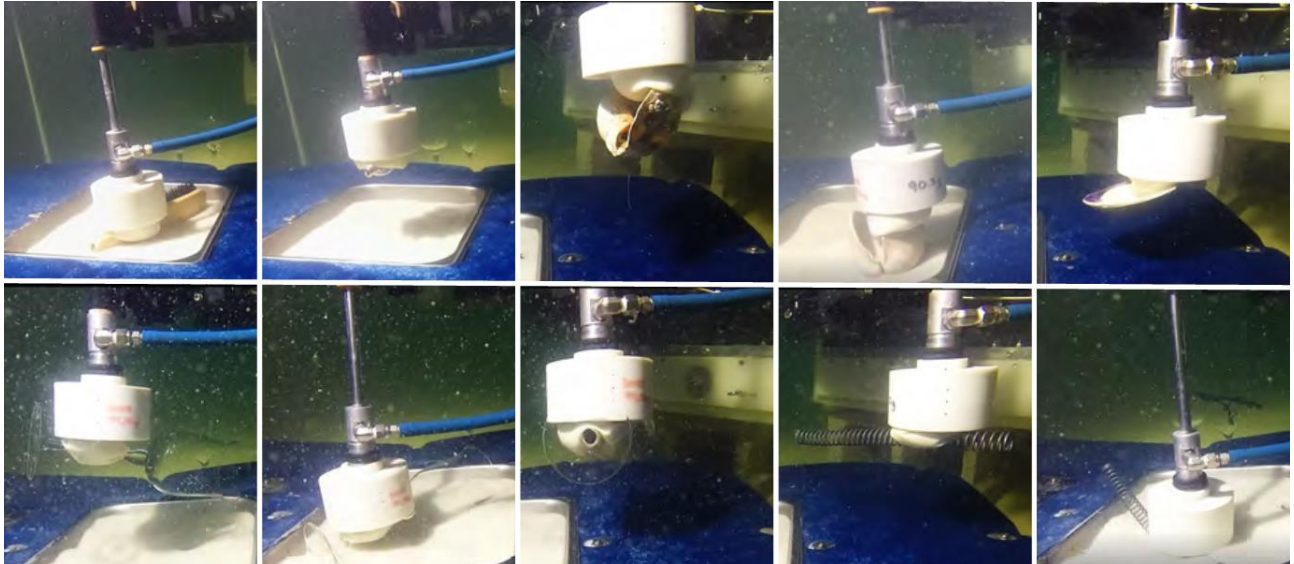
Figure 4. 39. Representative images demonstrating robotic operation of partially filled gripper on various objects resting on soft sediment and foam. The failure mode for the only unsuccessful grasp is shown in the bottom right figure.

All of the objects shown in Figure 4. 34 were successfully picked up from foam, sediment, and hard plastic, with the sole exception of the metal spring, which could not be retrieved from the sediment. The metal spring settled into the sediment underneath the gripper with each attempt, likely due to the very low contact area to resist burying. No object (other than the spring) required more than three attempts to grasp on sediment or foam. Grasp failures were observed to be due to the uncontrolled manner in which the membrane draped over the objects. With the partially filled membrane, the failed attempts did not push the objects any farther into the sediment than the successful attempts, and thus did not preclude subsequent successful grasp attempts.

Fully filled gripper

To verify that the partially filled membrane succeeds where the fully filled membrane would not, the gripper was also manually tested in the fully filled configuration. When attempting to grasp each of the target objects on soft sediment, the fully filled gripper only succeeded with the larger lightbulb (object d in Figure 4. 34). As predicted in the bench top tests, this was the result of achieving a suction grip on the smooth glass surface, despite pushing it almost entirely into the sediment. When attempting to grasp the target objects on foam, the gripper was able to grasp this light bulb and the two wine glasses (by the stems) when resting on the foam.

The failure modes were a combination of (a) failure to adequately conform to the object shape to achieve interlock and (b) pushing objects into the sediment until the gripper was in contact with the sediment itself, as seen in representative screen captures in Figure 4. 40.

Figure 4. 40. Images demonstrating typical failure mode when attempting to grasp object on soft sediment with a fully filled gripper. Successful grasp was only achieved on object d, as shown in the lower three frames.

163

In conclusion, the ability to grasp irregularly shaped objects resting freely on soft sediments and compliant surfaces is highly desirable for marine archaeologists attempting to sample fragile objects. In this trials, we demonstrate that a partially filled jamming gripper, submerged and mounted on a robotic arm, is capable of picking up objects freely resting on sand and foam. The partially filled gripper was capable of picking up a wide range of objects from sand and foam that could not be picked up by the fully filled gripper. The fully filled gripper was observed to fail by pushing objects down in to soft supporting substrates, while the partially filled gripper draped over and surrounded the objects without exerting enough force to push them into the substrate.

4.3. Hybrid toroidal soft gripper

4.3.1. Previous work

The growing interest in soft robotics involved the R-CUE team research to focus on various alternative prototypes of the universal gripper for further possible applications in the deep sea. The term "hybrid" is referred to the ability of the system to combine the mechanism of traditional rigid manipulator claws with the jamming compliant gripper mechanism. This led to the idea of developing a hybrid prototype of the soft gripper.

The first two concepts design of hybrid grippers are depicted in Figure 4. 41, developed for the Saab ROV/Hydro-Lek arm (a) and for Hercules ROV/Predator arm (b).
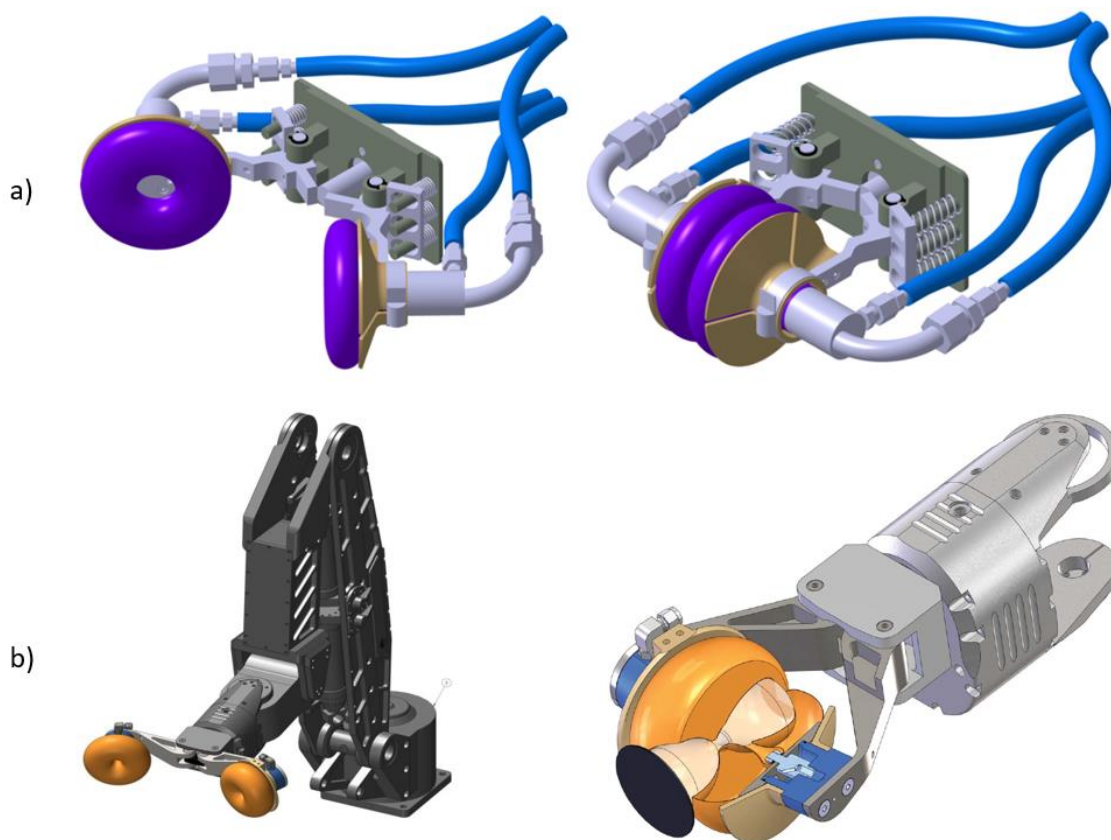
Figure 4. 41. The CAD models of the Hybrid gripper developed for Saab ROV/Hydro-Lek arm (a) and for Hercules ROV/Predator arm (b). Source: Pr. Licht.

With a quick mockup in the lab, the first prototype for the Hydro-Lek arm has been realized and tested in the air (Figure 4. 42).
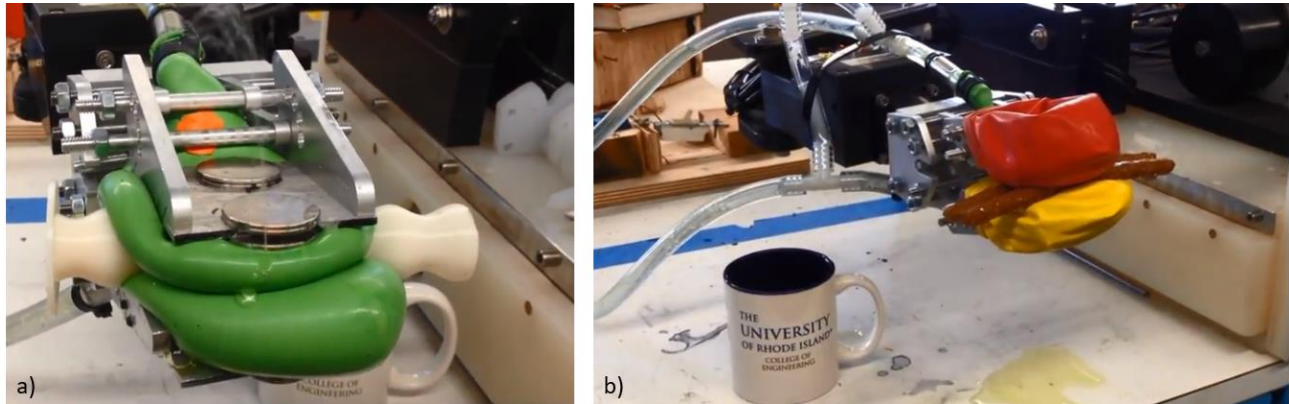
Figure 4. 42. Air trials. a) ABS plastic wavy cylinder. b) Pretzel rods. Source: Pr. Licht.

The hybrid gripper thought for Saab ROV/Hydro-Lek arm was originally designed for coral sampling, using the small volume created by the toroidal shape to insert a fluid such as RNA buffer to help to preserve samples after collection. Basically, what the hybrid gripper demonstrated is that it is possible to use two toroidal jamming pads to grasp irregular, fragile and brittle objects with a hydraulically actuated system without the need for active force sensing.

The gripper was redesigned and prototyped for the purpose to carry out extended trials at the sea. To this end, a design requirement was to create a multi-output low-pressure drive that integrated with the hydraulic arm sled for the Hydro-Lek drive (Figure 4. 43) and designed a passive force limiting gripper apparatus using springs with two jamming pads for deployment (Figure 4. 44).
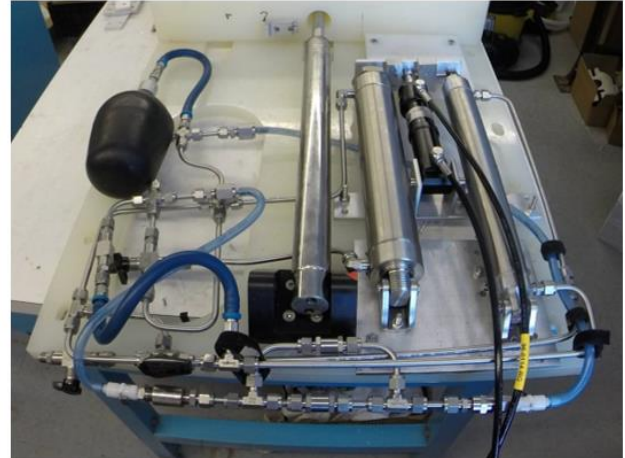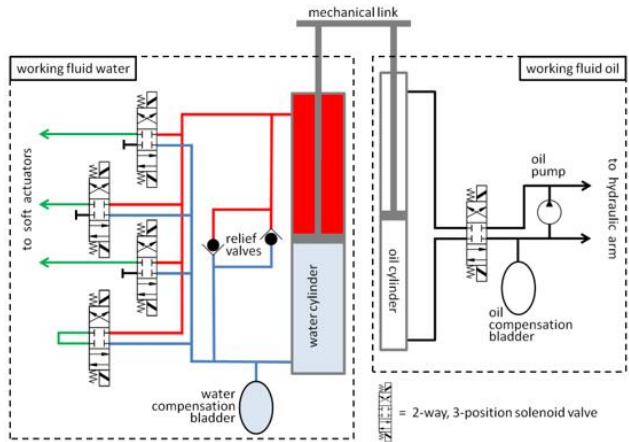
Figure 4. 43. Multi-Channel Low-pressure drive. Source: Pr. Licht.

In fact, if the gripper utilizes both a spring mechanism and filled balloons it becomes capable of limiting passively the total force applied by the pincer.
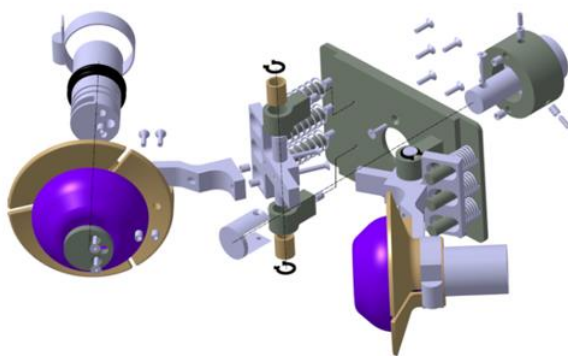
Figure 4. 44. Design and prototype of the gripper. Source: Pr. Licht.

The latest updates developed on the gripper had two opportunities to get involved in deep-sea trials with the system on loan from CUNY (The City University of New York) Baruch College and Harvard University working on a 200 meters' deep coral reef in Israel (Figure 4. 45), and with the Inner Space Center at URI working from the UNOLS ship Endeavor succeeding to collecting a clam for 50 meters (Figure 4. 46).
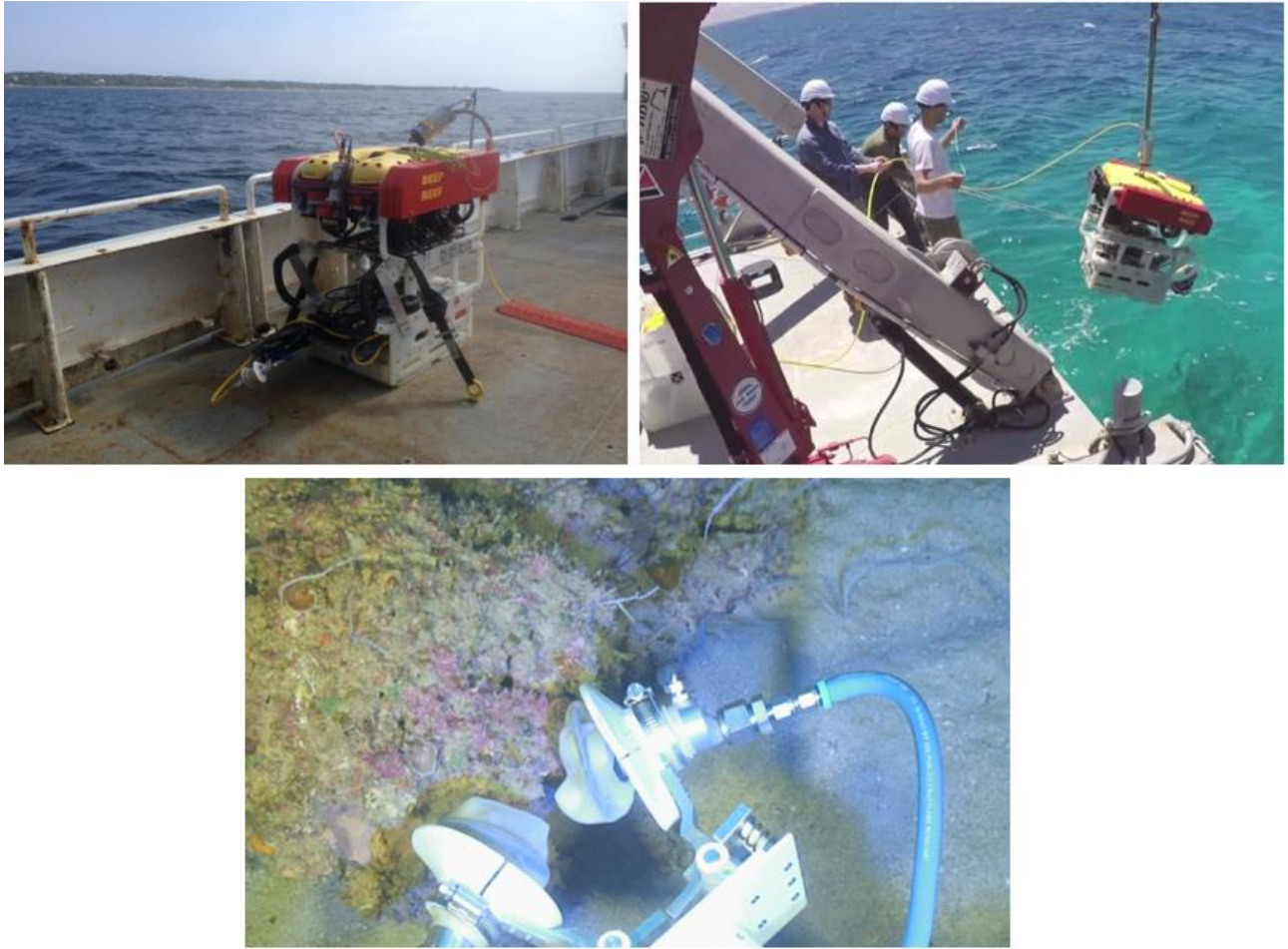
Figure 4. 45. Trials at 200 meters' deep coral reef. Source: Pr. Licht.
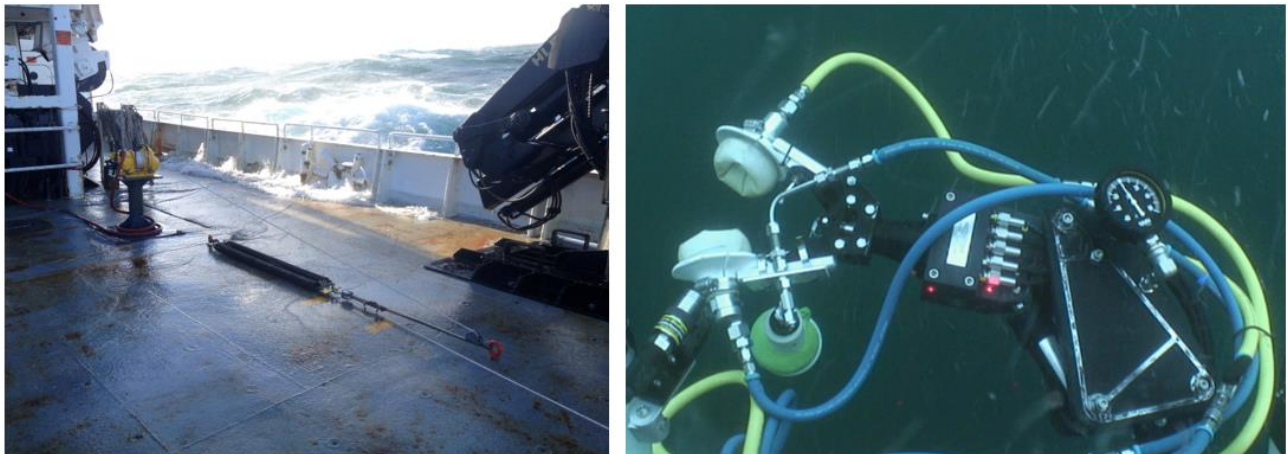
Figure 4. 46. Deep sea trials in exciting conditions off the coast of Rhode Island, and visibility of approximately one meter. Source: Pr. Licht.

Many problems were pointed out on the grippers pad during the previous expeditions. The system connection between the cone and manifold was being assured by the compression of the cone with a hose clamp. This was not an optimal solution since the driving mechanism of the gripper was attached to the cone. The force of movement generated by the driving mechanism was causing the detachment of the cone and manifold.

On previous design iterations, a holding plate had been installed to shape the balloon so that the gripper could keep the same initial shape independently of the orientation. This holding plate was also being used as a surface to glue the filter. Nevertheless, whenever the cone moved because of the driving mechanisms forces and the lack of good assembly with the manifold, the granular material would go in between the holding plate and the cone, nor being therefore useful for jamming anymore. Installation of the holding plate was very difficult because of its size. In fact, because of its purpose to shape the balloon the holding plate had to be near to the same size as the balloon largest radius, the problem is that it had to be introduced through the collar of the balloon, which is very small and may shear often even though it has good stretching proprieties.

The donut or toroidal shape had to keep to the creation of a cavity to allow the introduction of RNA (Coral DNA) fixation chemical (a substance that fixates the RNA so it is not lost when the coral is removed from its position) for coral samples. Better sealing was needed around the donut shape to avoid leakages since the balloon had to be cut to create a space for the RNA agent to pass through. The fluid connection was being welded again with rubber cement, making them irreversible. Finally, this design configuration made the manifold extremely long, which increased the gripper overall size.

These considerations lead the R-CUE team to develop a new concept of the gripper pad. Furthermore, in order to get a potential funding, the function of the hybrid gripper has slightly changed. In fact, instead of sampling corals, the gripper's first mission would now be to grasp degraded metal aircraft components. And depending on the project, the gripper may be mounted on the ROV Hercules equipped with Predator 7 function arm and tested at USS Independence wreck where aircrafts are still lying quite undamaged. The final design for the hybrid toroidal gripper is shown in Figure 4. 47.
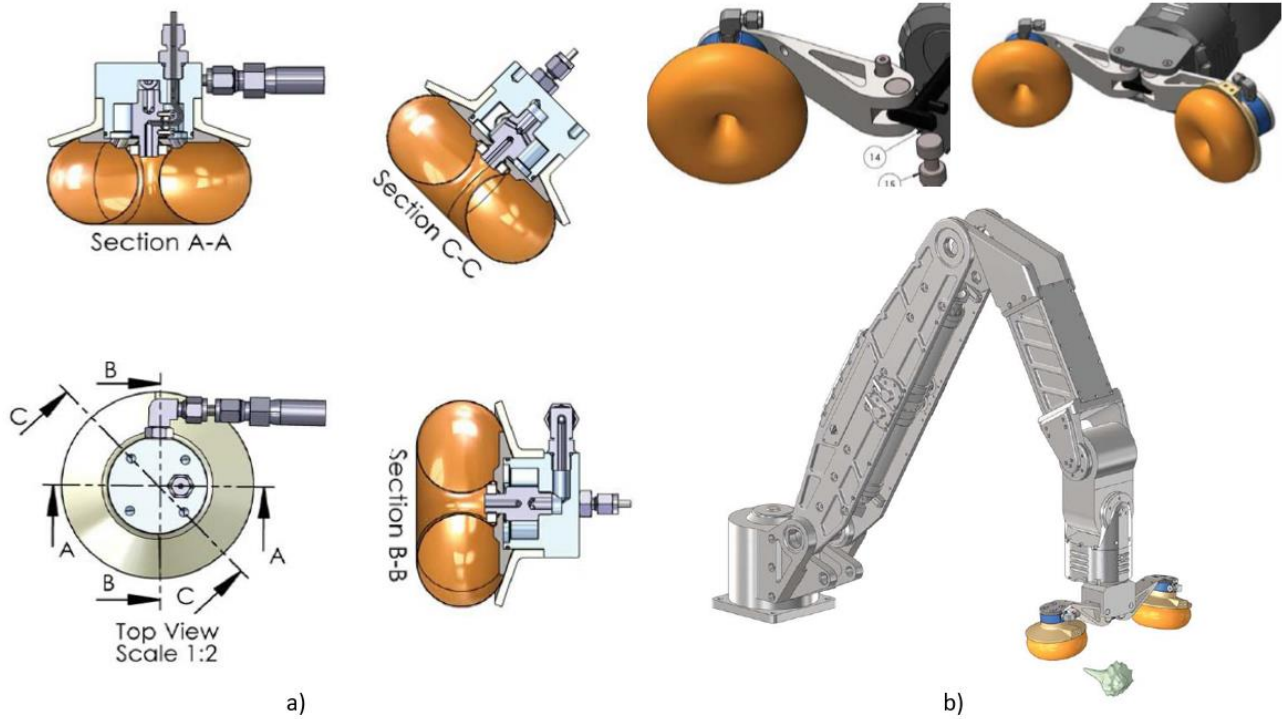
Figure 4. 47. a) Hybrid gripper pad. b) Integration with Predator Arm. Source: Pr. Licht.

Due to the change of gripper's mission, the RNA buffer solution was no longer needed and the design had to be modified accordingly. The latest version of the gripper was prototyped, taking advantage of the low cost of 3D printing, and qualitatively tested in the water tank (Figure 4. 48).

Figure 4. 48. Prototyping and qualitative testing of the gripper. Source: Pr. Licht.

History of USS Independence

USS Independence CVL-22 was launched in 1942 in Camden, New Jersey and commissioned by the Navy in early 1943 (Figure 4. 49). Independence was among the class of carriers created by converting cruiser hulls.

Figure 4. 49. USS Independence CVL-22 with the aircraft on deck.

After completing training in the Caribbean, she sailed through the Panama Canal and joined the Pacific Fleet in San Francisco. She participated in crucial training exercises in Pearl Harbor and later sailed with fellow carriers Essex and Yorktown to raid Marcus Island to destroy the majority of installations on the island. Independence followed up this success through a similar operation against Wake Island in 1943. Independence continued her attacks, finding success in shooting down six Japanese planes. After refueling at Espiritu Santo, she continued on to the Gilberts and completed strikes on Tarawa. The Japanese launched a counterattack on Independence. She was attacked by aircraft that shot torpedoes. One of the torpedoes hit her and caused serious damage. She returned to San Francisco in early 1944 for repairs.

Independence continued to serve missions designed to destroy the enemy. When it became clear that the Japanese were not launching counterattacks, she shifted to regular day-type duties and provided night-time reconnaissance duties where needed. She further played important roles in missions in the Philippines and Okinawa. After the war,

she helped transport veterans home from the Pacific theatre. Her distinguished service during World War II earned her eight battle stars. After her valiant service during WWII, Independence served as a target vessel during the atomic bomb tests on Bikini. Though she did not sink from the blasts, she did sustain damage and was studies for radioactive exposure. She was decommissioned and sunk off the coast of the Farallon Islands on 29 January 1951.

In 2009 the position of the wreck of Independence in 2,600 feet (790 m) of water in the Monterey Bay National Marine Sanctuary off the Farallon Islands at approximately 37°30′00″N 123°05′00″W was confirmed. In March 2015, scientists and technicians of the U.S. National Oceanic and Atmospheric Administration (NOAA) embarked aboard the sanctuary vessel R/V Fulmar used the autonomous underwater vehicle Echo Ranger to make a survey of the wreck, employing the Echoscope three-dimensional imaging sonar to make a series of images of it. The wreck is resting upright with a slight list to starboard and most of the flight deck intact, although there are gaping holes in the flight deck leading to the hangar deck below it. No signs of radioactive contamination were detected, and an NOAA spokesman described the wreck as "amazingly intact."

In 2016, a mission led by Pr. Robert Ballard, deep-sea oceanographer, a faculty member at Ocean Engineering and GSO of The University of Rhode Island, and partnered with the Ocean Exploration Trust and the National Oceanic and Atmospheric Administration, brought investigators closer to the wreckage than ever before. Using robotic exploration vehicles, the team surveyed the USS Independence for the first time since it sank 65 years ago, streaming footage online (Figure 4. 50).
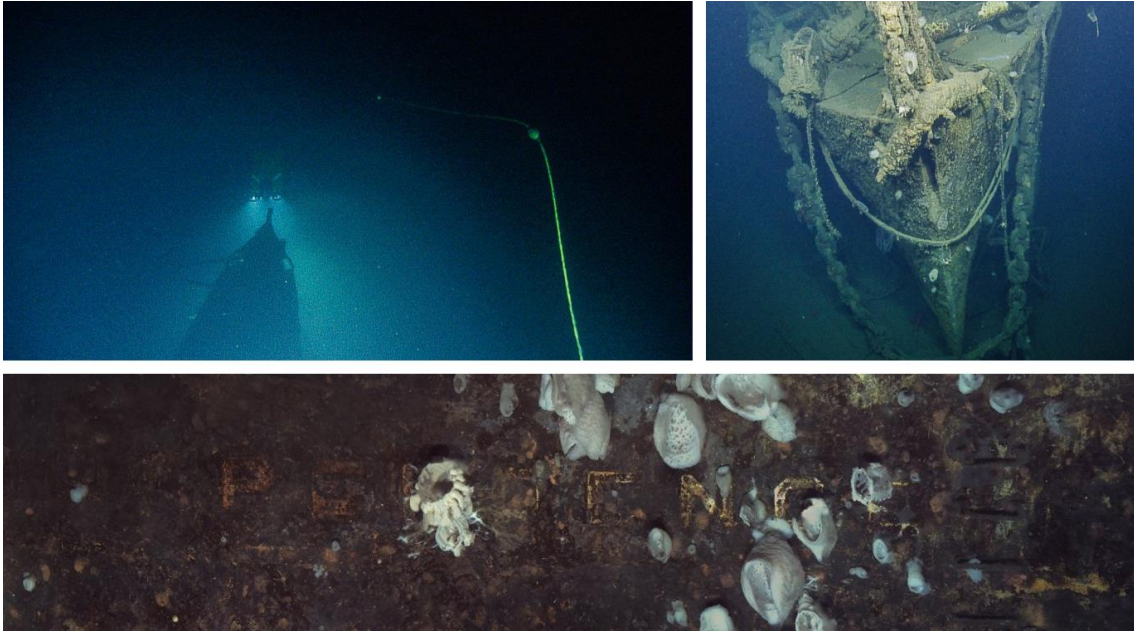
Figure 4. 50. Lights of the ROV Hercules illuminate the bow of the USS Independence.

While investigating the wreckage, researchers found evidence of at least one existing Grumman Hellcat plane as well as anti-aircraft weaponry (Figure 4. 51).
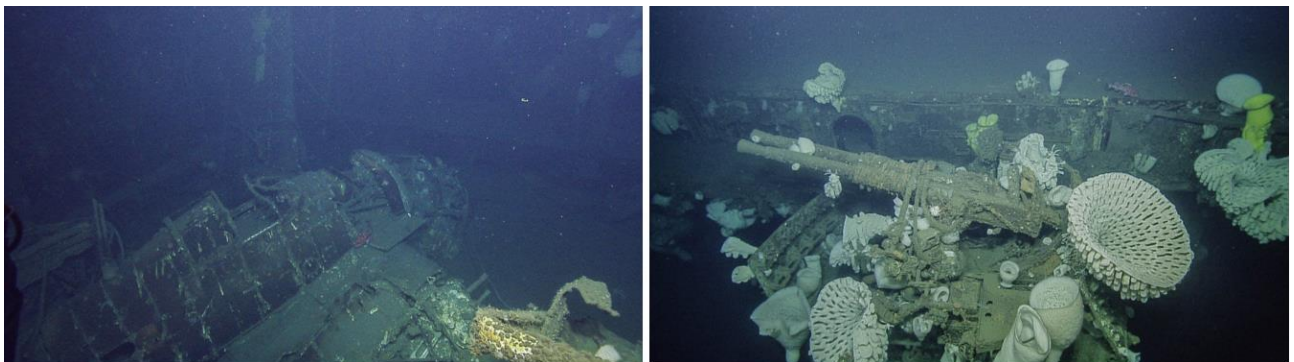
Figure 4. 51. Grumman Hellcat fighter aircraft seen in aircraft elevator hatch. Anti-aircraft weaponry surrounded by massive glass sponges.

The NOAA is now interested in collecting metal samples from this wreck and especially from the planes found inside during the expedition. The metal aircraft components are likely to be degraded and fragile, hence the need for soft grasping solutions. The hybrid gripper is the solution proposed by the R-CUE to address this issue.

4.3.2. Design of the hybrid toroidal soft gripper

The hybrid toroidal soft gripper design, developed during my internship research at the URI, is an evolution of the universal jamming gripper described in Licht et al. (2017).

The term "toroidal" is referred obviously to the shape of the balloons, while the term "hybrid" is referred to the ability of the system to combine the mechanism of traditional rigid manipulator claws with the jamming compliant gripper mechanism.

The primary goal has been to integrate the soft gripper to the existing Hydro-Lek 5-DOF hydraulic arm and to use 1-DOF to control the opening/closing mechanism of the two fingers. Secondly, the fluid path has been connected to an ad-hoc hydraulic cylinder to satisfy a required flow and vacuum pressure. Lastly, a relative sliding between the manifold and the fingers has been designed in order to prevent overpressure on the object due to closing mechanism of the fingers.

Concept design

Before advancing any analysis or evaluation regarding the design of a new soft gripper, the designer must first generate a design proposal. This is often regarded as the mysterious, creative part of the design, where the client exhibits a brief declaration of requirements, and the designer responds with a design proposal. Actuality, the process is less magical than it appears. In fact, we follow a common thread that leads to materialize ideas, which in some ways is imposed with very strict criteria, following a step-by-step design. Again, drawings are a key element of the design process. In this initial phase of the process, the design that the designer usually does is not intended to be communicated to anyone else, but only to the development team, which has the same propensity to perceive the problem. At the beginning of the design process, the designer is generally faced with an undefined problem, and he has to find a definite solution. Each goal to reach determines particular constraints that must be known if the designer wants to achieve the optimal solution. To this end, analyzing the state of the art of underwater soft robotics (section 1.3.2) and studying the previous work (section 4.3.1) is very

important to understand new functional requirements that the redesign of soft gripper must have. Therefore, it is crucial that the design phase is preceded by functional analysis, with the aim of determining the functional requirements (Figure 4. 52).
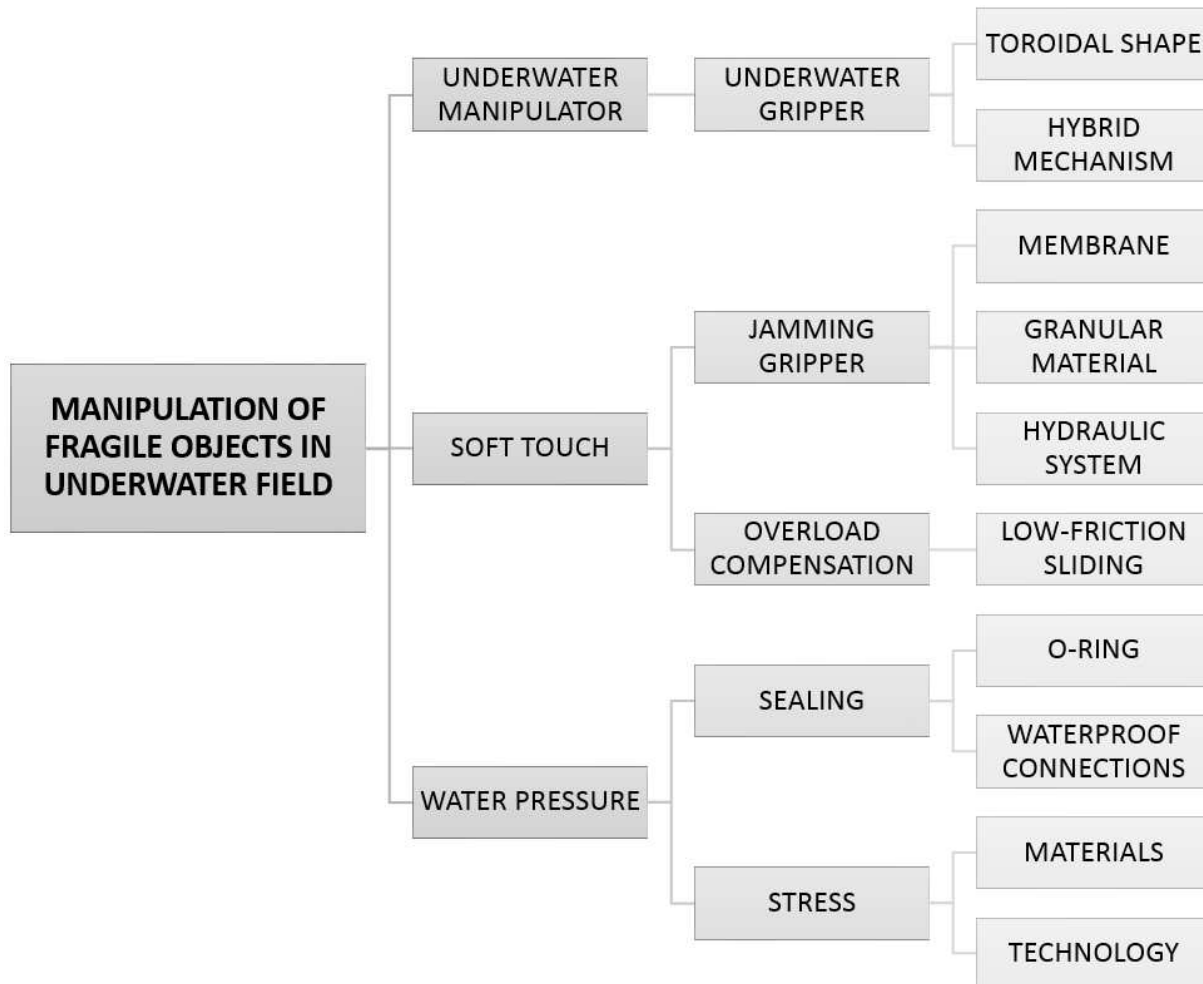
Figure 4. 52. Functional requirements.

Figure 4. 52 underlines the requirement of design an underwater soft gripper by means of jamming granular material contained into two sealed toroidal-shaped membranes. Subsequently, the functional requirements are translated into ideas and therefore primordial geometries of the product. Here different sketch drawings, ideas, and solutions have been investigated and detailed through an intense brainstorming activity with my teamwork at URI. Gradually, the solutions were discarded and improved, carrying out, finally, the concepts.

Concept 1

Considering the functional requirements, the first developed concept, depicted in Figure, consists of 5 main components:

- Base;
- Finger (2x);
- Soft end-effector (2x).
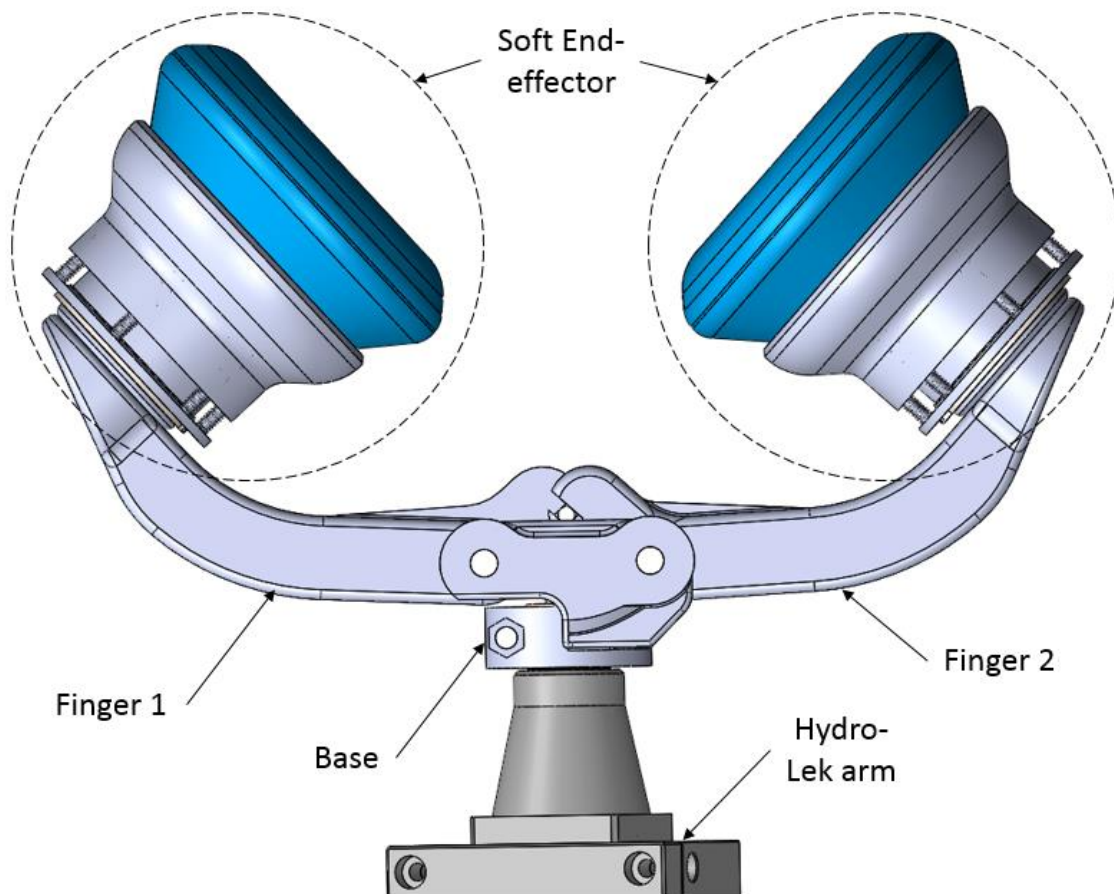
Figure 4. 53. CAD model of the Concept 1.

The two Finger are assembled to the to the Base using two pins and corresponded bushing, in order to make easily the rotation. The movement of the finger is demanded to the piston of the Hydro-Lek arm, as shown in Figure 4. 27. In particular, the excursion of the piston is 28.8 mm, with maximum and minimum elongation of 40 mm and 11.20 mm

respectively. The diameter of the piston is Ø $16,00^{0}_{-0.12}$ mm. At the distance of 8.20 mm from the end of the piston, there is a drill hole of Ø $6,00^{0}_{-0.05}$ mm, that is used with a pin to create the opening/closing mechanism of the fingers, as depicted in Figure 4. 54.
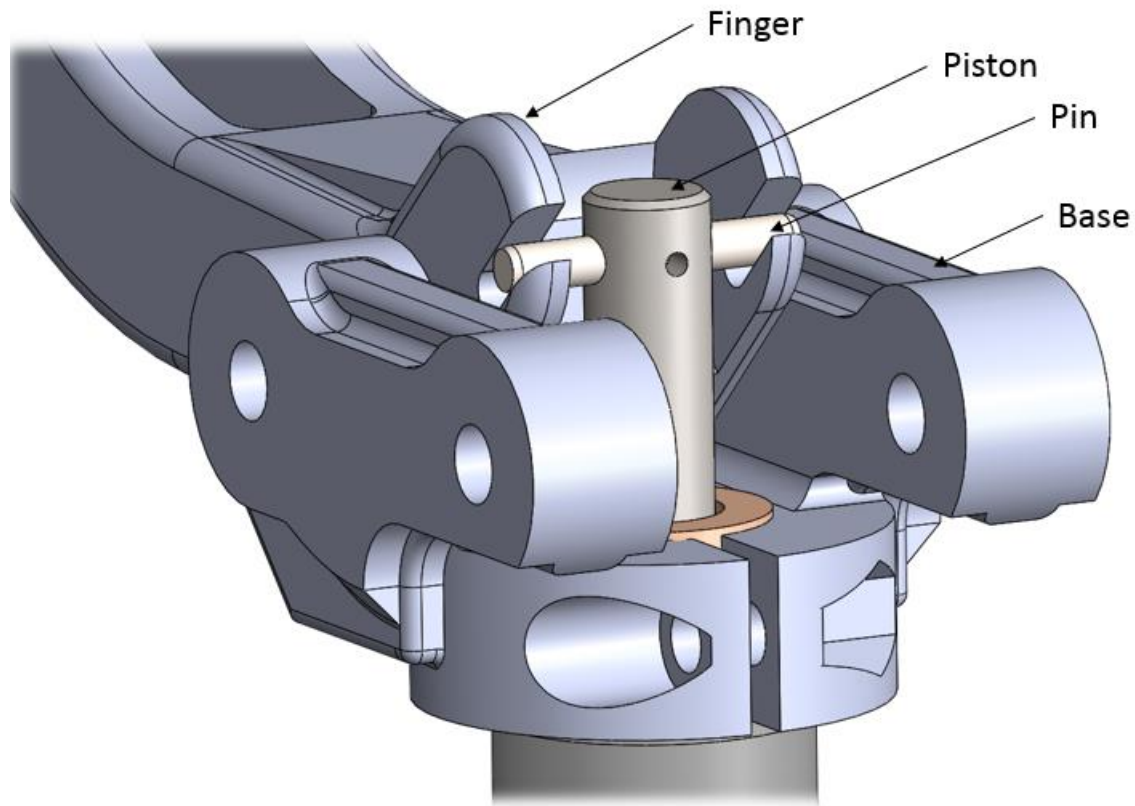
Figure 4. 54. The opening/closing mechanism of the fingers.

The two soft end-effectors are rigidly mounted at the end of the finger using 4 screws. The components of the end-effector are the follows (depicted in Figure 4. 55):
- Membrane;
- Internal support with filter;
- Internal manifold;
- Manifold;
- Cap;
- Support;
- Spring;

- Bushing;

- O-Ring;

- Retaining Ring.
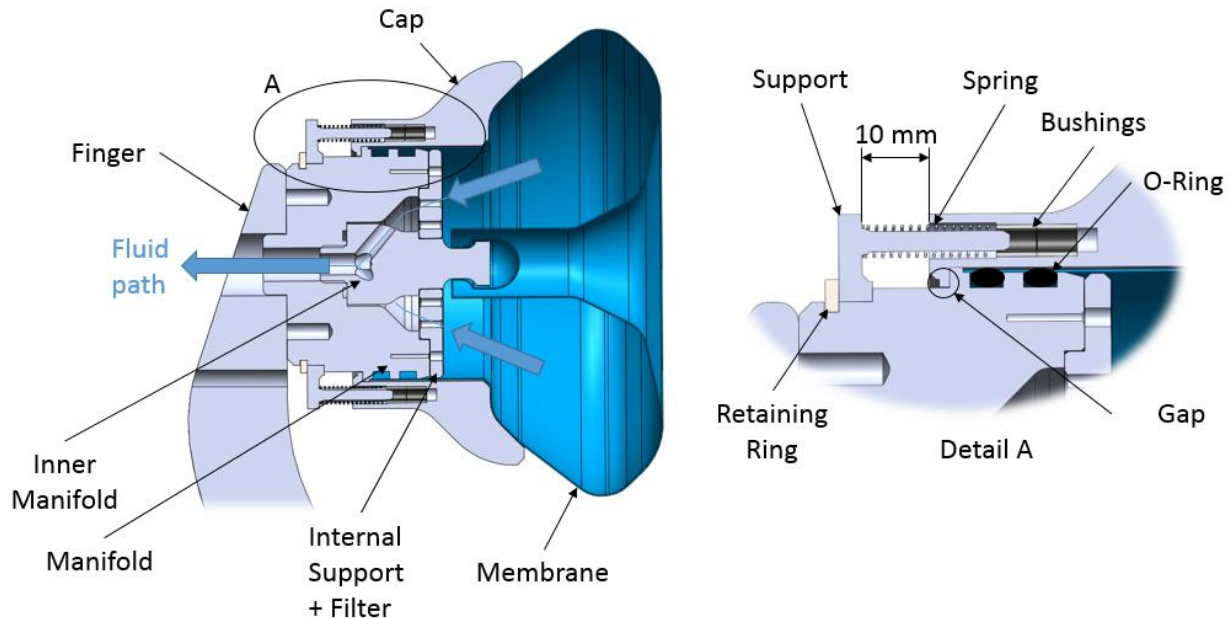
Figure 4. 55. Components of the soft end-effector.

In Figure 4. 55 is evident the solution adopted to set a toroidal shape to the membrane. In fact, using a zip tie, or elastic ring, is possible to lock the membrane around the pin of the Internal Manifold. Furthermore, the membrane is held with interference between the manifold and the cap using two O-Rings. To this end, careful attention needs the design of the two O-Ring housing in the manifold and the surface roughness of the cap, that is sliding above them. Moreover, in order to avoid the overpressure on the object while the two soft end-effector get together, a system of low-friction sliding involving the pin of the support, the bushing placed on the cap, and springs has been designed, as shown in the detail A in Figure 4. 55.

The proposed solution, although it fulfills all the functional requirements correctly, presents some critical points to figure out. In particular, the questions are regarding:

- The sliding system using springs can actually work properly?

- The two O-Rings are able to guarantee the sealing of the membrane?

- The part of the finger in contact to the pin of the piston is able to support the stress generated to open/close the mechanism?

The first two questions require more investigations. Regarding the third question, prior to proceed with physical prototyping, the finger has been subjected to FEM analysis in order to simulate and verify its reliability and integrity to support the stress generate to open/close the mechanism. In particular, the finger has been subjected to static analysis taking into account the materials that can be adopted in the laboratory for the additive manufacturing: PA2200, a polyamide with high strength and stiffness. The results demonstrated that the steel component (Figure 4. 56) keeps a full functionality at the maximum force applied between the two membranes of about 100 N, with factor of safety of 1.2.
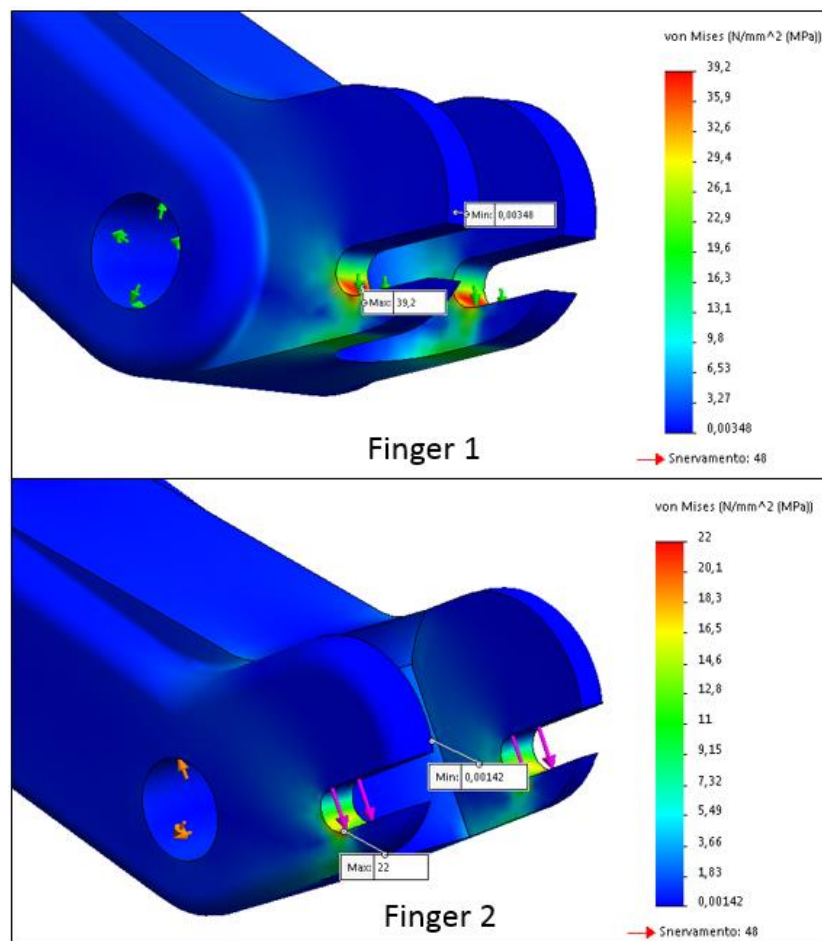
Figure 4. 56. Static FEM analysis of the two fingers.

Concept 2

In the concept 2 of the soft gripper has been investigated the above unsolved two questions. In order to improve the low-friction sliding between the two membrane while approaching the object, the solution moved to the use of a couple of small diaphragm hydraulic cylinder working antagonist each other (Whitney et al., 2014). Figure 4. 57 shows the basic design of a single-acting rolling diaphragm cylinder.
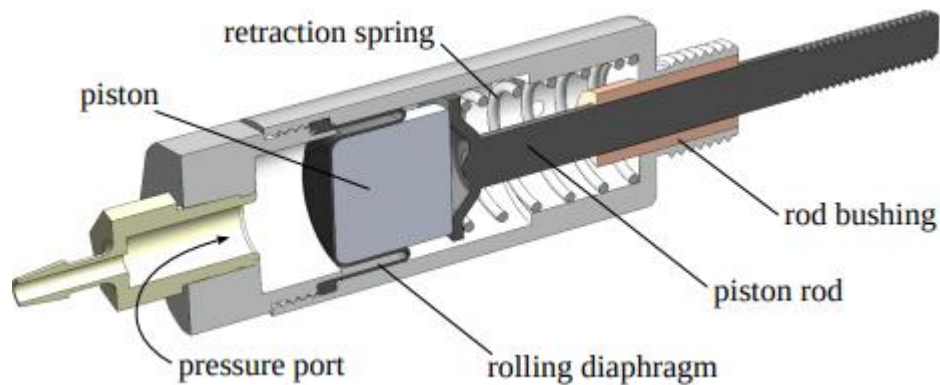
Figure 4. 57. A rolling diaphragm cylinder. Image taken from (Whitney et al., 2014).

The approach is to use pairs of cylinders pre-loaded against each another, one of which the internal reaction spring has been removed. The two cylinders were connected by flexible reinforced tubing to form a symmetric constant volume closed system. The cylinder with spring is mounted on the finger, in order to push the manifold away using the internal rod. To this end, when the closing mechanism gets together the membranes, the manifold pushes the piston back and, in turn, the antagonist cylinder (without the spring) compensates the movement pushing its piston rod away.

The new configuration of the gripper is depicted in Figure 4. 58.

17 mm

Rolling diaphragm
cylinder (with spring)

Piston rod

Sliding shaft (3x)
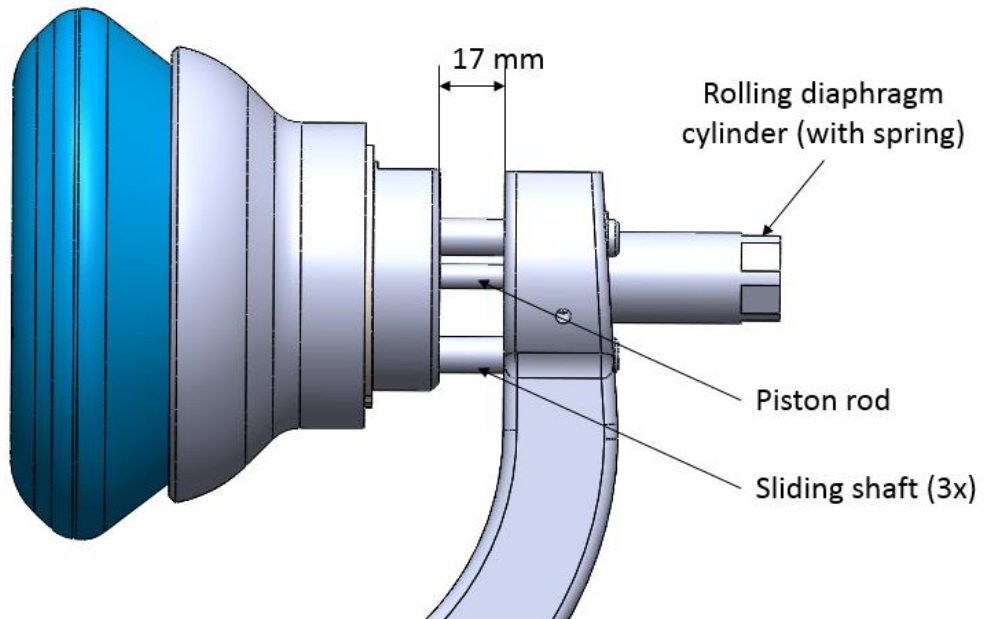
Figure 4. 58. New configuration of the gripper.

Finally, concept 2 open our mind towards a final version of the gripper.

Final design version

In the final design version, the length of the finger has been optimized in order to allow a distance of 20 mm between the caps of the soft end-effector (Figure 4. 59), considering the sliding of 17 mm of the two cylinders as well, when the gripper is closed (minimum excursion of the piston of the arm).
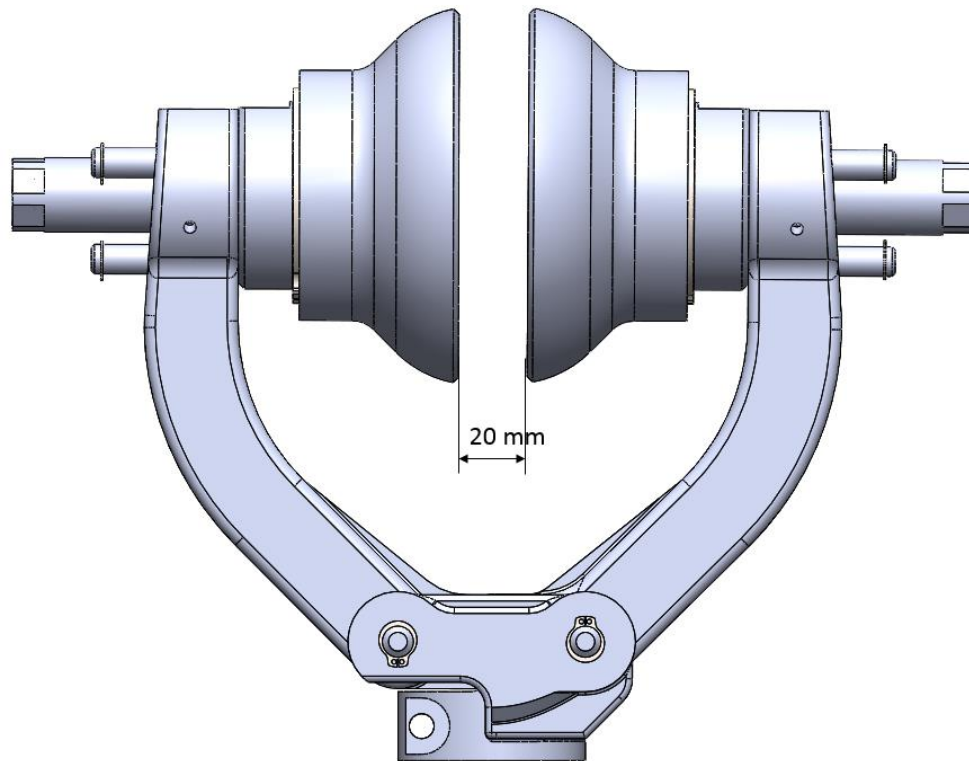
Figure 4. 59. The gripper in the closing mechanism configuration.

The result of the design proposal, prototyping and assembly of the hybrid toroidal soft gripper is depicted in Figure 4. 60.
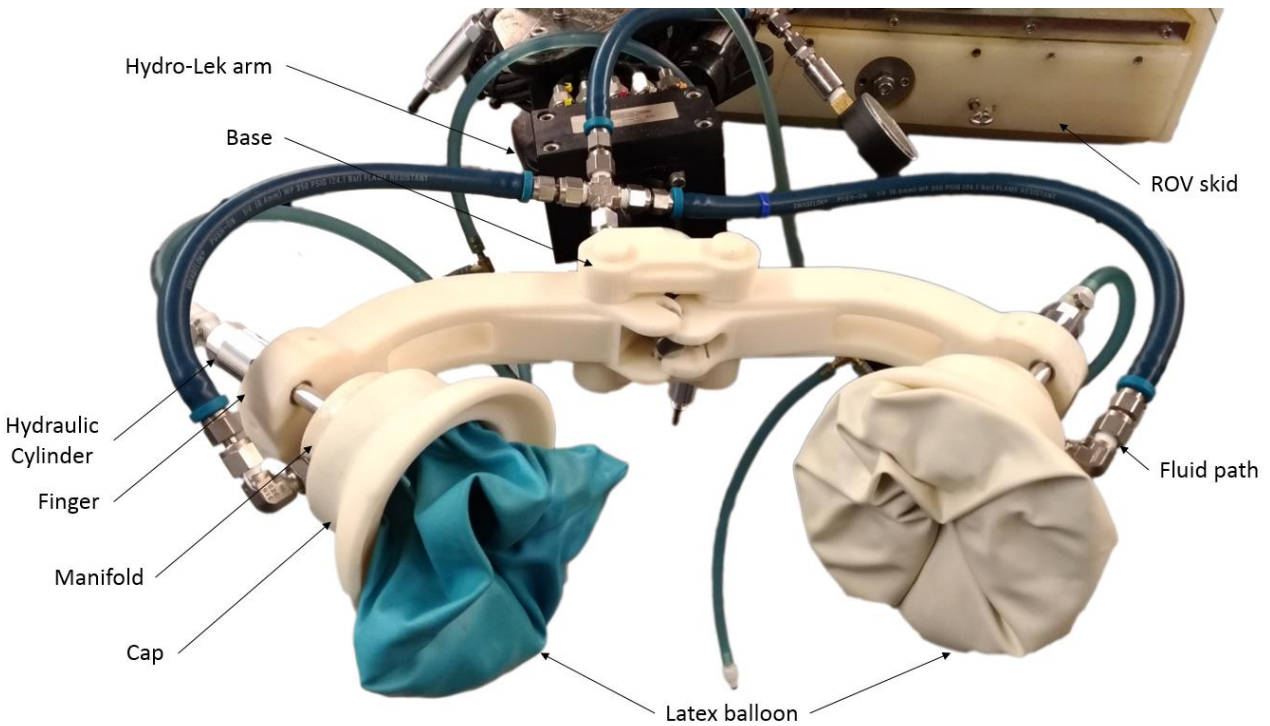
Figure 4. 60. Assembled soft robotic gripper mounted on the Hydro-Lek arm.

The physical prototype of the soft gripper has been manufactured by means of additive manufacturing technologies. In particular, the Stratasys Dimension Elite P14759 machine (FDM, Fused Deposition Modeling) has been used to build the polymeric components. Other components have been manufactured using a standard lathe machine, a small CNC Milling machine (Sherline 5400), and a manual Mill (Grizzly G0463). Standard components have been bought using McMaster-Carr platform.

The membrane is a commercial latex balloon (Qualatex® 30'' Round) filled with two different type of low-density ceramic hollow spheres (SphereOne®), one of which is neutrally buoyant in the water to compensate distributions due to the gravity. The uninflated volume of the membrane is about 560 cc. About 25% of the volume of the membrane is filled with 150 g of spheres, of which 50 % are Extendosphere® 200/600 (with mean particle size of 450 microns and density of 0.65 g/cc), while 50 % are Reluminasphere® HB-150 (with mean particle size of 100 microns and density of 0.70 g/cc).

The membrane is held with interference between the manifold and the cap, wrapping up two O-rings in their housing (Figure 4. 61). In order to avoid a dangling movement of the membranes in the water while approaching the object in the soft state, the membrane is holding through a cable tie on the internal support attached to the manifold to assume a donut-like geometry. The fluid path is equipped with two filters (304 stainless steel wire cloth 400 x 400 mesh size, 0.0015" opening size) mounted between the closing cap and the manifold that allows water flow, but blocks the spheres on the balloon.

Hydraulic cylinder
Linear bearing
Finger
Rod piston
Manifold
Shaft
Retaining ring
O-Ring
Closing cap
Filters
Internal support
Cap
Latex Balloon
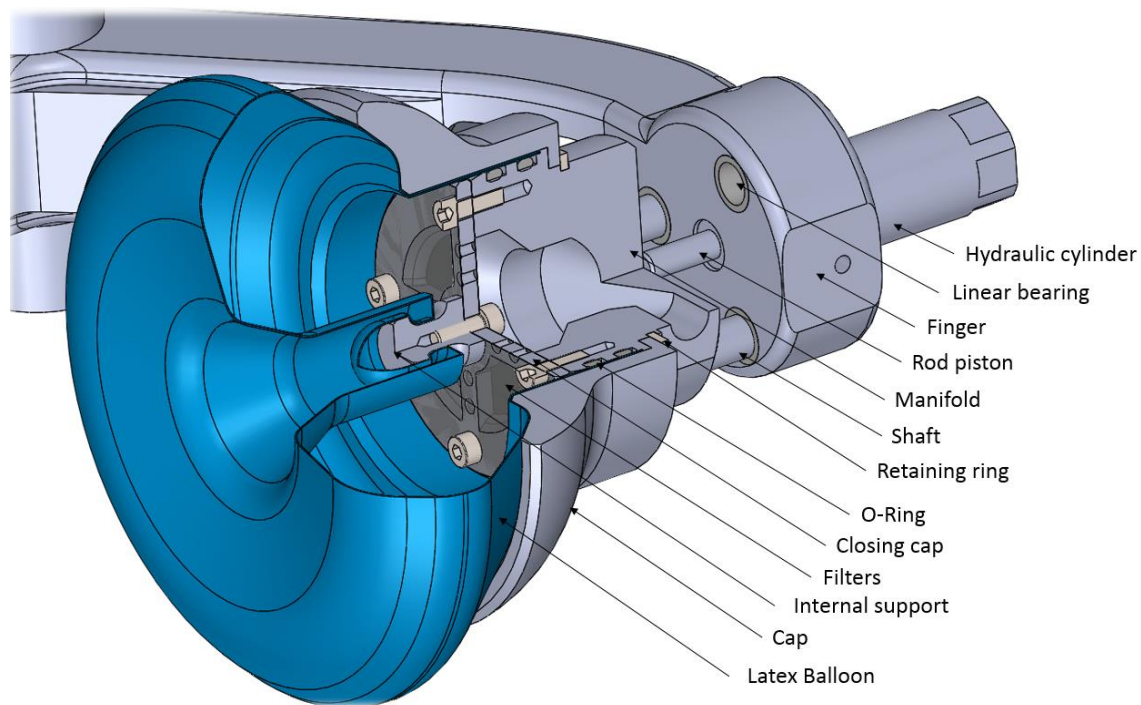
Figure 4. 61. CAD model of the jamming gripper.

The fluid path is connected on a home-made hydraulic cylinder, that consists of a 125-mm bore Delrin water-filled cylinder and a 25-mm bore oil-filled cylinder (Hydro-Lek), connected end to end between the two 64-mm stroke rod pistons (Figure 4. 62). The 80 bar oil-hydraulic system on board of the ROV is used to reach the maximum vacuum pressure across the jamming membranes of about 1.3 bar. The volume of the cylinder is 840 cc, that represents the 75% of the uninflated volume of both membranes.
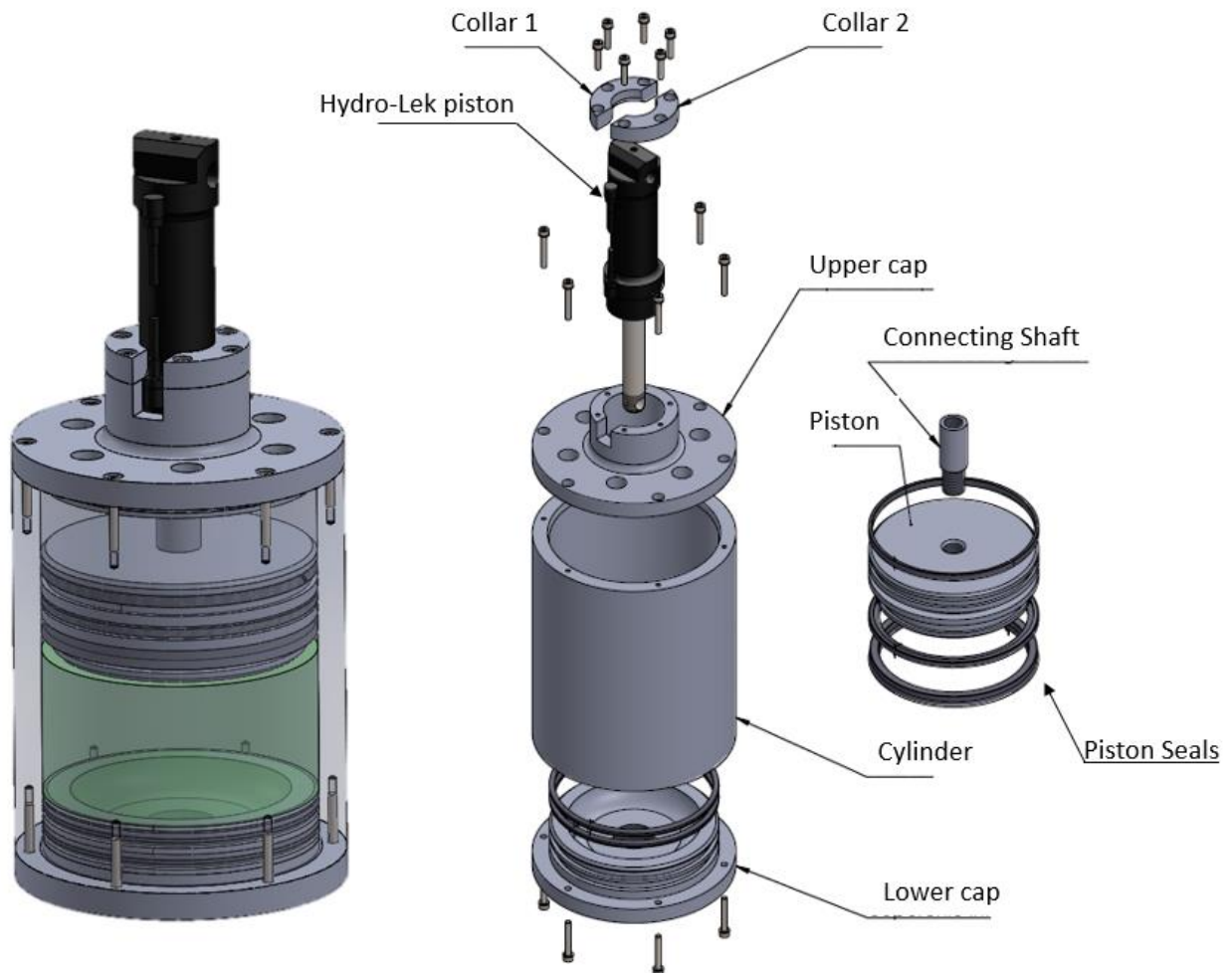
Figure 4. 62. CAD model of the home-made hydraulic cylinder.

The purpose to use a two finger-like mechanism is to increase the contact surfaces between the object and the soft membranes before jamming. The problem with this solution is the high risk to damage soft objects due to the high-pressure closing mechanism of the fingers. To figure this out and ensure a soft touch, a system of compensation of the axial compression has been designed through a pair of low friction hydraulic cylinders (Mini Mights) in a closed-circuit system with incompressible fluid pressurized at 9 psi (0.62 bar).

One of the hydraulic cylinders is attached to the finger of the gripper using a threaded hole, while the other one is connected at the opposite end of the circuit. In the first cylinder, the internal reaction spring has been removed, so that the pressure in the circuit

pushes the piston out, into the condition of maximum elongation (about 0.7 inches). This, in turn, moves the manifold away from the finger using the three shafts, arranged at 120° around the piston and screwed up on the manifold, that are sliding on linear bearings mounted on the finger.

The hydraulic cylinder on the other side of the circuit is equipped with a reaction spring with an elastic constant K = 10 lbs/in, such us not to allow the piston excursion at the circuit pressure of 9 psi.

To this end, as soon as the two membranes approach the object in the soft state, adapting to the surface, the closing mechanism continues to move sliding the manifold through the three shafts and accordingly pushing down the piston of the cylinder (Figure 4. 63 a, b). In particular, using an incompressible fluid inside the closed-circuit, the piston excursion in the first cylinder, integral with the finger, will actuate the sliding of the piston with spring on the other side, increasing the pressure in the circuit of K * x. Considering the maximum excursion of the piston in the cylinder of about 0.7 inches, the pressure lying on the object is 9 psi plus the effect of the spring. In particular, the force of the spring is 7 lbs, the effective area of contact between the piston and the rolling diaphragm is 0.384 in^2, so the effect of the spring is 7 lbs / 0.384 in^2 = 18.23 psi, that obviously will be split to both cylinders. Therefore, theoretically, each membrane exerts on the object a pressure of about 9 + 9.1 = 18.1 psi (1.25 bar). When the object is released, the pressure into the circuit carries the cylinders in the initial condition.

Moreover, this system can be very effective in underwater trials, using the axial sliding as visual feedback. Another reason that carries out this solution is given by previous experience with universal gripper trials. In particular, when the particles are transformed from the soft state in the hard state, the membrane try to pull and lift the object in the direction of the manifold (the same direction with which the fluid flow out by the membrane). Using two membranes we are expecting by experimental test a movement of the membranes to meet and approaching each other while jamming. To this end, a linear shifting of the manifold is essential to compensate this "jamming effect" of the membranes (Figure 4. 63 c), otherwise, the grip can fail.
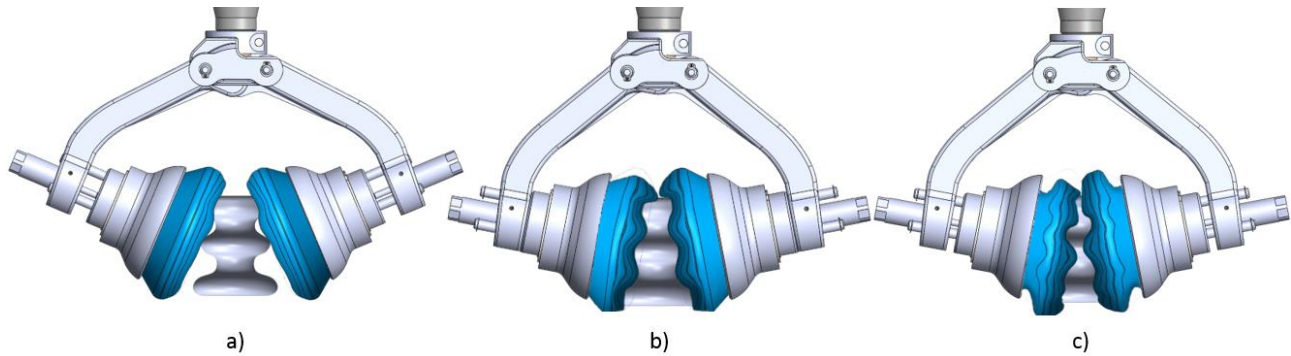
Figure 4. 63. a) Approaching the object. b) The manifolds slide into linear bearings while the membranes are surrounding the object. c) "Jamming effect".

A requirement of the system is the linear sliding of the manifold through the shafts on the finger, which means that the thrust is transmitted in the axial direction with respect to the piston, otherwise, there will be a component that the system will not be able to compensate. Besides, to know the actual distribution of the pressures between the membranes and the object before and after jamming, it is necessary to proceed experimentally.

4.3.3. Trials in the water tank

To think about what sort of test is valuable to characterize the performance of the soft gripper, we need to understand what the goals are. There are two benefits to the jamming approach: the ability to grasp irregular objects without damage, and the ability to grasp objects with high strength/high torque resistance. The first characteristic is a selling point for all soft grippers. The second characteristic (high strength and high torque grasp) is a specific strength of jamming grippers.

At the lowest level, we wish to show that we can grasp and hold fragile objects without damaging them, even if the weight is off center. At the higher level, we need to show that successful grasp is insensitive to the exact relative position of the gripper and the object. At the highest level, we need to show that the combination of these two characteristics results in a system that can be used on a poorly controlled remote platform.

These levels are progressively more difficult to demonstrate. Therefore, two types of trials have been performed:

- Manual test) Place objects on a support platform in the center of the gripper closing location, and close the gripper. We can then demonstrate successful grasp by removing the support platform from the object. In fact, a simplified description of grasping is the ability to pick up and hold an object against external disturbances.
  - An important variation on this would be to gently grasp and firmly hold objects that will naturally try to twist out of the grasp. For example, attach a long rod with a weight on the end of it.
- Manipulation test) Place objects in the same way, but now have an operator approach the object with the arm, grasp it, and move away. It should be noted that manipulation is the ability to exert forces on an object and thus cause its rotation and displacement with respect to the reference frame of the manipulator.
  - Again, make sure to include objects that will want torque out of the grasp.

All tests will be carried out with the following variations:

- nearly full membranes (~90%) vs partially filled membranes (~50%).
- Jamming and no jamming after grasp.

Finally, we want to approach objects with the membranes unjammed and close the grippers enough to activate the spring cylinders before jamming. Although at least one demonstration of approaching with jammed grippers and breaking something would be instructive.

To this end, we selected a range of demonstration objects with relatively high aspect ratios and/or long edges, that will naturally try to torque out of the grasp, as shown in Figure 4. 64 and described in Table 4.1. All tests were performed fully submerged in a 0.5 m deep water tank, and filmed using a GoPro camera in a waterproof housing.

Figure 4. 64. Objects used in the trials.

Object	Name	Image	Shape	Dry Weight [g]
1	Printed pincer		L 210 mm	175
2	Light bulb (small)		φ 35 mm	30
3	Light bulb		φ 60 mm	45
4	Energy saving light bulb		φ 47 mm	90

5	Printed cylinder		φ 64 mm	155
6	Wine glass (white)		φ 86 mm	195
7	Wine glass (red)		φ 96 mm	225
8	Bottle 1		φ 81 mm	355
9	Bottle 2		φ 67 mm	270
10	Bottle 3		φ 56 mm	200
11	Can		φ 57 mm	135
12	White jar		φ 130 mm	745

13	Amphora		φ 112 mm	460
14	Long rod		L 600 mm φ 30 mm	440
15	Tube 1		φ 63 mm	635
16	Tube 2		φ 80 mm	930
17	Torque rod		L 350 φ 23 mm	1365 + 200

Table 4.1. Characteristic of the objects used in the trials.

4.3.3.1. First extended trials

The first extended trials were carried out at the Department of Mechanics, Energy, and Management (DIMEG) at the University of Calabria, using the skid and the arm available at the laboratory. Firstly, before start with trials is necessary check the functionality of the whole system (mechanical, hydraulic, electrical, and control). Therefore, the soft gripper has been integrated with the arm and the hydraulic system. The experimental set-up of the trials has been carried out using a commercial 5 meters round swimming pool in about 0.5 m of deep water, as depicted in Figure 4. 65.
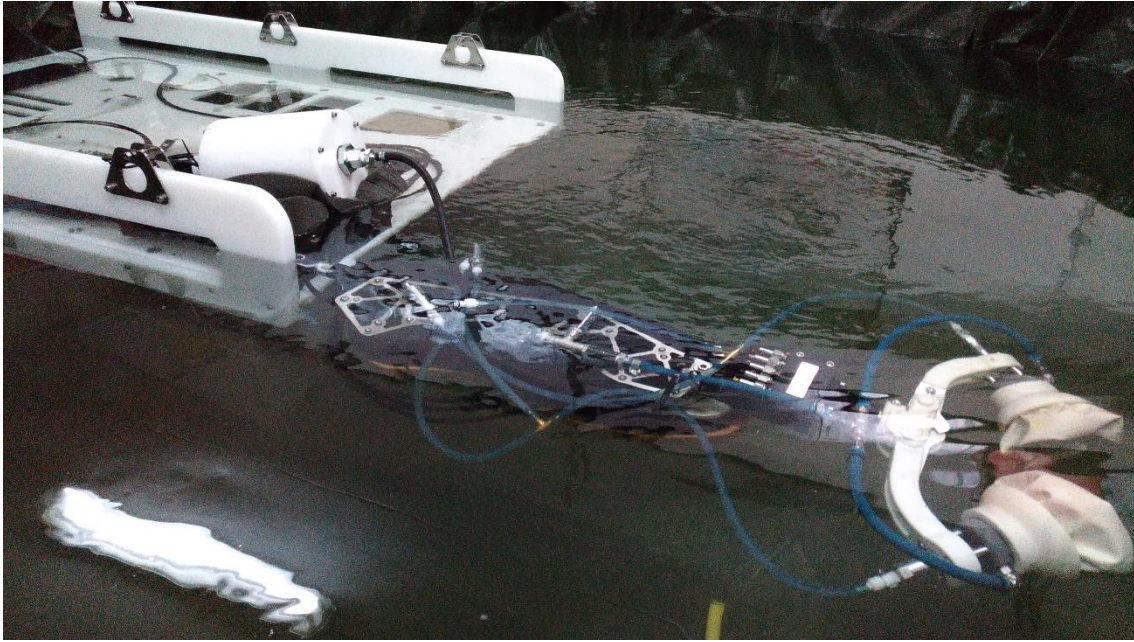
Figure 4. 65. The experimental set-up of the trials carried out at DIMEG.

Manual tests

All of the objects shown in Figure 4. 64 were successfully grasped and hold for more than 60 seconds by the soft gripper during the above mentioned manual test (Figure 4. 66), almost with one of the proposed variation of the state of the balloons, such as nearly full membranes (~90%), partially filled membranes (~50%) and jammed after grasp (Figure 4. 67).

a)   b)   c)
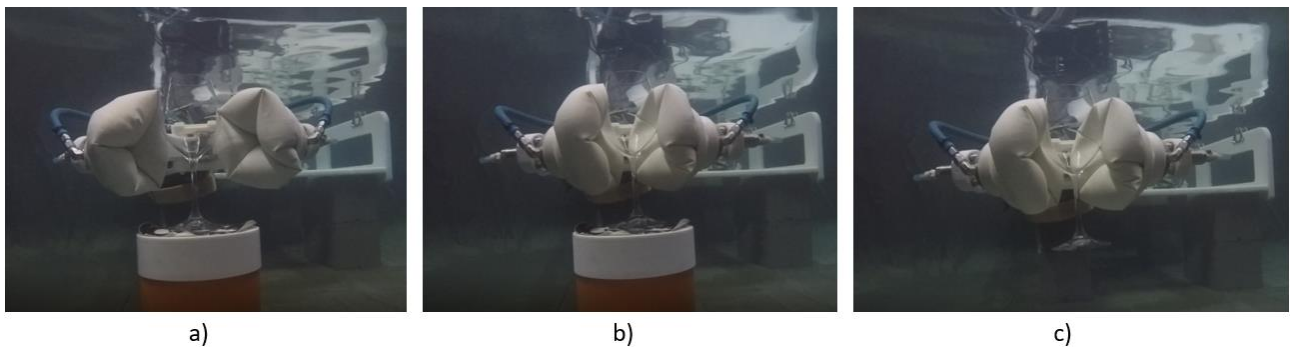
Figure 4. 66. Manual tests on object 6. a) Positioning. b) Approaching. c) Holding.

a)   b)   c)
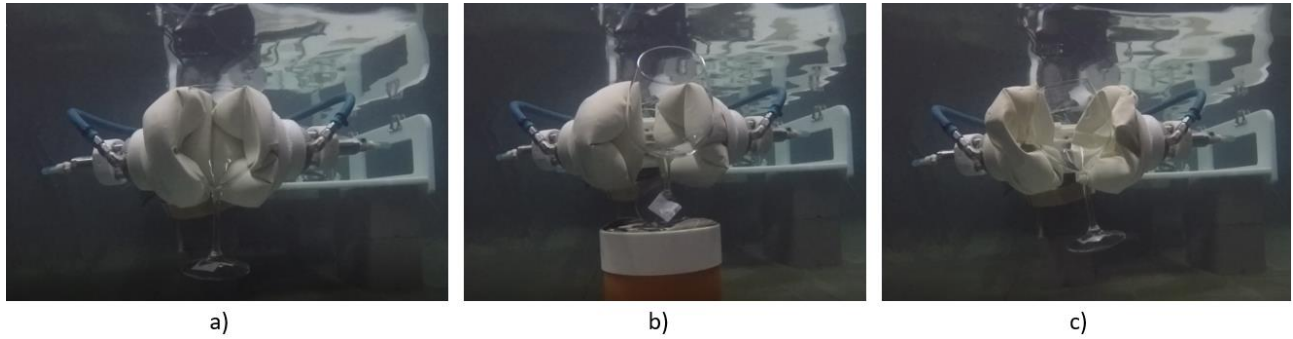
Figure 4. 67. Membrane condition variation shown during grasping of the object 7. a) partially filled 50%. b) nearly full 90% (grasp failed). c) Jammed.

Representative screen captures of the tests are shown in Figure 4. 68.

Object 1, jammed   Object 2, 90%, failed   Object 3, 90%, failed
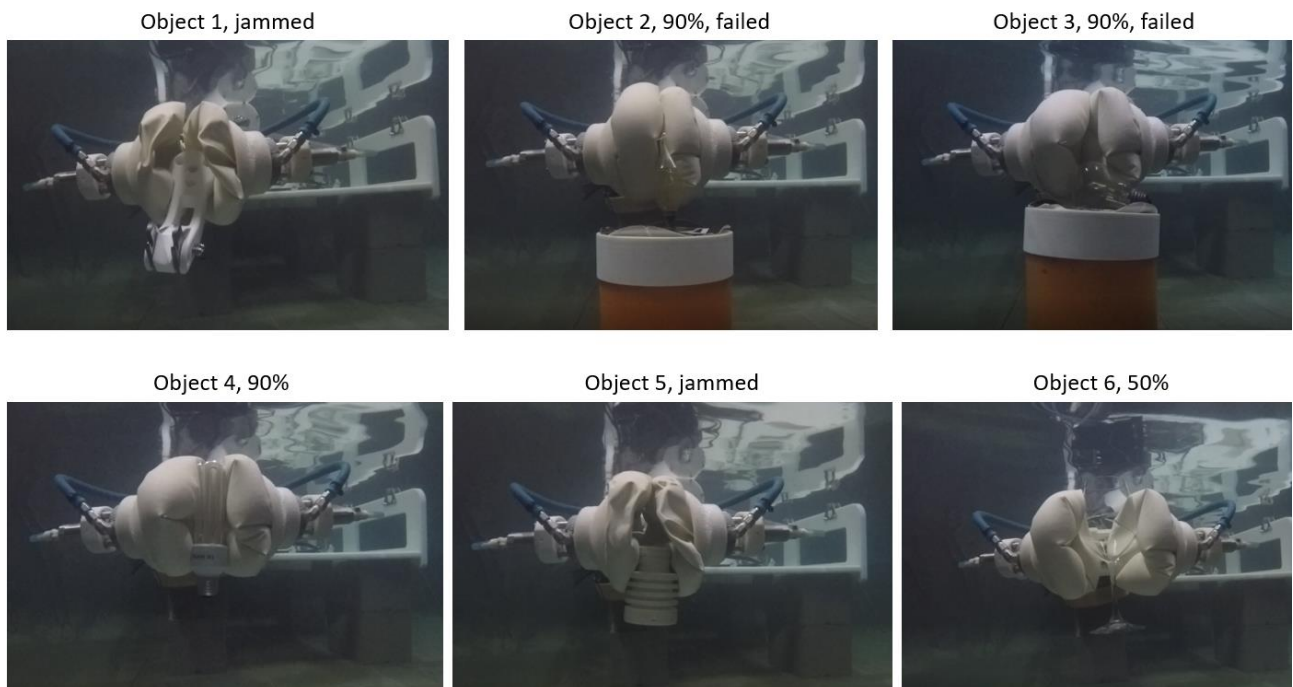
Object 4, 90%   Object 5, jammed   Object 6, 50%

Object 7, 50%
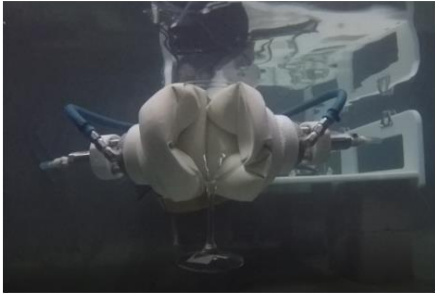
Object 8, 50%

Object 9, 90%
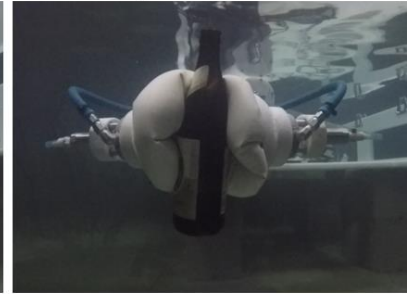
Object 10, 50%

Object 11, 50%
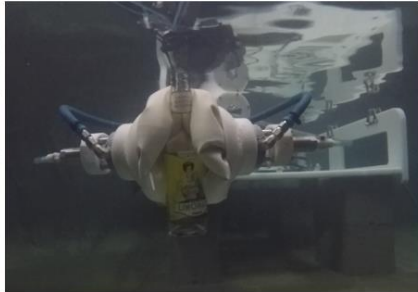
Object 12, jammed, failed

Object 13, 50%

Object 14, jammed
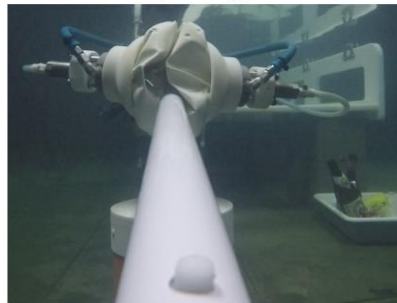
Object 15, 50%

Object 16, 90%

Object 17, jammed

Object 17, jammed, 100 mm
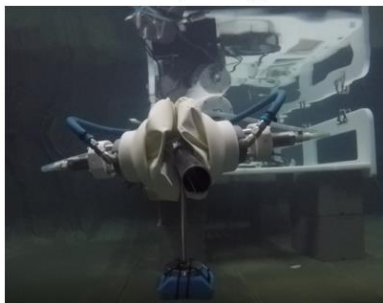
Object 17, jammed, 200 mm   Object 17, jammed, 300 mm
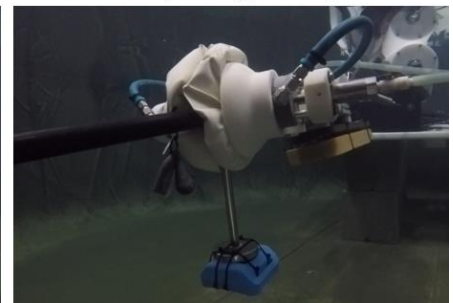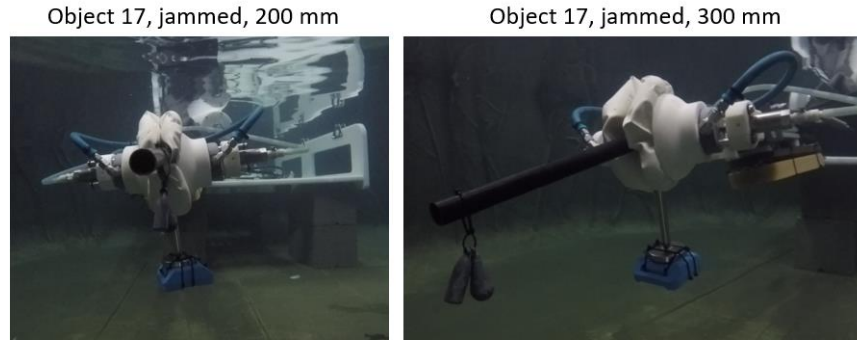
Figure 4. 68. Representative images demonstrating manual test of the gripper on selected objects.

Grasp failure was observed on the light bulbs (object 2 and 3) due to the uncontrolled movement in which the membranes approach the object, and the white jar (object 12) probably due to the weight of the jar filled with water. The results of the trials are reported in Table 4.2.

Object	Name	50%	90%	Jammed
1	Printed pincer	√	√	√
2	Light bulb (small)	X	X	X
3	Light bulb	X	X	X
4	Energy saving light bulb	√	√	√
5	Printed cylinder	√	√	√
6	Wine glass (white)	√	X	√
7	Wine glass (red)	√	X	√
8	Bottle 1	√	√	√
9	Bottle 2	√	√	√
10	Bottle 3	√	√	√
11	Can	√	X	√
12	White jar	X	X	X
13	Amphora	√	√	√
14	Long rod	X	X	√
15	Tube 1	√	√	√

16	Tube 2	√	√	√
17	Torque rod	√	X	√
18	Torque rod, 200 g - 100 mm	√	X	√
19	Torque rod, 200 g - 200 mm	√	X	√
20	Torque rod, 200 g - 300 mm	√	X	√
	Total successful grasp	16	9	17

Table 4.2. Results of the trials.

In Table 4.2 is possible to notice that almost the successful tests have been carried out with the balloons 50% filled and jammed.

Manipulation Tests

All of the objects shown in Figure 4. 64 were grasped with an operator approach with the arm, manipulated and collected on a tray. In Figure 4. 69 is shown the sequence of operations to manipulate the object 6 (wine glass).
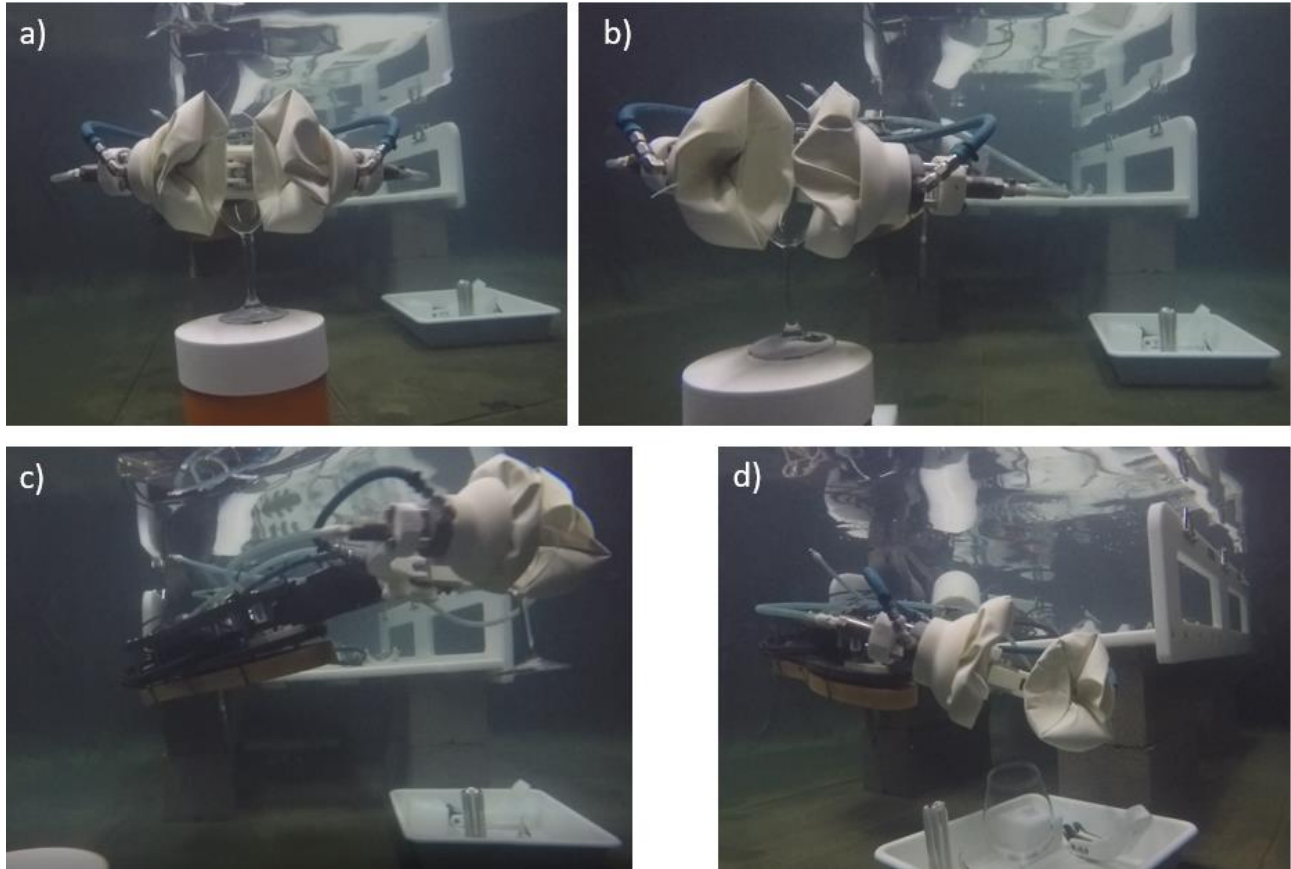
Figure 4. 69. Manipulation test of the object 6. a) Approaching the object with the arm, balloons 50% filled. b) Jamming the balloons. c) Manipulation. d) Release of the object on a tray.

Almost all objects require jamming the balloons before manipulating, because of the jerky movement of the arm. This effect is clearly visible during manipulation of objects 14 (Figure 4. 70), 15, 16 and 17 since they try to torque out of the grasp the balloons (Figure 4. 71).
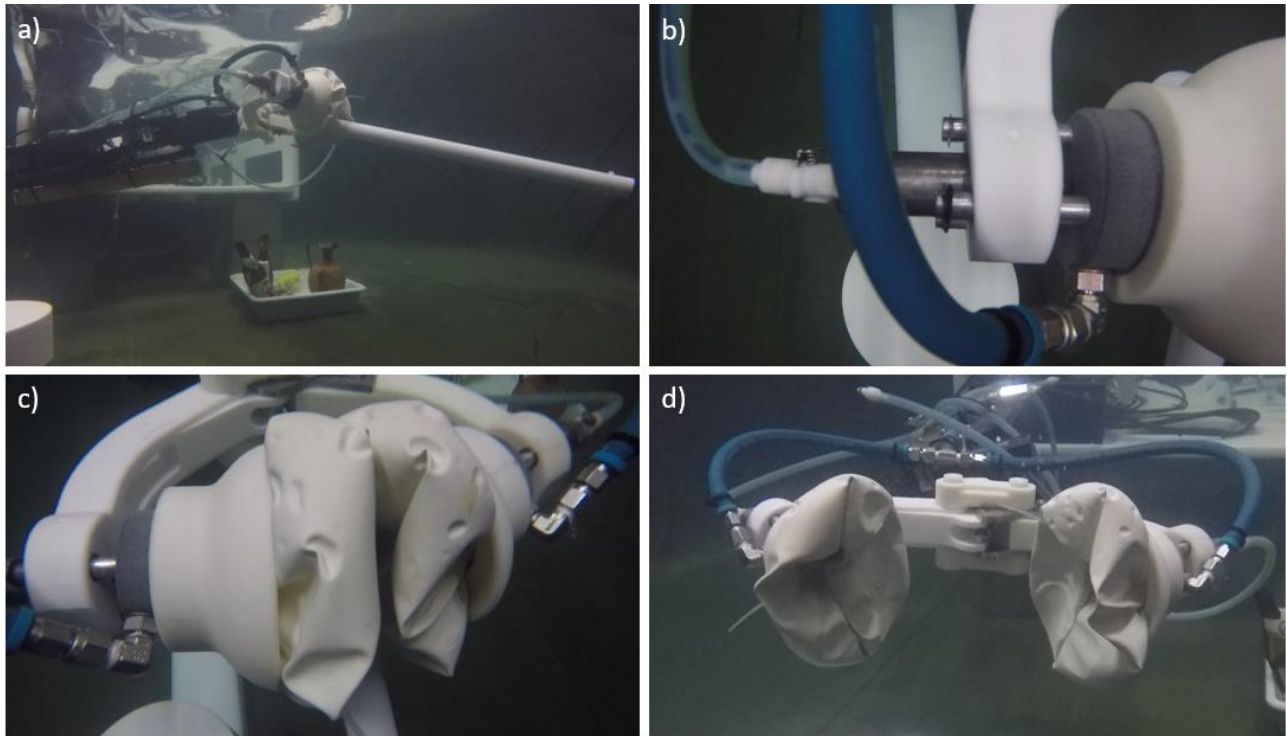
Figure 4. 70. Manipulation of the object 14. a) Manipulation. b) Sliding of the Mini Might and shafts to prevent overpressure on the object. c) Detail of the jamming balloons during manipulation. d) Detail of the balloons after release of the object.
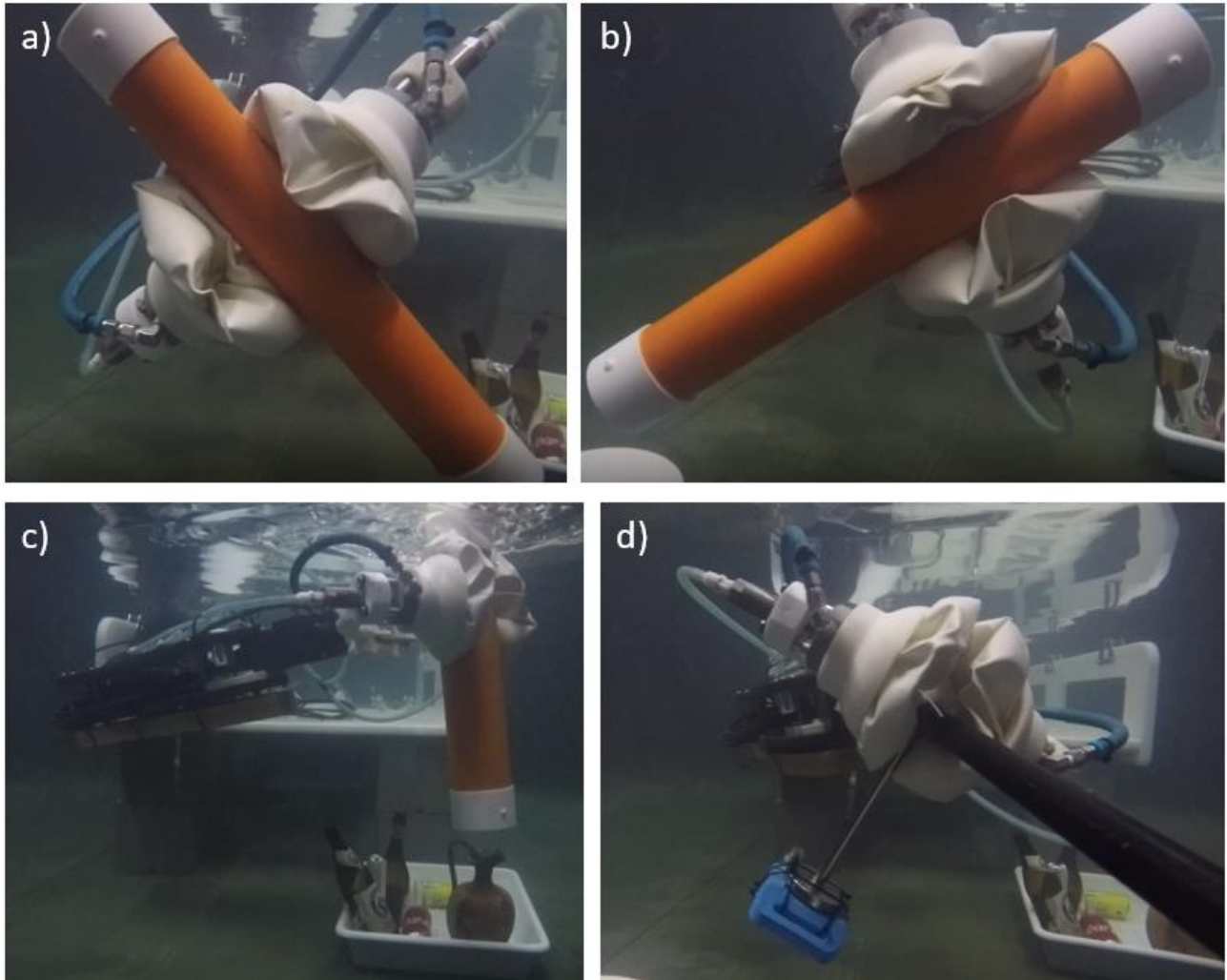
Figure 4. 71. Torque tests. Manipulation of the object 15 (a, b), 16 (c) and 17 (d).

The manipulation and collecting of the object 13 (amphora) in Figure 4. 72 is representative of the effective use of the soft gripper in the field of underwater archaeology, where soft touch is required to manipulate ancient and fragile artifact.
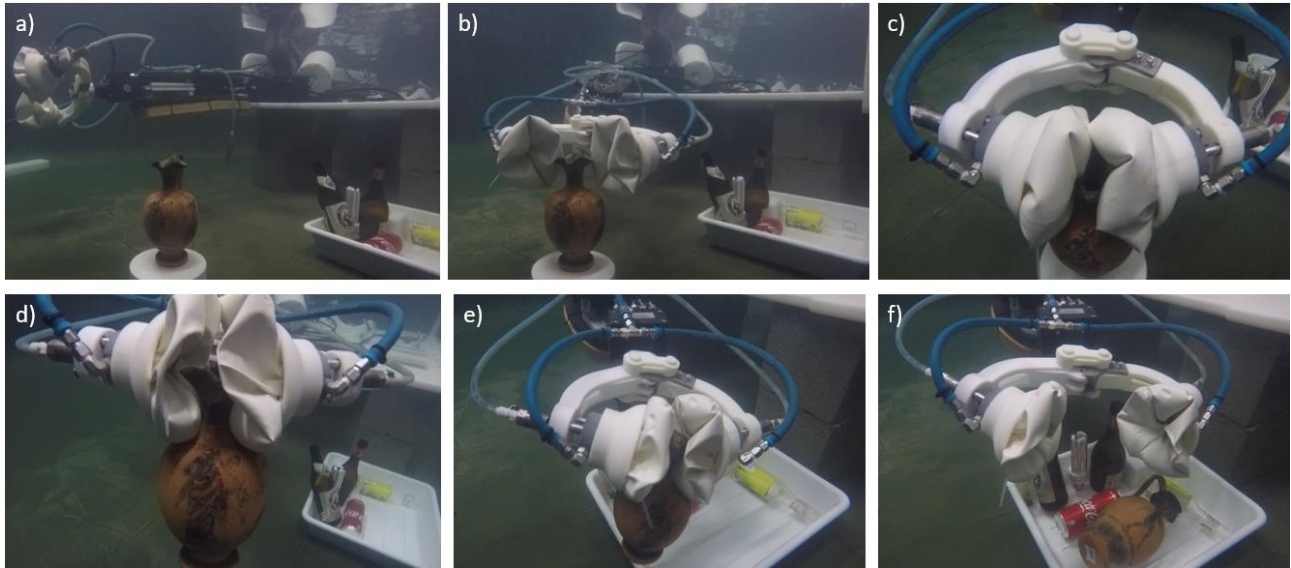
Figure 4. 72. Manipulation of the amphora. a) All extended arm. b) Approaching the amphora. c) Closing the pincer – balloons 50% filled. d) Jamming and grasping. e) Manipulating. f) Releasing on a tray.

Many problems were pointed out on the arm after these qualitative trials, related to the dynamic behavior of the hydraulic system. During manipulation, there is an increasing pressure in the whole system, that causes the opening of the pincer. There is the same problem while jamming the balloons.

Furthermore, the sliding of the rod of the Mini Might and the three shafts placed around them is not complete while approaching the object, probably due to the fact that the force exchanged between balloons and object is not axial. In particular, the best goal to achieve is to increase the spacing between the two cups of the manifold when the pincer is closed as shown in Figure 4. 73. To figure this out a redesign and optimization of the fingers of the pincer is required.
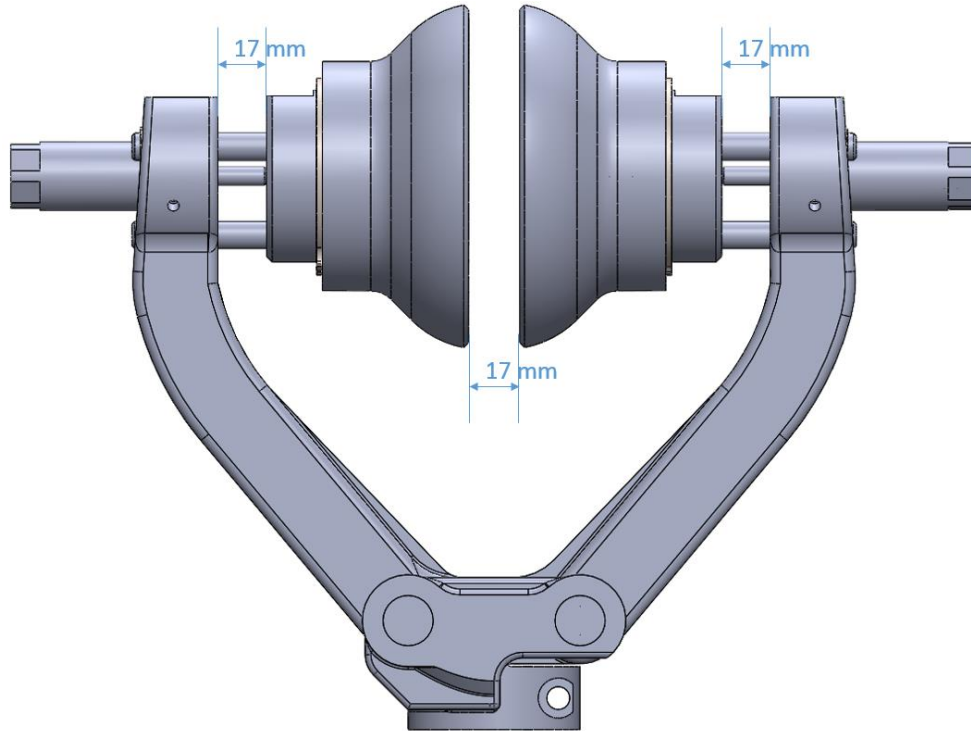
Figure 4. 73. Redesign of the fingers.

Regarding the problems related to the dynamic of the hydraulic system, we can proceed by adding a manual valve pack dedicated to the closing/opening mechanism. In this way, the grasp could be isolated from the whole hydraulic system during manipulation.

4.3.3.2. Second extended trials

The aim of the second extended trials is to quantify the performance of the modified soft gripper. To this end, an operation procedure changes need to be made to be valuable: close the gripper more prior to jamming (motion along the linear bearings during gripping and during jamming must be clear). Unfortunately, due to limitation time, it was not possible to carry out the tests before writing this thesis.

4.4. Future development

The present section highlighted new issues to solve, and new possible characterization of the soft gripper to the end of carrying out future in situ expedition. In particular, even if the trials satisfy the requirement of delicately grasp and manipulate objects without damaging them, the characterization of gripper requires a significantly quantitatively trials. Since these gripper designs do not rely on force sensors feedback, the question is: "How much pressure the latex balloons release on the object?". This issue concerns both developed prototypes of soft grippers. To figure this out an extended pressure mapping test is required in the near future.

Nowadays, Galloway et al. (2016) have been presented a quantitative bench-top characterization of the grasping performance of the soft gripper using a pressure mapping system.

The system that has been individuated for the test is I-Scan, based on the use of contact pressure sensors, manufactured by Tekscan (https://www.tekscan.com/).

Conclusions

This final chapter outlines the work presented throughout the thesis. After a summary of treated topics, it points out the main contributions of the work, the main unsolved issues, and possible further developments. Finally, it lists the publications related with the carried out research.

In the Chapter 2 has been presented the evaluation and characterization of the kinematic performances of an underwater robotic arm mounted on a light work class ROV that is able to perform maintenance operations in underwater archeological sites. The results of the study have been of fundamental importance in the development of the control strategies for the control of the ROV and its manipulator. In fact, on the basis of the maximum error positions found and the kinematic performances of the arm it has been defined a "safety range" that allows to avoid collisions among the end-effector's tool and the artefacts. In particular, when the end-effector's cleaning tool is within the safety range the operator controls the manipulator in order to approach the target very slowly until the contact feedback is provided by the load cell sensors.

In the Chapter 3 has been presented a novel system based on a sensorized robotic arm, a stereoscopic 3D perception, and augmented reality visualization to provide users a visual feedback of the distance between the end-effector and the underwater scene. The system takes advantage of the modern augmented reality techniques to enrich the information available to the ROV pilots in order to support and improve the overall efficiency of their work. The 3D data of the underwater scene, acquired by the optical-stereo camera mounted on the ROV's skid, are augmented on the visual feedback in order to provide to the pilots a depth map of the distances between the end-effector of the manipulator and the underwater framed scene. As future works, the optical-stereo camera can be integrated with other sensors capable to calculate the depth map and perform an on-line 3D reconstruction of the underwater scene. For example, could be

interesting to evaluate the integration of a 3D acoustic camera (Lagudi et al., 2016) that, unlike the optical sensors, do not suffer from seawater turbidity and allow the pilot to operate also in case of poor visibility conditions. In considering the limitations and disadvantages derived from the technologies now adopted in the underwater manipulation field, the proposed AR visualization system represents an added value especially in the Underwater Cultural Heritage field where soft touch is required for the manipulation of the archaeological artefacts. In fact, as attested by the ROV pilots that have participated to the first qualitative tests, the proposed system allows a better perception of the position and orientation of the end-effector and its distances from the target objects, and improve the situational awareness of the underwater scene.

Chapter 4 focused on continues the development, prototyping, and testing of the compliant jamming grippers developed at the R-CUE. In particular, the subject has been divided into two main projects, studying both a universal jamming gripper and a hybrid toroidal soft gripper. In particular, has been demonstrated that a partially filled jamming gripper, submerged and mounted on a robotic arm, is capable of picking up objects freely resting on sand and foam. The partially filled gripper has been capable of picking up a wide range of objects from sand and foam that could not be picked up by the fully filled gripper. The fully filled gripper has been observed to fail by pushing objects down in to soft supporting substrates, while the partially filled gripper draped over and surrounded the objects without exerting enough force to push them into the substrate.

Regarding the hybrid toroidal soft gripper has been demonstrated that the developed prototype is able to manipulate fragile objects in the water tank without damaging them. Future work will regard to characterize the quantitative performance of the grippers.

Related publications

- Domenico Rizzo, Fabio Bruno, Loris Barbieri, Maurizio Muzzupappa, "Kinematic performances evaluation of a hydraulic underwater manipulator," Proceedings of MTS/IEEE OCEANS 2017 International Conference, Aberdeen, Scotland (UK).
- Fabio Bruno, Antonio Lagudi, Loris Barbieri, Domenico Rizzo, Maurizio Muzzupappa, Luigi De Napoli, "Augmented Reality visualization of scene depth for aiding ROV pilots in underwater manipulation," Ocean Engineering, 168 (2018) 140–154.
- Stephen Licht, Domenico Rizzo, George Badlissi, and Everett Collins, "A Partially Filled Jamming Gripper for Underwater Recovery of Objects Resting on Soft Surfaces," IROS Conference, 2018

References

Alici, G., & Shirinzadeh, B. (2005). A systematic technique to estimate positioning errors for robot accuracy improvement using laser interferometry based sensing. *Mechanism and Machine Theory, 40*, 879-906.

Amend, J., & Lipson, H. (2017). The JamHand: Dexterous Manipulation with Minimal Actuation. *Soft Robotics, 4*(1), 70-80.

An, C., Atkeson, C., & Hollerbach, J. (1988). *Model-Based Control of a Robot Manipulator.* Cambridge: MIT Press.

Antonelli G., Underwater robots. Motion and force control of vehicle-manipulator systems, Springer Tracts in Advanced Robotics, Springer-Verlag, Heidelberg, D, 2nd edition, June 2006.

Barbieri, L., Bruno, F., De Napoli, L., Gallo, A., & Muzzupappa, M. (2017). Design of an electric tool for underwater archaeological restoration based on a user centred approach. *Advances on Mechanics, Design Engineering and Manufacturing. Springer International Publishing*, 353-362.

Barbieri, L., Bruno, F., Gallo, A., Muzzupappa, M., & Russo, M. L. (2018). Design, prototyping and testing of a modular small-sized underwater robotic arm controlled through a Master-Slave approach. *Ocean Engineering*, 253-262.

Bar-Cohen Y., T. Xue, M. Shahinpoor, J. Simpson, J. Smith, Proc. Robotics '98, American Society of Civil Engineers, ASCE, Albuquerque, NM 1998, pp. 15–21.

Becquet, M. (1987). Analysis of flexibility sources in robot structure. *Proceedings of IMACS/IFAC International Symposium Modeling and Simulation of Distributed Parameters*, 419-424.

Behl M., A. Lendlein, Mater. Today 2007, 10, 20.

Behl M., K. Kratz, J. Zotzmann, U. Nöchel, A. Lendlein, Adv. Mater. 2013, 25, 4466.

BionicTOYS GmbH, fin-ray-bionicTOYS, http://bionictoys.de/fin-ray (accessed: November 2018).

Bingham, B., Foley, B., Singh, H., Camilli, R., Delaporta, K., Eustice, R., . . . Sakellariou, D. (2010). Robotic tools for deep water archaeology: Surveying an ancient shipwreck with an autonomous underwater vehicle. *Journal of Field Robotics, 27(6)*, 702-717.

Bouguet. (2013). Retrieved from http://www.vision.caltech.edu/bouguetj/calib_doc/

Brown, D. C. (1971). Close-range camera calibration. *Photogramm. Eng., 37*(8), 11007-11031.

Brown, E., Rodenberg, N., Amend, J., Mozeika, A., Steltz, E., Zakin, M. R., . . . Jaeger, H. M. (2010). Universal robotic gripper based on the jamming of granular material. *Proceedings of the National Academy of Sciences, 107*(44), 18809–18814.

Bruno, F., Gallo, A., Barbieri, L., Muzzupappa, M., Ritacco, G., Lagudi, A., . . . Guida, R. (2016). The CoMAS project: new materials and tools for improving the in-situ documentation, restoration and conservation of underwater archaeological remains. *Marine Technology Society Journal, 50(4)*, 108-118.

Bruno, F., Gallo, A., De Filippo, F., Muzzupappa, M., Davidde, B., & Caputo, P. (2013). 3D documentation and monitoring of the experimental cleaning operations in the underwater archaeological site of Baia (Italy). *Int. Conf. on Digital Heritage*.

Bruno, F., Muzzupappa, M., Gallo, A., Barbieri, L., Spadafora, F., Galati, D., . . . Petriaggi, R. (2015a). Electomechanical devices for supporting the restoration of underwater archaeological artefacts. *International Conference, OCEANS, Genova*.

Bruno, F., Muzzupappa, M., Lagudi, A., Gallo, A., Spadafora, F., Ritacco, G., . . . Laschi, C. (2015b). A ROV for supporting the planned maintenance in underwater archaeological sites. *Proceeding of IEEE/MTS OCEANS Conference.* Genova (Italy).

Calisti M., M. Giorelli, G. Levy, B. Mazzolai, B. Hochner, C. Laschi, P. Dario, Bioinspiration Biomimetics 2011, 6, 36002.

Casalino, G., Angeletti, D., Bozzo, T., & Marani, G. (2001). Dexterous underwater object manipulation via multi-robot cooperating systems. *Proceedings - IEEE International Conference on Robotics and Automation*, 3220 - 3225 .

CoMAS project, 2013. In-situ conservation planning of underwater archaeological artefacts. 28.11.18. http://www.comasproject.eu.

Davidde, B. (2002). Underwater archaeological parks: a new prospective and a challenge for conservation - the italian panorama. *The International Journal of Nautical Archaeology, 31.1*, 83-88.

Deimel R. and Brock O., "A novel type of compliant and underactuated robotic hand for dexterous grasping". Int. J. Rob. Res. 2016, 35, 161.

Delaney J., Beauchamp P., McNutt M., Barnes C., Chave A., and Madden J., "Project NEPTUNE: an interactive, regional cabled ocean observatory in the Northeast Pacific," Oceans Conf. Record (IEEE), vol. 2, pp. 1038-1042, 2003.

Denavit, J., & Hartenberg, R. (1955). A kinematic notation for lower-pair mechanisms based on matrices. *Journal of Applied Mechanics, 77 (2), 215-221*.

Deole U., R. Lumia, M. Shahinpoor, M. Bermudez, J. Micro-Nano Mechatronics 2008, 4, 95.

De Novi G., Melchiorri C., Garcia J. C., Sanz P. J., Ridao P., and Oliver G., "A new approach for a reconfigurable autonomous underwater vehicle for intervention," Proceedings of the 3rd. Annual IEEE International Systems Conference, pp. 23-26, 2009.

Driels, M., & Swayze, W. (1994). Automated partial pose measurement system for manipulator calibration experiments. *IEEE Transactions on Robotics and Automation*, 430-440.

Dunnigan M. W. and Russell G. T., "Evaluation and reduction of the dynamic coupling between a manipulator and an underwater vehicle," IEEE Journal of Oceanic Engineering, vol. 23, no. 3, pp. 260-273, July 1998.

Elatta, A. Y., Gen, L. P., Zhi, F. L., Daoyuan, Y., & Fei, L. (2004). An overview of robot calibration. *Information Technology Journal*, 74-78.

Escartin, J., Garcia, R., Delaunoy, O., Ferrer, J., Gracias, N., Elibol, A., . . . Renard, J. (2008). Globally aligned photomosaic of the Lucky Strike hydrothermal vent field (Mid-Atlantic Ridge, 3718.5N): Release of georeferenced data, mosaic construction, and viewing software. *Geochem. Geophys. Geosyst., 9(12)*.

Eustice, R., Singh, H., & Leonard, J. (2006). Exactly Sparse Delayed-State Filters for View-Based SLAM. *IEEE Transactions on Robotics, 22(6)*, 1100-1114.

F. Bruno, G. Bianco, M. Muzzupappa, S. Barone, & A. V. Razionale. (2011). Experimentation of structured light and stereo vision for underwater 3D reconstruction. *Journal of Photogrammetry and Remote Sensing, ISPRS, 66*(4), 508-518.

Ferrer, J., Elibol, A., Delaunoy, O., Gracias, N., & Garcia, R. (2007). Large-area photo-mosaics using global alignment and navigation data. *MTS/IEEE OCEANS Conference, Vancouver, Canada*.

Festo Co. Ltd., MultiChoiceGripper | Festo Corporate, https://www.festo.com/group/en/cms/10221.htm (accessed: November 2018).

Festo Co. Ltd., FlexShapeGripper | Festo Corporate, https://www.festo.com/group/en/cms/10217.htm (accessed: November 2018).

Fossen T.I., Guidance and Control of Ocean Vehicles, Chichester New York, 1994.

Fujii T. and Ura T., "Development of an autonomous underwater robot "Twin- Burger" for testing intelligent behaviors in realistic environments," Autonomous Robots, vol. 3, pp. 285-296, 1996.

G. Bianco, A. Gallo, F. Bruno, & M. Muzzupappa. (2013). A comparative analysis between active and passive techniques for underwater 3D reconstruction of close-range objects. *Sensor, 13*(8), 11007-11031.

Galloway, K. C., Becker, K. P., Phillips, B., Kirby, J., Licht, S., Tchernov, D., . . . Gruber, D. F. (2016). Soft Robotic Grippers for Biological Sampling on Deep Reefs. *Soft Robotics, 3*(1), 23-33.

Gatti, G., & Danieli, G. (2006). Validation of a calibration technique for 6-DOF instrumented spatial likages. *Journal of Biomechanics*, 1455-1466.

Gatti, G., & Danieli, G. (2008). A practical approach to compensate for geometric errors in measuring arms: application to a six-degree-of-freedom kinematic structure. *Measurement Science and Technology*, 1-12.

Ge Q., A. H. Sakhaei, H. Lee, C. K. Dunn, N. X. Fang, M. L. Dunn, Sci. Rep. 2016, 6, 1.

Geiger, A., Roser, M., Urtasun, R., 2011. Efficient large-scale stereo matching. In: Computer Vision-ACCV 2010. Springer, Berlin Heidelberg, pp. 25–38.

Goswami, A., Quaid, A., & Peshkin, M. (1993). Identifying robot parameters using partial pose information. *IEEE Control Systems* , 6-14.

Grabit Inc., Grabit electroadhesion robotic each pick gripper -boxes, bags, cans, bare goods, https://www.youtube.com/watch?v=RiAiNjd6ukk (accessed: November 2018).

Hager, G. D., Chang, W.-C., & Morse, A. S. (1995). Robot hand-eye coordination based on stereo vision. *IEEE Control Systems* , 30-39.

Hawkes E. W., D. L. Christensen, A. K. Han, H. Jiang, M. R. Cutkosky, in IEEE Int. Conf. Robotics and Automation, IEEE, Piscataway, NJ, USA 2015, pp. 2305–2312.

Heikkila, J., & Silvén, O. (1997). A Four-step Camera Calibration Procedure with Implicit Image Correction. *IEEE Computer Society Conference on Computer Vision and Pattern Recognition*, (p. 1106-1112). San Juan, Puerto Rico.

Heshmati-Alamdari S., Nikou A., Kyriakopoulos K. J., and Dimarogonas D. V., "A Robust Control Approach for Underwater Vehicle Manipulator Systems in Interaction with Compliant Environments," arXiv preprint arXiv:1611.07399, 2016.

Hildebrandt, H., Christensen, L., Kerdels, J., Albiez, J., & Kirchner, F. (2009). Realtime Motion Compensation for ROV-based Tele-operated Underwater Manipulators. *Oceans.* Biloxi, MS, USA.

Hollerbach J. M., A survey of kinematic calibration The Robotics Review 1 ed O Khatib, J J Craig and T Lozano (Cambridge, MA: MIT Press) 207– 42, 1989.

Hollerbach, J., & Wampler, C. (1996). The calibration index and taxonomy of kinematic calibration methods. *The International Journal of Robotics* , 573-591.

Ilievski F., A. D. Mazzeo, R. F. Shepherd, X. Chen, G. M. Whitesides, Angew. Chem., Int. Ed. Engl. 2011, 50, 1890.

Inglis, G., Smart, C., Vaughn, I., & Roman, C. (2012). A pipeline for structured light bathymetric mapping. *IEEE/RSJ Int. Conf. on Intelligent Robots and Systems*.

ISO 9283, 1998. Manipulating Industrial Robots - Performance Criteria and Related Test Methods. Standard. International Organization for Standardization, Geneva, Switzerland.

Johnson-Roberson, M., Pizarro, O., Williams, S. B., & Mahon, I. (2012). Generation and visualization of large-scale three-dimensional reconstructions from underwater robotic surveys. *Journal of Field Robotics, 27(1),* 21-51.

Jun B. H., Lee P. M., and Lee J., "Manipulability analysis of underwater robotic arms on ROV and application to task-oriented joint configuration," In: Proceeding of MTS/IEEE/TECHNO-OCEAN, November 2004.

Kawaguchi K., Momma H., and Iwase R., "VENUS PROJECTsubmarine cable recovery system," 1998 Int. Symp. on Underwater Technology (Cat. No.98EX101), pp. 448-452, 1998.

Kim, J., Yu, S.-C., & Yuh, J. (2013). Armless underwater manipulation using a small deployable agent vehicle connected by a smart cable. *Ocean Engineering, 70*, 149-159.

Kim H. Il, M. W. Han, S. H. Song, S. H. Ahn, Composites, Part B 2016, 105, 138.

Kofod G., W. Wirges, M. Paajanen, S. Bauer, Appl. Phys. Lett. 2007, 90, 89.

Kyo M., Hiyazaki E., Tsukioka S., Ochi H., Y. Amitani, T. Tsuchiya, T. Aoki, and S. Takagawa, "The sea trial of KAIKO", the full ocean depth research ROV," Proceedings of MTS/IEEE OCEANS 1995, vol. 3, pp. 1991-1996, 1995.

La Russa, M., Ricca, M., Belfiore, C., Ruffolo, S., Álvarez De Buergo Ballester, M., & Crisci, G. M. (2015). The contribution of earth sciences to the preservation of underwater archaeological stone materials: an analytical approach. *International Journal of Conservation Science, 6 (3)*, 335-348.

Lagudi, A., Bianco, G., Muzzupappa, M., Bruno, F., 2016. An alignment method for the integration of underwater 3D data captured by a stereovision system and an acoustic camera. Sensors 16 (4), 536.

Lan C., C. Lin, C. Fan, IEEE/ASME Trans. Mechatronics 2011, 16, 141.

Lane, D. M., Davies, J. B., Casalino, G., Bartolini, G., Cannata, G., Veruggio, G., . . . Gracia, E. (1998). AMADEUS: advanced manipulation for deep underwater sampling. *IEEE Robotics & Automation Magazine*, 4(4):34 - 45.

Lau G. K., K. R. Heng, A. S. Ahmed, M. Shrestha, Appl. Phys. Lett. 2017, 110, 182906.

Laschi, C., Cianchetti, M., Mazzolai, b., Mergheri, L., Follador, M., & Dario, P. (2012). Soft Robot Arm Inspired by the Octopus. *Advanced Robotics*, 709-727.

Laschi, C., Mazzolai, B., & Cianchetti, M. (2016). Soft robotics: Technologies and system pushing the boundaries of robot abilities. *Science Robotics*, 1-11.

Lau, K., Hocken, R., & Haynes, L. (1985). Robot performance measurements using automatic laser tracking techniques. *Robotics and Computer-Integrated Manufacturing*, 227-236.

Lee P., Jun B., Kim K., Choi H., J. Li, C. Lee, S. Ryu, H. Baek, S. Hong, Y. Lim, D. Kim, S. Cho, D. Park, B. Gu, J. Lee, H. Jung, S. Yoon, C. Park, M. Choi, and Y. Seo, "Sea trials and experimental results of the deep-sea unmanned underwater vehicles," Hemire and Henuvy. In: Proceedings of International Symposium on Underwater Technology 2007, Tokyo, April 17–20, pp. 276–284.

Li Y., Y. Chen, Y. Yang, Y. Wei, IEEE Trans. Rob. 2017, 33, 446.

Liang X., Y. Sun, H. Wang, R. C. H. Yeow, S. L. Kukreja, N. Thakor, H. Ren, in IEEE RAS EMBS Int. Conf. Biomedical Robotics and Biomechatronics, IEEE, Piscataway, NJ, USA 2016, pp. 401–406.

Licht, S., Collins, E., Mendes, M. L., & Baxter, C. (2017). Stronger at Depth: Jamming Grippers as Deep Sea Sampling Tools. *Soft Robotics, 4*(4), 305-316.

Liu C. H., Huang G. F., Chiu C. H., Pai T. Y., J. Intell. Rob. Syst. Theory Appl. 2017, 1.

Ma R., Dollar A., IEEE Rob. Autom. Mag. 2017, 24, 32.

Marani, G. C., & Yuh, J. (2009). Underwater autonomous manipulation for intervention missions AUVs. *Ocean Engineering*(36), 15-23.

Marchand, E., Chaumette, F., Spindler, F., & Perrier, M. (2001). Controlling the manipulator of an underwater ROV using a coarse calibrated pan/tilt camera. *IEEE Int. Conf. on Robotics and Automation ICRA'*.

McMillan S., Orin D. E., and McGhee R. B., "Efficient dynamic simulation of an underwater vehicle with a robotic manipulator," IEEE Transaction on Systems, Man, and Cybernetics, vol. 25 (8), pp. 1194– 1206, 1995.

Mirman C. and Gupta K., "Identification of position independent robot parameter errors using special Jacobian matrices," International Journal of Robotics Research, vol. 12 (3), pp. 288–298, 1993.

Meggiolaro, M. A., Scriffignano, G., & Dubowsky, S. (2000). Manipulator calibration using a single endpoint contact constraint. *2000 ASME Design Engineering Technical Conference.* Baltimore, MD.

Menna, F., Nocerino, E., Remondino, F., 2018a. Photogrammetric modelling of submerged structures: influence of underwater environment and lens ports on threedimensional (3D) measurements. In: Remondino, F., Georgopoulos, A., González- Aguilera, D., Agrafiotis, P. (Eds.), Latest Developments in Reality-based 3d Surveying and Modelling. MDPI, Basel, Switzerland, pp. 279–303 2018.

Menna, F., Nocerino, E., Drap, P., Remondino, F., Murtiyoso, A., Grussenmeyer, P., Börlin, N. 2018. Improving underwater accuracy by empirical weighting of image observations. In ISPRS Technical Commission II Symposium 2018, Riva del Garda, Italy, June 3-7, 2018 (vol. 42), pp. 699–705.

Mooring, B., Roth, Z., & Driels, M. (1991). *Fundamentals of Manipulator Calibration.* New York: Wiley Interscience.

NaturalPoint Inc, 2017. OptiTrack Flex 13. 01.08.18. http://www.naturalpoint.com/ optitrack/products/tracking-tools-bundles.

Neuman, C. P., & Khosla, P. K. (1985). Parameter identification for robot control. *ASME Dynamic Systems: Modeling and Control*, 213-223.

NextEngine 3D Laser Scanner, 2017. ⟨http://www.nextengine.com⟩ (accessed 01.08.18).

Omodei, A., Legnani, G., & Adamini, R. (2001). Calibration of aMeasuring Robot: Experimental Resultson a 5 DOF Structure. *Journal of Robotic Systems*, 237-250.

Paduan, J., Caress, D., Clague, D., Paull, C., & Thomas, H. (2009). High-resolution mapping of mass wasting, tectonic, and volcanic hazards using the MBARI Mapping AUV. *Int. Conf. os Seafloor Mapping for Geohazard Assessment,* 7, 181-186.

Paek J., I. Cho, J. Kim, Sci. Rep. 2015, 5, 10768.

Peer, P., Solina, F., 2006. Where physically is the optical center? Pattern Recogn. Lett. 27 (10), 1117–1121.

Petkovic D., Pavlovic N. D., Shamshirband S., Anuar N. B., Ind. Rob. Int. J. 2013, 40, 610.

Phillips, B., Becker, K. P., Kurumaya, S., C.Galloway, K., Whittredge, G., M.Vogt, D., . . . J.Wood, R. (2018). A Dexterous, Glove-Based Teleoperable Low-Power Soft Robotic Arm for Delicate Deep-Sea Biological Exploration. *Scientific Reports, 8*, 1-9.

Pizarro, O., Eustice, R. M., & Singh, a. H. (2009). Large area 3-D reconstructions from underwater optical surveys. *IEEE Journal of Oceanic Engineering, 34(2)*, 150-169.

Prats, M., Fernandez, J., & Sanz, P. (2012). An approach for Semi-Autonomous Recovery of Unknown Objects in Underwater Environments. *IEEE Int. Conf. Optimization of Electrical and Electronic Equipment*.

Rahman, T., Krouglicof, N., 2012. An efficient camera calibration technique offering robustness and accuracy over a wide range of lens distortion. IEEE Image process 21, 626–637.

Renders, J.-M., Rossignol, E., Becquet, M., & Hanus, R. (1991). kinematic calibration and geometrical parameter identification for robots. *IEEE Transcation on robotics and automation*, 721-732.

Ribas, D., Ridao, P., Turetta, A., Melchiorri, C., Palli, G., Fernandez, J., & Sanz, P. (2015). I-AUV Mechatronics Integration for the TRIDENT. *IEEE-ASME Transactions on Mechatronics, 20*, 2583-2592.

Richmond, K., & Rock, S. M. (2006). An operational real-time large-scale visual mosaicking and navigation system. *IEEE OCEANS*.

Ridao, P., Carreras, M., Ribas, D., & Garcia, R. (2010). Visual inspection of hydroelectric dams using an autonomous underwater vehicle. *Journal of Field Robotics, 27(6)*, 759-778.

Rizzo, D., Bruno, F., Barbieri, L., Muzzupappa, M., 2017. Kinematic performances evaluation of a hydraulic underwater manipulator. In: Proceeding of IEEE/MTS OCEANS Conference. Aberdeen (UK).

Roth Z.S., Mooring B.W., and Ravani B., "An overview of robot calibration," in: IEEE Southcon Conference, Orlando, Florida, pp. 377– 384, 1986.

Rus D., Tolley M. T., "Design, fabrication and control of soft robots". Nature 2015, 521,467.

Ryu J. H., Kwon D. S., and Lee P. M., "Control of underwater manipulators mounted on an ROV using base force information," in Proceedings of the IEEE International Conference on Robotics and Automation (ICRA '01), pp. 3238–3243, May 2001.

Sagara, S., & Ambar, R. (2015). Development of a master controller for a 3-link dual-arm underwater robot. *Artif Life Robotics, 20*, 327–335.

Sagara, S., Ambar, R., & Imaike, K. (2014). Experiment on a dual-arm underwater robot using resolved acceleration control method. *Artif Life Robotics, 20*, 34-41.

Sakagami, N., Shibata, M., & Inoue, T. (2010). Development of a Human-Sized ROV with Dual-Arm. *Oceans Sydney*.

Sarkar N. and Podder T. K., "Coordinated motion planning and control of autonomous underwater vehicle-manipulator systems subject to drag optimization," IEEE Journal of Oceanic Engineering, vol. 26, no. 2, pp. 228–239, 2001.

Schaler E. W., D. Ruffatto, P. Glick, V. White, A. Parness, in IEEE/ RSJ Int. Conf. Intelligent Robots and Systems, IEEE, Piscataway, NJ, USA 2017, pp. 1172–1179.

She Y., J. Chen, H. Shi, H.-J. Su, Soft Rob. 2016, 3, 71.

Shepherd, R. F., Ilievski, F., Choi, W., Morin, S. A., Stokes, A. A., Mazzeo, A. D., . . . Whitesides, G. (2011). Multigait soft robot. *PNAS*, 20400–20403.

Shian S., K. Bertoldi, D. R. Clarke, Adv. Mater. 2015, 27, 6814.

Shim, H., Jun, B.-H., Lee, P.-M., Baek, H., & Lee, J. (2010). Workspace Control System of Underwater TeleOperated Manipulators on ROVs. *Ocean Engineering, 37*, 1036–1047.

Shintake, J., Cacucciolo, V., Floreano, D., & Shea, H. (2018). Soft robotic Grippers. *Advanced Materials*, 1-33.

Shintake, J., Rosset, S., Schubert, B., Floreano, D., & Shea, H. (2016). Versatile Soft Grippers with Intrinsic Electroadhesion Based on Multifunctional Polymer Actuators. *Advanced Materials*, 231-238.

Shirinzadeh, B., Teoh, P., Tian, Y., Dalvand, M. M., Zhong, Y., & Liaw, H. C. (2010). Laser interferometry-based guidance methodology for high precision positioning of mechanisms and robots. *Robotics and Computer-Integrated Manufacturing, 26*, 74-82.

Shortis, M., 2015. Calibration techniques for accurate measurements by underwater camera systems. Sensors 15 (12), 30810–30826.

Simetti E., Casalino G., Torelli S., Sperind A., and Turetta A., "Floating underwater manipulation: Developed control methodology and experimental validation within the trident project," Journal of Field Robotics, vol. 31(3), pp. 364-385, 2014.

Singh, H., Howland, J., & Pizarro, O. (2004). Advances in large-area photomosaicking underwater. *IEEE Journal of Oceanic Engineering, 29(3)*, 872-886.

Skarlatos, D., Agapiou, A., Rova, M., 2010. Photogrammetric support on an underwater archaeological excavation site: The Mazotos shipwreck case. Euromed 2010, Limassol. Cyprus 8–11.

Song S., D.-M. Drotlef, C. Majidi, M. Sitti, Proc. Natl. Acad. Sci. USA 2017, 114, E4344.

Stone H. W., Kinematic Modeling, Identification, and Control of Robotic Manipulators (Dordrecht: Kluwer Academic), 1987.

Stonex, 2017. X300 laser scanner. 01.08.18. http://www.stonexpositioning.com/index.php/en/product/laser-scanners/x300-detail.

Sivčev, S., Coleman, J., Omerdić, E., Dooly, G., and Toal, D. (2018). Underwater manipulators: A review. *Ocean Engineering*, 431-450.

Song S., M. Sitti, Adv. Mater. 2014, 26, 4901.

Sun, T., Zhai, Y., Song, Y., & Zhang, J. (2016). Kinematic calibration of a 3-DoF rotational parallel manipulator using laser tracker. *Robotics and Computer-Integrated Manufacturing*, 78-91.

Sun Z., L. Hao, W. Chen, Z. Li, L. Liu, Smart Mater. Struct. 2013, 22, 95027.

Suresh S. A., D. L. Christensen, E. W. Hawkes, M. Cutkosky, J. Mech. Rob. 2015, 7, 21005.

Suzumori, K., Iikura, S., & Tanaka, H. (1991). Development of flexible microactuator and its applications to robotic mechanisms. *IEEE Int. Conf. Robotics and Automation*, 1622-1627.

Suzumori, K., Iikura, S., & Tanaka, H. (1992). Applying a flexible microactuator to robotic mechanisms. *IEEE Control System*, 21-27.

Švaco, M., Šekoranja, B., Šuligoj, F., & Jerbić, B. (2014). Calibration of an Industrial Robot using a Stereo Vision System. *Proceding Engineering*, 459-463.

Tang, G.-R., & Liu, L.-S. (1993). Robot calibration using a single laser displacement meter. *Mechatronics*, 503–516.

Tavakoli M., P. Lopes, J. Lourenço, R. P. Rocha, L. Giliberto, A. T. De Almeida, C. Majidi, IEEE Sens. J. 2017, 17, 5669.

Terryn S., J. Brancart, D. Lefeber, G. Van Assche, B. Vanderborght, Sci. Rob. 2017, 2, eaan4268.

Tekscan. Accessed on 30/11/2018. https://www.tekscan.com/.

Unesco. (2001, November 2). *Convention on the protection of the underwater cultural heritage*. Tratto da http://www.unesco.org

Vaichav R. and Magrab E., "A general procedure to evaluate robot positioning errors," International Journal of Robotics Research, vol. 6 (1), pp 59–74, 1987.

Veitschegger, W. K., & Wu, C. H. (1986). Robot Accuracy Analysis Based on Kinematics. *IEEE Journal of Robotics and Automation*.

Vincze, M., Prenninger, J., & Gander, H. (1994). A laser tracking system to measure position and orientation of robot end effectors under motion. *International Journal of Robotics Research*, 305-314.

Waldron K. and Kumar V., "Development of a theory of errors for manipulators," in: Proceedings of the Fifth World Congress on the Theory of Machines and Mechanisms, pp. 821–826, 1979.

Wampler, C. W. (1995). An implicit loop method for kinematic calibration and its application to closed-chain mechanism. *IEEE Transactions on robotics and automation*.

Wang, L., Yao, J., Jia, P., & Wang, Z. (2009). Development of a 7-function Hydraulic Underwater manipulator System. *IEEE International Conference on Mechatronics and Automation*.

Wang W., H. Rodrigue, H. Il Kim, M. W. Han, S. H. Ahn, Composites, Part B 2016, 98, 397.

Wei, Y., Chen, Y., Ren, T., Chen, Q., Yan, C., Yang, Y., & Li, Y. (2016). A Novel, Variable Stiffness Robotic Gripper Based on Integrated Soft Actuating and Particle Jamming. *Soft Robotics, 3*(3), 134-143.

Weng, J., Cohen, P., & Herniou, M. (2002). Calibration of stereo cameras using a non-linear distorsion model. *IEEE Xplore*, 246-253.

Whitney, D., Lozinski, C., & Rourke, J. (1986). Industrial robot forward calibration method and results. *ASME Journal of Dynamic Systems, Measurement, and Control*, 1-8.

Whitney John P., Matthew F. Glisson, Eric L. Brockmeyer, and Jessica K. Hodgins, "A low-friction passive fluid transmission and fluid-tendon soft actuator", IROS conference, 2014.

Wu, C. H. (June 22-24, 1983). The kinematics error model for the design of robot manipulator. *American Control Conference.* San Francisco.

Wu C., "A kinematic CAD tool for the design and control of a robot manipulator," International Journal of Robotics Research, vol. 3 (1), pp 58–67, 1984.

Xiong, Y., Hirvonen, J., & Kallio, P. (2013). Three-dimensional calibration of micromanipulators using stereo vision. *Journal of Micro-Bio Robotics*, 13-24.

Z. Xu, E. Todorov, in IEEE Int. Conf. Robotics and Automation, IEEE, Piscataway, NJ, USA 2016, pp. 3485–3492.

Yamaguchi A., K. Takemura, S. Yokota, K. Edamura, Sens. Actuators. A 2011, 170, 139.

Yang, Y., Li, Y., & Chen, Y. (2018). Principles and methods for stiffness modulation in soft robot design and development. *Bio-Design and Manufacturing, 1*, 14-25.

Yuh J., "Design and Control of Autonomous Underwater Robots: A Survey," Autonomous Robots, vol. 8, pp. 7-24, 2000.

Yuh J., K. Choi S., C. Ikehara, G. H. Kim, G. McMurty, M. Ghasemi- Nejhad, N. Sarkar, and K. Sugihara, "Design of a semi-autonomous underwater vehicle for intervention missions (SAUVIM)," Proceedings of International Symposium on Underwater Technology. pp. 63-68, 1998.

Yuk H., S. Lin, C. Ma, M. Takaffoli, N. X. Fang, X. Zhao, Nat. Commun. 2017, 8, 1.

Zhu T., H. Yang, W. Zhang, in Int. Conf. Advanced Robotics and Mechatronics, IEEE, Piscataway, NJ, USA 2016, pp. 512–517.

Zhuang H., Wu J., and Huang W., "Optimal planning of robot calibration experiments by genetic algorithms," in: Proceedings of IEEE 1996 International Conference on Robotics and Automation, Minneapolis, pp. 981–986, 1996.

Zhuang, H., Masory, O., & Yan, J. (1995). Kinematic Calibration of a Stewart Platform Using Pose Measurements Obtained by a Single Theodolite. *IEEE Intelligent Robots and Systems*, 329-334.